Harmonic Domain Modelling and Analysis of the Electrical Power Systems of Onshore and Offshore Oil and Gas Field /Platform

by

Ikpe Chikwe Okara

A thesis submitted to the

School of Engineering

University of Glasgow

for the degree of

Doctor of Philosophy

October 2014

Electronics and Electrical Engineering
www.glasgow.ac.uk/engineering

Dedications

To Almighy God and the God of Chosen

Abstract

This thesis first focuses on harmonic studies of high voltage cable and power line, more specifically the harmonic resonance. The cable model is undergrounded system, making it ideal for the harmonics studies. A flexible approach to the modelling of the frequency dependent part provides information about possible harmonic excitations and the voltage waveform during a transient. The power line is modelled by means of lumped-parameters model and also describes the long line effect. The modelling depth and detail of the cable model influences the simulation results. It compares two models, first where an approximate model which make use of complex penetration is used and the second where an Bessel function model with internal impedance is used. The both models incorporate DC resistance, skin effect and their harmonic performances are investigated for steady-state operating condition. The methods illustrate the impotance of including detailed representation of the skin effect in the power line and cable models, even when ground mode exists. The cable model exhibit lower harmonics comparable to overhead transmission lines due to strong influence of the ground mode.

Due to the application of voltage source converter (VSC) technology and pulse width modulation (PWM) the VSC-HVDC has a number of potential advantages as compared with CSC-HVDC, such as short circuit current reduction, independent control of active power and reactive power, etc. With these advantages VSC-HVDC will likely be widely used in future oil and gas transmission and distribution systems. Modular multilevel PWM converter applies modular approach and phase-shifted concepts achieving a number of advantages to be use in HVDC power transmission. This thesis describes the VSC three-phase full-bridge design of sub-module in modular multilevel converter (MMC). The main research efforts focus on harmonic reduction using IGBTs switches, which has ON and OFF capability. The output voltage waveforms multilevel are obtained using pulse width modulation (PWM) control. The cascaded H-bridge (CHB) MMC is used to investigate for two-level, five-level, seven-level, nine-level converter staircase waveforms. The results show that the harmonics are further reduced as the sub-module converter increases.

The steady-state simulation model of the oil platform for harmonic studies has been developed using MATLAB. In order to save computational time aggregated models are used.

The load on the platforms consists of passive loads, induction motors, and a constant power load representing variable speed drives on the platforms. The wind farm consists of a wind turbine and an induction machine operating at fixed speed using a back-to-back VSC. Simulations are performed on system harmonics that are thought to be critical for the operation of the system. The simulation cases represent large and partly exaggerated disturbances in order to test the limitations of the system. The results show low loss, low harmonics, and stable voltage and current.

With the developments of multilevel VSC technology in this thesis, multi-terminal direct current (MTDC) systems integrating modular multilevel converters at all nodes may be more easily designed. It is shown that self-commutated Voltage Source Converters (VSC) is more flexible than the more conventional Current Source Converter (CSC) since active and reactive powers are controlled independently. The space required by the equipment of this technology is smaller when compared to the space used by the CSCs. In addition, the installation and maintenance costs are reduced. With these advantages, it will be possible for several oil and gas production fields connected together by multi-terminal DC grid. With this development the platforms will not only share energy from the wind farms, but also provide cheaper harmonic mitigation solutions.

The model of a multi-terminal hypothetical power system consisting of three oil and gas platforms and two offshore wind farm stations without a common connection to the onshore power grid is studied. The connection to the onshore grid is realized through a High Voltage Direct Current (HVDC) transmissions system based on Voltage Source Converter (VSC) technology.

The proposed models address a wide array of harmonic mitigation solutions, i.e., (i) Local harmonic mitigation (ii) semi-global harmonic mitigation and (iii) global harmonic mitigation. In addition, a computationally-efficient technique is proposed and implemented to impose the operating constraints of the VSC and the host IGBT-PWM switches within the context of the developed harmonic power flow (HPF). Novel closed forms for updating the corresponding VSC power and voltage reference set-points are proposed to guarantee that the power-flow solution fully complies with the VSC constraints. All the proposed platform models represent (i) the high voltage AC/DC and DC/AC power conversion applications under balanced harmonic power-flow scenario and (ii) all the operating limits and constraints of the nodes and its host modular converter (iii) three-phase VSC coupled IGBT-PWM switches.

Acknowledgements

First, I would like to express my deepest gratitude to Professor Olimpo Anaya-Lara and Calum Cossar, my supervisors, for giving me the opportunity to explore the field of harmonics in power systems engineering, and for their encouragement and guidance during the research.

I would like to thank Professor Enrique Acha for his very useful comments and encouragement at the first, one and half year of the research.

I gratefully acknowledge my colleagues and friends at the Department of Electronics and Electrical Engineering for making such a productive working environment.

Finally, I would like to thank my wife Joy, my three sons Dominion, Chris and Prosper, my daughter Joyce and my mother Lucy for their prayers and support.

Contents

Abstract **iii**

Acknowledgements ..... **v**

List of Figures ..... **xi**

List of Tables ..... **xvi**

Abbreviations and Nomenclature ..... **xvii**

Symbols **xviii**

1. Introduction **1**

1.1. Linear and Nonlinear Loads 3

1.2. Motivation of the Research Project 8

1.3. Objectives of the Research Project 9

1.4. Contributions 9

1.5. Thesis Outline 10

1.6. Journal Papers 11

1.6.1. Conference Papers 12

1.7. References 12

2. Contemporary and Future Oil and Gas Field/Platforms Power Systems **14**

2.1. Introduction 14

2.2. Early Oil and Gas Field/Platform Electrical Power Systems 18

2.3. The Present Day Oil and Gas Platform Electrical Power Systems 19

2.4. Future Development of Electrical Power Systems with zero-load Generator in Oil and Gas Field/Platform. 22

2.5. Conclusions **27**

2.6. References **28**

3. Power Network Analysis in the Harmonic Domain **37**

3.1. Introduction 37

3.3. Harmonic Modelling and Simulation 38
3.3.1. Frequency Scan 39
3.3.2. Simple Distortion Calculations 40
3.3.3. Harmonic Power Flow Methods 43
3.4. Modelling of Harmonic Source 44
3.4.1. Power Electronics Converters 46
3.4.2. VSC-HVDC Stations 46
3.5. Harmonic Producing Loads 47
3.6. Methods for Determining Sources of Harmonic Distortion 48
3.6.1. Harmonic Power Flow Direction Method 49
3.6.2. Load Impedance Variation Method 51
3.7. Total Harmonic Voltage Distortion (V_{THD}) and Current Distortion(I_{THD}) 53
3.8. Total Harmonic Distortion 53
3.9. Harmonic Current Magnitude and its Effect on Voltage Distortion 54
3.10. General Discussion on Fourier Series 54
3.10.1. Harmonic Power 57
3.11. Conclusions 57
3.12. References 58
4. Harmonic Modelling of Power Line and Power Cable Systems 62
4.1. Introduction 62
4.2. Harmonic Modelling of Overhead Transmission Lines 63
4.2.1. Evaluation of Lumped Parameters 64
4.2.2. Matrix of Potential Coefficients (P) 64
4.2.3. Impedance Matrix of Ground Return (Z_{G-E}) 65
4.2.4. Skin Effect Impedance Matrix Z_{Skin} 68
4.2.5. Reduced Equivalent Matrices Z_{abc} and Y_{abc} 71
4.3. Evaluation of Distributed Parameters 72

4.3.1. Modal Analysis at Harmonic Frequencies 72
4.3.2. Non-Homogeneous Lines 72
4.4. Test Case 1 76
4.4.1. Simulation Results 79
4.5. Harmonic Modelling of Underground and Subsea Cables 83
4.5.1. Ground Return Impedance of Underground Cables 85
4.6. Formation of Approximation Cable Model 88
4.6.1. Voltage Drops in the Cable System 89
4.6.2. The Impact of Skin Effect in Power Cables System 90
4.6.3. Test Case 2 92
4.6.4. Simulation Results 94
4.7. Bessel Function Concept Cable Model 98
4.7.1. The Impedance (Z) of Three-Layer Conductor 100
4.7.2. The Component Impedance 101
4.7.3. The Admittance (Y) of a Cable 103
4.7.4. The Potential Coefficient (P) of a Cable 104
4.8. Test Case 3 104
4.8.1. Simulation Results 106
4.9. Conclusions 110
4.10. References 111
5. Modular Multi-Level Voltage Source Converters for HVDC Applications 116
5.1. Introduction 116
5.1.1. Three-Phase Full-Bridge VSC and Operating Principle 118
5.2. Design of the DC Capacitor 123
5.3. Modular Multi-Level VSC with PWM-Unipolar 124
5.4. Multilevel Output-Voltage Generation 127
5.5. Modulation Method and Simulations Results 131
5.6. Conclusions 141

5.7. References 142

6. Harmonic Analysis of Wind Energy Generator with Voltage Source Converter Based HVDC Powering Oil and Gas Operations 145

6.1. Introduction 145

6.2. Offshore Operation of Wind Turbine Feeding Oil Platform 149

6.2.1. Wind Turbine Model 149

6.3. Induction Generator Modelling for Offshore Wind Turbine 154

6.3.1. SEIG with External Capacitor 154

6.3.2. Test Case Impact of Harmonic Injection Stabilizer and Capacitor Excitation 161

6.4. Steady-State Harmonic Model of the VSC-HVDC 165

6.4.1. VSC-HVDC Steady State Model 170

6.4.2. Sending and Received Voltage in Terms of Power and Reactive Power 172

6.5. Harmonic Determination Needed in the Capacitor Bank 176

6.6. Harmonic Deriving Point Impedance of Oil Platform 180

6.6.1. Determination of the Base Voltages 183

6.6.2. Further Simulation Results 190

6.6.3. Impact of Advance Static Var Controller (ASVC) 192

6.6.4. Impact of Tuned Reactor Filter 198

6.7. Conclusions 200

6.8. References 201

7. Harmonic Modelling of Multi-Terminal HVDC-VSC Oil and Gas Platforms 206

7.1. Introduction 206

7.2. Harmonic Power Flow 209

7.2.1. Switching Function Mode of the Rectifier Process 209

7.3. Potential Application of the Admittance (Y) Matrix of the Five Buses 211

7.4. Deriving Unknown Nodal Harmonic Voltages and Currents 213

7.4.1. Newton-Raphson Conventional Power Flow: Test Case 1 216

7.5. Harmonic Power Flow: Test Case 2 220

7.6. Conclusions 231

7.7. References 232

8. Conclusions and Further Works 234

8.1. Conclusions 234

8.2. Recommendations 237

8.3. Further Work 238

Appendix 240

List of Figures

Figure 1.1 Voltage signals: (a) Undistorted current signal (b) Distorted current signal..... 1

Figure 1.2 Relation among voltages in a purely resistive circuit..... 4

Figure 1.3. Relation among voltages in a distorted resistive circuit..... 6

Figure 2.1. Early oil platform electrical power system. 14

Figure 2.2. Present day oil and gas electrical power system layout 15

Figure 2.3. Active harmonic filters (AHF) in power systems to monitors the AC line..... 17

Figure 2. 4a. Block Diagram of multi-terminal HVDC-VSC Scheme for oil and gas 25

Figure. 2.4b. Proposed multi-terminal systems of onshore platform, offshore platform..... 26

Figure. 3.1 Resonance peaks..... 40

Figure. 3.3 (a) Typical harmonic spectrum and (b) signal..... 42

Figure. 3.4 (a) Typical harmonic spectrum and (b) signal..... 42

Figure 3.5. A single dominant source of harmonics (a) the phase signal (b) magnitude..... 45

Figure 3.6. Norton equivalent circuits for harmonic current source type load 47

Figure 3.7. Thevenin equivalent circuit for harmonic voltage source type load..... 48

Figure. 3.8. Norton equivalent circuit of a utility customer interface..... 49

Figure. 3.9. Thevenin equivalent circuit of a utility customer interface..... 50

Figure. 3.10 Plot of load parameter variation..... 52

Figure. 3.11 (a) Voltage waveform (b) harmonic spectrum..... 56

Figure 4.1. Line geometry and its image..... 65

Figure 4.2. Line geometry and its image using the complex penetration approach 66

Figure 4.3. ACSR conductors..... 70

Figure 4.4. Transmission equivalent line π-circuits..... 75

Figure 4.5. Power transmission line 77

Figure 4.6. Transmission line terminal conditions (a) voltage of source and open-ended..... 77

Figure 4.7. Three-phase receiving end harmonic voltage excitation, 100km long 80

Figure 4.8. Three-phase receiving end harmonic voltage excitation, 300km long 80

Figure 4.9. Three-phase receiving end harmonic voltage excitation, 500km long 80

Figure 4.10. Three-phase receiving end harmonic voltage excitation, 800km long 81

Figure 4.11. Three-phase receiving end harmonic current excitation, 100km long 82

Figure 4.12. Three-phase receiving end harmonic current excitation, 300km long 82

Figure 4.13. Three-phase receiving end harmonic current excitation, 500km long 82

Figure 4.14. Three-phase receiving end harmonic current excitation, 500km long 83

Figure 4.15 Internal impedance of the cable system (a) without ground returns 86

Figure 4.16 Geometric configurations of two SC underground cables and its images 87

Figure 4 .17. An equivalent circuit for impedances of a single-core underground cable 89

Figure 4.18. A cable sheath solidly bonded to the ground 89

Figure 4.19. Geometry of the case study three single-phase cables laying in a flat 92

Figure 4.20. Harmonic Impedance without voltage and current excitation 95

Figure 4. 21.1km long cable with first resonant peak appear at h = 350, NH = 500 96

Figure 4.22 5km long cable with first resonant peak to appear at h = 70, NH = 400, ... 97

Figure 4.23 10km long cable with first resonant peak to appear at h = 30, NH = 250 98

Figure 4.24An equivalent circuit for impedances of single-core cables (SC cable) 100

Figure 4.27. Receiving end in open circuit and 1 p.u. harmonic voltage injection 5km 108

Figure 4.28. Receiving end in open circuit and 1 p.u. harmonic voltage injection 10km 109

Figure 5.1 Two-Level Three-Phase VSC 118

Figure 5.2 Reference signals and carrier signal 119

Figure 5.3. Two-level Phase Switching Function of a VSC one Unipolar PWM Converter (a)Output voltage of phase a and phase b; (b) The amplitude of all harmonic spectrum for the output voltage of phase a and phase b; (c) Output voltage of phase b and phase c; (d) The amplitude of all harmonic spectrum for the output voltage of phase b and phase c; (e) Output voltage of phase c and phase a; (f) The amplitude of all harmonic spectrum for the output voltage of phase c and phase a 122

Figure 5.4: Modular Multi-Level Three-Phase VSC 127

Figure 5.5 Five-level Phase Switching Function of a two VSC Unipolar PWM Converters (a)Output voltage of phase a and phase b; (b) The amplitude of all harmonics for the output voltage of phase a and phase b; (c) Output voltage of phase b and phase c; (d) The amplitude of all harmonics for the output voltage of phase b and phase c; (e) Output voltage of phase c and phase a; (f) The amplitude of all harmonics for the output voltage of phase c and phase a..... 129

Figure 5.6 Five-level line-to-line Switching Function of a two VSC Unipolar PWM Converters Output voltage of phase a and phase b; (b) The amplitude of all harmonics for the output voltage of phase a and phase b; (c) Output voltage of phase b and phase c; (d) The amplitude of all harmonics for the output voltage of phase b and phase c; (e) Output voltage of phase c and phase a; (f) The amplitude of all harmonics for the output voltage of phase c..... 130

Figure 5.7 Seven-level Phase Switching Function of a three VSC Unipolar PWM Converters Output voltage of phase a and phase b; (b) The amplitude of all harmonics for the output voltage of phase a and phase b; (c) Output voltage of phase b and phase c; (d) The amplitude of all harmonics for the output voltage of phase b and phase c; (e) Output voltage of phase c and phase a; (f) The amplitude of all harmonics for the output voltage of phase c and phase a..... 132

Figure 5.8 Seven-level line-to-line Switching Function of a three VSC Unipolar PWM Converters. Output voltage of phase a and phase b; (b) The amplitude of all harmonics for the output voltage of phase a and phase b; (c) Output voltage of phase b and phase c; (d) The amplitude of all harmonics for the output voltage of phase b and phase c; (e) Output voltage of phase c and phase a; (f) The amplitude of all harmonics for the output voltage of phase c..... 133

Figure 5.9 Nine-level Phase Switching Function of a fourVSC Unipolar PWM Converters. Output voltage of phase a and phase b; (b) The amplitude of all harmonics for the output voltage of phase a and phase b; (c) Output voltage of phase b and phase c; (d) The amplitude of all harmonics for the output voltage of phase b and phase c; (e) Output voltage of phase c and phase a; (f) The amplitude of all harmonics for the output voltage of phase c and phase a..... 135

Figure 5.10 Nine-level line-to-line Switching Function of a four VSC Unipolar PWM Converters. Output voltage of phase a and phase b; (b) The amplitude of all harmonics for the output voltage of phase a and phase b; (c) Output voltage of phase b and phase c; (d) The amplitude of all harmonics for the output voltage of phase b and phase c; (e) Output voltage of phase c and phase a; (f) The amplitude of all harmonics for the output voltage of phase c..... 136

Figure 5.11. Eleven-level Phase Switching Function of a five VSC Unipolar PWM Converters Output voltage of phase a and phase b; (b) The amplitude of all harmonics for the output voltage of phase a and phase b; (c) Output voltage of phase b and phase c; (d) The amplitude of all harmonics for the output voltage of phase b and phase c; (e) Output voltage of phase c and phase a; (f) The amplitude of all harmonics for the output voltage of phase c and phase a..... 138

Figure 5.12. Eleven-level line-to-line Switching Function of a five VSC Unipolar PWM Converters Output voltage of phase a and phase b; (b) The amplitude of all harmonics for the output voltage of phase a and phase b; (c) Output voltage of phase b and phase c; (d) The amplitude of all harmonics for the output voltage of phase b and phase c; (e) Output voltage of phase c and phase a; (f) The amplitude of all harmonics for the output voltage of phase c 139

Figure 6.1. Schematic of Wind Farm Fed Oil Platform 146

Figure 6.2. Wind generator power curves at various wind speed 151

Figure 6.3. Wind turbine rotor mechanical power 152

Figure 6.4 speed characteristic of wind turbine with low and high gear ratios. 153

Figure 6.5. Self-excited induction generator with external capacitor. 155

Figure 6.6. Equivalent circuit of self-excited induction generator with R-L Load. 156

Table 6.1: Planning Levels for Harmonics Voltage 158

Figure 6.7. Maximum capacitance at 5^{th} harmonic 161

Figure 6.9. Maximum capacitance at 7^{th} harmonics 162

Figure 6.10 Exciter load-saturation curve at 7^{th} harmonic 162

Figure 6.11 Maximum capacitance at 13^{th} harmonic 163

Figure 6.12 Exciter load-saturation curve at 13^{th} harmonic 163

Figure 6.14. Exciter load-saturation curve at 29^{th} harmonic 164

Figure 6.15 Voltage source converter equivalent model 165

Figure 6.16 shows the charging and discharging curves 166

Figure 6.17. Voltage and current of DC capacitor 166

Figure 6.18. PI controller design and responses 167

Figure 6.19. Voltage and current in the DC side 169

Figure 6.20. Frequency Contents of Vdc 170

Figure 6.21. Frequency Content of Vdc with its complex conjugate 170

Figure 6.22. Input current of the (a) rectifier and (b) inverter 171

Figure 6.23. Output voltage of wind speed side and AC output voltage 171

Figure 6.24. Active and reactive power of VSC1 and VSC2 with DC link impedance 174

Figure 6.25. Active and reactive power of VSC1 and VSC2 without DC 174

Figure 6.26. Load angle and voltage magnitude control of the generator-side converter 175

Figure 6.27. Load angle and voltage magnitude control of the platform-side converter 175

Figure 6.28. Series resonance harmonic point with damping in OG 1 177

Figure 6.29. Series resonance harmonic point without damping in OG 1 178

Figure 6.30. Series resonance harmonic point with damping in OG 2 179

Figure 6.31. Series resonance harmonic point without damping in OG 2 179

Figure 6.32. (a) Harmonic resonance impedance with capacitor bank (b) Harmonic 192

Figure 6.33. Static Var compensator 192

Figure 6.34. (a) Harmonic resonance impedance with SVC (b) Harmonic voltage 195

Figure 6.35. (a) Harmonic resonance impedance with SVC and capacitor bank 196

Figure 6.36. (a) Harmonic resonance impedance with motor starting (b) Harmonic 197

Figure 6.37. (a) Harmonic resonance with tune filter (b) Harmonic voltage spectrum of 199

Figure 6.38. SVC current and capacitor current as afunction of system impedance 200

Figure 7.1. Multi-terminal network with modular multi-level converter used to obtain 208

Figure 7.2. Instantaneous input signal waveforms at (a) bus 1 (b) bus 2 (c) bus 3 (d) bus 218

Figure 7.3. Three Phase Current Waveform 219

Figure 7.4. Load bus current waveform 220

Figure 7.5. Voltage control bus waveform 220

Figure 7.6. DC voltage and current at switching frequency 222

Figure 7.7. Frequency Content of Vdc with its complex conjugate 222

Figure 7.8. Input Current 223

Figure 7.9. (a)Capacitor voltage (b) Capacitor current 223

Figure 7.10. Voltage conditions at each node of the five VSCs bus 224

Figure 7.11. The instantaneous real and reactive powers of the five-bus network 226

Figure 7.13. The instantaneous real and reactive powers of the five-bus network 230

List of Tables

Table 1.1. Examples of linear loads **5**

Table 1.2. Example of nonlinear loads **5**

Table 6.1: Planning Levels for Harmonics Voltage **158**

Table 6.2. Platform component datas **181**

Table 6.3. The base impedances and currents **184**

Table 6.4. Convert transformer impedances to per unit **184**

Table 6.5. Transformer Impedances **185**

Table 6.7. Convert motor impedances to per unit **186**

Table 6.8. Motor impedances **186**

Table 6.9. Harmonic currents for the variable frequency drive **187**

Table 6.10. Convert generator impedance to per unit **187**

Table 6.11. Generator impedance **188**

Table 6.12: Capacitor bank impedances **189**

Table 7.3: Simulation Parameters **221**

Abbreviations and Nomenclature

HVDC	High Voltage Direct Current
VSC	Voltage Source Converter
HVDC-VSC	HVDC station based on voltage source converter
GTO	Gate-Turn-Off Thyristor
IGBT	Insulated Gate Bipolar Transistor
PWM	Pulse-Width Modulation
STATCOM	Static Compensator
AC or ac	Alternating Current
DC or dc	Direct Current
HVC	High Voltage Cable
PCC	Point of Common Coupling
SC	Single-Core
HD	Harmonic Domain
HPF	Harmonic Power Flow
PQ	Power Quality
EMI	Electromagnetic Interference
THD	Total Harmonic Distortion
IHPA	Instantaneous Harmonic Power Analytical
Fis	Is the phase angle in radian of the modulation signal
CO_2	Carbon Dioxide
EMF	Electromotoric Force, Induced Voltage
ESC	Equivalent Short Circuit Power
ESCR	Equivalent Short Circuit Ratio
MAP	Maximum Available Power
PI	Proportional+Integral
PLL	Phase Locked Loop
RMS	Root Mean Square
SC	Short Circuit Power
SCR	Short Circuit Ratio
Sm^3	Standard Cubic metre
SVC	Static VAr Compensator
TCR	Thyristor Controlled Reactor
TOV	Temporary Overvoltages
CHB	Cascaded H-Bridge
MMC	Modular Multilevel Converter
DFT	Discrete Fourier Transform
UPS	Uninterruptible Power Supply

Symbols

α		Firing angle
β		Pole wheel angle
b	B	Susceptance
c	C	Capacitance
Δt		Firing delay time
D		Damping constant
d_{xN}		Rated relative inductive voltage drop
e	E	Induced voltage, EMF
e_k		Relative short circuit voltage
	ESC	Equivalent short circuit power
	ESCR	Equivalent short circuit ratio
γ		Extinction angle
g	G	Conductance
i_{s0}		Initial short circuit current
j		Complex operator
J		Inertia
k		Constant
l	L	Inductance
m	M	Torque
p	P	Active power
q	Q	Reactive power
r	R	Resistance
ra	Ra	Stator resistance
s	S	Apparent power
SC		Short circuit power
SCR		Short circuit ratio
τ		Period
T		Time constant
u	U	Voltage
u_{dio}	U_{dio}	Ideal no-load direct voltage
x	X	Reactance
x_{ad}	X_{ad}	Mutual reactance
xk	Xk	Commutation reactance
ψ		Magnetic flux
y	Y	Admittance
z	Z	Impedance
	Ω	Rotational speed
*		Complex conjugate
r_0		Outer radius (m)
r_i		Inner radius (m)
σ		Earth conductivity in S/m
ω		Angular frequency $\omega = 2\pi f$
μ_0		Magnetic permeability of vacuum $\mu_0 = 4\pi * 10^{-7} H/m$
a, b, c		Phases a, b, c, respectively
$i_a(t)$		Line current in phase a in time domain

$i_b(t)$	Line current in phase b in time domain
$i_c(t)$	Line current in phase c in time domain
$v_a(t)$	Phase voltage in phase a in time domain
$v_b(t)$	Phase voltage in phase b in time domain
$v_c(t)$	Phase voltage in phase c in time domain
ε_0	Permittivity of vacuum $\varepsilon_0 = 8.85*10^{-12} F/m$
ε_r	Insulation relative permittivity

Chapter 1

1. Introduction

Voltages and currents in power systems are sinusoidal in nature with a fundamental frequency typically 50 Hz or 60 Hz [1]. The design of these systems is based on an assumption that the voltages and currents are not distorted by harmonic components as shown in Fig. 1.1a. In the majority of existing power systems this assumption is true and the effects of harmonics can be ignored in the absence of nonlinear loads.

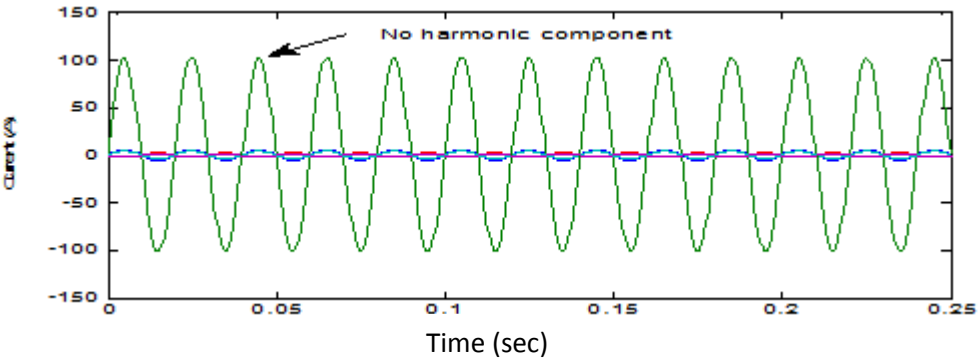

(a)

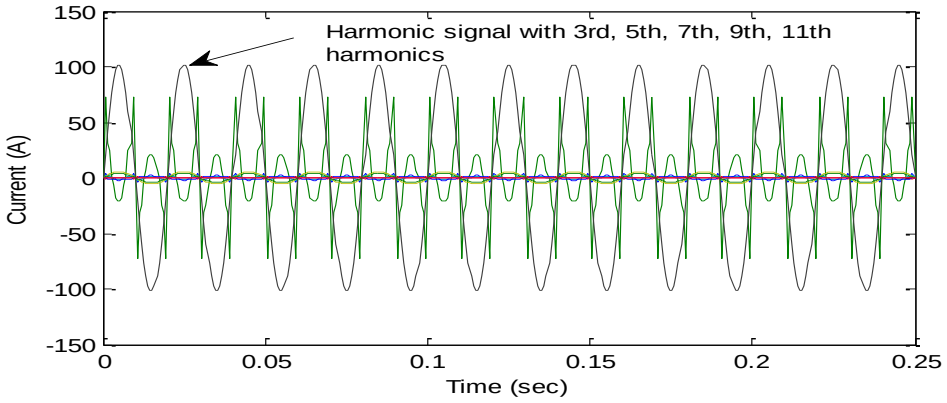

(b)

Figure 1.1 Voltage signals: (a) Undistorted current signal (b) Distorted current signal

However, situations do arise when the design must take account of harmonics as shown in Fig. 1.1b. Such consideration may be necessary at the beginning of a new project or for a plant that already exists. In the former, the minimisation of the negative effects of

harmonics is reasonably easy to accomplish. While in the latter it is usually more difficult due to constraints that may not be removable or reducible.

In AC power system applications where the current naturally goes through zero, the thyristor remains popular due to its low conduction power losses, its reverse voltage blocking capability and very low control power requirement. In fact, in very high power (in excess of 50 MW) AC – DC (phase-controlled converters) or AC – AC (cyclo-converters) converters, thyristors remain the device of choice. The development of the gate-turn-off thyristor (GTO) and the insulated-gate bipolar transistor (IGBT) which are fast, cheaper and more reliable with ON and OFF characteristics has facilitated the increase of power electronic applications in power systems. With the advent of the high-power Insulated-Gate Bipolar Transistor (IGBT), a new era in HVDC technology commenced. This new component was introduced as the main building block of the valves of a new generation of HVDC converters. The main difference between thyristors and IGBTs in the operation of the power converter is the turn-off capability of the latter. This seemingly small difference has completely revolutionised the world of HVDC: the use of IGBTs instead of thyristors is not a development comparable to the transition from mercury-arc valves to thyristor valves, but a step change that required a complete change in the layout and design philosophy of the converter stations, greatly expanding the range of applications of HVDC [2]. Converters with IGBTs did not replace converters with thyristors: both systems exist because their field of application is not the same. To distinguish between both systems, the term Current Source Converter (CSC) HVDC is used for the thyristor converter HVDC, and Voltage Source Converter (VSC) for the IGBT converter HVDC. Alternatively, they are referred to as line-commutated and self-commutated converters respectively. VSC-HVDC is more flexible than CSC HVDC, requires less space and opens up a wide range of new applications, such as integration of renewable energy. The increasing use of nonlinear loads in oil and gas power networks is in turn increasing levels of harmonic distortion. The most used nonlinear devices are perhaps rectifiers, multipurpose motor speed drives, and electrical transportation systems (VSC-HVDC). In addition, a scenario that has increased waveform distortion levels in distribution networks is the application of capacitor banks for power factor correction used in industrial plants and by power utilities to enhance voltage profile. When reactive impedance constitutes a tank circuit with system inductive reactance at a certain frequency, this may result to collision with one of the characteristic harmonics of the load. In this situation large oscillatory currents and voltages will be generated which may cause insulation stress.

When a voltage and/or current waveform is distorted, it causes abnormal operating conditions in a power system network such as:

- Voltage harmonics can cause additional heating in induction and synchronous motors and generators.
- Voltage harmonics with high peak values can weaken insulation in cables, windings, and capacitors.
- Voltage harmonics can cause malfunction of different electronic components and circuits that utilize the voltage waveform for synchronization or timing.
- Current harmonics in motor windings can create Electromagnetic Interference (EMI).
- Current harmonics flowing through cables and transformer can cause higher heating over and above the heating that is created from the fundamental component.
- Current harmonics flowing through circuit breakers and switchgear can increase their heating losses.
- Resonant currents which are created by current harmonics and the different filtering topologies of the power system can cause capacitor failures and/or fuse failures in the capacitor or other electrical equipment.
- False tripping of circuit breakers and protective relays.

1.1. Linear and Nonlinear Loads

A load that draws current from a sinusoidal AC source presenting a waveform like that of Fig. 1.2 can be conceived as a linear load. Examples of nonlinear loads are shown in Table 1.1.

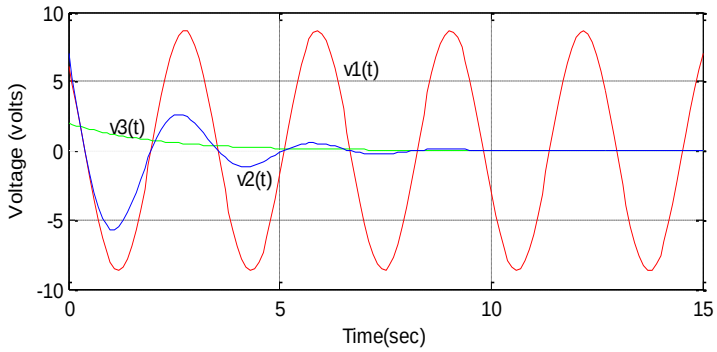

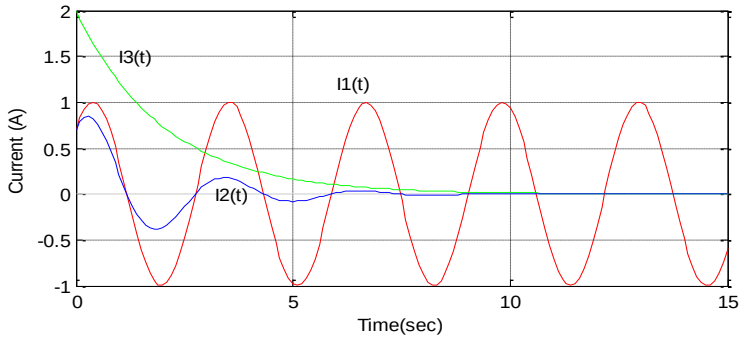

Figure 1.2 Relation among voltages in a purely resistive circuit.

Linear loads are those in which voltage and current signals follow one another considerably, such as the voltage drop that develops across a constant resistance, which varies as a direct function of the current that passes through it. This relation is better known as Ohm's law and states that the current through a resistance fed by a varying voltage source is equal to the relation between the voltage and the resistance, as described by:

$$i(t) = \frac{v(t)}{R} \tag{1.1}$$

If the source is a clean open circuit voltage, the current waveform will look identical, showing no distortion. Circuits with linear loads therefore make it simple to calculate voltage and current waveforms.

The involved power can also be determined as the product of the two quantities, voltage and current, i.e $P = V * I$.

A voltage and current waveform in a circuit with resistive loads will show the two waveforms in phase with one another. Voltage and current involving inductors make voltage lead current and circuits that contain power factor capacitors make current lead voltage. Therefore, in both cases, the two waveforms will be out of phase from one another. However, no waveform distortion will take place.

Nonlinear loads draw non-sinusoidal current, even when connected to a sinusoidal voltage source. Also, the voltage and current waveforms are not of the same shape and contain the fundamental frequency as well as harmonics of that fundamental due to a number of reasons. For example, the use of electronic switches that conduct load current only during a fraction of the power frequency period. Therefore, we can conceive nonlinear loads as those in which Ohm's law cannot describe the relation between V

and I. The breakdown of the current waveform including the six dominant harmonics is shown in Figure 1.3. Examples of nonlinear loads are shown in Table 1.2.

Table 1.1. Examples of linear loads

Resistive elements	**Inductive elements**	**Capacitive elements**
• Incandescent lighting • Electric heaters	• Induction motors • Current limiting reactors • Induction generators (wind generators) • Damping reactors used to attenuate harmonics • Tuning reactors in harmonic filters • Electrical motors driving fans • Water pumps • Oil pumps	• Power factor correction capacitor banks • Underground cables • Insulated cables • Capacitors used in harmonic filters

Table 1.2. Example of nonlinear loads

Power electronics	**ARC devices**
• Power converters/Inverters • Variable frequency drives • DC motor controllers • Cycloconverters • Power supplies • UPS • Battery chargers	• Fluorescent lighting • ARC furnaces • Welding machines

Variable speed DC motors are mainly used in the oil industry for powering drilling equipment such as the drill string, draw-works, mud pumps, cement pumps, winches and the propulsion systems in semi-submersible rigs and barges. They are typically rated at approximately 800 kW, 750 volts, and several motors may be operated mechanically in parallel. Each bridge that supplies a motor has a typical current rating of 2250 amps. The bridges are fed from a three-phase power source which is usually earthed by a high resistance fault detection device that gives an alarm but does not trip the source.

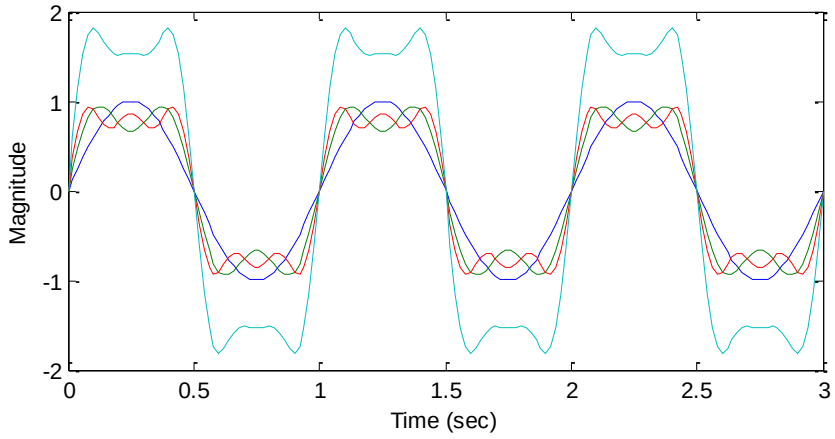

Figure 1.3. Relation among voltages in a distorted resistive circuit.

Oil and gas platforms harmonic studies are often faced with difficulties linked to solving high-order equations representing the system as a whole formed by a large number of facilities and loads. In the past decades it was difficult to model hundreds of nodes. Today, the development of simulation tools (such as MATLAB/SimPower) allows large power systems (with hundred nodes) to be modelled.

Oil installations in the North Sea utilize gas-fired turbines in order to generate their required electric energy. The turbines are placed on the platform and operate with a low efficiency due to area constraints and operation requirements. The efficiency lies in the range of 30 % for a typical offshore gas turbine. The turbines are often operated at part-load, causing further reductions in efficiency [4]. Impinging on this is the need for more sustainable energy supply (like wind energy) due to fast growing in oil and gas production. If an onshore/offshore wind farm is to take place, it is important to evaluate all different ways of harmonics studies and grid connection.

Offshore wind power is in the spotlight as an important renewable energy source. The location of the wind farms tends to be far from the shore to benefit from the stronger

and more constant wind. Also, the power output of the wind farm is increasing with large scale projects in the range of several hundred MW.

To allow for considerable amounts of offshore wind power and implement a stable supply to oil and gas installations an offshore grid has to be established. Due to the distance to shore HVDC transmission may be needed. The establishment of offshore AC grids offered the opportunity to connect wind farms and oil platforms within the limited distance of the AC cables. Several of these AC grids can be interconnected and connected to shore by a multi-terminal DC grid. A HVDC-VSC can be used as a link between these AC grids and a DC grid.

The use of back-to-back converters for wind turbine variable speed operation is promising to achieve maximum energy capture in a wide range of wind conditions. There is however little reference to the harmonics and control of back-to-back converters for low voltage ride-through capability of wind farms connected to the network [5][6].

Installation of offshore wind combined with supplying oil and gas installations raises important issues related to technical solutions, design and operation of the integrated system. In order to connect oil platforms it is important that the grid can deliver reliable power quality within given standards [7].

The modern oil and gas production field power systems are supplied with an increasing number of non-linear loads. These loads are harmonics and interharmonics sources which require accurate assessment. The harmonic analysis of the systems could be achieved with the use of Fast Fourier Transform (FFT) due to its faster and computational efficiency. Moreover, power metering and digital relays in oil and gas platforms could utilize FFT-Based algorithm to characterize harmonics of the measured signals [8].

An FFT approach will compute the values at multiple frequencies of the harmonic spectrum simultaneously, but will consume more resources. To achieve the performance levels, the amount of memory needed to store the samples used by the FFT algorithm is significantly high [9].

FFT algorithms are based on the fundamental principle of decomposing the Discrete Fourier Transform (DFT) computation of a sequence of length N into successively smaller DFT. Such algorithms vary in efficiency but all of them require fewer multiplications and additions than direct DFT does. Algorithms in which decomposition is based on decomposing a sequence x [n] into successively smaller subsequence are

called decimation in time algorithm. The basic idea is illustrated by considering special case of N as 2 to the power of a special integer, i.e. $N = 2^m$. Thus now N is an even integer. Then $F[k]$ can be computed by separating $f[n]$ into two (N/2) point sequences that consist of even harmonics of points and odd harmonics of points, in $f[n]$ [10].
With $F[k]$ given by:

$$F[k] = \frac{1}{N}\sum_{n=0}^{N-1} f[n] e^{-jkn2\pi/N} \qquad k = 0,1,2,\ldots,N-1 \tag{1.1}$$

Separating $f[n]$ into its even and odd number points, gives:

$$F[k] = \sum_{n=even} f[n] e^{-jn2\pi/N} + \sum_{n=odd} e^{-jkn2\pi/N} \tag{1.2}$$

1.2. **Motivation of the Research Project**

Modern oil and gas electrical power systems are being upgraded with a new breed of power electronics technology based on high switching frequency devices such as GTOs, IGBTs and PWM control. This new technology is creating new research and exciting challenges and opportunities at the transmission and distribution levels.

The new HVDC technology is entirely suitable for underground/submarine transmission and avoids the need for the existence of commutating sources (e.g. synchronous generators) on the oil platform. However, questions remain concerning the quality of the voltage waveform supplied by the new breed of HVDC converter technology, due to the significant amount of high-order harmonic distortion that the PWM control action introduces. Moreover, oil platforms contain a large number of non-linear loads such as power electronic rectifiers and saturated induction motors, which may interact adversely with the distorted incoming supply. The potential benefits promised by the off-site generation (wind farm) oil platforms are many, such as smaller footprints and increased security of supply; however, a comprehensive assessment of the oil platform power system is required at this stage of development. Harmonic generation, harmonic interactions, harmonic instabilities, harmonic elimination and non-linear load behaviour are all issues that should be well addressed with the use of harmonic models of relevant power plant components.

1.3. **Objectives of the Research Project**

This research project is concerned with developing comprehensive models of electrical power systems of both on-shore and off-shore oil platforms multi-terminal HVDC transmission links fed via remote wind farm generation. The HVDC converter stations involve use of IGBT-based VSCs operating at switching frequencies well above power frequencies but in the low range of kHz.

1.4. **Contributions**

The main contributions of the research work presented in this thesis are as follows:

- A flexible and comprehensive harmonic domain model of single-core, three-phase high power cables has been developed. The model is very flexible and takes proper account of the voltage magnitude reduction at harmonic resonance points due to the skin effect. The model was obtained using the complex depth concept. The approach may be used to develop accurate models of submarine cables.

- For the cable model, a simple equation which can be used for resonance analysis is obtained. The model was compared with an alternative formulation implemented in MATLAB using Bessel function techniques.

- A comprehensive harmonic domain model of three-phase VSC-PWM converters which caters for one, two and three unipolar PWM converters has been developed. The model takes proper account of the dc capacitor effect and the voltage ripple on the dc side which comes in the form of a three-phase equivalent circuit in the harmonic domain, where switching functions are used to represent the PWM control. The steady-state condition is taken into account by using an iterative process in order to maintain zero dc current through the capacitor.

- Using the VSC model as the basic building block, models for a modular multilevel converter that uses IGBTs or GTOs were obtained, which resulted in reduction of more harmonics and increased voltage levels.

- The two-terminal HVDC-VSC configurations were; the back-to-back and point-to-point. An explicit representation of the point-to-point is used since the model is in the frequency domain.

- An oil and gas multi-terminal HVDC-VSC model with integration of wind turbines was obtained. The mathematical equations are based on harmonic power flow methods. The power systems and power electronics equipment are modelled entirely in the harmonic domain. The Newton-Raphson method is used to solve the non-linear equations resulting from the network constraints.
- A flexible harmonic domain analysis solution of typical oil and gas platforms is obtained. Different cases such as, the effect of Static Var Compensator (SVC) with harmonic voltages and currents injection, power factor correction (capacitor bank), active and passive filters with uprising harmonic resonances are addressed. Each component is modelled based on harmonic domain considerations.

1.5. **Thesis Outline**

The thesis is organised as follows:

Chapters 2. This chapter reviews present oil and gas power networks and proposed future transmission and distribution levels where modular multi-terminal will offer smart wind turbine integration to oil and gas fields.

Chapter 3 presents the methodologies for harmonic studies.

Chapter 4 presents a new comparative approach to high voltage power cable, power line and functions in power network. This approach is based on an analysis of Bessel function simulation in simple steady states, to come up with principles and a comparative approximate model. It focuses on harmonic resonances. The approximate model results are compared with those obtained by the Bessel function expressions. Complete mathematical justifications of the process are provided.

Chapter 5 gives an explanation of the technological aspects of steady-state operation of MMC voltage source converters. The chapter presents a general model of the VSC for harmonic analysis using the harmonic domain technique. The chapter further proposes a new Modular Multi-Level VSC with PWM-unipolar for the first time using three-phase sub-modules, aiming at synthesizing a desired ac voltage from several levels of DC voltages and harmonic cancellations. The new cascaded-multilevel VSC with minimum number of isolated DC capacitors is also demonstrated to improve the switching loss and to increase the range of operation. A novel optimum modulation technique applied to the multilevel voltage-source converters is suitable for high-voltage power supplies and flexible AC transmission system devices are also introduced.

Chapter 6 analyses an electrical system for wind turbines with squirrel cage induction generators interfaced to the grid with back-to-back converters feeding an oil platform. Matlab simulations evaluate the fault ride-through capability under short circuits in the power system for different setting conditions of the converters. A model for the HVDC-VSC point to-point is also presented.

Chapter 7 presents the harmonic domain modelling of an oil/gas multi-terminal network integrating an offshore wind farm via an HVDC-VSC link. This involves integration of HVDC-VSC models in the unifying frame of reference afforded by the multi-node, multi-phase harmonic domain, a frame-of-reference that plays the role of a computing engine and is amenable to robust iterative solutions using Newton-type methods suitable for power flow studies.

Chapter 8. In this chapter the conclusions of the work and suggestions for future research are presented.

1.6. **Journal Papers**

1. **I.C. Okara**, and O. Anaya-Lara, Modelling and Analysis of Modular Multilevel Voltage Source Converter using Harmonic Domain Algebra.
   Under review

2. **I.C. Okara**, and O. Anaya-Lara, Comparative Assessment of Harmonic Resonance in High Voltage Cable Systems using Bessel and Approximate Models Submitted to *IEEE Transactions on Industry Applications.* December 2013.

3. **I.C. Okara**, O. Anaya-Lara, Harmonic Impedances and Resonances in Oil and Gas Field Power Systems with Wind Energy Integration.
   Submitted to *IET Renewable Power Generation.* January 2014.

4. **I.C. Okara**, O. Anaya-Lara, Harmonic Modelling of a Multi-terminal Offshore Network Interconnecting Oil and Gas Platforms and Wind Energy Sources. Submitted to *IET Generation Transmission & Distribution.* January 2014.

1.6.1. **Conference Papers**

2. **I.C. Okara**, and O. Anaya-Lara, Offshore Wind Farm Integration to Offshore Oil and Gas Platform using a New VSC-HVDC Model: Harmonic Analysis. Submitted to International Universities' Power Engineering Conference. September 2014.

3. **I.C. Okara**, and O. Anaya-Lara, Harmonic Injection Stabilizer for Offshore Wind Farm Induction Generator. Submitted to Renewable Power Generation Conference. September 2014.

1.7. References

[1] R.P. Bingham,"HARMONICS – Understanding the Facts"

[2] S. Cole and R. Belmans, "Transmission of bulk power: The history and applications of voltage-source converter high-voltage direct current systems," *IEEE Ind. Electron. Mag.*, p. 6, September 2009.

[3] J.Dorn, H. Huang, and D. Retzmann,"Novel voltage source converters for HVDC and FACTS applications," Cigr' eSymposium, Osaka Japan, 2008.

[4] T.F. Nestli, L. Stendius, M.J Johansson, A. Abrahamsson, and P.C Kjaer. "Powering troll with new technology". ABB REVIEW, (2):15–19, 2003.

[5] M. Godoy, B. K. Bose, and R. Spiegel, " Fuzzy logic based intelligent control of a variable speed cage machine wind generation system", IEEE Transactions on Power Electronics, vol. 12, NO. 1, pp. 87-95 (1997).

[6] J. Marvik, T. Bjørgum, B. Næss, T. Undeland, and T. Gjengedal, "Control of a wind turbine with a doubly fed induction generator after transient failures", 4th Nordic Workshop on Power and Industrial Electronics Proc., Norway, (2004)

[7] C. Gopalakrishnan, K. Udayakumar.and T.A. Raghavendiran, "Survey of harmonic distortion from power quality measurements and the application of standards including simulation" Transmission and Distribution Conference and Exhibition 2002: Asia Pacific. IEEE/PES (Volume:2)

[8] X. Yan, S. Tan, J. Wang, and Y. Wang, "A High Accuracy Harmonic Analysis Method Based on All-Phase and Interpolated FFT in Power System". 2011 *IEEE.*

[9] J. Yang, C. Yu, and C. Liu, "A New Method for Power Signal Harmonic Analysis". *IEEE Transactions on Power Delivery*, Vol. 20, No. 2, April 2005.

[10] J. Valenzuela, and J. Pontt, "Real-Time Interharmonics Detection and Measurement Based on FFT Algorithm".

Chapter 2

2. Contemporary and Future Oil and Gas Field/Platforms Power Systems

2.1. Introduction

The offshore and onshore oil and gas industry is a mature industry; it has been so for many decades. During that time hundreds of megawatts of power generation (such as diesel generators) have been mounted on oil and gas production fields/platforms as shown in Fig. 2.1.

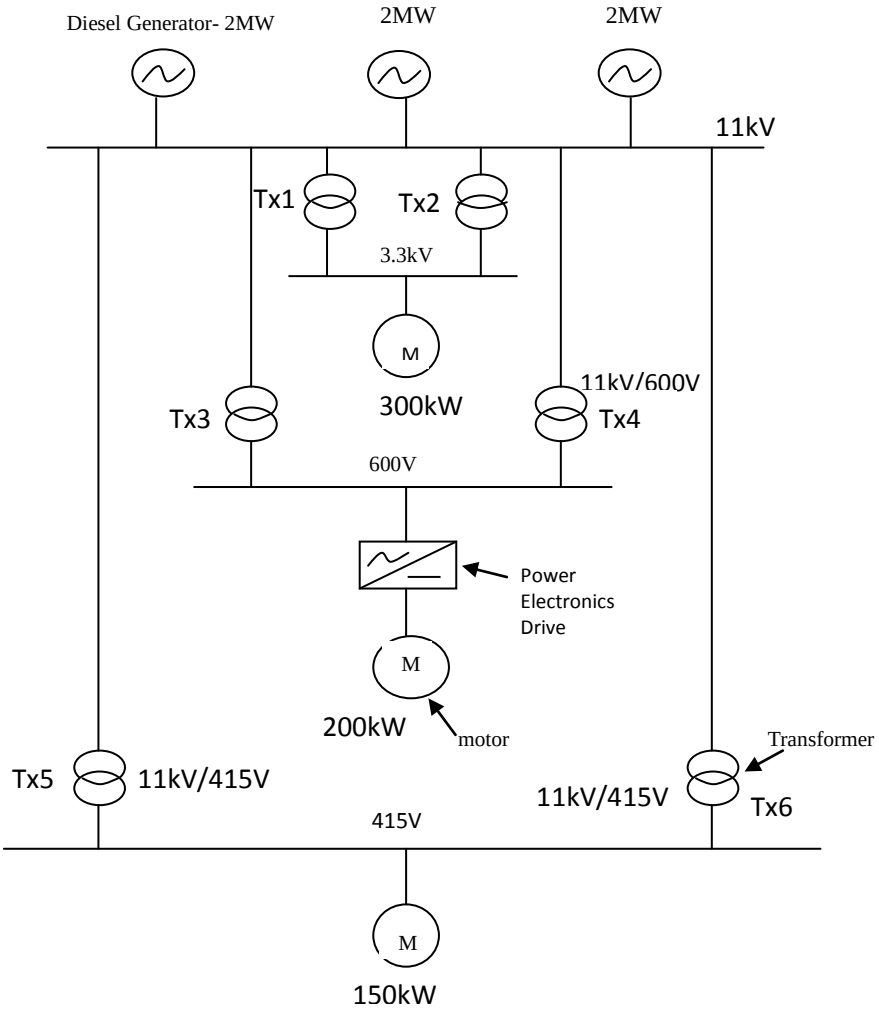

Figure 2.1. Early oil platform electrical power system.

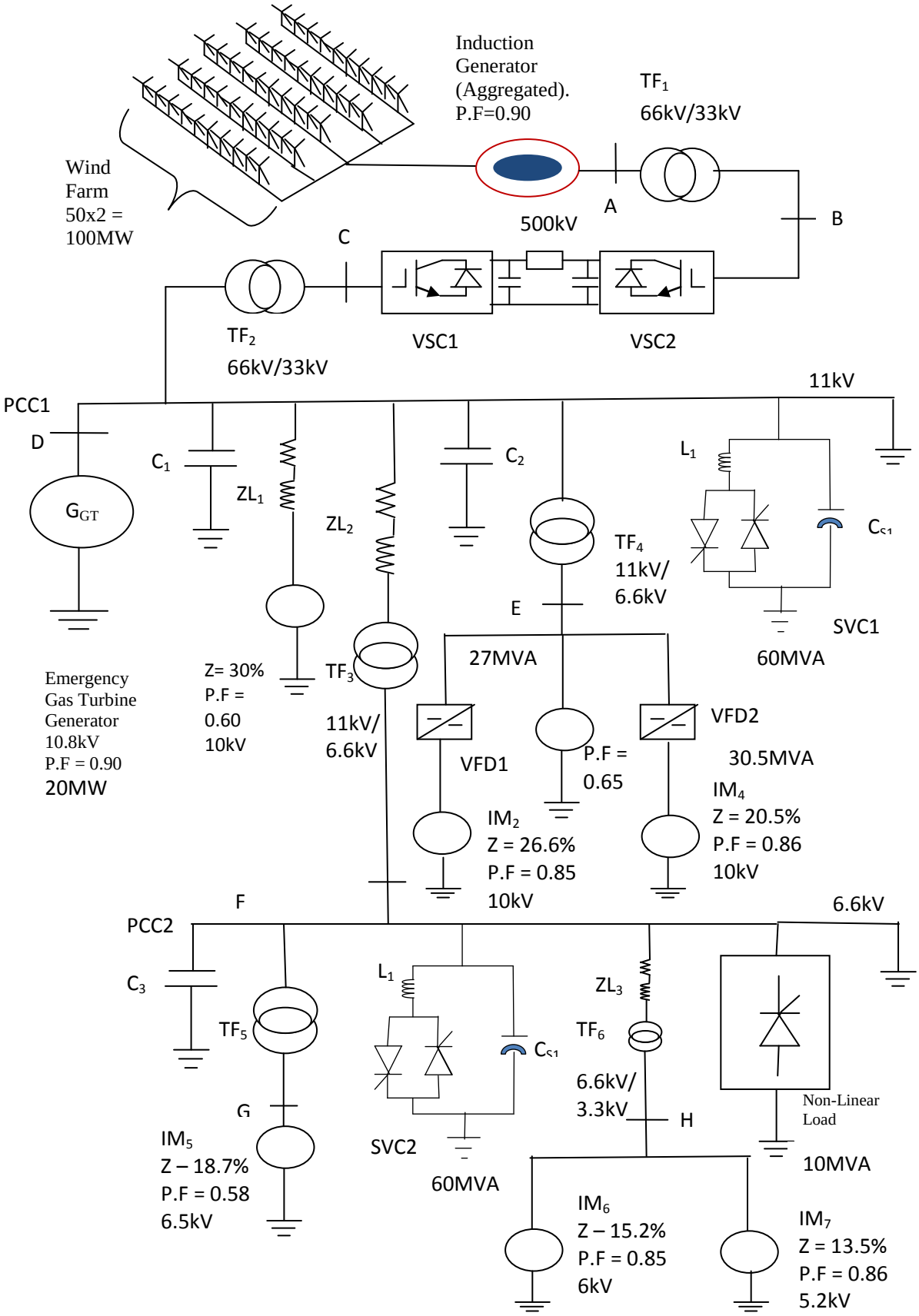

Figure 2.2. Present day oil and gas electrical power system layout

The ever-increasing size of electrical loads on the platforms has called for a gradual increase in the size of on-site power generators. As the oil and gas production declines, new frontier areas are being researched, opening opportunities for new research in its electrical power systems.
Electrical energy generation using gas turbine driven synchronous generators have been in operation in onshore and offshore fields/platforms for many years as shown in Fig. 2.2. [1-4].

Throughout this time, the rating of generators on the platforms has been on the increase due to, among other reasons, the widespread use of power electronics-based equipment. Paradoxically, the development in power electronics in the area of Voltage Source Converters (VSC) could hold the key to the removal of gas turbine-driven synchronous generators from the platforms altogether. Current VSC technology has been found to be highly reliable and commercially attractive and may offer the onshore and offshore oil and gas industry a viable alternative in electrical energy provision using HVDC transmission with wind turbine integration which could extend oil and gas exploration and production well in to the future [5-7].

When designing/modelling any onshore or offshore platform power system, a model is needed to predict the behaviour of the system with the new loads and to ensure that equipment ratings are not exceeded. The early platforms actually had few or no facilities for gas export or reinjection for enhanced oil recovery and for domestic electricity generation, hence the extra process modules installed when these facilities were needed have their own dedicated high-voltage switchboards. Moreover, power requirement for such a heavy consumer as sea water injection is underestimated at the time of construction [8].

The present oil platform distribution at medium voltage normally consists of transformer feeders with circuit breaker and other power electronics equipment for main oil line (MOL) pumps, sea water lift and water injection pumps, and gas export and reinjection compressors electrical motors with Variable Speed Drives (VSD) [11-15]. Depending on process cooling demand, cooling medium pumps may also be driven by medium-voltage variable speed drive motors.

Active power filters are now well established in the current oil and gas fields [20-22]. However, some issues still require further research. The filter dynamics depend strongly

on the switching frequency; higher frequencies giving better results but at the cost of higher losses [23]. Specific modulation strategies and control algorithms such as PWM must be improved. In particular selective harmonic elimination methods can advance power quality (PQ). More attractively, multilevel converter based topologies allow Active Harmonic Filters (AHF) to reach higher voltage levels and so permit the possibility of being applied in the high voltage power systems domain [24]. The AHF that monitors the AC line current to determine the precise amount of reactive and harmonic current that the loads need to operate is as shown in Fig. 2.3. The net result is to off load the source from providing both reactive and harmonic current [25]. The lack of effective techniques during the early stages of the oil and gas industry slowed its development for a number of years. The wide spread use of IGBT components and the availability of new multilevel VSC-PWM are both paving the way to a much brighter future for the AHF plus PQ in the oil industry. This AHF-VSC introduces current components, which cancel the harmonic components of the non-linear loads [26]. Within each topology there are issues of required component ratings and the method of rating the overall filter for the loads to be compensated.

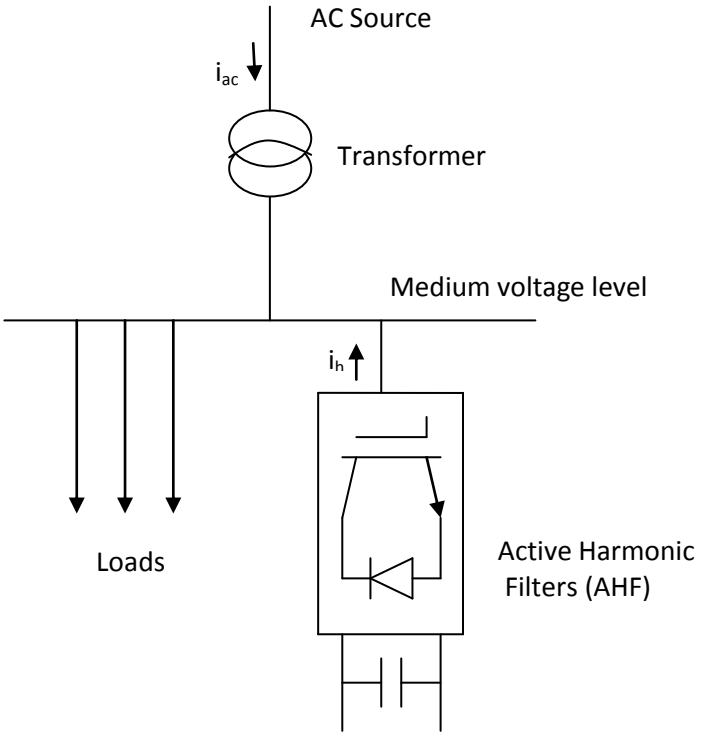

Figure 2.3. Active harmonic filters (AHF) in power systems to monitors the AC line current

In order to meet the voltage harmonic distortion of 5% for various equipment ratings, it will be necessary to attenuate as many of the harmonics generated by the power electronic converters as possible over a wide frequency range. This is because of the unusually high power source impedance and the high percentage of converter type loads. The basic objective will be to limit the voltage harmonic distortion to not more than 5% at the oil and gas platform main generator bus for all platform loads [38].
However, depending on the load variations only one or more generators may be powering the platform at any one time which tends to increase the distortion levels and may cause harmonic problems. To reduce the harmonic distortion levels on the system all equipment characteristics should be carefully modelled, such as the VSC, power line, power cable, energy generation (e.g. wind turbine) etc. The harmonic analysis of onshore/offshore harmonic distribution level at the point of common coupling determines the different levels of harmonic distortion.

2.2. **Early Oil and Gas Field/Platform Electrical Power Systems**

A large number of diesel generators are used in the oil and gas drilling industry for day-to-day operations [39-42]. Despite this, the design and the analysis of these electrical systems are mainly based on short-circuit; load-flow, protective-device coordination, motor starting and arc flash studies. Although, transient stability studies were fundamental in determining the nature of the corrective measures aiming to mitigate the negative effects in the system performance following the occurrence of severe disturbances, harmonics mitigations were deemed unnecessary [43-45]. Diesel generator runaway is a serious hazard in oil and gas drilling and production, refining, petrochemical, and similar industries where flammable hydrocarbon emissions or leaks may occur [46-47]. Oil and gas production facilities experience frequent sudden hydrocarbon releases in their operation and this provides external fuel for the diesel generator to cause runaway [48].

The early Oil and Gas electrical power systems had as their main components, the oil line pumps powered directly from a diesel generator. By way of example, Fig. 2.1 represents a typical oil platform power system with a total electrical power load of about 6 MW. The platforms do not have variable speed drives and so the AC supply is a highly dependable and simple source of sinusoidal voltage and current. As shown, there are three diesel generators connected at the 11 kV bus-bars. Motors are connected at 3.3 kV for sea water lift pumps, DC drilling motors are connected at 600V and motors of up

to about 150 kW are connected at 415V. There are no motors connected directly to the 11 kV switchboard [49].

In this platform, electric power is determined by the diesel generator design. Diesel generators are rated at the brake horsepower developed at the smoke limit. For a given engine, varying fuel properties within the ASTM D 975 specification range (Standard Specification for Diesel Fuel Oils) does not alter power significantly [50-54]. However, fuel viscosity outside of the ASTM D 975 specification range causes poor atomization, leading to poor combustion, which leads to loss of power and fuel economy.

2.3. **The Present Day Oil and Gas Platform Electrical Power Systems**

Oil and gas production advancement have led to a continued growth in the size of compressors, electric motors, drilling machines and pumps used in modern oil and gas platforms [55]. Power consumption on offshore platforms can vary from 6-7 MW to 20-40 MW dependent on size and type of the platform with additional emergency generators and battery power (UPS) for critical situations, when main power fails [56-57].

The need for power on onshore and offshore installations is almost without exception, met by local production, mainly in two ways. Heavy machinery such as gas compressors and pumps are in most cases powered directly from gas turbines or diesel motors for emergency supply, with if necessary a gear in the middle. The main part of the electrical energy is consumed by electric motors, electric heating in the production process and lighting, comfort heating and auxiliary equipment. Also, heating is provided from heat exchangers, and in the early years some heat was produced in direct-fired boilers, but this is not common today due to safety reasons.

The need for power varies for different installations, from 10-100 kW for small wellhead installations to more than 100 MW for the biggest platforms. The total need for power for large fields is close to 500 MW.

The choice between a compressor and a gas turbine for powering heavy oil and gas facilities is mainly decided by the short circuit capability of the network. This decides how large squirrel cage motors can be directly started without unallowable disturbances

on the network. The limit for directly started electric motors has gradually increased, from 5 MW in the early days up to 8 MW today, with increasing electric power rating in the supply systems. In the case of adjustable speed drives the start-up is far less disturbing for the network and drives up to 13 MW have been installed recently. For machines of higher ratings, gas turbines have been the main power source. The limits on motor size are not absolute; they depend on many other factors as well, company traditions among others. So the ratio between electric powering and turbine powering varies widely.

Nowadays, a total platform load that exceeds 100MW is usually powered directly from a gas turbine-driven synchronous generator with the aid of electric drives of less than 1 MW and gas compressors [58]. The contemporary oil and gas fields/platforms in Fig. 2.2 use two equal-size generators (gas turbine) of half the rated system load and a small unit diesel generator to supply emergency loads.

Gas turbines consist of a compressor, combustor, and turbine-generator assembly that converts the rotational energy into electric power output. Gas turbines of all sizes are now widely used in the power industry. Small industrial gas turbines of 1 – 20 MW are commonly used in combined heat and power (CHP) applications. They are particularly useful when higher temperature steam is required (higher than the steam produced by a reciprocating engine). The maintenance cost is slightly lower than for reciprocating diesel engines. Gas turbines can be noisy. Emissions are somewhat lower than for combustion engines, and cost-effective NO_X emission-control technology is commercially available [59].

Micro turbines extend gas turbine technology to smaller scales. The technology was originally developed for transportation applications, and oil and gas production, but is now finding a niche in power generation in some part of the world. One of the most striking technical characteristics of micro turbines is their extremely high rotational speed, up to 120,000 rpm. They produce high frequency ac power, and a power electronic inverter converts this high frequency power into a usable form. Individual micro turbines range from 30 - 200 kW, but can be combined readily into systems of multiple units. Low combustion temperatures can assure very low NO_X emission levels. They make much less noise than a turbine of comparable size [59]. Most micro turbines use natural gas. The use of renewable energy sources, such as ethanol, is also possible [60]. The main disadvantages of micro turbines at the moment are their short track record and high costs compared with gas combustion engines.

A prime mover such as a gas turbine exhibits the effects of wear and tear on the performance of its engine [61]. In this system, the airflow (and thus the compressor operating point) is determined by the turbine flow, capacities, while the compressor absorbed power has to be balanced by the power produced by the gas generator turbine [62]. The compressor discharge pressure is dictated by the engine firing temperature, which in turn impacts the engine power. As such any of the components can show wear and tear over the lifetime of the gas turbine, and thus can adversely affect the operation of the oil and gas production process [63]. The degradation of engine components has a consequent effect on engine performance and thereby poor power quality [64]. Understanding the mechanisms that cause degradation, as well as the effects that the degradation of certain components can cause for the overall system forcing breakdown are a matter that have opened ways for cleaner power plant research such as wind turbine [65]. Moreover, transmission lines above 2km the gas turbine losses its performance [66]. Today's platforms may use large power electronic variable speed drives for gas compression duties [67], as illustrated in Fig. 2.2.

The requirement of variable speed drive (VSD), inverter, and rectifier or thyristor control of some form is used in the platform powered directly from a gas turbine [68]. The combination of these pieces of equipment will cause harmonic currents to be drawn from the supply [69]. These harmonics will cause two secondary problems. Firstly, the harmonic currents will flow in cables, transformers and generator windings and in so doing will immediately produce harmonic volt-drops in these series circuits [70]. This in turn will cause the voltages at various points in the system to contain harmonic components, e.g. either side of a transformer, at motor control centres and switchboards, and other driving motors. Hence the voltages throughout the system will be contaminated by harmonics. This can be troublesome and difficult to accommodate or remove. In some situations, the current drawn from the supply by the inverter or controller can be filtered and smoothed to an almost pure sine wave but this requires extra equipment which can be large, bulky and expensive [71-72]. The second effect of the harmonic currents is to induce harmonic emfs by mutual coupling [73-74], and consequently additional harmonic currents, into cables that are run close to the power cables feeding the driving motor or its controller.

These induced harmonic currents and emfs can be damaging to electronic equipment in particular and troublesome to computer systems [75]. Often the induced emfs and currents contain very ‘spikey’ components that have large peak values, and these can be difficult to remove or suppress.

2.4. **Future Development of Electrical Power Systems with zero-load Generator in Oil and Gas Field/Platform**.

The use of conventional HVDC power transmission to supply off-shore oil and gas platforms has been a matter of research in the past. However, the technology was deemed to be economically and technically unsuitable on grounds of the relatively short distances and low voltages and power involved, as well as the need for a commutating source at the inverter side – this implied the installation of a synchronous generator/condenser on the platform. Furthermore, the substantial amount of reactive power provisions and filtering that thyristor-based converters require in order to function, make up for a rather costly and large foot-print installation.

More specifically, conventional HVDC technology use line-commutated current source converters (CSC). These converters contain valves; each consisting of a number of thyristors that are connected in series. The turn-on of the thyristor is controlled by gate signals while the turn-off takes place at the zero crossing of the AC current which is determined by the AC network voltage (that is line commutation). Both the sending and receiving ends of the HVDC system absorb reactive power from the AC system. Therefore, the HVDC system requires an AC system at least at one end, to have an AC voltage to commutate. This reactive power demand is a constraint for HVDC stations connecting to a weak AC system such as oil or a gas offshore AC network [76-77].

HVDC-Capacitor Commutated Converters (CCC) and HVDC-Voltage Sourced Converters (VSC) technologies can operate at a lower Short Circuit Ratio (SCR) [78-81]. In addition HVDC-VSC can also actively provide voltage support for the ac network, within rating and control limits [82-85]. The presence in the ac networks of many HVDC converters of potentially different technologies or Flexible AC Transmission components such as STATCOMs and series compensation, in close electrical proximity, affect the characteristics of the network [82,86]. The new HVDC transmission technology based on the use of VSC converters seems to be a more adept technology for feeding onshore and off-shore oil and gas platforms. They do not require

large amounts of reactive power compensation with their large footprint, filtering requirements are much reduced, and there is no need for a commutation source at the load side [87-88]. Having all these attributes, the HVDC-VSC technology offers a wide range of applications to the future oil and gas fields/platforms. Further operational advantages are:

- Capability to control reactive power independently of active power
- No risk of commutation failures
- Faster response due to the use of PWM switching frequency
- Capacity to feed a weak AC network or a network without internal generation

It is clear that the HVDC-VSC technology has the potential to improve many of the problems faced by the oil and gas production field/platform transmission and distribution systems, but further research and study are required, such as a comprehensive harmonic domain model and analysis. Other applications of the HVDC-VSC is the back-to-back tie station, where no DC line or cable is used, this does not only control power flow, it can also supply reactive power as well as providing independent dynamic voltage control at its two terminals [89-91].

This new technology which permits the integration of renewable energy sources such as wind turbines is shown in Fig. 2.4b [92-93]. There are two main control strategies for this topology, namely

- Master-slave: In this strategy one of the VSCs controls the DC bus voltage and the other VSCs follows predetermined power reference point which can be constant or assigned by the master converter. If the main converter is found faulty, next converter automatically takes over the HVDC voltage control.
- Coordinated control: Also, in this method the VSCs controls the DC bus voltage and power transfer in a coordinated way. The HVDC voltage control uses the dc droop-based method where each converter has a given linear relationship between HVDC voltage and extracted power.

Gas turbine degradation could be offset and internal combustion engines (ICEs) removed from the oil and gas drilling fields by the deployment of wind turbines. Wind energy plays a key role in voltage stability feeding oil and gas drilling platforms.

Today, large wind power plants are competing with fossil-fuelled power plants in supplying economical clean power in many parts of the world [95].

In this sense, wind power is more like central generation than Distributed Generation (DG). The size of commercial wind turbines has increased significantly from 50 kW in early 1980s to be up to 4.5 MW recently [96]. This increase obviously creates an economy of scale for the wind power technology.

Wind turbines offer dynamic control of the active and reactive power and supply continuity against voltage drop-downs (Fault Ride-Through). These features allow wind farms to act as standard power plants, providing full support to oil and gas industry and the grid especially during grid transients. Fig. 2.4a shows the block diagram of an HVDC-VSC scheme while Fig. 2.4b shows HVDC-VSC links feeding offshore/onshore platforms/fields from a remote power station via an AC overhead transmission line. The overall benefit of this scheme is that gas turbines or diesel generators are eliminated from the offshore platforms as the main energy supply reducing greenhouse emissions and reducing the overall size of the platform. The VSC converters can operate at variable frequency to more efficiently drive large compressor or pumping loads using high voltage motors. Fig. 2.4b shows a clustered oil field that requires supply network extension from 30kV to 220kV.

The main challenges of wind power technology are intermittency and grid reliability [97]. Since wind power generation is based on natural forces, it cannot provide power on demand. On the other hand, utilities must supply power in close balance to demand. Thus, as the share of wind energy increases, such integration into the oil and gas drilling electric network will need more attention. Another barrier is transmission availability. This is because, sometimes, the best locations for wind farms are in remote areas without close access to a suitable transmission line.

Wind turbine generator systems integration in conventional isolated power systems such as offshore oil platform can significantly lower operating costs due to increased fuel savings, but can also have considerable impact on the system stability. In this research, the stability assessment of an isolated offshore oil platform power system with wind power main generator is investigated using MATLAB/SIMPOWER. Simulation results show that the wind power expansion in the isolated offshore oil platform power system with emergency synchronous generators can keep system voltage and frequency stability at a desired level. Grid connection between the offshore oil platform power

system and wind turbine generators supported by HVDC-VSC will improve the contribution of wind power to the voltage and frequency stability [98-99].

A novel power transmission scheme for delivering large generated active power of doubly-fed induction generator (DFIG)-based offshore wind farms (OWFs) fed to oil and gas offshore/onshore AC grids using a multi-terminal (MT) HVDC-VSC system is represented in [100-102]. It is found that large scale wind power SEIG generator integration at the transmission level has the potential to improve the long-term voltage stability of the grid by injecting reactive power [103].

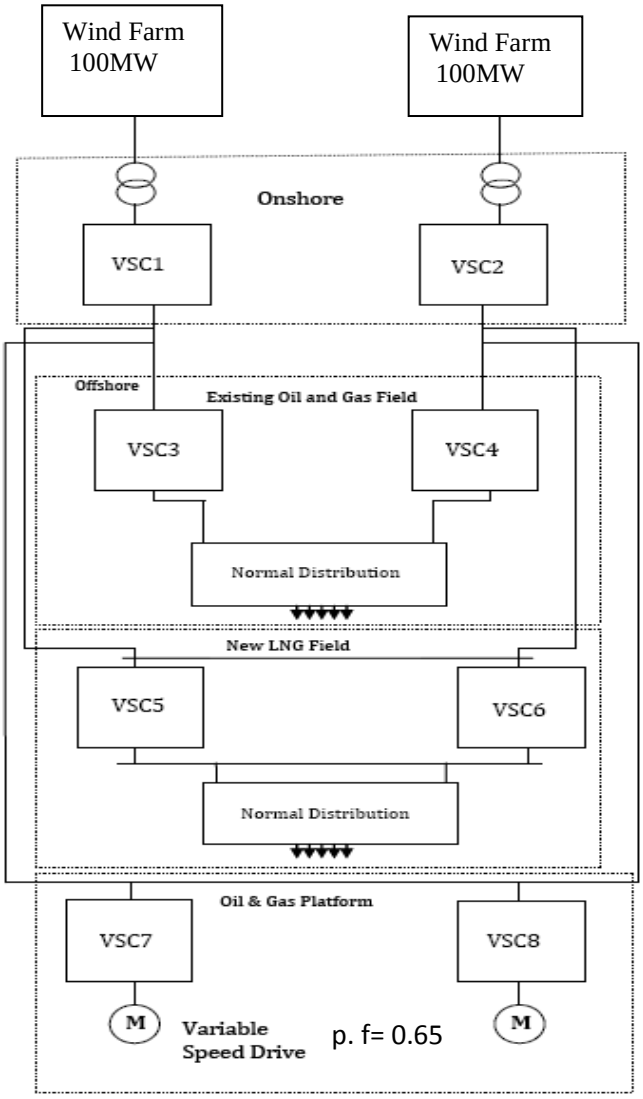

Figure 2. 4a. Block Diagram of multi-terminal HVDC-VSC Scheme for oil and gas

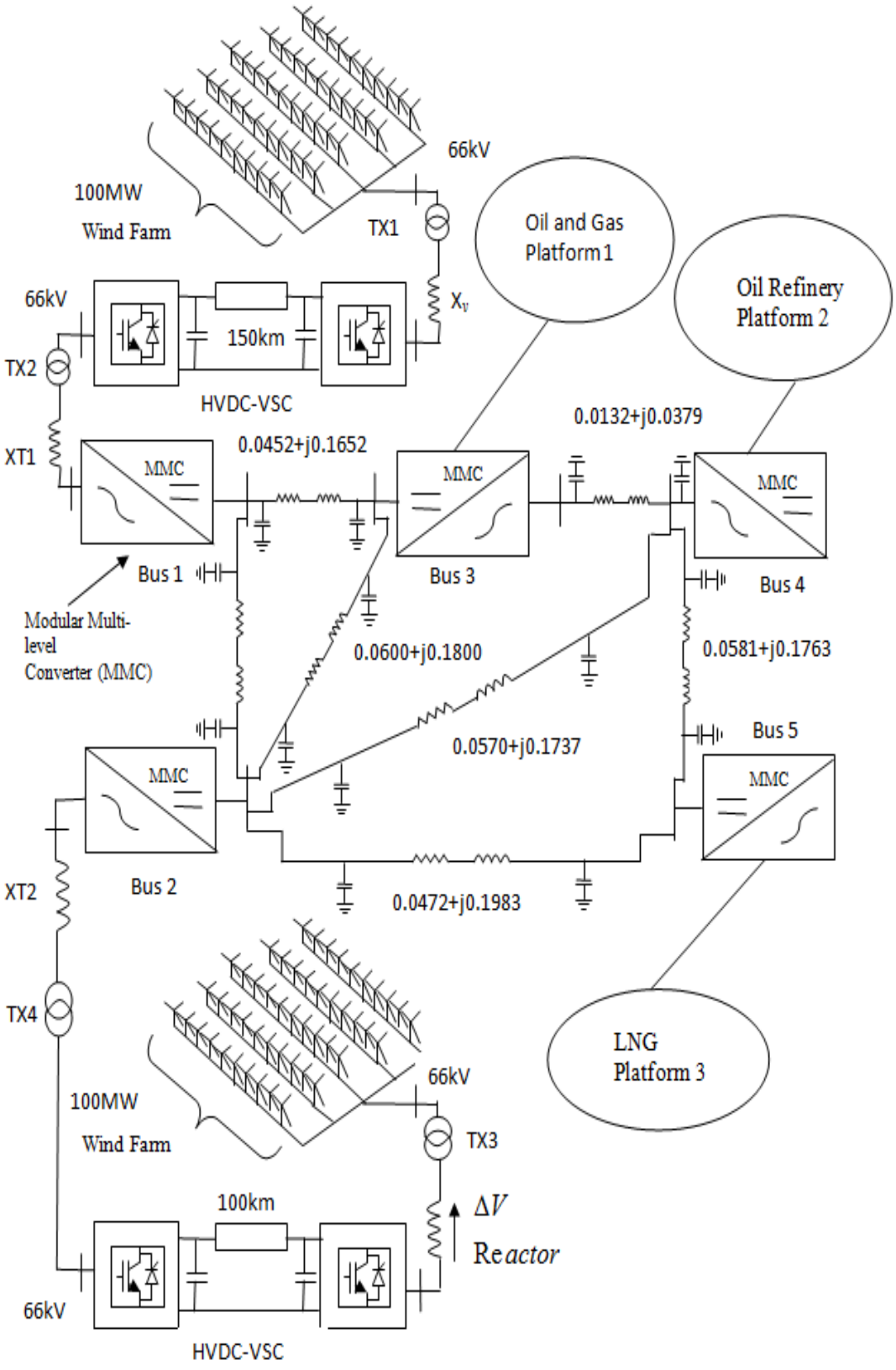

Figure. 2.4b. Proposed multi-terminal systems of onshore platform, offshore platform and oil and gas production field with modular multi-level converter

The harmonic current injection is used to carry out harmonic propagation and control scheme for the multi-terminal system is proposed and designed to transmit total generated active power to five grids under various AC operating condition.

2.5. **Conclusions**

The purpose of this study is to carry out harmonic analysis for power quality and stability in oil and gas production field. The following are key issues that could ascertain a safe, stable and continuous power supply:

Main studies including harmonic load flow, harmonic resonance and short circuit study assist to confirm stability of the power system. Furthermore, it should be noted that any modifications to each study will influence on the results of other studies.

Accurate cable model is important in many aspects such as harmonic resonance studies, voltage drop and reactive power losses. Wrong cable model can adversely affect the system leading to emergency shutdown of the oil and gas production field.

Although in this thesis capacitor bank is recommended for improving power factor for the purpose of having lower reactive losses, and better control on voltage drops. But static var compensators (SVC) were utilized to reduce the harmonic resonance introduced by the capacitor bank in the distribution systems.

By adjusting short circuit impedance of transformer, it is possible to control short circuit current. But the higher short circuit impedance, the higher losses. That is why utilizing transformers with higher sizes are recommended such as tap changer transformer. The tap changer transformer eliminates harmonics distortion as well as assuring required voltage level on the platform.

2.6. References

[1] J M. Wall, R. Lee and S. Frost, "Offshore gas turbines (and major driven equipment) integrity and inspection guidance notes", ESR Technology Ltd, *First published 2006.*

[2] J.C. Bruno, L. Massegues, and A. Coronas, "Power Quality and Air Emission tests in a Micro Gas Turbine Congeneration Plant. *Proceedings of the International Conference on Renewable Energy and Power Quality (ICREPQ'03), 2003.*

[3] J.C. Bruno, and A. Coronas, "Distributed Generation of Energy using Micro Gas Turbines: Ploygeneration Systems and Fuel Flexibility". *Autovia de salou, s/n, 43006 Terragona.*

[4] A. D. Oswald and S. D. Hiner, "More efficient applications for naval gas turbines—addressing the mismatch between available technology and the requirements of modern naval gas turbine inlets," in *Proceedings of the ASME Turbo Expo Power for Land, Sea and Air*, Barcelona, Spain, 2006, GT2006-90305.

[5] G. Ding, G. Tang, Z. He, and M. Ding, "New technologies of voltage source converter (VSC) for HVDC transmission system based on VSC "Power and Energy Society General Meeting Conversion and Delivery of Electrical Energy in the 21st Century, 2008 *IEEE*

[6] S. G. Johansson, G. Asplund, E. Jansson, and R. Rudervall, "Power system stability benefits with VSC DC-transmission systems," in *CIGR´E 2004*, Paris, France, August 2004.

[7] G. Asplund, K. Eriksson, H. Jiang, J. Lindberg, R. P°alsson, and K. Svensson, "DC transmission based on voltage source converters," in *International Conference on Large High Voltage Electric Systems. CIGR´E 98*, vol. 4, Paris, France, 1998.

[8] P. Jakobsen, G, Peck, and E, Snow, "Electrical Power System Challenges During the Expansion of Offshore Oil & Gas Facilities" Petroleum and Chemical Industry Conference Europe Conference IEEE Proceedings (PCIC EUROPE), 2012.

[9] R.E.Cossé, Terence G. Hazel and Gorges Thomasset,"IEC Medium-Voltage Circuit-Breaker Interrupting Ratings – Unstated Short-Circuit Considerations" IEEE Transactions on Industry Applications, Vol.36 No.3 May/June 2000

[10] DS/EN62271-100 (2009) High-voltage switchgear –= Part 100: Alternating-current circuit-breakers.

[11] M. Hernes and B.Gustavsen, "Simulation of shaft vibrations due to interaction between turbine-generator train and power electronic converters at the Visund oil platform", *IEEE Proceedings of the Power Conversion Conference, 2002. PCC-Osaka 2002*

[12] K.W.L. Burbridge, "Users View of Variable Speed Drives on Petrochemical Plant" Electrical Machines and Drives, 1993. Sixth International Conference No. 376.

[13] M.Tsukakoshi, M.Al Mamum, K. Hashhimura, H. Hosoda, and T. Kojima, "Performance evaluation of a large capacity VSD system for Oil and Gas industry" Energy Conversion Congress and Exposition, 2009. ECCE 2009. *IEEE.*

[14] J.O. Lamell, T.Trumbo, and T.F. Nesti, "Offshore Platform Powered with New Electrical Motor Drive System" Petroleum and Chemical Industry Conference, 2005. Industry Applications Society 52nd Annual. *IEEE*

[15] M. Didden, H. De, C. Jean, and D.J. Emmanuael, "Installing variable speed drives: Energy efficiency profits versus power quality losses", Electricity Distribution, 2005. CIRED 2005. 18th International Conference. *IEEE*

[16] H.L. Jou, J.C.Wu, J.J. Yang, and W.P.Hsu, "Novel Circuit Configuration for Hybrid Reactive Power Compensator", Power Electronics and Motion Control, 2006. IPEMC 2006. CES/*IEEE*.

[17] X. Liu, L. Sun, Y. Sun, and Z. Dean, "The synthetical compensation research on high-order harmonic and reactive power", Industrial Technology, 2008. ICIT 2008. *IEEE.*

[18] S. Shankar, A. Kumar, and W. Gao, "Operation of unified power quality conditioner under different situations", Power and Energy Society General Meeting, 2011 IEEE.

[19] M. Izhar, C.M. Hadzer, M. Syafrudin, S. Taib, and S. Idris, "Performance for Passive and Active Power Filter in Reducing Harmonics in the Distribution System", Power and Energy Conference, 2004. PECon 2004. IEEE Proceedings

[20] I. Faegheh, and S.H. Hosseinian, "Using the Instantaneous Power Theory in order to control the current in the parallel active filter to compensate reactive power and reduction of harmonics", Power Electronics, Drives and Energy Systems (PEDES), 2012 *IEEE.*

[21] D. Gao, Q. Lu, and X. Sun, "Design and performance of an active power filter for unbalanced loads", Power System Technology, 2002. *IEEE* Proceedings. PowerCon 2002.

[22] J.C. Wu, H.L.. Jou, Y.T. Feng, W.P. Hsu, M.S. Huang, and W.J. Hou, "Novel Circuit Topology for Three-Phase Active Power Filter". *IEEE Transactions on Power Delivery, Jan. 2007.*

[23] C.Po-Tai, S. Bhattacharya, and D. Divan, "Experimental Verification of Dominant Harmonic Active Filter (DHAF) for High Power Applications", Industry Applications Conference, 1998. Thirty-Third IAS Annual Meeting. *The 1998 IEEE*

[24] Z.H. Yuan, "A Shunt Active Harmonic Filter Based on a Voltage Detection Method for Harmonic Voltage Control", Electric Utility Deregulation, Restructuring and Power Technologies, 2004. (DRPT 2004). *Proceedings of the 2004 IEEE*

[25] J.H. Xu, S. Saadate, and B. Davat, "Compensation of AC-DC converter input current harmonics using a voltage-source active power filter", Power Electronics and Applications, 1993. Fifth European Conference

[26] M.E. Ortuzar, R.E. Carmi, L.W. Dixon, and L.Moran, "Voltage-Source Active Power Filter Based on Multilevel Converter and Ultracapacitor DC Link", *IEEE Tranasactions on Industrial Electronics.*

[27] R.Majumder,"Reactive Power Compensation in Single-Phase Operation of Microgrid", *IEEE Tranasactions on Industrial Electronics.*

[28] A.Cetin, M. Ermis. "VSC Based D-STATCOM with Selective Harmonic Elimination", Industry Applications Conference, 2007. 42nd IAS Annual Meeting. Conference Record of the 2007 *IEEE*

[29] R.E. Betz, T.J. Summers, and G. Mirzaeva, "Active filtering and VAR control of a cascaded H-bridge multi-level StatCom", Power Electronics and Drive Systems, 2009. PEDS 2009.

[30] S.H. Hosseini, and M. Sabahi, "Three-Phase Active Filter using a Single-Phase STATCOM Structure with Asymmetrical Dead-band Control", Power Electronics and Motion Control Conference, 2006. IPEMC 2006. *CES/IEEE* 5th International.

[31] T. Jin, L. Li, and K. Smedley, "A universal vector controller for three-phase PFC, APF, STATCOM, and grid-connected inverter", Applied Power Electronics Conference and Exposition, 2004. APEC '04. Nineteenth Annual *IEEE.*

[32] P.S. Sensarma, K.R. Padiyar, and V. Pamanarayanan "A STATCOM for composite power line conditioning", Industrial Technology 2000. Proceedings of *IEEE* International.

[33] X. Wang, and S. Hua"Extended state feedback control for active power filter", Computer Science and Automation Engineering (CSAE), 2011 *IEEE* International.

[34] O. De, E.M. Sebastiao, and J.O.R. Guimuraes, "Effects of Voltage Supply Unbalance on AC Harmonic Current Components Produced by AC/DC Converters", *IEEE Tranasactions on Power Delivery. 2007.*

[35] K. M. Nor, L.W. Jeun, M. Abdel-Akher, and A.H. Abudul-Rashid, "Reusing Three-Phase Power-Flow Object Components for Unbalanced Harmonic Analysis", Power and Energy Conference, 2006. PECon '06. *IEEE* International.

[36] T. Zheng, E.B. Makram, and A.A. Girgis, "Evaluating power system unbalance in the presence of harmonic distortion", *IEEE Tranasactions on Power Delivery. April 2003*

[37] K.Nohara, A. Ueda, A. Torii, and K. Doki, "Compensating Characteristics of a Series-Shunt Active Power Filter Considering Unbalanced Source Voltage and Unbalanced Load", *IEEE* Power Conversion Conference - Nagoya, 2007. PCC '07.

[38] *IEEE*, Recommended Practices and Requirements for Harmonic Control in Electrical Power Systems, *IEEE Std. 519-1992.*

[39] M.L. Rizzone, "Electric Drilling Rig Developments", *IEEE Transactions On Industry and General Applications Vol. IGA-3, No. 2*

[40] Y. Xiong, H.Wang ,and S. Lu, "Study on Micro-Biological Degradation of Diesel Oil cooperated with Plants"

[41] P.M. David, "Increasing the Electrical Output of a Cogeneration Plant", IEEE Trans. On Industry Applications, vol. 38, no. 3, pp. 726- 735, May/Jun 2002.

[42] S.R. Stanley, "Electrical Transient Stability and under frequency Load Shedding Analysis for a Large Pump Station", IEEE Trans. On Industry Applications, vol. 33, no. 1, pp. 194-201, Jan/Feb 1997.

[43] S.P.Thomas,"Power System Studies for Cement plants", IEEE Industry Applications magazine, pp. 56-65, July/August 2007

[44] D.P. Mathew. and J.L. Kohler , "An Improved Model for Analyzing Industrial Power Systems", IEEE Trans. On Industry Applications, Vol. 31, No. 5, pp. 1140-1146, September/October 1995

[45] J. R. Dunki-Jacobs and C. E.Davis, "An Argument and Procedure for Conceptual Power System Design Studies", IEEE Trans. On Industry Applications, Vol. 30, No. 2, pp. 253-261, March/April, 1994

[46] D.L.Hodgson, M. McKinney, S. DeGrate, "Increasing electrical safety by reducing the risk of arc flash hazards", Petroleum and Chemical Industry Conference (PCIC), 2011. *IEEE*

[47] G.S. Lawler, "Fires of Electrical Origin in Factories", Electrical Engineering. *IEEE.*

[48] D. Buscher, "Avoiding loss of voltage sensing runaway for generator excitation systems", Industry Technical Conference (PPIC), 2011 Annual *IEEE.*

[49] G. Gerrard, "Offshore Electrical Engineering" British Library 1992.

[50] A. Marcus "Diesel Fuel Basics", *PASSAGEMAKER • Fall 1999* PassageMaker Magazine, Inc.

[51] P. Lu, J.Wu, and W. Pan, "Particulate Matter Emissions from a Coal-Fired Power Plant", Bioinformatics and Biomedical Engineering (iCBBE), 2010. *IEEE*..

[52] J.Deng, A. Ordys, and Y. Wang, "Input choices of Particulate Matter Models for Diesel Engines", Control and Decision Conference (CCDC), 2012. *IEEE*

[53] S. Sakulniyomporn, K. Kubaha, and C. Chullabodhi, "Estimating the health damage costs of electricity generation in Thailand", Energy and Sustainable Development: Issues and Strategies (ESD), *IEEE* 2010 Proceedings.

[54] V. Dawar, B. Lesieutre, T. Holloway, and E. Bickford, "An efficient approach to reduce emissions by coupling atmospheric and electricity market models", North American Power Symposium (NAPS), 2012. *IEEE.*

[55] J.O.Lamell, T.Trumbo, T.F. Nestli, **"**Offshore platform powered with new electrical motor drive system", Petroleum and Chemical Industry Conference, 2005. Industry Applications.*IEEE*

[56] S.K.Salman, F.Jiang, W.J.S. Rogers, "Investigation of the operating strategies of remotely connected embedded generators to help regulating local network voltage", Opportunities and Advances in International Electric Power Generation, International Conference on *IEEE March 1996.*

[57] W.J.S.Rogers,**"**Impact of embedded generation on design, operation and protection of distribution networks", Embedded Generation on Distribution Networks (Digest No. 1996/194), IEE Colloquium on the Impact of *IEEE* Oct; 1996.

[58] D.M.Soto,A.Hasanzadeh, and C.S. Edrington,**"**Gas turbine-synchronous generator system emulation using power electronics converters", North American Power Symposium (NAPS), Sept; 2012.*IEEE.*

[59] IEA, Distributed Generation in Liberalised Electricity Markets, International Energy Agency, France, 2002.

[60] M.W.Davis, "Micro turbines – an economics and reliability evaluation for commercial, residential and remote load applications", *IEEE Transaction on Power Systems, vol. 14, no. 4, pp. 1556-1562, 1999.*

[61] H.D. Hollis, R.G. Arno, S.J. Briggs, and P.S. Hale, "Operational maintenance data for power generation distribution and HVAC components", Industrial and Commercial Power Systems Technical Conference, May 1996, *IEEE*

[62] H.J. Nern, H. Kreshman, F.Fischer, H.A. Eldin, "Modelling of the long term dynamic performance of a gas turbo generator set", Control Applications, 1994., Proceedings of the Third *IEEE*, Aug; 1994.

[63] J. Sumner, A. Encinas-Oropesa, M. Seraffon, N.J. Simms, J.R. Nicholls, "Lifetime prediction for gas turbine materials in power generation", Sustainable Power Generation and Supply (SUPERGEN 2012),

[64] N. Gebraeel, A. Elwany, J. Pan, "Residual Life Predictions in the Absence of Prior Degradation Knowledge" *IEEE* Transactions on Reliability. March 2009.

[65] E. Muljadi, C.P. Butterfield, J. Chacon, and H. Romanowitz, "Power quality aspects in a wind power plant", Power Engineering Society General Meeting, 2006. *IEEE.*

[66] S. Mohammad, S. Zadeh,**"**Economic Operation of Long Distances Power Networks Using On-line Control of Superconducting Magnetic Energy Storage", EUROCON 2007. *IEEE.*

[67] M. Bressani, A. Odorico, and M. Sica, "High-speed, large-power induction motors for direct coupling to variable-speed gas compressors", Power Electronics and Applications, 1993. *IEEE.*

[68] J. Arai, K. Iba, T. Funabashi, Y**.** Nakanishi, K. Koyanagi, and R. Yokoyama, "Power electronics and its applications to renewable energy in Japan", *IEEE* Circuit and Systems Magazine.

[69] D.D.Shipp, W. Vilcheck, M.E. Swartz, and N.H. Woodley, "Expert system for analysis of electric power system harmonics", *IEEE* Industry Applications Magazine, March/April 1995.

[70] H. Funato, C. Sasaki, Y. Chiku, and S. Ogasawara, "Analysis of loss of receiving transformer caused by harmonic current and voltage for loss reduction", Power Electronics and Motion Control (EPE/PEMC), *IEEE*, Sept; 2010.

[71] J.C.Das,"Passive Filters-Potentialities and Limitations",*IEEE Trans. Ind. Applications, vol. 40, No. 1, Jan/Feb; 2004.*

[72] D. A. Gonzalez and J. C. McCall, "Design of filters to reduce harmonic distortion in industrial power systems," *IEEE Trans. Ind. Applicat.*, vol. IA-23, pp. 504–512, May/June 1987.

[73] E.Semail, X. Kestelyn, and A. Bouscayrol, "Right harmonic spectrum for the back-electromotive force of an n-phase synchronous motor", Industry Applications Conference, 2004. 39th IAS

[74] P. Ioannides, and C.A. Balanis, "Mutual coupling in adaptive circular arrays", Antennas and Propagation Society International Symposium, 2004. *IEEE*

[75] L. Wa**,** S. Saodah, and J. Nurahmat, "Current harmonic analysis of electronics loads on induction generator", Condition Monitoring and Diagnosis (CMD), Sept; 2012. *IEEE.*

[76] A. Reidy and R. Watson, "Comparison of VSC base HVDC and HVAC interconnections to a large offshore wind farm", *Proc. IEEE Power Eng. Soc. General Meeting, Jun.2005, pp. 71-78.*

[77] F. Schettler, H. Huang, and N. Christl, "HVDC Transmission Systems using Voltage Sourced Converters –Design and Applications". *In Proc. IEEE PES Summer Meeting, vol. 2, Seattle, WA, 2000, pp. 715-720.*

[78] Y.Jiang-Häfner, M. Hyttinen, and B. Pääjärvi, "On the Short Circuit Current Contribution of HVDC Light",

[79] CIGRE "Guide for planning dc links terminating at AC systems locations having low short-circuit capacities—part I: AC/DC interaction phenomena". Report 68, June 1992

[80] P. F. de Toledo, B. Bergdahl, and G. Asplund "Multiple Infeed Short Circuit Ratio – Aspects Related to Multiple HVDC into one AC Network", ABB Power System, HVDC Division

[81] "Guide for planning DC Links terminating at AC system having low short-circuit capacity, Part I: AC/DC interaction phenomena", CIGRE Guide No 68, Paris 1992

[82] J. Pan, R. Nuqui, K. Srivastava, T. Jonsson, P. Holmberg, and Y. Hafner, "AC Grid with Embedded VSC-HVDC for Secure and Efficient Power Delivery", EEE Energy 2030, 17-18 November, 2008 Atlanta, USA.

[83] Stefan G Johansson, Gunnar Asplund, Erik Jansson, Roberto Rudervall, "Power System Stability Benefits with VSC DC Transmission Systems", CIGRE Conference, 2004, Paris, France.

[84] Peter Sandeberg and Lars Stendius, "Large scale Offshore Wind Power Energy evacuation by HVDC Light®", European Wind Energy Conference & Exhibition, March-April 2008, Brussels Belgium.

[85] Gunnar Asplund, "Electric Transmission System in Change", Key Notes, *IEEE* Power Electronics Specialists Conference, June 2008, Rhodes, Greece

[86] M. P. Bahrman, J. G. Johansson, and B. A. Nilsson "Voltage Source Converter Transmission Technologies - the right fit for the Application", ABB.

[87] R. S. Rani, and B. Jyothi, "VSC Based DSTATCOM & Pulse-width modulation for Power Quality Improvement", *International Journal of Engineering Trends and Technology- Volume2Issue2- 2011*

[88] J. Dixon , L. Morán, J. Rodríguez, and R. Domke "Reactive Power Compensation Technologies, State of-the-Art Review".

[89] J. Liu, L. Yao, T. Wu, Y. Guo,Y. An, and C. He "Application of back-to-back VSC-HVDC in Power Grids Synchronization Parallel Operation", *IEEE 2010 International Conference on Electrical and Control Engineering*

[90] M. Bahrman , A. Edris , and R. Haley, “Asynchronous Back-to-Back HVDC Link With Voltage Source Converters”, *PRESENTED AT MINNESOTA POWER SYSTEMS CONFERENCE, NOV 1999, USA.*

[91] A. L'Abbate and G. Fulli “Modeling and Application of VSC-HVDC in the European Transmission System” International Journal of Innovations in Energy Systems and Power (Vol. 5 no. 1, April 2010)

[92] “HVDC-VSC: transmission technology of the future”, Alstom Grid///Spring-Summer 2011.

[93] M.Häusler,“Multi-terminal HVDC for High Power Transmission in Europe”. Presented at CEPEX99, Poznan Poland, March 1999. ABB Calor Emag Schaltanlagen AG, Mannheim, Germany

[94] M.Chinchilla, S. Arnaltes, and J. C. Burgos. “Control of Permanent Magnet Generators Applied to Variable-Speed Wind-Energy Systems Connected to the Grid”. IEEE Trans. Energy Conversion, vol. 21, no. 1,pp. 130-135, Mar.2006.

[95] A.Reidy and R.Watson,“Comparison of VSC base HVDC and HVAC Interconnections to a Large Offshore Wind Farm”. 0-7803-9156-X/05.

[96] D. Hu, X. Zhao, X. Cai and J. Wang. “Impact of Wind Power on Stability of Offshore Platform Power Systems”. 978-7-900714-13-8/08.

[97] O. Lamell, F. Nestli,“Offshore Platform Power With New Electrical Motor Drive System”. *IEEE* paper No. PCIC-2005-29.

[98] D. Hu, X. Zhao, X. Cai, and J. Wang, “Impact of wind power on stability of offshore platform power systems”, Electric Utility Deregulation and Restructuring and Power Technologies, April 2008.

[99] F. Shewarrga, I. Erich, and J.L. Rueda, “Impact of large offshore wind farms on power system transient stability”, Power Systems Conference and Exposition, March 2009. PSCE '09. *IEEE/PES*

[100] E. Spahic, and G. Balzer, “Impact of the VSC HVDC Connection of Large Offshore Wind Farms on Power System Stability and Control”, Power Tech, July 2007 *IEEE* Lausanne

[101] M.S. Nguyen, and L. Wang, “Stability analysis of power transmission of offshore wind farms fed to onshore power grids using a multi-terminal VSC-HVDC system”, Circuits and Systems (APCCAS), 2012 IEEE Asia Pacific Conference on Dec; 2012.

[102] L. Wang, and D.N. Truong, “Stability improvement of a DFIG-based offshore wind farm fed to a multi-machine power system using a static VAR compensator” Industry Applications Society Annual Meeting (IAS), Oct; 2012 *IEEE*

[103] D. Devaraj, and R. Jeevajyoth, “Impact of wind turbine systems on power system voltage stability”, Computer, Communication and Electrical Technology (ICCCET), March 2011.

Chapter 3

3. Power Network Analysis in the Harmonic Domain

3.1. Introduction

The increasing use of nonlinear equipment in power systems demands exact prediction of the harmonic contents [1]. Harmonic producing equipment has become wide-spread in their demand; its effect on electrical equipment, in particular sensitive electronic equipment has become apparent [2]. Two important recommendations in the development of a suitable algorithm for harmonic modelling are the frame of reference and the nature of the sources [3]. Field evaluations indicate that the harmonic content in a power transmission line is said to be asymmetrical, hence its harmonic prediction must take place in the three-phase frame of reference. In the nature of the sources, a clear distinction is required between the fundamental and harmonic frequencies. For the former the specification of the generators as voltage sources remains valid. While in the latter the nonlinear components are represented as current harmonic sources [4-5]. A general frame of reference suitable for the harmonic solution of power systems has been formulated based on the concept of convolution in the complex Fourier harmonic domain and numeric evaluation of non-linear functions. These are numerical procedures that are more suitable for digital computer solutions. Several harmonic transforms can be used for carrying out convolution operations, namely complex Fourier, real Fourier, Hartley, Walsh, wavelet, etc. The harmonic domain (HD) permits the harmonic response of a non-linear element to be obtained by a fast Fourier transform (FFT) or fast Hartley transform (FHT) algorithm. These FFT and FHT have revolutionised the modern signal and harmonic analysis, and paved the way for the introduction of modal analysis. The FFT algorithm applies only to signals comprising a number of elements which is equal to 2^n (e.g. 2^8 = 256, 2^{10} = 1024 etc). Its main advantage is that it significantly reduces the computation time by a factor of the order $n/\log_2 n$, that is, more than 100 times for a sample of 1024 elements. The only limitation in achieving results using FFT is the algorithm that is limited to using samples of power two. The characteristic may be expressed in equation form. Through the method of linearization in the HD, non-linear components can be represented in the form of harmonic Norton

equivalents, which permits the harmonic solution for the overall system to be analyzed by an iterative procedure based Newton-Raphson method.

3.2. **Harmonics in Oil and Gas Field/Platform**

Harmonics are a growing concern in the management of oil and gas electrical systems today. Designers are requested to pay more and more attention to energy savings and power quality. In this context, the issue of harmonics is often considered. Power electronic devices have received a lot of attention in oil and gas industry due to precise process control and energy savings benefits. However, they also bring drawbacks to electrical distribution systems.

The increased use of power electronics controlled equipment and converters used in automated production lines and variable speed drives in power systems has led to high distortion of the voltage waveform in oil and gas fields. It is worth mentioning that in onshore and offshore isolated power systems, the level of harmonic distortions has reached levels that are well in excess of the recommended limits. The Total Harmonic Distortion (THD) limit is 8% and it has been reported that in some of the existing operations that THD is in excess of 20% [3]. The main source of harmonic distortion comes from DC drilling drives and AC variable speed drives. The former produces transient disturbances, whereas the latter gives a more periodic steady state condition. It is understood that high levels of harmonic distortion in a power system leads to a number of detrimental effects in the operation of electrical plant in oil and gas platform, such as [15-20]:

- Malfunctioning of equipment (particularly controllers)
- Increased power loss, due to eddy currents, hysteresis, and skin and proximity effects leading to equipment overheating
- Electromagnetic interference (EMI) and radiation
- Additional noise and vibration in electromechanical systems
- Pulsating torques in AC motors
- Stress of insulation due to high rate of change of voltage

3.3. **Harmonic Modelling and Simulation**

The identification, classification, quantification and mitigation of power system harmonics signals is the burning issue for various stakeholders including oil and gas companies, utilities and manufacturers world widely.

To accomplish this task mathematical and computational tools like MATLAB and SimPower have been used to conduct this research. The aim of harmonic studies is to quantify the distortion in voltage and current waveforms at various points in a power system. The advantages of it are useful for evaluating corrective measures and troubleshooting harmonic caused problems. A request for a harmonic study may be the result of measuring excessive distortion in existing systems or by the installation of a harmonic producing load. Similar to other power systems studies the harmonics study takes the following stages:

- Definition of harmonic producing equipment and determination of models for their representation.
- Determination of the models to represent other components in the system including external networks.
- Simulation of the system for various cases.

It is appropriate to note that a large number of harmonic related problems encountered in practice involve systems with relatively low distortion and often a single dominant harmonic source. In these cases simplified resonant frequency calculations, for example, can be performed by hand [21] and distortion calculations can be made with a simple spreadsheet. For larger systems and complicated harmonic producing loads like gas field, more formal harmonic power flow analysis methods are needed. In this section, techniques presently being used for harmonics studies are reviewed. These techniques vary in terms of data requirements, modelling complexity, problem formulation, and solution algorithms.

Mathematically, the harmonic study involves solving the network equation written in matrix form as

$$[I_m] = [Y_m][V_m] \qquad \text{m} = 1,2 \ldots \text{n} \tag{3.1}$$

where

$[Y_m]$ represents the nodal admittance matrix,
$[\mathbf{I}_m]$ is the vector of source currents and
$[\mathbf{V}_m]$ is the vector of bus voltages for harmonic number m

3.3.1. Frequency Scan

The frequency scan is usually the first step in a harmonic study. A frequency or impedance scan is a plot of the driving point (Thevenin) impedance at a system bus

versus frequency. The bus of interest is one where a harmonic source exists. For a simple system this impedance can be obtained from an impedance diagram. More formally, the Thevenin impedance can be calculated by injecting a 1 per unit source at the appropriate frequency into the bus of interest. The other currents are set to zero and (3.1) is solved for bus voltages. These voltages equal the driving-point and transfer impedances. The calculation is repeated over the harmonic frequency range of interest. Typically, a scan is developed for both positive and zero sequence networks. If a harmonic source is connected to the bus of interest, the harmonic voltage at the bus is given by the harmonic current multiplied by the harmonic impedance. The frequency scan thus gives a visual picture of impedance levels and potential voltage distortion. It is a very effective tool to detect resonances which appear as peaks (parallel resonance) as depicted in Fig. 3.1 and valleys (series resonance) in the plot of impedance magnitude versus frequency.

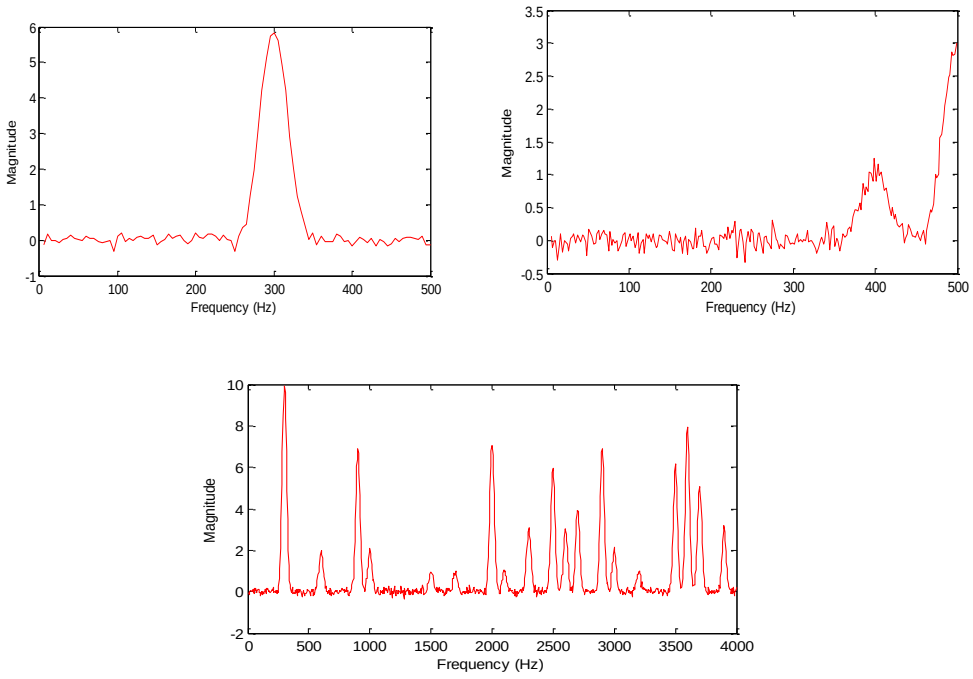

Figure. 3.1 Resonance peaks

3.3.2. Simple Distortion Calculations

In the simplest harmonic studies harmonic sources are represented as current sources (Fig. 3.2) specified by their current spectra. Admittance matrices are then constructed and harmonic voltage components are calculated from (3.1). The harmonic current

components have a magnitude determined from the typical harmonic spectrum as shown in Fig. 3.3a, 3.4a and rated load current for the harmonic producing device:

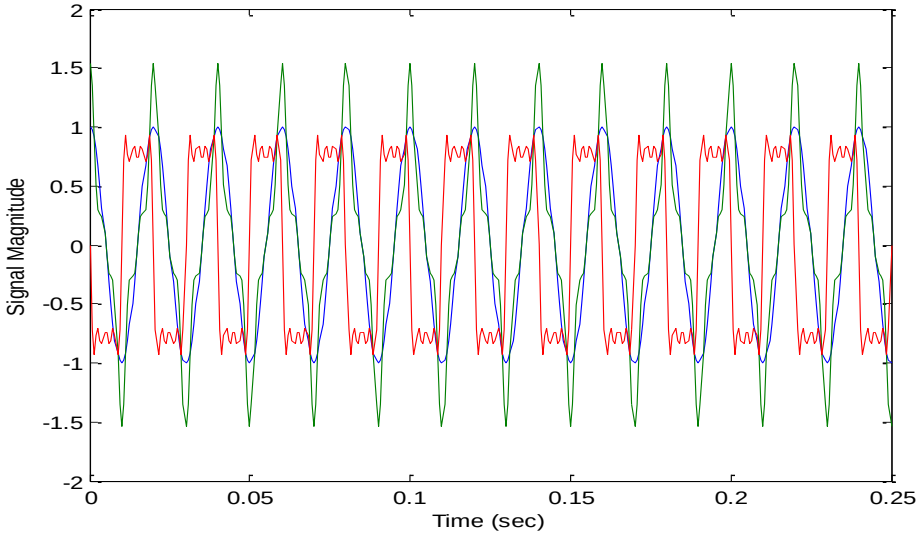

Figure. 3.2 Signal with harmonic components

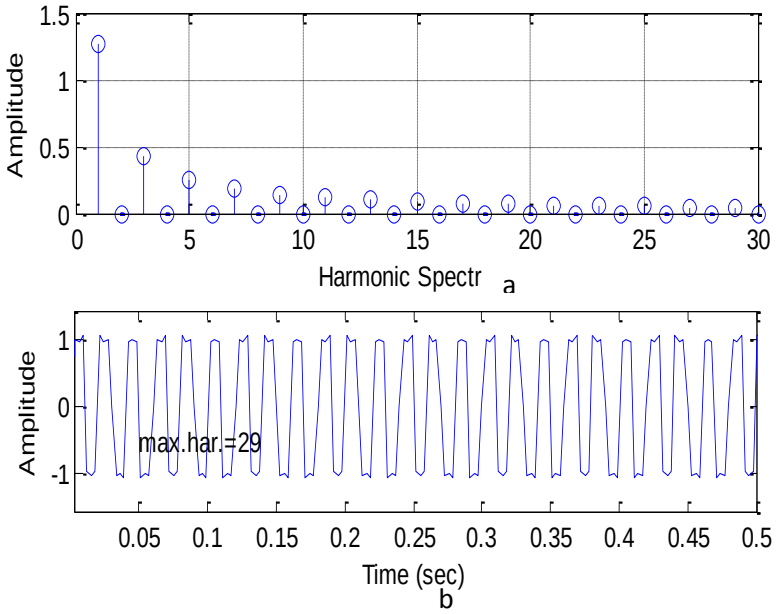

Figure. 3.3 (a) Typical harmonic spectrum and (b) signal

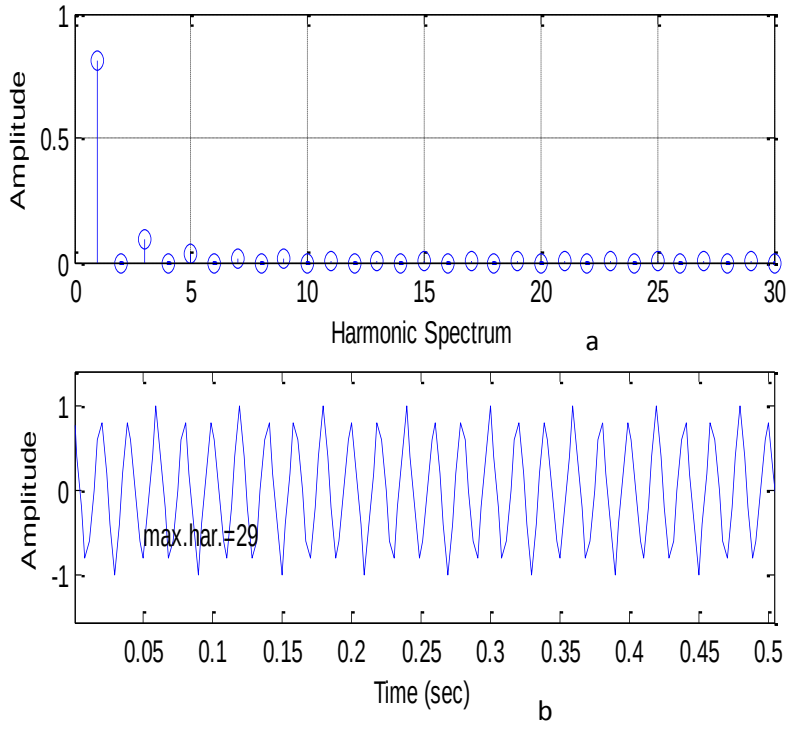

Figure. 3.4 (a) Typical harmonic spectrum and (b) signal

$$I_n = I_{rated} I_{n-spectrum} / I_{1-spectrum} \tag{3.2}$$

where n is the harmonic order and the subscript ‘spectrum’ indicates the typical harmonic spectrum of the element.

For the multiple harmonic source cases it is important to also model the phase angle of harmonics. A fundamental frequency power-flow solution is needed, because the harmonic phase angles are functions of the fundamental frequency phase angle as follows:

$$\theta_n = \theta_{n-spectrum} + n\left(\theta_1 - \theta_{1-spectrum}\right) \tag{3.3}$$

where θ_1 is the phase angle of the harmonic source current at the fundamental frequency.
$\theta_{n\text{-spectrum}}$ is the phase angle of the n-th harmonic current spectrum.

Depending on the phase angles used, the effects of multiple harmonic sources can either add or cancel. Ignoring phase relationships may, therefore, lead to worst possible outcome case or optimistic results.

3.3.3. Harmonic Power Flow Methods

The simple distortion issue discussed above is the basis for most harmonic study software and is useful in many practical cases. The main drawback of the method is the use of 'typical' spectra. This prevents inclusion of non-typical operating conditions. Such conditions include partial loading of harmonic-producing devices, excessive distortion and unbalance. To explore such conditions the researcher must develop typical spectra for each condition when using the simplified method such as Newton-Raphson. The negative effects have prompted the development of advanced harmonic analysis methods. The goal is to model the physical aspects of harmonic generation from the device as a function of actual system conditions.

The general idea is to create a model for the harmonic producing device in the form

$$F\left(V_1, V_2, ...V_n, I_1, I_2, ...I_n, C\right) = 0 \tag{3.4}$$

Where V_1, V_2, ...,V_n are harmonic voltage components, I_1,I_2, ...,In are corresponding harmonic current components and C represents multiple operating and design parameters. Equation (3.4) allows the derivation of harmonic currents from voltages and includes power flow constraints.

A popular method is the so called “harmonic iteration method” [22,23]. Equation (3.4) is first solved using an estimated supply voltage. The resulting current spectrum is used in (3.1) to calculate the supply voltage. This iterative process is repeated until convergence is achieved. Reliable convergence is achieved although difficulties may occur when sharp resonances exist. Convergence can be improved by including a linearized model in (3.1). A particular advantage of this “fast decoupled” approach is adopted; the device model in the form of (3.4) can be in a closed form, a time-domain model, or in any other suitable form.

Alternatively, (3.1) and (3.4) can be solved simultaneously using Newton-Raphson type algorithms. This method requires that device models should be available in closed form wherein derivatives can be efficiently computed [24]. Both (3.1) and (3.4) are cast in a multiphase framework [22][25]. The focus of this approach can have several advantages. Foremost is the modelling of zero sequence current flow. Another is the capability of solving non-characteristic harmonics.

It should be reiterated that harmonic studies can be performed in the time domain, by running a time-domain simulation until a steady state is reached. The challenge is first to identify that a steady-state has indeed been achieved. Secondly, in lightly damped systems techniques are needed to obtain the steady-state conditions within a reasonable amount of computation time [25][26].

3.4. **Modelling of Harmonic Source**

The most common model for harmonic studies is the one of harmonic current source, specified by its magnitude and phase spectrum [27]. The phase is usually defined with respect to the fundamental component of the terminal voltage. The data can be obtained from an idealized theoretical model or from actual measurements. In many cases, the measured waveforms bring more realistic representation of the harmonic sources to be modelled. This is particularly the case if noninteger harmonics are present. When a system contains a single dominant source of harmonics the phase spectrum is not important as shown in Fig 3.5.

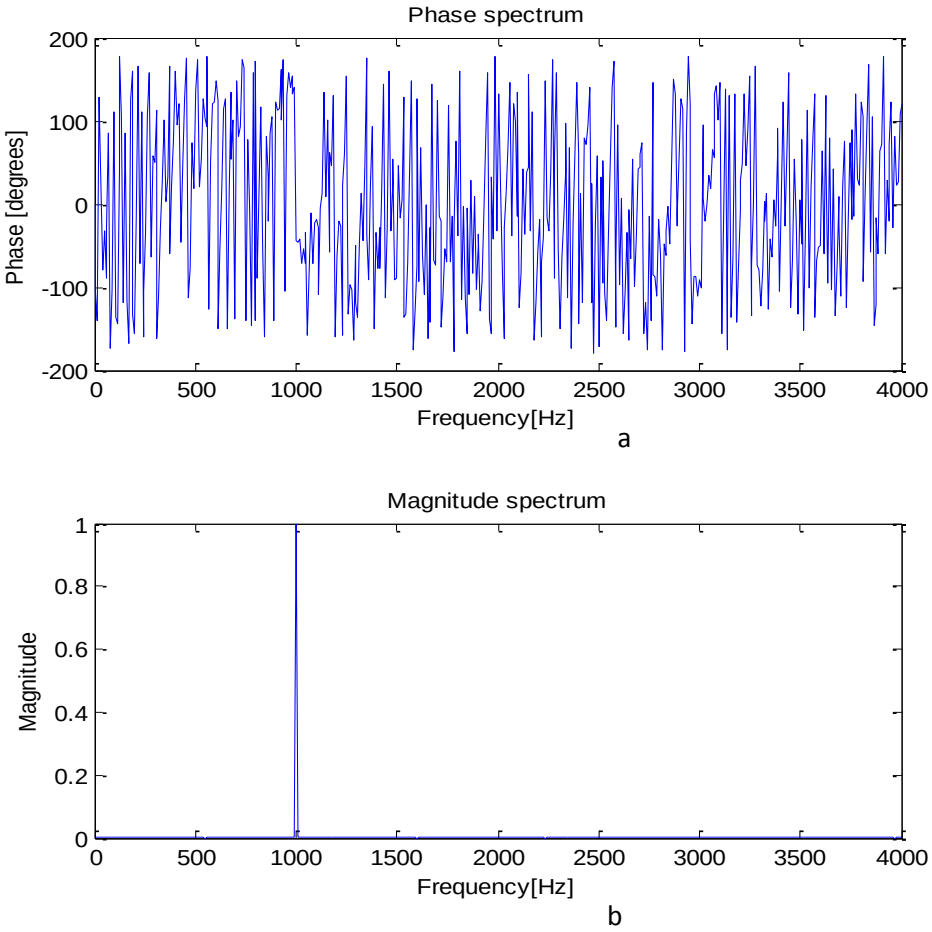

Figure 3.5. A single dominant source of harmonics (a) the phase signal (b) magnitude spectrum

However, phase angles must be represented when multiple sources are present. A common method is to modify the phase spectrum according to the phase angle of the fundamental frequency voltage seen by the load. Ignoring phase angles does not always result in the 'worst scenarios'.

If voltage distortion is significant or unbalanced, a more detailed model becomes necessary. There are three basic approaches that can be taken to derive detailed models:

- Develop analytical formulas for the Fourier series as a function of terminal voltage and operating parameters for the device.
- Develop analytical models for device operation and solve for device current waveform by a suitable iterative method.
- Solve for device steady state current waveform using time domain simulation.

In the analysis of distribution systems one may deal with a harmonic source that is an aggregate of many sources. Such a source can be modelled by measuring the aggregate

spectrum or developing a current source type model analytically based on load composition data [28].

3.4.1. Power Electronics Converters

Examples of power electronics devices are adjustable speed drives, VSC-HVDC stations, static VAR compensator (SVC), the thyristor-controlled series compensator (TCSC), the static synchronous compensator (STATCOM) and the unified power flow controller (UPFC) [29]. Harmonic current source models are commonly used to represent these devices. The phase angles of the current sources are functions of the supply voltage phase angle. They must be modelled adequately for harmonic analysis involving more than one source. The devices are sensitive to supply voltage unbalance. For large power electronics devices such as HVDC terminals and transmission level VSCs, detailed three-phase models may be needed. Factors such as firing–angle dependent harmonic generation and supply voltage unbalance are taken into account in the model [30]. These studies normally scan through various possible device operating conditions and filter performance.

3.4.2. VSC-HVDC Stations

The conventional HVDC transmission systems use line commutated current source converters (CSC) [31]. In these converters each valve consists of a number of thyristors connected in series. The turn-on of the thyristor is controlled by the gate signal while the turn-off occurs at the zero crossing of the AC current which is determined by the AC network voltage (i.e. line commutation), where both the sending end and receiving end of the HVDC system absorb reactive power from the AC systems. Hence, the HVDC system requires an AC system at least at one end to have an AC voltage to commutate. The reactive power requirement is a constraint for HVDC stations connecting to a weak AC system or small island AC network [32].

An alternative for HVDC applications is the use of VSCs, which eliminate the reactive power compensation requirements and this approach are used this studies [33]. Having this advantage, the VSC-HVDC technology opens a wide range of applications

[34][35]. Some of the most interesting applications and possibilities of VSC-HVDC are as follows:

- Multi-terminal DC grid.
- Connection of wind farms to the main grid.
- Utilizing existing right-of way.

Other application of the VSC-HVDC stations is the point-to-point tie station, where no DC line or cable exists. The VSC-HVDC point-to-point station comprises two VSCs sharing a DC capacitor in the DC link [36]. The HVDC-VSCs are not only capable of controlling the power flow, but can supply reactive power and provide independent dynamic voltage control at its two terminals.

3.5. Harmonic Producing Loads

Nonlinear loads inject harmonic currents or harmonic voltages into the distribution network, even when fed by a sinusoidal voltage or current waveform. Nonlinear loads can be broadly divided into two categories;

- Harmonic current source type loads
- Harmonic voltage source type loads

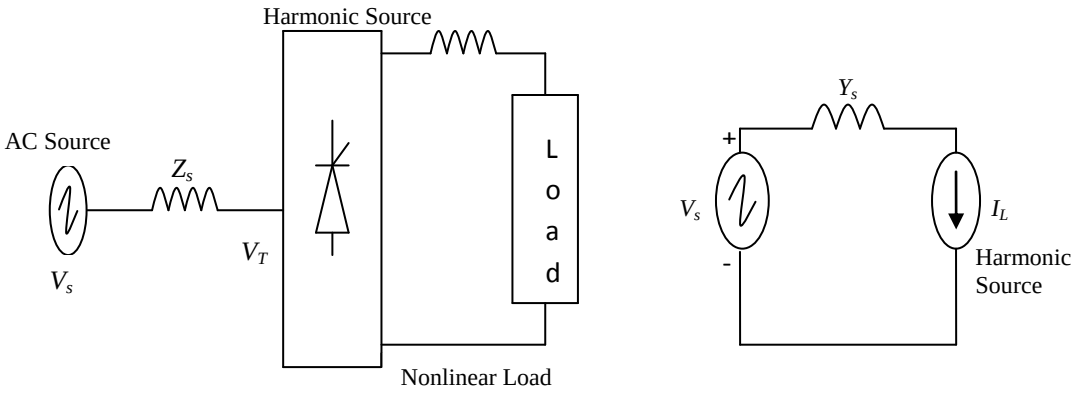

(a) Current Source nonlinear load (b) Per-phase equivalent circuit of thyristor rectifier

Figure 3.6. Norton equivalent circuits for harmonic current source type load

Thyristor controlled loads such as those used for dc drives; current-source inverters (CSIs), etc. constitute harmonic current source type loads. These loads produce harmonic currents on the ac supply side of the rectifier.

Therefore, harmonic current source type loads can be modelled by a simple current source or Norton equivalent circuit as shown in Fig. 3.6.

In contrast, VSC with dc side capacitors constitute harmonic voltage source type loads. These loads produce voltages on the dc side of the inverter to operate.

These simple Norton and Thevenin equivalent circuit models are however to be used with caution, since under special conditions such as resonance conditions, they do not accurately model the harmonic sources. Similarly, harmonic voltage source type loads can be modelled by simple voltage source or Thevenin equivalent circuit as shown in Fig. 3.7.

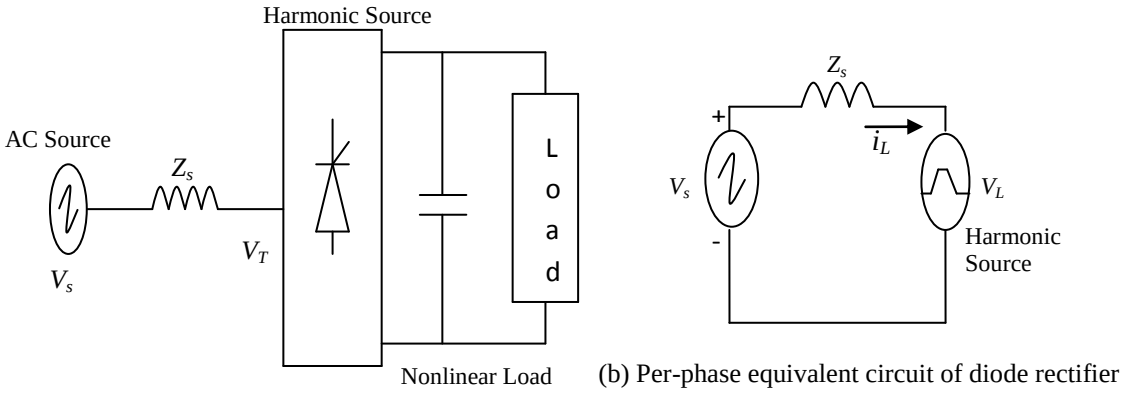

(a) Diode rectifier for ac drives, electronic equipment, etc

(b) Per-phase equivalent circuit of diode rectifier

Figure 3.7. Thevenin equivalent circuit for harmonic voltage source type load

3.6. **Methods for Determining Sources of Harmonic Distortion**

Harmonic distortions have become an important concern for oil and gas explorations and production companies. Two basic approaches have been proposed for controlling the amount of harmonic pollution present in a distribution system. The first scheme involves the establishment of limits on the amount of harmonic currents and voltages generated by platforms and utilities [37-38]. A second scheme, based on the power factor management practice, aims at charging harmonic generators to an amount commensurate with their harmonic pollution level when the limits are exceeded. A great deal of work in this area was described by [39] and [40].

The challenge in the implementation of the above schemes is the need to separate the harmonic generated by the customer equipment from that of the supply system.

3.6.1. Harmonic Power Flow Direction Method

The harmonic source detection is the power direction method which checks the direction of harmonic power flow [41][42]. The side that generates harmonic power is considered to contain the dominant harmonic source or to have a larger contribution to the harmonic distortions observed at the measurement point. This can be analysed using a harmonic Norton equivalent circuit of a utility customer interface as shown in Fig. 3.8.

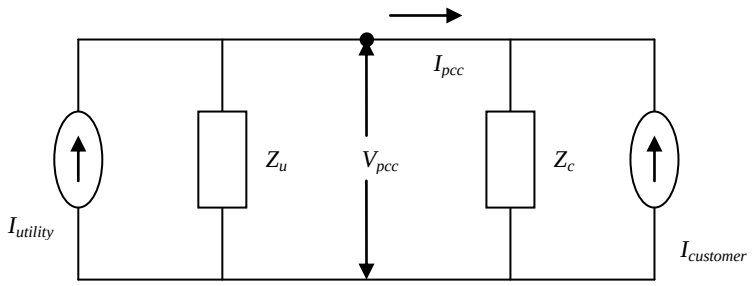

Figure. 3.8. Norton equivalent circuit of a utility customer interface

where

I_{customer} the disturbance sources are the customer harmonic source

$I_{utility}$. the utility harmonic source

Z_u and Z_c are the harmonic impedances of the respective parties.

The circuit is applicable to different harmonic frequencies. The task of harmonic source detection is to determine which side contributes more to the harmonic distortion at the PCC, subject to the constraint that measurements can only be taken at the PCC. To determine which side causes more harmonic distortion at the harmonic order *h*, the power direction method first measures voltage and current at the PCC and then calculates the following harmonic power index:

$$P = V_{PCC} I_{PCC} \tag{3.5}$$

where V_{pcc} and I_{pcc} are the harmonic voltage and current at the PCC for a particular harmonic number. The direction of P is defined as positive when it flows from the *U* side to the *C* side. Conclusions of the power direction method are the following:

If $P > 0$, the *U* side causes more h^{th} harmonic distortion

If $P < 0$, the *C* side causes more h^{th} harmonic distortion

If there is no change in the utility and customer harmonic impedances, then the PCC current flow variation is affected by I_u and I_c only. It is common practice in industry that utilities provide Z_u information to customers when a plant is built or major changes are made to the utility systems. The data is used for harmonic filter design and for harmonic limit compliance verification. Z_u is normally referred to as the contract impedance and should therefore be known [43]. The same applies to Z_c since a harmonic limit compliance check also needs this impedance. An important assumption for this analysis is that both Z_u and Z_c are known to be accurate.

The explanation of harmonic power flow direction is theoretically equivalent to examining the magnitude of $I_u Z_u$ and $I_c Z_c$.

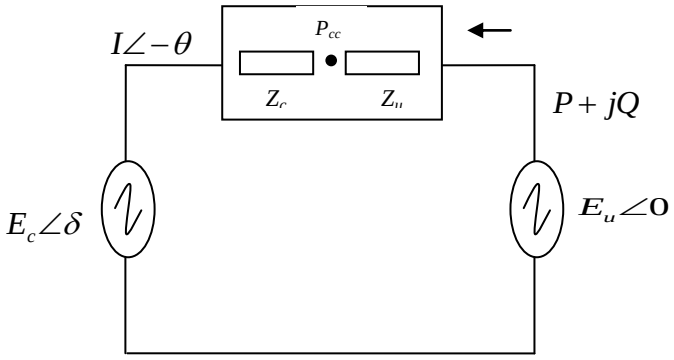

Figure. 3.9. Thevenin equivalent circuit of a utility customer interface

If $I_u Z_u$ is greater than $I_c Z_c$, then it can be shown that the utility side source contributes more to PCC I, and vice versa. Therefore, the circuit of Fig. 3.8 is transformed into the Thevenin equivalent circuit as shown in Fig. 3.9.

In this figure, $Z = Z_u + Z_c$, $E_u = I_u Z_u$, and $E_c = I_c Z_c$. The phase angle of E_u is set to zero and that of E_c is denoted as δ. The harmonic source detection problem is to identify which voltage source E_c or E_u has a higher magnitude [43].

However, following the classic power angle equation, if $Z = jX$, then the active power flowing into E_u is:

$$P = E_u I \cos\theta = \frac{E_u E_c}{X} \sin\delta \tag{3.6}$$

The significance of this equation is that the direction of active power is a function of δ instead of the magnitudes of the voltage sources. As a result, the active power direction-based harmonic source detection method may not be accurate, as it cannot reveal the difference between the magnitudes of the two sources [44].

It is common knowledge to power engineers that the phase angles of bus voltages mainly affect the flow of active power while the magnitudes of bus voltages mainly affect the flow of reactive power. On examining the reactive power flowing into E_u,

$$Q = E_u I \sin\theta = \frac{E_u}{X}\left(E_c \cos\delta - E_u\right) \tag{3.7}$$

The above equation shows that the direction of reactive power is indeed related to the voltage magnitudes. Hence the direction of reactive power could indicate the relative magnitudes of two harmonic sources. However, even the reactive power is not a conclusive indicator of the source of harmonics. The reason is, for instance, that reactive power can still flow from the utility side to the customer side if $E_c > E_u$. The direction of power flow is always dependent on δ and has to be considered while carrying out any measurements [43].

3.6.2. Load Impedance Variation Method

In [44], the paper focus on finding the relationship between the distorted voltage waveform, the distorted current waveform, and the parameters that relates these waveforms, i.e. the load parameters (*R* and *L*). Monitoring the load parameter (*R* & *L* values) variations under the influence of harmonics plays an important role in determining the origin of harmonic distortion and evaluating the load nonlinearity. The load with higher *R* and *L* value variations contains more nonlinear elements and produces larger harmonic magnitudes. A sinusoidal voltage applied to a linear load yields a sinusoidal current. On the other hand, a distorted current waveform will result if a sinusoidal voltage is applied to a nonlinear load. Likewise, if a sinusoidal current is injected through nonlinear impedance, the voltage across that element will be distorted. Thus, nonlinear loads indicate distorted voltage and/or distorted current waveforms but the opposite is not true.

A load with a distorted current or voltage waveform is not necessarily nonlinear. So, considering only the distorted current and voltage waveforms, it is not possible to pronounce the source of the harmonics. It is mainly dependent on the behaviour of the load impedance. Thus, the first step is to find a simple way to monitor the load pattern under the influence of harmonics. Generally for a *RL* load,

$$v(t) = R(t)\cdot i(t) + \frac{d\left(L(t)\cdot i(t)\right)}{dt} \tag{3.8}$$

For an incremental time dt , R & L can be considered constant, hence the equation becomes

$$v(t) = R \cdot i(t) + L \cdot \frac{di(t)}{dt} \tag{3.9}$$

If $v(t)$ indicates an instantaneous voltage value for a distorted voltage waveform for a certain load, and $i(t)$ indicates an instantaneous current value for the corresponding distorted current waveform, then R & L indicate the load pattern under the influence of harmonics. For two successive time intervals *t1* and *t2*, the equations can be written as

$$\begin{bmatrix} v(t_1) \\ v(t_2) \end{bmatrix} = \begin{bmatrix} i(t_1) & \frac{di(t_1)}{dt_1} \\ i(t_2) & \frac{di(t_2)}{dt_2} \end{bmatrix} * \begin{bmatrix} R \\ L \end{bmatrix} \tag{3.10}$$

Solving the above equation numerically yields the solution as

$$z = [i]^{-1} \cdot v \tag{3.11}$$

The above calculation should be repeated for n successive intervals for the current and voltage waveforms with period T. So for times t_1 to t_n , there are $n/2$ sets of values for R &L A sample plot of load parameter variations against time illustrated in Fig. 3.10 shows whether it is linear or nonlinear.

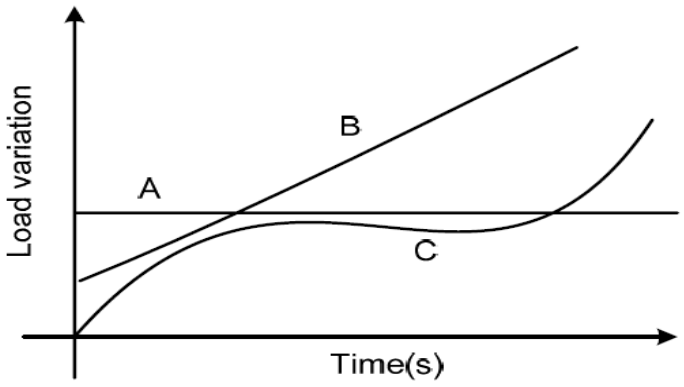

Figure. 3.10 Plot of load parameter variation

If the instantaneous R &L parameters represent linear variation or have constant values during the waveform period (pattern A or B), then it indicates that the load under study is linear (non distorting load). On the other hand, if the instantaneous R &L parameter values have nonlinear variations (pattern C), then it indicates that the load is a source of harmonics.

This mathematical approach can be applied to any set of measured values of *v* and *i,* for any load category. From the plots of load parameter variation versus time, it can be predicted whether the load that possesses sharp variations in its *R* &*L* parameters would be the higher harmonic producing load.

3.7. Total Harmonic Voltage Distortion (V_{THD}) and Current Distortion(I_{THD})

The voltage total harmonic distortion (V_{THD}) is dependent on the magnitude of each harmonic current at its specific harmonic frequency acting upon the source impedance and other individual circuit impedances to produce individual harmonic voltage drops. These are summed and compared with the fundamental voltage to obtain, in percentage terms, the V_{THD}. The resultant voltage distortion, unless resonance is present in the system, tends to decrease further in its measured values from the harmonic-producing load. It is usually highest nearer to the harmonic load and progressively reduces the nearer to the source it is measured, due to the effect of cables, transformers and other impedances, and to a degree, the amount of linear load (such as induction motors), which tends to act as a "harmonic sink" (i.e., it absorbs harmonic current) in the circuit. The higher the magnitude of harmonic current, the higher the voltage distortion for given impedance.

In nonlinear loads, the magnitude of the characteristic harmonic currents is normally proportional to the load demand. At rated load, the harmonic current levels tend to be at the highest levels, except under resonant conditions where specific harmonic currents at the resonant frequency can have significantly higher values. The effect of loading, therefore, will affect the percentage current total harmonic distortion (I_{THD}).

3.8. Total Harmonic Distortion

The most commonly used measure for harmonics is total harmonic distortion (THD), also known as the distortion factor. It is applied to both voltage and current. If DC is ignored, then the THD for a current waveform is defined as:

$$THD_I = \frac{\sqrt{\sum_{k=2}^{\infty}\left(\frac{I_k}{\sqrt{2}}\right)^2}}{\frac{I_1}{\sqrt{2}}} = \frac{\sqrt{\sum_{k=2}^{\infty}(I_k)^2}}{I_1} \qquad (3.12)$$

THD and RMS values are directly linked as shown below:

$$I_{rms} = I_{I,rms}\sqrt{1+THD_I^2} \tag{3.13}$$

Line losses always increase when harmonics are present because these losses are proportional to the square of the rms current. Sometimes they increase more rapidly due to the resistive skin effect.

The total harmonic distortion quantifies the thermal effect of all the harmonics. THD applies to both current and voltage and is defined as the rms value of harmonics divided by the rms value of the fundamental, and then multiplied by 100%. THD of current varies from a few percent to more than 100%. THD of voltage is usually less than 5%. Voltage THDs below 5% are widely considered acceptable, but values above 10% are definitely and will cause problems for sensitive equipment and loads.

3.9. Harmonic Current Magnitude and its Effect on Voltage Distortion

It should be re-emphasized that it is not the percentage of current total harmonic distortion (I_{THD}) which is of main concern. It is the magnitude of the harmonic currents associated with the I_{THD} which is of more importance, as it is the magnitudes of these harmonic currents which interact with the system impedances to produce the individual harmonic voltage drops at the harmonic frequencies which result in the voltage total harmonic distortion (V_{THD}).

It is therefore the total harmonic voltage distortion (V_{THD}) which is to be the main concern in order to minimize any adverse effects on the installed system and equipment. Therefore, it should be the purpose of any harmonic mitigation measure employed to reduce the total harmonic voltage distortion (V_{THD}) to within the necessary limits under all operating conditions.

3.10. General Discussion on Fourier Series

Any physically realizable periodic waveform can be decomposed into a Fourier series of DC, fundamental frequency, and harmonic terms. In sine form, the Fourier series is

$$i(t) = I_{dc} + \sum_{k=1}^{\infty} I_k \sin\left(k\omega_0 t + \theta_k\right) \tag{3.14}$$

where

I_{dc} is the DC (i.e., average) value, I_k are peak magnitudes of the individual harmonics, ω_0 is the fundamental frequency (in radians per second), and θ_k are the harmonic phase angles.

A plot of normalized harmonic amplitudes I_k/I_1 is called the harmonic magnitude spectrum, as illustrated in Figure 3.11a. The superposition of harmonic components to create the original waveform is shown in Figure 3.11b.

The time period of the waveform is

$$T = \frac{2\pi}{\omega_0} = \frac{1}{f_0} \tag{3.15}$$

For a discrete/sampled signal, the frequency spectrum can be obtained as follows:

$$I(k) = \sum_{n=0}^{N-1} i(n) e^{-j2\pi \frac{k}{N} n} \tag{3.16}$$

where N is the number of samples over the period T, $i(n)$ is the amplitude at each sample and $k = 0,1,2,....N-1$. Each frequency is separated by 1/T, with the highest frequency component at $k = N/2$. The highest frequency becomes $k = N/2T$.

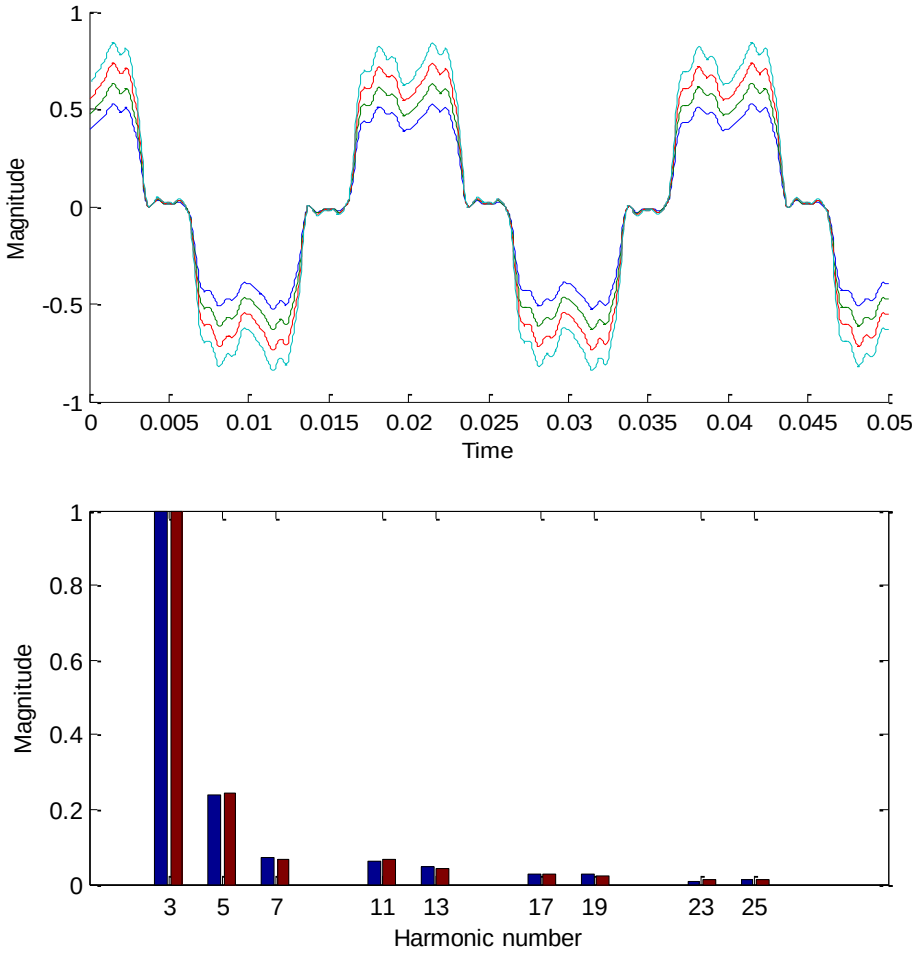

Figure. 3.11 (a) Voltage waveform (b) harmonic spectrum

The sampling frequency to avoid aliasing, also known as the Nyquist frequency, is defined as:

$$fs > 2f(n) \tag{3.17}$$

where f_s is the sampling frequency and the highest frequency component contained in the signal. For power system and harmonic studies, waveforms are normally sampled at 96 – 128 samples/cycle.

Power electronic and nonlinear loads [45][46] exhibit a special property known as half-wave symmetry. Half-wave symmetry occurs when the positive and negative halves of a waveform are identical but opposite, i.e.

$$i(t) = -i\left(t \pm \frac{T}{2}\right) \tag{3.18}$$

where T is the period. Waveforms with half-wave symmetry have no even-ordered harmonics.

3.10.1. Harmonic Power

Harmonic powers (including the fundamental) add and subtract independently to produce total average power. Average power is defined as:

$$P_{avg} = \frac{1}{T}\int_{t}^{t+T} v(t)i(t)dt \tag{3.19}$$

By substituting the Fourier series for voltage and current in (3.19), the average value of all the sinusoidal terms becomes zero, leaving only the time invariant terms in the summation, or

$$P_{avg} = V_{dc}I_{dc} + \sum_{k=1}^{\infty} V_{k,rms} \cdot I_{k,rms} \cdot dpf_k = P_{dc} + P_{1,avg} + P_{2,avg,.....,}P_{k,avg} \tag{3.20}$$

where dpf_K is the displacement power factor for harmonic k .

The harmonic power terms are mostly losses and are usually small in relation to the total power. However, harmonic losses may sometimes be a substantial part of total losses. According to (3.20), if there is no harmonic voltage at the terminals of a generator, then the generator produces no harmonic power. However, due to nonlinear loads, harmonic power does indeed exist in power systems and causes additional losses [47].

3.11. Conclusions

This chapter has outlined a systematic harmonic mitigation of all the relevant issues related with electric network in oil and gas circuits operating under non-sinusoidal and sinusoidal conditions. The mitigation is based on the theory of Fourier series. The generic apparent power has been assumed to comprise active power, reactive power and distortion power. Utilizing the expressions of apparent power and active power, yield the true power factor.

Realistic harmonic domain evaluations are carried out using computed software. This method permit harmonic analysis to be performed by direct frequency domain evaluation techniques based on self and mutual convolutions. This operation avoids the errors introduced by numeric interpolation and aliasing due to the FFT algorithm.

More also, this chapter has developed from first principles the theory of harmonic domain linearization. It has been shown that a non-linear function, when linearised around a base operating point, leads to a harmonic Norton equivalent representation. The admittance matrix equation contains some interesting information that leads to derive the harmonic current and harmonic voltage of the power network. Further more, the admittance matrix with the harmonic current and harmonic voltage of the power network hold a strong tool for the harmonic resonance analysis.

3.12. **References**

[1] J. Sun, and H. Grotstollen, "Solving nonlinear equations for selective harmonic eliminated PWM using predicted initial values", Industrial Electronics, Control, Instrumentation, and Automation, 1992. *IEEE.*

[2] J.G. James, and T.K. Saha, "An Investigation of Harmonic Content in a Remote Mine Site," The sixth International Power Engineering Conference (IPEC2003), 27-29 November 2003, Singapore.

[3] IEEE Recommended Practices and Requirements for Harmonic Control in Electrical Power Systems. Approved June 18, 1992 IEEE Standards Board, Approved January 4, 1994 American National Standards Insitute. IEEE Std 519-1992.

[4] L.Miegeville, and P.Guerin,"Analytical Model for Assessment of the Line Harmonic Currents Generated by a Variable Speed Drive". European Transaction on Electrical Power, Vol. 11. No. 1. January/February, 2001.

[5] R.M.Waggoner, "Practical Guide to Quality Power for Sensitive Electronic Equipment, EC&M Books, Kansas 1997.

[6] Excelsys,"Regulation of Harmonics", Application Note –AN1108 http://www.excelsys.com/wp-content/uploads/2011/09/ApplicationNoteAN1108-RegulationofHarmonics_000.pdf

[7] R.F. Martin "Harmonic Current", http://www.cemag.com/99ARG/Martin103.html

[8] M.Contrearas, V.Cardenas, and H. Calleja, "A Review of Solutions for Harmonic Propagation Damping in Power Distribution Networks", International Power Electronics Congress, 10th *IEEE*

[9] A.Mansoor, and J.McKim,"An examination of the rationale for limiting harmonic emissions from low-voltage equipment", Electromagnetic Compatibility, 1999 *IEEE*

[10] G.G. Balazs, M. Horvath, I. Schmidt, and P. Kiss, "Examination of new current control methods for modern PWM controlled AC electric locomotives", Power Electronics, Machines and Drives (PEMD 2012), IET.

[11] A. Damnjanovic, A. Islam, and A. Domijan, “Aging of distribution transformers due to harmonics”, Harmonics and Quality of Power (ICHQP), 2010

[12] A. Damnjanovic, A. Islam, and A. Domijan, “Harmonic domain modelling of transformer nonlinear characteristic with piece-wise approximation”, Harmonics and Quality of Power (ICHQP), 2010

[13] C.W. Cheah, A.S. Allana, T. Lye, C.S. Chang, S.K. Panda, and S.K. Sahoo, “Investigation of current harmonics in thruster AC drives in oil-rig platforms”, Power Electronics and Drive Systems, Nov; 2009. PEDS.

[14] J. Portos, M.P. Reddy, and D.Eaton, “Application and advantages of PAM multi speed motors in petroleum and chemical industries”, Petroleum and Chemical Industry Conference (PCIC), Sept; 2010.

[15] J.R.Yacamini, L. Hu and R.A Fallaize, “Calculation of commutation spikes and harmonics on offshore platform”, IEE Proc. Vol. 137, PIB, No. 1, pp35-48.

[16] R.Yacamini and I. D. Stewart, “Harmonic problems and calculations on offshore Platforms,” Trans IMaee, Vol 102, pp249-259.

[17] I.D. Stewart, “Offshore Power Systems Harmonic Distortions- Problem, Nuisance or Fact of Life”, ERA Conf Proc, Protecting Electrical Networks and Quality of supply in a DC –Regulated Industry, pp5.2.1-5.2.11

[18] J. Rico, E. Acha, Manuel Madrigal. Dynamic Harmonic Evolution Using the Extended Harmonic Domain. *IEEE Transaction On Power Delivery, Vol. 18, No. 2, April 2003.*

[19] E.Acha, A. Semlyen, N. Rajakovic. A Harmonic Domain Computational Package for Nonlinear Problems and Its Application to Electric Arcs. IEEE TRANSACTION ON POWER DELIVERY, Vol. 5. No 3, July, 1990.

[20] S.J. Subjak, Jr., J.S. McQuikin. “Harmonic-Causes, Effects, Measurements and Analysis”- Update. IEEE Cement Industry Technical Conference

[21] IEEE Recommended Practices and Requirements for “Harmonic Control in Electric Power Systems,” *IEEE Standard 519-1992, IEEE, New York, 1992.*

[22] W. Xu, J.R. Jose and H.W. Dommel, “A Multiphase Harmonic Load Flow Solution Technique”, *IEEE Trans on Power Systems, vol. PS-6, Feb. 1991, pp-174-182.*

[23] V. Sharma, R.J. Fleming, L. Niekamp, “An iterative Approach for Analysis of Penetration in Power Transmission Networks,” *IEEE Trans. on Power Delivery, vol. 6, No. 4, October 1991, pp. 1698-1706.*

[24] D. Xia and G.T. Heydt, "Harmonic Power Flow Studies, Part I - Formulation and Solution, Part II -Implementation and Practical Application", *IEEE Transactions on Power Apparatus and Systems, Vol. PAS-101,* June 1982, pp.1257-1270.

[25] X. Lombard, J. Mahseredjian, S. Lefebvre, C. Kieny,”Implementation of a new Harmonic Initialization Method in EMTP,” *Paper 94- SM 438-2 PWRD,IEEE Summer Power Meeting, San Francisco, Ca., July 1994.*

[26] A. Semlyen, A. Medina, ”Computation of the Periodic Steady State in Systems with Nonlinear Components Using a Hybrid Time and Frequency Domain Methodology,” *Paper 95- WM 146-1 PWRS, IEEE Winter Power Meeting, New York, NY, Jan. 1995.*

[27] “Understanding Power System Harmonics”; *IEEE* Power Engineering Review, November 2001 W.Mack Grady, Surya Santoso.

[28] L. William, P.E. Cotten, R. Sol and P.E. Brandell, “Analysis of Harmonic Pollution on Power Distribution Systems”. *IEEE* PCIC-89-46.

[29] M. A. Kamarposhti, M. Alinezhad, H. Lesani, and N. Talebi, “Comparison of SVC, STATCOM, TCSC, and UPFC Controllers for Static Voltage Stability Evaluated by Continuation Power Flow Method”. *2008 IEEE* Electrical Power & Energy Conference.

[30] A. V. Jaén, E. Acha, and A. G. Expósito, “Voltage Source Converter Modeling for Power System State Estimation: STATCOM and VSC-HVDC”. *IEEE* Transactions on Power Systems, Vol. 23, No. 4, November 2008.

[31] C. Hahn, A. Semerow, M. Luther, and O. Ruhle, *Member*, “Generic Modeling of a Line Commutated HVDC System for Power System Stability Studies”. 2014 *IEEE*

[32] H.Y.TIAN and E.K.K.SNG, “Study of Line-Commutated Thyristor Inverter under Voltage Dips and Novel Ride-Through Solution”.*IEEE.*

[33] N. Gibo, K. Takenaka, M. Takasaki, and T. Hayashi, “Enhancement of Continuous Operation Performance of HVDC with Self Commutated Converter”. *IEEE* Transactions on Power Systems, Vol. 15, No. 2, May 2000.

[34] K. Friedrich, “Modern HVDC PLUS application of VSC in Modular Multilevel Converter Topology”. 2010 *IEEE*.

[35] F. Wang, L. Bertling, and T. Le, “ An Overview Introduction of VSC HVDC: State-of-art and Potential Applications in Electric Power Systems”. BOLOGNA 2011.

[36] E.M. Callavik, P. Lundberg, M.P Bahrman, and R.P. Rosenqvist, “HVDC technologies for the future onshore and offshore grid”. 2012 Grid of the Future Symposium.

[37] V. Sharma and A.C. Thomson, “Power system harmonic guidelines and how to evaluate the impact of customer generated harmonics,” in *Proceedings of the IEEE Communications, Computers and Power in the Modern Environment (WESCANEX 93)*, Saskatoon, Canada, pp. 797 - 800, May 1993.

[38] Electromagnetic Compatibility (EMC)-Part 3: Limits-Section 6:Assessment of Emission Limits for Distorting Loads in MV and HV Power Systems, IEC 1000-3-6,1996.

[39] A. McEachern, W.M. Grady, W.A. Moncrief, G.T. Heydt, and M. McGranaghan, “Revenue and Harmonics: An evaluation of some proposed rate structures,” *IEEE Transactions on Power Delivery*, Vol. 101, Issue 1, pp. 474 - 482, January 1995.

[40] A. Ferrero, L. Peretto, and R. Sasdelli, “Revenue metering in the presence of distortion and unbalance: myths and reality,” in *Proceedings of the International Conference on Harmonics and Quality of Power (ICHQP98),* Athens, Greece, Vol. 1, pp. 42-47, October 14-16, 1998.

[41] W. Xu, “Power Direction Method cannot be used for Harmonic Source Detection”. 2000 *IEEE.*

[42] E. Alex. Emanuel, "On the Assessment of Harmonic Pollution", *IEEE* Transactim on Power Delivery. 3 Jul. l995.

[41] C. Li, W. Xu and T. Tayjasanant, “A Critical Impedance Based Method for Identifying Harmonic Sources,” *IEEE Transactions on Power Delivery*, Vol. 19, No. 2, pp. 671-678, April 2004.

[42] W. Xu and X. Liu, “An Investigation on the Validity of Power Direction Method for Harmonic Source Determination,” *IEEE Transactions on Power Delivery*, Vol. 18, No. 1, pp. 214-219, Feb. 2003.

[43] A. A. Moustafa, A. M. Moussa, and M. A. El-Gammal, “Separation of customer and supply harmonics in electrical power distribution systems,” in *Proceedings of IEEE International Conference on Harmonics and Quality of Power(ICHQP00),* Orlando, FL, Vol. 1, pp. 208 – 213, October 1-4, 2000.

[44] N. Mohan, T.M. Undeland and W.P. Robbins, “Power Electronics: Converters, Applications and Design,” Wiley, 3rd edition, 2002, ISBN 0-4712-2693-9.

[45] M.H. Rashid, “Power Electronics: Circuits, Devices and Applications,” Prentice Hall, 3rd edition, 2003, ISBN 0-1310-1140-5.

Chapter 4

4. Harmonic Modelling of Power Line and Power Cable Systems

4.1. Introduction

Future offshore wind farms will have large power ratings and will be situated much further offshore than current projects. An important question is how the wind energy produced either onshore or offshore is to be transported to feed into the onshore/offshore oil and gas production weak power system. Until now grid connection had been considered exclusively on a per project basis. Since existing wind farms have moderate distances to the shore of up to 25 km and power ratings up to hundreds MW, three-phase ac transmission through underground or submarine cables at medium or high-voltage levels has to be applied exclusively [1-2]. The high power cable transmission challenges the realization of onsite-efficient grid connections of such wind parks [3-7]. They introduce a problem of parallel resonance due to the interaction of shunt capacitance of the cables with the rest of the network. As the length increases, the shunt capacitance increases and the natural resonance frequency decreases [8].

Harmonic resonance is one of the main consequences of harmonics in power systems. Since resonance is characterized by the inductive and the capacitive elements in the network, changes in system impedance leads to the alteration of the resonant point. Many harmonic related issues can be traced to this phenomenon and the tools available to analyze the phenomenon are very limited. Frequency scan analysis is probably the only viable method at present to identify the existence of resonance and to determine the resonance frequency. Unfortunately the tool cannot offer additional information required to solve the problem effectively [9-10]. Therefore, a new method has been introduced known as modal domain analysis. In the modal domain, a number of modal voltage waves equal to the number of active conductors is assumed to exist. In a transmission line with more than one conductor, one of the modes will travel with a smaller velocity and higher attenuation than the rest, and this is attributed to the ground penetration, called the ground mode. At the sending and receiving end of the line harmonic voltage and current excitations offer very strong tools for the cancellation of harmonic parallel resonances.

4.2. **Harmonic Modelling of Overhead Transmission Lines**

In the most general terms, a transmission line is a system of dielectric insulating media that is capable of guiding the electric energy transfer between a generator and a load, irrespective (at least with a good approximation) of the bends that the line undergoes because of installation needs. From this point of view, a one dimensional propagation phenomenon takes place on a transmission line.

When dealing with multi-conductor transmission all the admittance matrices of the unconnected branches of the original network components are symmetric and therefore, the functions that represent the elements need only be evaluated for elements on or above the leading diagonal.

The formulation of mathematical models of transmission line parameters at harmonic frequencies is more complex than that of transmission line parameters at power frequencies. Many factors that are normally neglected at power frequencies are needed at harmonic frequencies [10], which include:

- Long-line effects
- VAR compensations
- Frequency dependence
- Line impedances
- Line transpositions

Information at a large number of points along the line is needed for the diagnosis of harmonic interference. The formulation of mathematical models for transmission line parameters suitable for harmonic studies of oil and gas production field/platform are:

- Evaluation of lumped parameters: The lumped parameters are generated from the geometric configuration of the transmission line considering the ground return and skin effects.

- Evaluation of distributed parameters: Here the long-line effects are combined with lumped parameters, to obtain exact models of transmission lines suitable for the harmonic analysis of electrical power in the oil and gas production industry.

4.2.1. **Evaluation of Lumped Parameters**

The definition of lumped series impedance and shunt admittance of a multi-conductor transmission line are as follows:

$$\mathbf{Z} = \mathbf{Z}_e + \mathbf{Z}_g + \mathbf{Z}_{skin}\ \Omega/km \tag{4.1}$$

$$\mathbf{Y} = j\rho\ \omega 2\pi\epsilon_0\mathbf{P}^{-1}\ 1/\Omega km \tag{4.2}$$

where

ε_0 = 8.854 x 10^{-9} F/km is the permittivity of free space
$\omega = \omega_0 h$, where $\omega_0 = 2\pi f_0$
f_0 is the base operating frequency in Hz
h is the harmonic order
10 Ω/m^3 - Resistivity (ρ) of swampy ground
100 Ω/m^3 - Resistivity (ρ) of average damp earth
1000 Ω/m^3 - Resistivity (ρ) of dry earth
P -Potential Coefficients

Equation (4.3) defines the impedance matrix due to the magnetic fluxes outside the conductors, and the impedance contribution due to a lossy earth return path. The skin effect ($\mathbf{Z}_{skin}$) is the impedance matrix due to the magnetic fluxes inside the conductors. The potential coefficients (**P**) form the matrix of Maxwell's coefficients [11].

4.2.2. **Matrix of Potential Coefficients (P)**

The images method used to obtain the potential coefficients are generated from the geometrical arrangement of the conductors in the tower. The method allows the conducting plane to be replaced by a fictitious conductor located at the mirror image of the actual conductors. Fig. 4.1 shows when conductor l and m above ground have been replaced by two equivalent conductors and their images located at their mirror image [11-12].

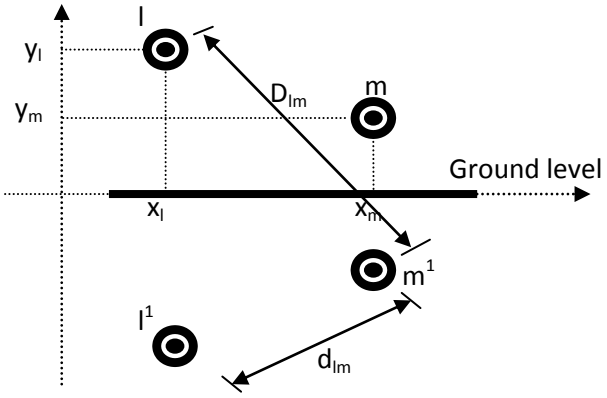

Figure 4.1. Line geometry and its image

The elements of the matrix of potential coefficients (P) are given by the self-potential coefficient p_l for the l_{th} conductor and the mutual potential coefficient P_{lm} between the l_{th} and m_{th} conductors, and are defined as follows:

$$P_l = \ln \frac{2y_l}{r_{ext,l}} \tag{4.3}$$

$$P_{lm} = \ln \frac{D_{lm}}{d_{lm}} \tag{4.4}$$

where

$$D_{lm} = \sqrt{(x_m - x_l)^2 + (y_m + y_l)^2}$$

$$d_{lm} = \sqrt{(x_m - x_l)^2 + (y_m - y_l)^2}$$

$r_{ext,l}$ is the external radius in m of the l_{th} conductor. All variables in Figure 4.1 are given in m. Potential coefficients depend entirely on the physical arrangement of the conductors and need only be evaluated once.

4.2.3. **Impedance Matrix of Ground Return (Z_{G-E})**

The development of a formula based on infinite series pertaining to a current-carrying wire above a lossy earth gave rise to the study of electromagnetic fields, propagation characteristics and magnetic induction effects caused by power lines [13]. A satisfactory solution to the related problem of a current carrying wire above a lossy earth was first

brought forward by Carson in 1926. Carson's integral was generated with the use of the so-called Maxwell's equations and basic concepts of circuit theory [14-15]. The solution was given in the form of an infinite integral, which has not a closed form or analytical answer, but it is conveniently expressed as a set of infinite series [16-18]. Carson's integral goes rather well with the more accurate integrals of Wedepohl or Wait, for most conditions prevailing in power circuit problems. Heavy computational cases are involved with the numerical solution of any of the three infinite integrals that limit their use on an everyday application. It is only in a reduced number of conductors in close proximity to the ground and radio frequency applications that the more accurate approaches are used [13].

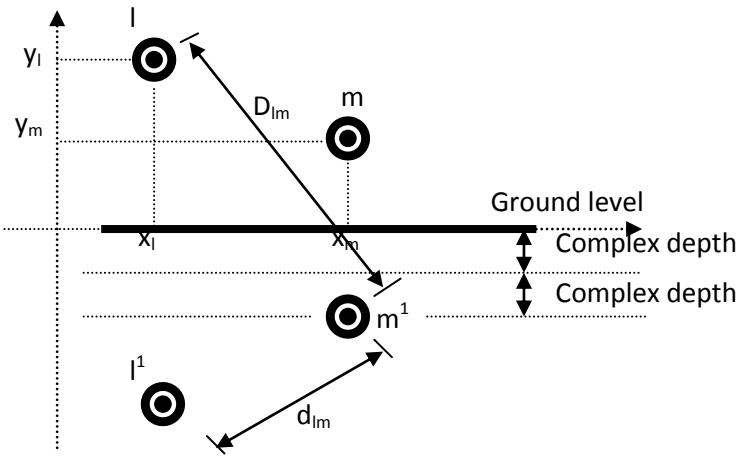

Figure 4.2. Line geometry and its image using the complex penetration approach

Based on Carson's work, in Fig. 4.2 the earth impedance can be concisely expressed as

$$z_e = \phi\left(J\left(r,\theta\right)\right) \tag{4.5}$$

where

$z_e \in [Z_e]$

ϕ = function of $(\cdot)$

$J_{(r,\theta)} = P_{(r,\theta)} + jQ_{(r,\theta)}$

$r_{Im} = \sqrt{\omega\mu\sigma}\ D_{lm}$

$D_{lm} = \sqrt{(y_l + y_m)^2 + d^2}$

$D_{ll} = 2y_l$

$$\theta_{ll} = \arctan\left(\frac{d}{y_l + y_m}\right)$$

$$\theta_{ll} = 0^o$$

$\mu = 4\pi 10^{-7}$ [H/m]

$\omega = 2\pi f$

σ is the ground's conductivity in S/m

The P and Q terms in the preceding equations are defined by Carson as an infinite series expressed in terms of two parameters, call them S and θ. However, the value of S and θ differ.

Carson's solution to equation (4.5), in terms of infinite series, is

$$P = (1 - S_4) \times \frac{\pi}{8} + \ln\frac{2}{\gamma^{1_r}} \times \frac{S_2}{2} + \theta \times \frac{S_2^{\,1}}{2} - \frac{\sigma_1}{\sqrt{2}} + \frac{\sigma_2}{2} + \frac{\sigma_3}{\sqrt{2}} \tag{4.6}$$

$$Q = \frac{1}{4} + \ln\frac{2}{\gamma^{1_r}} \times \frac{1 - S_4}{2} - \theta \times \frac{S_4^{\,1}}{2} + \frac{\sigma_1}{\sqrt{2}} - S_2 \times \frac{\pi}{8} + \frac{\sigma_3}{\sqrt{2}} + \frac{\sigma_4}{2} \tag{4.7}$$

where γ^1 is the Euler's constant 1.7811 and $S_2, S_2^{\,1}$, S_4, $S_4^{\,1}, \sigma_1, \sigma_2, \sigma_3$ and σ_4 are infinite series, which converge quickly for most power system applications, but the amount of required computation increases with frequency and the separation between conductors.

For very high frequency applications and when large distances are involved the series given in equations (4.6) and (4.7) present convergence problems.

In the late 1970s and early 1980s C. Dubanton brought forward an elegant and accurate solution with simpler formulas aiming at a reduction in computing time, while keeping accuracy at a reasonable level in system applications. Due to its simplicity and high degree of accuracy for the whole frequency span for which Carson's equations are valid, though, for a wide range of frequencies it becomes increasingly inaccurate as the angle θ approaches the $\pi/2$ radians. Dubanton's formulae for the evaluation of the self and mutual impedances of the conductors' *l* and *m* of Fig. 4.2 are,

$$Z_{G-E_U} = \frac{j\rho\omega\mu_0}{2\pi} \ln\frac{2(y_l + p)}{r_{ext,l}} \ \Omega/\text{km} \tag{4.8}$$

$$Z_{G-E_{lm}} = \frac{j\rho\omega\mu_0}{2\pi} \ln\frac{\sqrt{\left((x_1 - x_m)^2 + (y_l + y_m + 2p)^2\right)}}{d_{lm}} \ \Omega/\text{km} \tag{4.9}$$

where

μ_0 = 4π x 10^{-7} H/m is the permeability of free space

$p = \frac{1}{\sqrt{j\omega\mu_0\sigma}}$ is the complex depth below the earth at which the mirroring surface located is

σ is the earth conductivity in S/m

(ρ) - resistivity of dry earth

4.2.4. **Skin Effect Impedance Matrix Z_{Skin}**

The impedance varies with frequency in a non-linear fashion, the reason being that the current flowing in the conductor does not distribute itself uniformly over the full area available, but it tends to flow on the surface. The effect of this behaviour is an increase in the resistance and a decrease in the internal inductance with increasing frequency [19]. This phenomenon is known as skin effect. This term accounts for the internal impedance of the conductors [20-21]. Both resistance and inductance vary with frequency in a non-linear manner and need to be computed at each particular harmonic frequency [22]. The reasons that the non-linear variation of these parameters with frequency have been very early recognized and are attributable mainly to the fact that the current flowing in the conductor does not distribute itself uniformly over the full area available, rather, it tends to flow on the surface. The overall effect is an increase in the resistance and a decrease in its internal inductance.

In the past, extensive research both theoretical and practical has been carried out for conductors with regular and non-regular shapes. Solid conductors, annular conductors (tubes), rounded, squared, stranded, etc. have been investigated and different models have been proposed. In power system applications the most successful approach has been the one that models the power conductor as a tube. The reason being that modern power transmission circuits utilize almost exclusively ACSR (Aluminium Conductor Steel Reinforced) conductors and, under the assumption that a negligible amount of current flows through the path of high resistance (the steel), the conductor can be approximated to a tube [23-26]. The evaluation of the internal impedance of an annular conductor with outer radio r_i and inner radio r_j, at a given frequency is determine by:

$$Z_c = \frac{j\omega\mu_o}{2\pi}\frac{1}{x_o}\frac{J_o(x_e)N_o^1(x_i) - N_o(x_e)J_o^1(x_1)}{J_o^1(x_e)N_o^1(x_i) - N_o^1(x_e)J_o^1(x_i)} \tag{4.10}$$

$$\omega L = \frac{j\omega\mu_o}{2\pi}\frac{1}{x_o}\frac{J_o(x_e)N_o^1(x_i)+N_o(x_e)J_o^1(x_1)}{J_o^1(x_e)N_o^1(x_i)+N_o^1(x_e)J_o^1(x_i)} \tag{4.11}$$

the function arguments x_e and x_i are obtained from

$$x = j\sqrt{j\omega\mu_o\sigma_e}\, r$$

where $r = r_e$ *or* $r = r_i$

Furthermore, J_o and N_o represent the Bessel functions of first kind and second kind of zero order, J_0^1 and N_0^1 their derivatives and σ_c the conductivity of the conductor.

The Bessel functions and their derivatives are solved, within a specified accuracy, by means of their associated infinite series. In some cases this is done without difficulties because the series present convergence problems and their asymptotic expansions have to be used. This is particularly the case at high frequencies and low ratios of thickness to external radius, i.e. t/r_e or $(r_e - r_i)/r_e$. An additional problem is also the time required for them to converge.

Once again the complex penetration concept has been successfully invoked, and based on it, an alternative solution has been proposed. The new formulation supersedes the problems encountered by the infinite series of the Bessel functions. It is a closed form solution, and although errors up to the 6.5 per cent exist at low frequencies, its accuracy increases with frequency. The method appeals to the two extreme cases of the impedance, the zero frequency solution and the infinite frequency solution. In power systems applications a power conductor is modelled as an annular conductor (tube). The reason behind this is that modern power transmission circuits make use exclusively of almost ACSR (Aluminium Conductor Steel Reinforced) conductors under the assumption that a negligible amount of current flows through the path of high resistance (the steel) the tube concept is a realistic one [27]. The radius of the conductor is the outer radius of the tube and the radius of the steel reinforcement is the inner radius of the tube as shown in Figure 4.3.

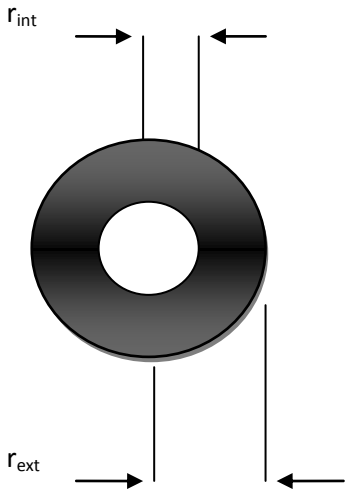

Figure 4.3. ACSR conductors

A suitable model to determine internal impedance of an ACSR conductor using the complex penetration concept may be established by using

$$Z_{Skin_U} = \sqrt{\left(R_0^2 + Z_\infty\right)} \quad \Omega/\text{km} \tag{4.12}$$

where

$$R_0 = \frac{1}{\pi\left(r_{ext,l}^2 - r_{\text{int},l}^2\right)\sigma_C} \tag{4.13}$$

$$Z_\infty = \frac{1}{2\pi r_{ext,l}\sigma_c\, pc} \tag{4.14}$$

$$pc = \frac{1}{\sqrt{j\omega\mu_0\sigma_c}} \tag{4.15}$$

where

$r_{\text{int},l}$ is the internal radius of the conductor l in m

Pc is the complex depth below the earth at which the mirroring surface is located.

σ_c is the conductivity of the conductor in S/m

R_o is the dc resistance per unit length

This model is a closed-form formulation which overcomes difficulties experienced with the lack of robustness of the infinite series of the Bessel functions.

4.2.5. **Reduced Equivalent Matrices $\mathbf{Z_{abc}}$ and $\mathbf{Y_{abc}}$**

Although AC Extra High Voltage transmission lines contain a large number of conductors, i.e. earth wires and several bundle conductors per phase, the interest of harmonic studies is not the individual conductors but the individual phases and steps must be taken to find reduced equivalent matrices, which should correctly account for the original configuration while keeping essential information only, i.e. one equivalent conductor per phase. Reduced equivalent matrices could be achieved in two different ways:

- The first method is to use the geometric mean radius (GMR), which is frequency independent.
- The second method uses matrix reduction techniques; it is frequency dependent for the series impedance. This method requires more computation and can be carried out using the following three steps at each frequency:

1. Matrices **Z** and **P** are set up with an order equal to the total number of conductors plus earth wires.
2. By assuming that the voltage from line to ground is exactly the same for all the conductors in the bundle, the transformation matrices $\mathbf{B}^T$ and **B** are built up, so that modified matrices $\mathbf{Z}_{Re}$ and $\mathbf{P}_{Re}$ are obtained,

$$\mathbf{Z}_{Re} = \mathbf{B}^T\mathbf{Z}\mathbf{B} \tag{4.16}$$

$$\mathbf{P}_{Re} = \mathbf{B}^T\mathbf{P}\mathbf{B} \tag{4.17}$$

3. This is followed by a partial inversion applied to $\mathbf{Z}_{Re}$ and $\mathbf{P}_{Re}$. Notice that a number of elements equal to the number of phases are inverted, with each of the non-inverted locations corresponding to one of the conductor per phase. The final reduced equivalent matrices $\mathbf{Z}_{abc}$ and $\mathbf{P}_{abc}$ are obtained, whose order equals the number of phases but implicitly accounts for the original configuration.

The reduced equivalent matrix of potential coefficients $\mathbf{P}_{abc}$ is inverted and multiplied by a constant factor to obtain the shunt admittance matrix, $\mathbf{Y}_{abc} = j1000\,\omega\,2\pi\varepsilon_0\,P^{-1}{}_{abc}$. The shunt admittance parameters vary linearly with frequency [30].

4.3. **Evaluation of Distributed Parameters**

Long-line effects must be taken into account in harmonic propagation analysis as the transmission line length increases. The nominal pi circuit model, described above, is not valid for long-line transmission. Alternatively, the use of equivalent pi circuit model or analogous formulations, derived from the wave propagation equation, is more robust [29].

4.3.1. **Modal Analysis at Harmonic Frequencies**

The incorporation of long-line effects into multi-conductor transmission lines is not as simple as for single phase lines, because it involves matrix rather than scalar operations. Operations such as square roots, logarithms, circular and hyperbolic functions, etc. are not directly defined in matrix theory. The solution adopted in power transmission line problems has been to diagonalize the matrices, through modal analysis, and then normal scalar operations are carried out for the decoupled matrices [30-31]. More recently, less time demanding, yet accurate solutions have been proposed.

In general, diagonalization procedures of matrices associated with three phase transmission lines are performed by means of iterative algorithms [32], i.e. QR (Quadratic Residue) methods and analytical formulas exist for the special case of configurations with centre-phase symmetry.

An alternative is a closed form approach, which is based on the solution of the cubic equation and applies to cases of three phase transmission lines of arbitrary configuration. However, the procedure does not solve the rather theoretical problem of irregular eigenvalues.

4.3.2. **Non-Homogeneous Lines**

Series and shunt compensation as well as transpositions will often be included in transmission systems. In such scenario each individual section of the transmission

system needs to be depicted as an independent unit [33-34]. All the units are then cascaded to derive an equivalent matrix equation of ABCD parameters, which effectively relates the input to the output taking into consideration all the discontinuities along the transmission system [35].

Capacitors produce no harmonic distortion and their reactance varies linearly with frequency. Reactors, on the other hand, are non-linear elements and their magnetizing branches are rich in harmonics. It has been shown that this introduces considerable complexities into the analysis. However, under the assumption that no saturation takes place, the reactance varies linearly with frequency and no harmonic distortion is produced.

In a multi-conductor transmission line the voltages and currents existing in an incremental line length Δx are expressed as

$$\frac{\partial^2 V}{\partial x^2} = \mathbf{Z}_{\text{abc}}\,\mathbf{Y}_{\text{abc}}\,\mathbf{V} \tag{4.18}$$

$$\frac{\partial^2 I}{\partial x^2} = \mathbf{Y}_{\text{abc}}\,\mathbf{Z}_{\text{abc}}\mathbf{I} \tag{4.19}$$

Solution of equations (4.18) and (4.19) for *V* and *I* may be expressed in a number of different ways which are suitable for harmonic studies involving multi-conductor transmission lines [36][37].

$$\begin{bmatrix} V_{ABC} \\ V_{abc} \end{bmatrix} = \begin{bmatrix} Z_{SS} & Z_{SR} \\ Z_{RS} & Z_{RR} \end{bmatrix} \begin{bmatrix} I_{ABC} \\ I_{abc} \end{bmatrix} \tag{4.20}$$

The subscripts *ABC* and *abc* are for the sending and receiving ends of the transmission line. Operations are carried out in the model domain and inverse transformations into the phase domain, yield the following solutions,

$$Z_{SS} = Z_{RR} = T_v Z_{c,m} \tanh^{-1}(diag(\Gamma_m) l) T_i^{-1} \tag{4.21}$$

$$Z_{SR} = Z_{RS} = T_v Z_{c,m} \sinh^{-1}(diag(\Gamma_m) l) T_i^{-1} \tag{4.22}$$

where

m include the two aerial modes and the ground mode, α, β, and 0, respectively

$$T_v = eig\{Z_{abc}Y_{abc}\}$$

$$T_i = eig\{Y_{abc}Z_{abc}\}$$

$$\Gamma_m = \sqrt{diag(Z_m Y_m)}$$

$$Z_{c,m} = \sqrt{diag(Z_m Y_m^{-1})}$$

$$Z_m = T_v^{-1} Z_{abc} T_i$$

$$Y_m = T_i^{-1} Y_{abc} T_v$$

$$T_v^{-1} = T_i^T$$

T_v and T_i contain the eigenvectors of $\mathbf{Z}_{abc}\mathbf{Y}_{abc}$ and $\mathbf{Y}_{abc}\mathbf{Z}_{abc}$, respectively.

Γ_m is a diagonal matrix which contains the propagation constants $\gamma_m = \sqrt{z_m y_m}$ per km.

$Z_{c,m}$ is a diagonal matrix which contains the characteristic impedances

$z_{c,m}\sqrt{z_{m/y_m}}$ in Ω where $z_m \in Z_m$ and $y_m \in Y_m$.

Z_m and Y_m are diagonal matrices of modal impedance and modal admittances, respectively.

l is the length of the transmission line in km.

Moreover

$$\mathbf{V}_{abc} = \mathbf{T}_v\mathbf{V}_m \tag{4.23}$$

$$\mathbf{I}_{abc} = \mathbf{T}_i\mathbf{I}_m \tag{4.24}$$

where

$\mathbf{V}_m$ and $\mathbf{I}_m$ are vectors of modal quantities.

The transmission line can be given in the form of a transfer admittance matrix, such as

$$\begin{bmatrix} I_{ABC} \\ I_{abc} \end{bmatrix} = \begin{bmatrix} Y_{SS} & Y_{SR} \\ Y_{RS} & Y_{RR} \end{bmatrix} \begin{bmatrix} V_{ABC} \\ V_{abc} \end{bmatrix} = \begin{bmatrix} Z_{SS} & Z_{SR} \\ Z_{RS} & Z_{RR} \end{bmatrix}^{-1} \begin{bmatrix} V_{ABC} \\ V_{abc} \end{bmatrix} \tag{4.25}$$

From this equation, an equivalent π-circuit of the transmission line is obtained, as shown in Fig. 4.4.

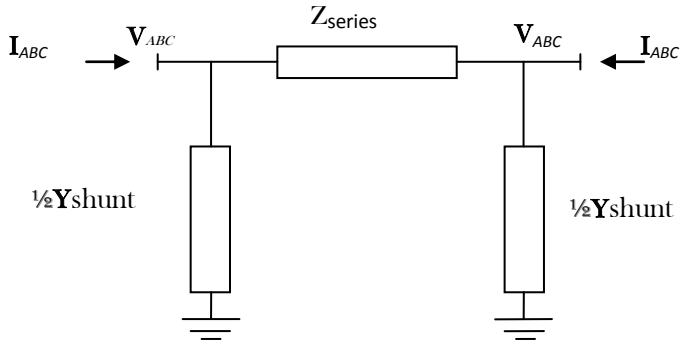

Figure 4.4. Transmission equivalent line π-circuits

The long line effects of a three-phase transmission can be incorporated using the following method:

$$Y_{SS} = Y_{RR} = Z_{series}^{-1} + \frac{1}{2} Y_{shunt} \tag{4.26}$$

$$Y_{SR} = Y_{RS}^{T} = -Z_{series}^{-1}$$

where

$$Z_{series} = Z_{abc} T_i \Gamma_m^{-1} \sinh(diag(\Gamma_m) l) T_i^{-1}$$

$$Y_{shunt} = 2 T_i \Gamma_m^{-1} \tanh(\tfrac{1}{2} diag(\Gamma_m) l) T_i^{-1} Y_{abc}$$

T_v = eigenvectors of { Z_{series} Y_{shunt}} (4.27)

T_i = eigenvectors of {Y_{shunt} Z_{series}} (4.28)

$$T_v^{-1} Z_{series} T_i = \begin{bmatrix} z_0 & 0 & 0 \\ 0 & z_\alpha & 0 \\ 0 & 0 & z_\beta \end{bmatrix} \text{ and } T_i^{-1} Y_{shunt} T_v = \begin{bmatrix} y_0 & 0 & 0 \\ 0 & y_\alpha & 0 \\ 0 & 0 & y_\beta \end{bmatrix} \tag{4.29}$$

$$z_{m,c} = \frac{1}{y_m} = \begin{bmatrix} \sqrt{z_0 y_0^{-1}} & 0 & 0 \\ 0 & \sqrt{z_\alpha y_\alpha^{-1}} & 0 \\ 0 & 0 & \sqrt{z_\beta y_\beta^{-1}} \end{bmatrix} \tag{4.30}$$

$$\Gamma_m = \begin{bmatrix} \sqrt{z_0 y_0} & 0 & 0 \\ 0 & \sqrt{z_\alpha y_\alpha} & 0 \\ 0 & 0 & \sqrt{z_\beta y_\beta} \end{bmatrix} \tag{4.31}$$

Equations (4.26)-(4.31) show that the equivalent-pi circuit model can accurately represent the line at specific frequency. This model is a lumped parameter model and it is good for the specific frequency of interest and particular line length. This model includes the hyperbolic corrections with no approximations involved and is the best model for steady-state solutions and for frequency scans. This model takes into account the skin effect and ground return corrections.

The equivalent pi model is also multi-phase transmission line model represented in the form of ABCD parameters matrix equation for distributed element given as

$$\begin{bmatrix} V_{ABC} \\ I_{ABC} \end{bmatrix} = \begin{bmatrix} A & B \\ C & D \end{bmatrix} \begin{bmatrix} V_{abc} \\ -I_{abc} \end{bmatrix} \tag{4.32}$$

where

$$A = T_v \cosh(diag(\Gamma_m)l) T_v^{-1}$$

$$B = T_v Z_{c,m} \sinh(diag(\Gamma_m)l) T_i^{-1}$$

$$C = T_i Z_{c,m}^{-1} \sinh(diag(\Gamma_m)l) T_v^{-1}$$

$$D = T_i \cosh(diag(\Gamma_m)l) T_i^{-1} = A^T$$

4.4. **Test Case 1**

The 500kV, three-phase transmission line of flat configuration shown in Figure 4.5 is used to assess its harmonic response to voltage and current excitations. The voltage excitation relates to a harmonic voltage excited line, specified as V_S = 1 p.u. and I_R = 0. This generates the maximum voltage harmonic level necessary for design purposes. While the current excitation is the harmonic current excited short-circuited ended line, specified as V_S = 0 and I_R = 1p.u. which is more likely to be of practical interest. Both cases are represented in Figure 4.6. It is assumed that the transmission line is 800km long and that its operating frequency is 50 Hz.

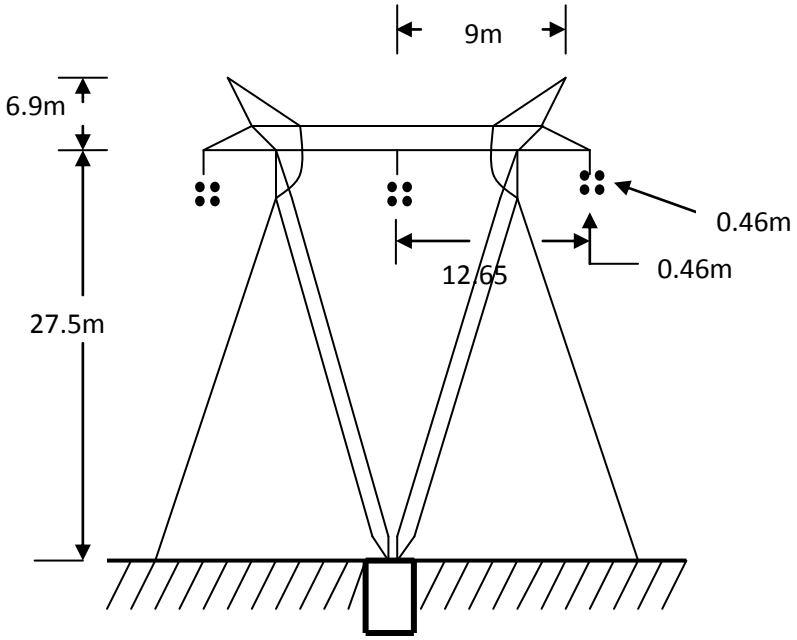

Figure 4.5. Power transmission line

The following terminal conditions are assessed:

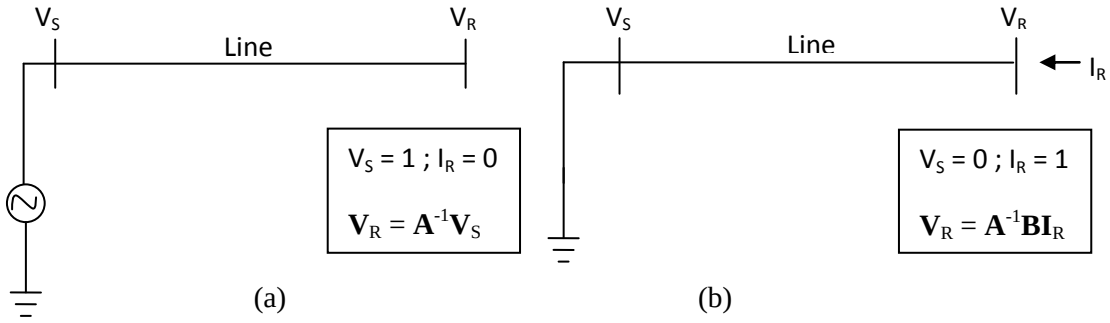

Figure 4.6. Transmission line terminal conditions (a) voltage of source and open-ended line; (b) current source and short-circuited line.

The analysis of the propagation of the voltage wave can be carried out in either the phase domain or the modal domain. Mutual couplings exist between the phases in the phase domain analysis and changes of voltage in one phase are a function of the changes of voltage in the other phase. In harmonic voltage excitation at the sending end of the line, $\mathbf{V_S}$, and open-ended line $\mathbf{I_R = 0}$, the receiving end voltage is given by

$$\mathbf{V_{abc}} = \mathbf{A}^{-1}\mathbf{V}_S \tag{4.33}$$

In the case of the harmonic current excitation at the receiving end, $\mathbf{I_R}$ and short circuit ended line at the sending end $\mathbf{V_S = 0}$, the receiving end voltage is given by

$$\mathbf{V_{abc} = A^{-1} BI_R} \tag{4.34}$$

Equations (4.33) and (4.34) provide a very important conclusion. It not only simplifies the proposed resonance mode analysis technique but also reveals the unique characteristics of harmonic resonance.

The transmission line exhibits a resonant peak at a harmonic order which is a function of both the length of the line and fundamental frequency,

$$\text{harmonic order} = \frac{\lambda}{kl} \tag{4.35}$$

where:

- λ is the wavelength at fundamental frequency
- l is the length of the transmission line
- k is equal to two when the excitation is produced by a current source and equal to four when the excitation is produced by a voltage source.

The main technical datas of this power line are given in Table A2.1.

ABCD parameters are generated as follows:

A =

-0.7277 + 0.5690i -0.3852 + 0.6127i -0.4982 + 0.7038i
-0.4431 + 0.7160i -0.7497 + 0.4663i -0.4431 + 0.7160i
-0.4982 + 0.7038i -0.3852 + 0.6127i -0.7277 + 0.5690i

B =

1.0e+002 *

-2.8054 + 2.7093i -2.7407 + 5.1861i -2.6910 + 5.5614i
-2.7407 + 5.1861i -2.9677 + 2.8606i -2.7407 + 5.1861i
-2.6910 + 5.5614i -2.7407 + 5.1861i -2.8054 + 2.7093i

C =

-0.0010 - 0.0012i -0.0008 + 0.0023i -0.0009 + 0.0022i
-0.0008 + 0.0023i -0.0009 - 0.0018i -0.0008 + 0.0023i
-0.0009 + 0.0022i -0.0008 + 0.0023i -0.0010 - 0.0012i

D =

-0.7277 + 0.5690i -0.4431 + 0.7160i -0.4982 + 0.7038i
-0.3852 + 0.6127i -0.7497 + 0.4663i -0.3852 + 0.6127i
-0.4982 + 0.7038i -0.4431 + 0.7160i -0.7277 + 0.5690i

Zseries =

1.0e+002 *

-2.8054 + 2.7093i -2.7407 + 5.1861i -2.6910 + 5.5614i
-2.7407 + 5.1861i -2.9677 + 2.8606i -2.7407 + 5.1861i
-2.6910 + 5.5614i -2.7407 + 5.1861i -2.8054 + 2.7093i

Yshunt =

0.0024 - 0.0057i 0.0005 + 0.0045i 0.0011 + 0.0028i
0.0005 + 0.0045i 0.0024 - 0.0074i 0.0005 + 0.0045i
0.0011 + 0.0028i 0.0005 + 0.0045i 0.0024 - 0.0057i

4.4.1. Simulation Results

The harmonic voltage excitation at the sending end of the transmission line is fed with fundamental frequency, 1 p.u. and the receiving end is an open circuit. In each case, the receiving end voltages are plotted for line distance 100km, 300km, 500km and 800km respectively.

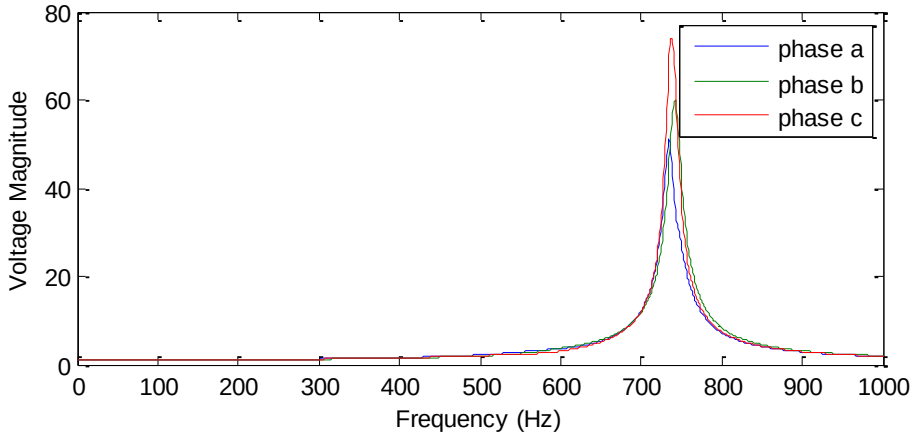

Figure 4.7. Three-phase receiving end harmonic voltage excitation, 100km long (open-circuited); for h = 1:1000; at 50 Hz.

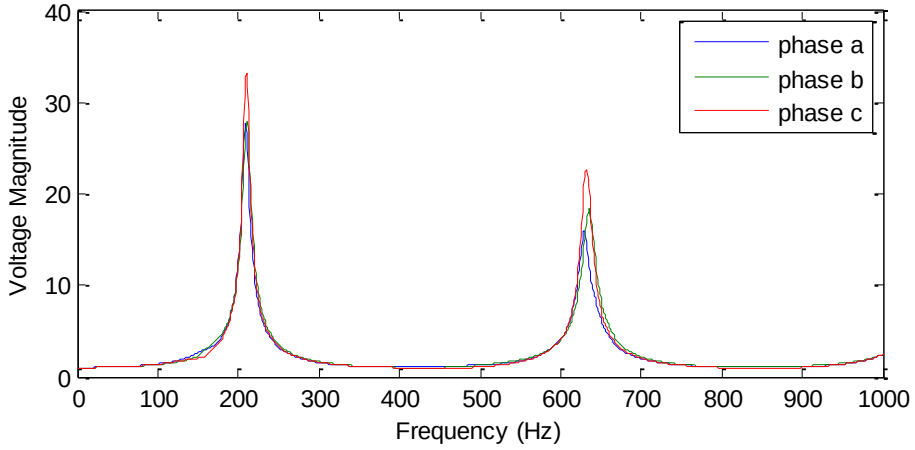

Figure 4.8. Three-phase receiving end harmonic voltage excitation, 300km long (open-circuited); for h = 1:1000; at 50 Hz.

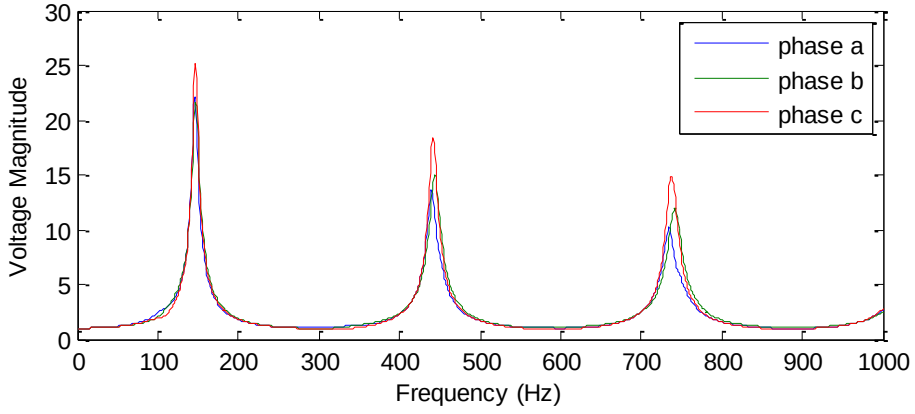

Figure 4.9. Three-phase receiving end harmonic voltage excitation, 500km long (open-circuited); for h = 1:1000; at 50 Hz

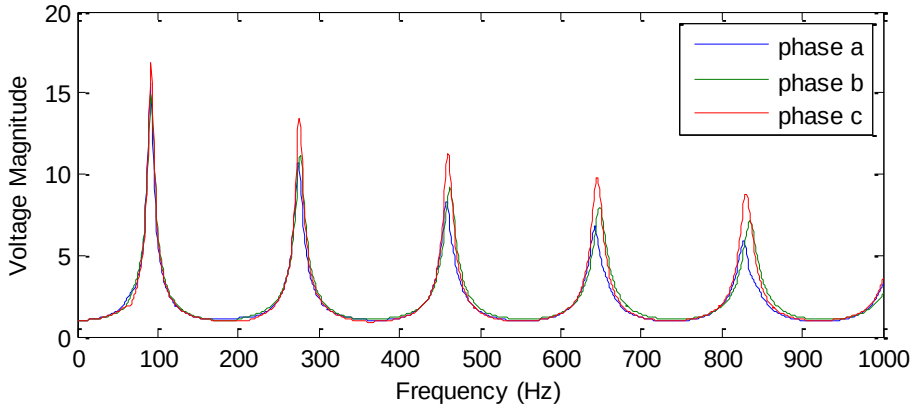

Figure 4.10. Three-phase receiving end harmonic voltage excitation, 800km long (open-circuited); for h = 1:1000; at 50Hz

The fundamental frequency characteristic of the open-ended transmission line is illustrated in Fig. 4.7 to 4.10 for line transposed. These figures indicate that in the absence of VAR compensation, which includes series and shunt compensation as well as transpositions, the line distances will be impractical. The line further corresponds to the case of a line excited by 1p.u 3rd harmonics voltage. The results strongly agree around the points of resonance. The resonant peaks of the three-phases occur at the same line distance. Therefore, for a particular long line distance the resonant frequencies will be the same, thus decreasing the risk of a resonant condition.

The results also reveal that the effect of attenuation with line distance, i.e. the conservable reduction of the peaks at resonant distances at the odd quarters of wavelength other than the first. Such attenuation is caused by the series and shunt resistive compensations of the equivalent π model.

The harmonic current excitation at the sending end of the transmission line is fed with fundamental frequency, 1 p.u. and the sending circuit ended is short circuited. Different transmission line lengths of 100km, 300km, 500km and 800km long line are considered, as shown in Fig. 4.11 to 4.14.

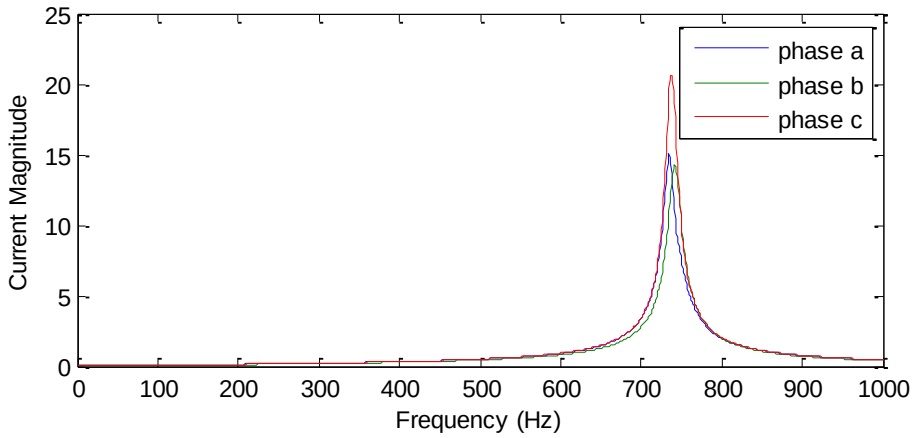

Figure 4.11. Three-phase receiving end harmonic current excitation, 100km long (short circuited); for h = 1:1000; at 50Hz.

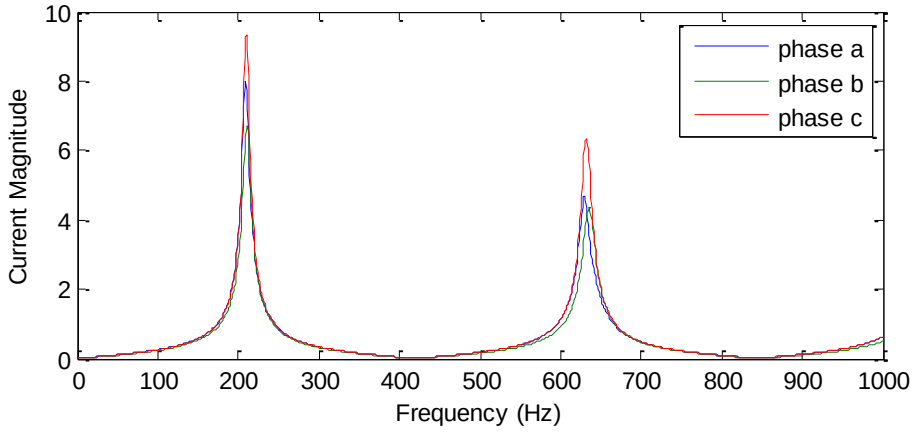

Figure 4.12. Three-phase receiving end harmonic current excitation, 300km long (short circuited); for h = 1:1000; length = 300km at 50 Hz.

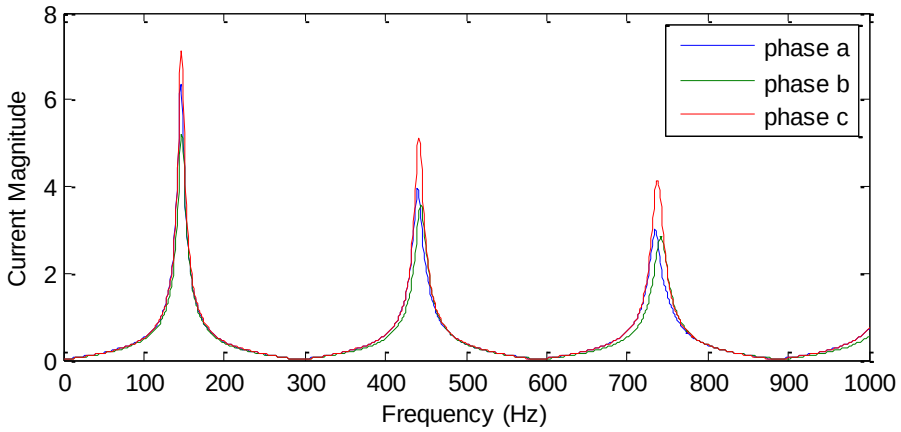

Figure 4.13. Three-phase receiving end harmonic current excitation, 500km long (short circuited); for h = 1:1000; length = 500km at 50 Hz

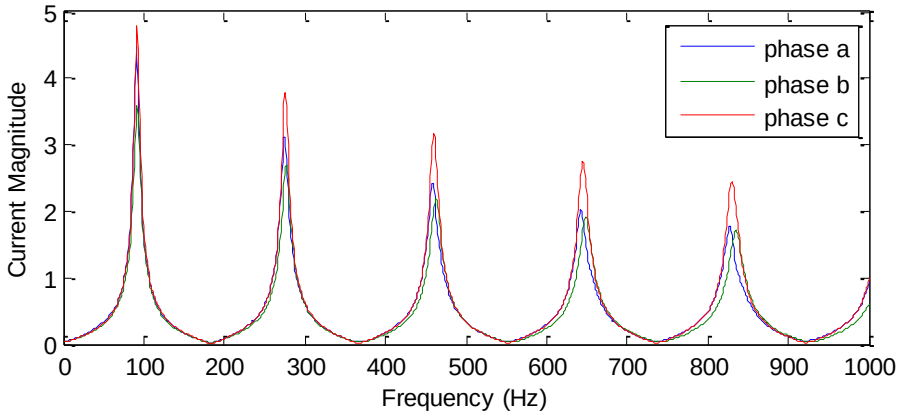

Figure 4.14. Three-phase receiving end harmonic current excitation, 500km long (short circuited); for h = 1:1000; length = 800km at 50Hz.

The harmonic modelling of a long transmission line feeding a static converter is as represented in Figure 4.6b. The harmonic voltages at the point of current harmonic injection follow the same pattern as those of the open circuit line with harmonic voltage excitation. As shown in Figure 4.11 to 4.14 is the case of 3rd harmonic current injection.

Voltage distortion occurs when the line length is close to a quarter wavelength, in the case of current excited short circuited line indicates that even a 1% of harmonic current injection can produce 3 to 4 % voltage harmonic content at the point of harmonic current injection, which is above the levels normally granted by harmonic regulations.

The harmonic resonance increase subject the line to suffer higher levels of voltage distortion, as shown in Figure 4.13 and Figure 4.14, the case of 5th harmonic current injection, showing a peak voltage of about 7.0% in one of the phases of Figure 4.13. While the case of 7th harmonic current injection, showing a peak voltage of about 4.8% in one of the phases of Figure 4.14.

However, in these scenarios the transposed line is to reduce considerably the peaks for the quarter wavelength distance line.

4.5. **Harmonic Modelling of Underground and Subsea Cables**

The offshore power generation industry has developed very rapidly in recent years. Therefore, to model onshore and offshore electrical power systems successfully, it is necessary to have accurate impedance models of the underground and subsea cables

otherwise, it is impossible to reliably predict system resonances and the effects of any generated harmonics from power electronics converters. As the oil and gas industry expand toward deeper sea, the cable circuits tend to increase in length. At present, cable circuits are being employed which have lengths of the order of 100km. To develop accurate impedance models, a good understanding of the physical phenomena that goes into the design of the cable impedance is necessary. Also, for the power system studies, the steady-state and harmonic generation of cables must be known. Over the years research has been tailored to determine a suitable model for calculating the impedance of overhead cables [38-42]. This is contrary to underground and subsea cables which have different layers of heavy armour on the outside to give added strength both for laying and protecting against mechanical damage. Because of the heavy armour, the electromagnetic effects between the layers within the subsea cable need to be considered carefully when developing impedance models. Subsea cable arrangements and structures are diverse with inductive and capacitive element which suggests that each cable type will generate a harmonic resonance characteristic [43-44].

A unified approach that matches the overhead transmission line is difficult for underground and submarine cables due to their extremely complex construction and layouts. In this thesis, a single conductor aluminium cable with a concentric lead sheath and with insulation of XLPE is studied in detail.
Cables are principally classified based on

- Their location, i.e. aerial, underground and subsea
- The number of conductors, i.e. single, two and three conductor and so on
- The type of insulation, i.e. oil-impregnated paper, cross linked polyethylene (XLPE) etc.
- Their protective finish, i.e. metallic (lead, aluminium) or non-metallic (braid)

The cross section of an XLPE cable is as shows in Fig. A2.4, the offshore cable (submarine cable systems) which is made up of a core, insulation, sheath and armour, suitable for energy transportation in upstream and midstream power systems, maybe also suitable for underground single-core coaxial cables (SC cables). However, SC cable with actual conductor, sheath and armour are quite often seen in the offshore power systems [45-46]. In this thesis two high frequency cable models are investigated and their harmonic resonance predictions are compared. The former is an approximate model. The approximate model can give the relative contributions of the various cable materials to the propagation characteristics of the cable. Emphasis is put on the current

excitation shorted end and voltage excitation opened end. The latter is a modified Bessel function model which permits perfectly representation of the electrical properties such as resistivity, permeability and permittivity of the earth which form the return path for current flowing in the cable [47-49].

The rigorous representation of such factors (electrical properties) would lead to very complex equations which may be solved by computational method and could offer more acceptable results. Simplifying assumptions are made:

- The cables are of circularly symmetric type. The longitudinal axes of cables which form the transmission system are mutually parallel and also parallel to the surface of the earth. This implies that the cable has longitudinal homogeneity. Alternatively, the electrical constants do not vary along the longitudinal axes.
- The change in electric field strength along the longitudinal axes of the cables is negligible compared to the change in radial electric field strength. This assumption allows the solution of the field equations in two dimensions only.
- The electric field strength at any point in the earth due to the currents flowing in a cable is not significantly different from the field that would result if the actual current was concentrated in an insulated filament placed at the centre of the cable and volume of the cable were replaced by the soil.
- Displacement currents in the air, conductor and earth could be ignored.

4.5.1. **Ground Return Impedance of Underground Cables**

The unit-length series impedance of cylindrical conductor with radius r_{ext} buried at depth y in the earth with conductivity σ, permeability μ_o and dielectric constant ε, consists of two terms: conductor internal impedance Z_i and impedance of ground return Z_o [45]. The conductor internal impedance only indicate constant response as represented in Fig. 4.15a, this reveal the internal impedance of the conductor as a function of the thickness of the conducting layer. At frequencies 50 Hz and 1 kHz, the impedance remains constant at the whole range of the thickness. While the summation of internal impedance together with impedance of ground return indicate resonance response as shown in Fig. 4.15b. As observed, we could apparently state that the impedance when loaded with ground return impedance affects very significantly the

magnitude of the frequency of the system response. In image theory the electromagnetic field for underground cables results from the conductors and their corresponding images. The earth contribution is much more significant as the actual conductors are buried inside it and their image in the air as shown in Fig. 4.15. This leads to infinite integrals for the self and mutual earth return impedances which are different from the corresponding overhead lines. They include highly oscillatory functions which are easily computed using Dubanton's formulas [50].

According to (4.56), $[Z_o]$ represent the impedance ground return path of a cable system using complex penetration as shown in Fig. 4.16.

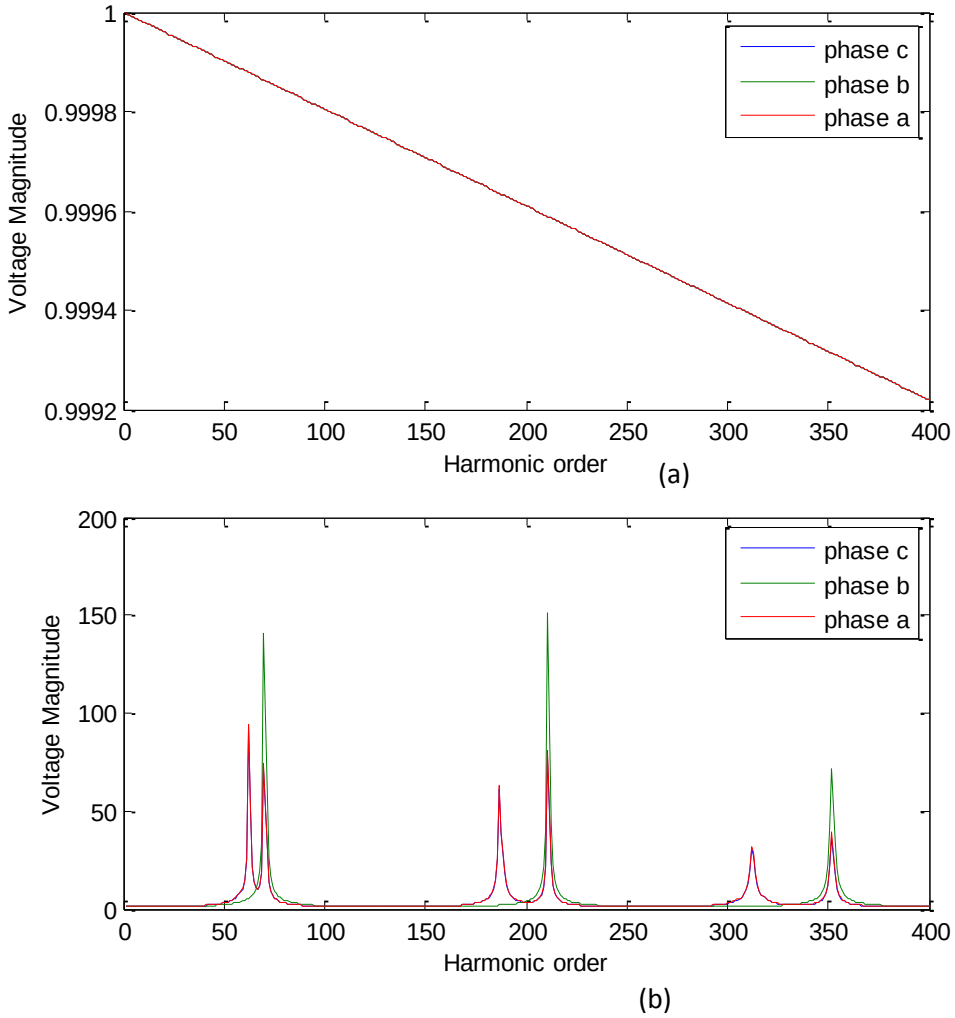

Figure 4.15 Internal impedance of the cable system (a) without ground returns impedance (b) with ground returns impedance

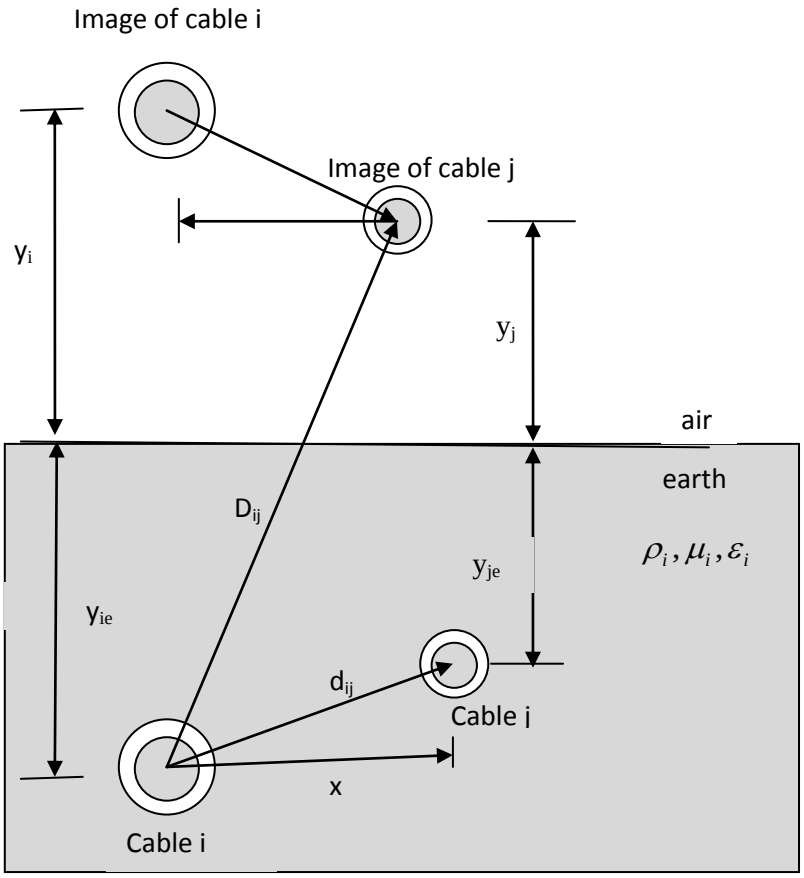

Figure 4.16 Geometric configurations of two SC underground cables and its images

The elements of the matrix of ground return path impedance Z using Dubanton's equations are given by the self ground impedance

$$Z_{0ls} = \frac{j1000\omega\mu_0}{2\pi} \ln\left(\frac{1+\rho}{r_{ext}}\right) \tag{4.36}$$

while the mutual ground impedance is given as

$$Z_{0lm} = \frac{j1000\omega\mu_0}{2\pi} \ln\left(\frac{1+\rho}{dij}\right) \tag{4.37}$$

where

$$dij = \sqrt{\left(x_i - x_j\right)^2 + \left(y_i - y_j\right)^2} \tag{4.38}$$

$$\rho = \frac{1}{\sqrt{j\omega\mu_0\sigma}} \tag{4.39}$$

where

ρ is the complex depth above the earth at which the mirroring surface is located.

μ_0 = 4π x 10^{-7} H/m is the permeability of free space

σ is the conductivity of the conductor in S/m

4.6. **Formation of Approximation Cable Model**

Several approximations with closed-form solutions have been investigated in the issue of overhead transmission line, but nothing promising has been investigated in the issue of underground and submarine cables.

In this approach of complex depth concept, the infinite integral of impedance of the conductor, and sheath taking due account of skin effect each of which is approximated using infinite series. The current inside conductor is concentrated around the surface due to the skin effect. It is assumed that the current density is uniform in the range covered by the skin depth. Under this assumption, the internal impedance can be derived by approximation method.

In the supporting routines cable parameters of harmonic study, the earth return impedances of cables are calculated using Dubanton's formula for a single case of two underground conductors, which is evaluated by infinite series. The model is valid for homogenous infinite earth, neglecting the displacement current [51-55].

Underground and submarine cables are usually divided into single or multiple core types. For high power, three-phase AC transmission cable systems could be designed as either a single-core cable or three single-core cables or as a single three-core cable. For the purpose of determining the significance of the skin effect in subsea and underground cables, single-core flat formation has been chosen for investigation in this work, where proximity effect is insignificant.

4.6.1. **Voltage Drops in the Cable System**

An equivalent circuit for the impedance of a single-core coaxial cable consisting of a core, insulation and sheath is as shown in Fig. 4.17. Currents flowing into the core, insulation, sheath and armour are through I_c, and I_s,

The voltage drop equation for the single-phase cable is given as:

$$\begin{bmatrix} \Delta V_c \\ \Delta V_s \end{bmatrix} = \begin{bmatrix} R_c + jX_c & -jX_m \\ -jX_m & R_s + jX_m \end{bmatrix} \begin{bmatrix} I_c \\ I_s \end{bmatrix} \tag{4.40}$$

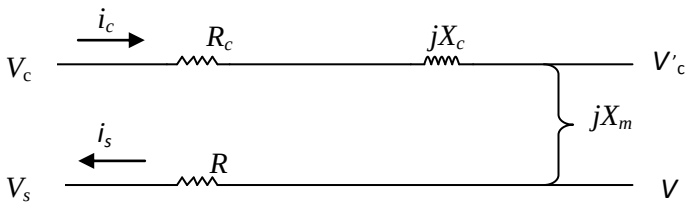

Figure 4 .17. An equivalent circuit for impedances of a single-core underground cable

Since there is no insulation between the metallic screen and the core conductor, it is therefore assumed that the two layers are short-circuited as seen in equation (4.40) [56-57].

$$I_c + I_s = I \tag{4.41}$$

where I_c and I_s are the current of the two-layer conductors, respectively and I is the total current of the conductor.

When the cable sheath is solidly bonded to the ground as shown in Fig. 4.18 give rise to equation (4.42)

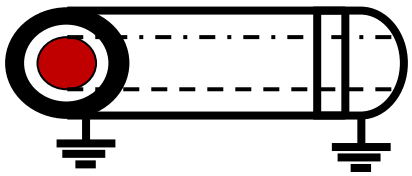

Figure 4.18. A cable sheath solidly bonded to the ground

$$\begin{bmatrix} \Delta V_C \\ 0 \end{bmatrix} = \begin{bmatrix} R_c + jX_c & -jX_m \\ -jX_m & R_s + jX_m \end{bmatrix} \begin{bmatrix} I_c \\ I_s \end{bmatrix} \tag{4.42}$$

where $$\Delta V_c = \left\{ \left(R_c + R_s \cdot \frac{X_m^2}{R_s^2 + X_m^2} \right) + j \left(X_c - X_m \cdot \frac{X_m^2}{R_s^2 + X_m^2} \right) \right\} I_c \tag{4.43}$$

4.6.2. **The Impact of Skin Effect in Power Cables System**

It is an established fact that skin and proximity effects generate non-uniformed current distribution as frequency increases, due to the magnetic field inside the conductor, the concentration of current at the centre gradually distribute the current towards the circumference of the conductor, thus increasing the resistance and decreasing the internal inductance.

The impedance of the conductor and sheath considering the skin effect are determined by the impedance of the cable conductor using complex depth concept (Z_c) which is given by [74]

$$Z_c = R_c + jX_c = \sqrt{R_{DC,c}^2 + Z_{\infty,c}^2} \tag{4.44}$$

where $R_{DC,c}^2$ is the DC resistance and is given as

$$R_{DC,c} = \frac{1}{\pi r_c^2 \sigma_c} \tag{4.45}$$

r_c is the radius (m) of the conductor

$Z_{\infty,c}$ is the impedance infinity of the conductor and is given as

$$Z_{\infty,c} = \frac{1}{2\pi r_c \sigma_c p_c} \tag{4.46}$$

where p_c is the complex penetration and is given as

$$p_c = \frac{1}{\sqrt{j\omega\mu_0\sigma_c}} \tag{4.47}$$

Whereas the impedance of the cable sheath (Z_s)

$$Z_s = R_s + jX_s = \sqrt{R_{DC,s}^2 + Z_{\infty,s}^2} \tag{4.48}$$

where

$R_{DC,s}^2$ is the DC resistance in the cable sheath , given as

$$R_{DC,s} = \frac{1}{\pi\left(r_0^2 - r_i^2\right)\sigma_s} \tag{4.49}$$

$\pi\left(r_0^2 - r_i^2\right)$ is the cross-sectional area (m) of the sheath

r_0 is the outer radius (m) of the sheath

r_i is the inner radius (m) of the sheath

σ is the earth conductivity in S/m

the $Z_{\infty,s}$ is the impedance infinity of the sheath , given as

$$Z_{\infty,s} = \frac{1}{2\pi r_0 \sigma_s p_s} \tag{4.50}$$

where p_s is the complex penetration and is given as

$$p_s = \frac{1}{\sqrt{j\omega\mu_0\sigma_s}} \tag{4.51}$$

The skin effect is determined by

$$Z_{skin} = \sqrt{R_{DC}{}^2 + Z_\infty{}^2} \tag{4.52}$$

The mutual reactance between the conductor and sheath is determined by

$$X_m = \frac{\omega\mu_0}{2\pi}.\ln\frac{r_0}{\frac{r_0 + r_i}{2}} \tag{4.53}$$

Due to the shielding effect of the conductor and sheath there is mutual magnetic coupling between the outer most loop. The coupling is entirely through the earth path. In the overhead transmission lines, the mutual reactance between phase conductors is the sum of external mutual reactance due to the magnetic fields in the air paths and those arising from the earth paths [51][56]. In the case of underground cable the mutual reactance are totally contributed by the earth path only.

The self ground impedance of cable i is given as

$$Z_{ll} = \frac{j\omega\mu_0}{2\pi}.\ln\left(1 + \frac{p_e}{r_0}\right) \tag{4.54}$$

The mutual ground impedance between cables i and j in Fig. 4.17 is given as

$$Z_{lm} = \frac{j\omega\mu_0}{2\pi}.\ln\left(1 + \frac{p_e}{d_{lm}}\right) \tag{4.55}$$

where p_e is the complex penetration and is given as

$$p_e = \frac{1}{\sqrt{j\omega\mu_0\sigma_g}} \tag{4.56}$$

The self ground admittance and the mutual ground admittance are determined by

$$Y_{sh} = \left(\frac{1}{R_i} + j\omega.2\pi\varepsilon_0\varepsilon_r \right).\left\{ \ln \frac{r_i}{r_c} \right\}^{-1} \tag{4.57}$$

where R_i is the insulation resistance

ε_r is the insulation relative permittivity

4.6.3. **Test Case 2**

A 400kV, three-phase underground cable system made up of three single-phase cables lying in the earth bed at a depth of 2m in a flat configuration and the conductor temperature is 90 °C under operation, as shown in Fig. 4.19, is used to assess its harmonic response to a voltage and current excitation. For safety reasons, solid-bonding of the sheath and armour have been adopted.

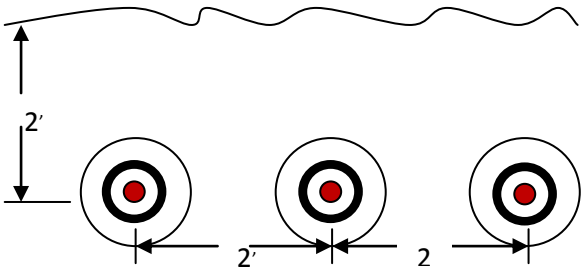

Figure 4.19. Geometry of the case study three single-phase cables laying in a flat configuration

The characteristics of the cable are: 250-kcmil, concentric strand, paper insulated with solidly bonded, grounded lead sheath.

The main technical datas of this approximation cable model are given in Table A2.2.

The equivalent impedance is given as

```
Z =
 1.0262 + 1.0069i        0                  0
      0             1.0262 + 1.0069i        0
      0                  0             1.0262 + 1.0069i
```

The ground return is given as

Z_{ground} =

1.0e+002 *

0.1973 + 1.8510i 0.1932 + 0.9393i 0.1891 + 0.7694i

0.1932 + 0.9393i 0.1973 + 1.8510i 0.1932 + 0.9393i

0.1891 + 0.7694i 0.1932 + 0.9393i 0

Total impedance of the cable is given as

$Z_{shortcable}$ =

1.0e+002 *

0.2075 + 1.8611i 0.1932 + 0.9393i 0.1891 + 0.7694i

0.1932 + 0.9393i 0.2075 + 1.8611i 0.1932 + 0.9393i

0.1891 + 0.7694i 0.1932 + 0.9393i 0.2075 + 1.8611i

Admittance of the cable

$Y_{shortline}$ =

1.0e-004 *

0 + 0.9345i 0 0

0 0 + 0.9345i 0

0 0 0 + 0.9345i

The distributed parameter ABCD of the cable are given as

A =

0.1405 - 0.2768i 1.0469 - 0.2698i 0.9238 - 0.2233i

1.0469 - 0.2698i 0.2084 - 0.2443i 1.0469 - 0.2698i

0.9238 - 0.2233i 1.0469 - 0.2698i 0.1405 - 0.2768i

B =

57.3321 - 45.8104i 64.8186 - 40.9288i 61.2272 -11.9246i

64.8186 - 40.9288i 66.3347 - 21.9019i 64.8186 - 40.9288i

61.2272 - 11.9246i 64.8186 - 40.9288i 57.3321 - 45.8104i

C =

0.0057 - 0.0065i 0.0074 - 0.0054i 0.0068 + 0.0051i

0.0074 - 0.0054i 0.0066 + 0.0033i 0.0074 - 0.0054i

0.0068 + 0.0051i 0.0074 - 0.0054i 0.0057 - 0.0065i

D =

0.1405 - 0.2768i 1.0469 - 0.2698i 0.9238 - 0.2233i

1.0469 - 0.2698i 0.2084 - 0.2443i 1.0469 - 0.2698i

0.9238 - 0.2233i 1.0469 - 0.2698i 0.1405 - 0.2768i

4.6.4. **Simulation Results**

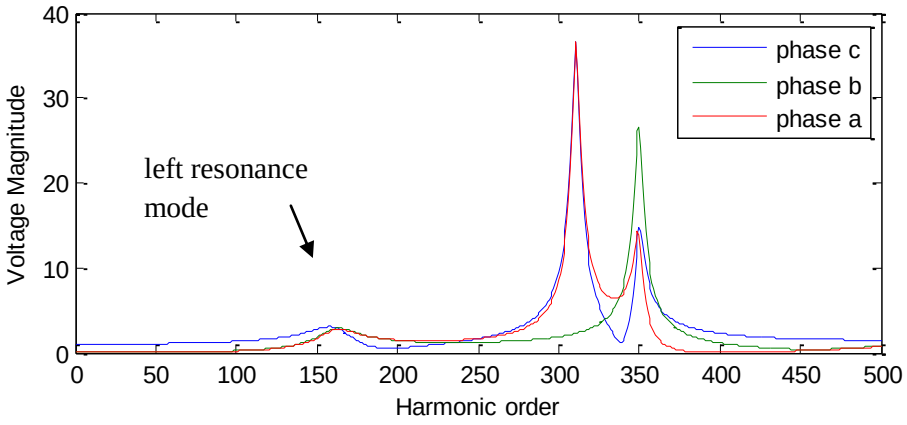

(a)

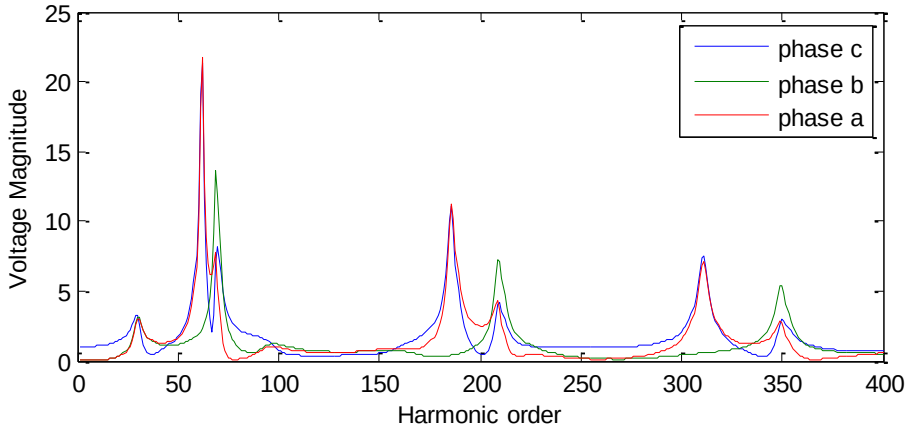

(b)

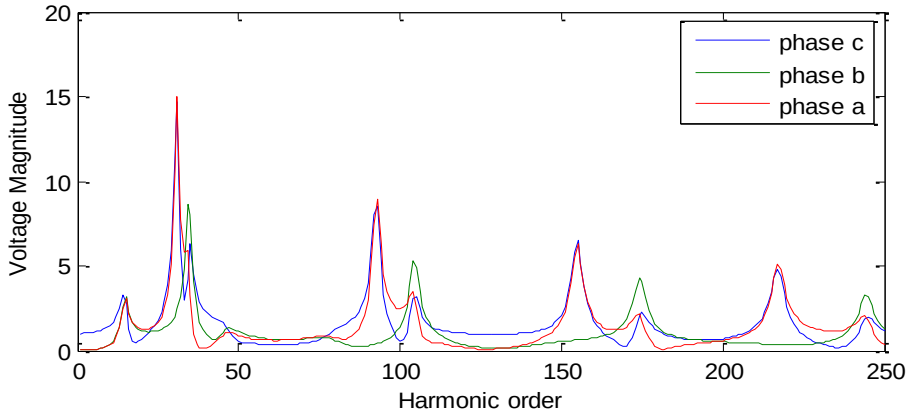

(c)

Figure 4.20. Harmonic Impedance without voltage and current excitation

Figure 4.20 establishes the relationship between the left and right resonance mode. As seen, the effect of including voltage or current excitation at high frequencies is desirable to avoid the left resonance mode, which introduced high standing wave distortion as the transmission line increases. The left resonance mode increases in peak with increase in the line length, while the right resonance mode decreases with lower peaks.

Z_{series} =

57.3321 - 45.8104i 64.8186 - 40.9288i 61.2272 -11.9246i

64.8186 - 40.9288i 66.3347 - 21.9019i 64.8186 - 40.9288i

61.2272 - 11.9246i 64.8186 - 40.9288i 57.3321 - 45.8104i

Y_{shunt} =

0.0163 - 0.0198i -0.0047 - 0.0614i 0.0012 + 0.0837i

-0.0047 - 0.0614i 0.0233 + 0.1145i -0.0047 - 0.0614i

0.0012 + 0.0837i -0.0047 - 0.0614i 0.0163 - 0.0198i

The skin effect is represented as

Z_{skin} = 1.5925 + 1.1804i 1.5925 + 1.1804i 1.5925 + 1.1804i

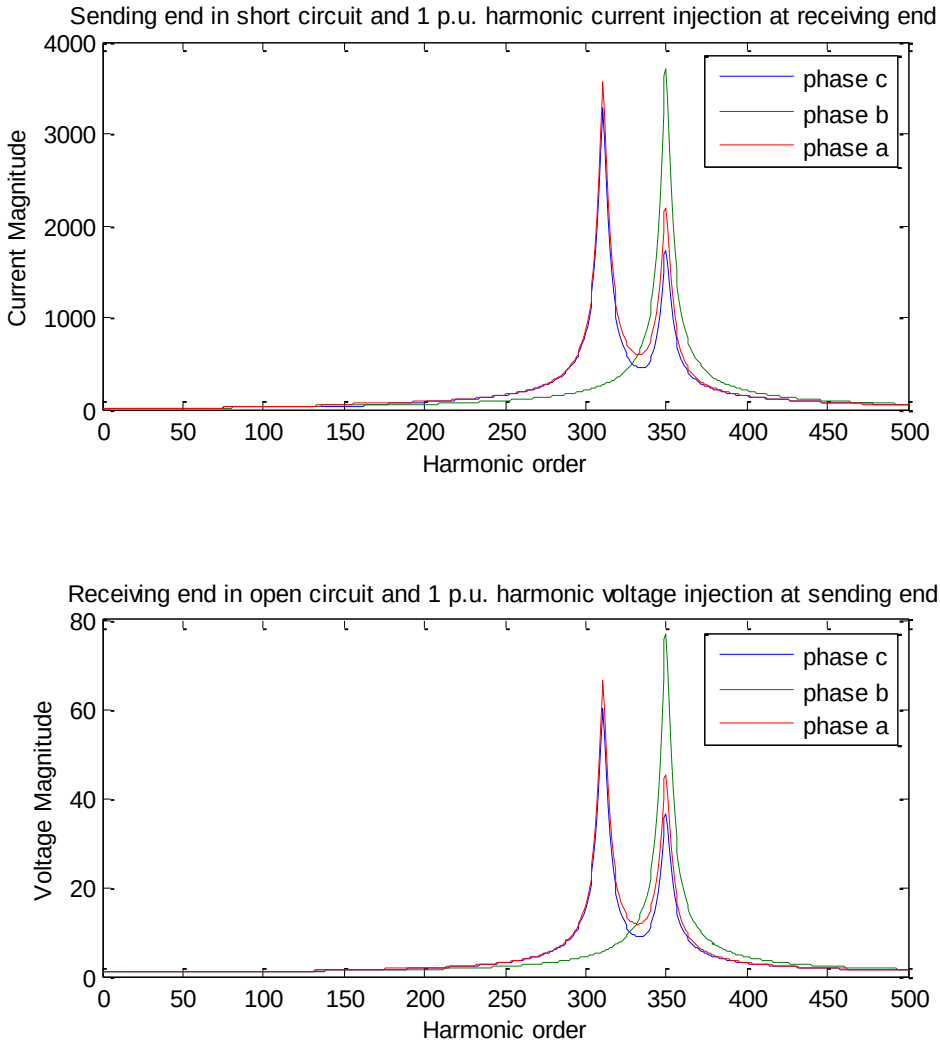

Figure 4. 21.1km long cable with first resonant peak appear at h = 350, NH = 500

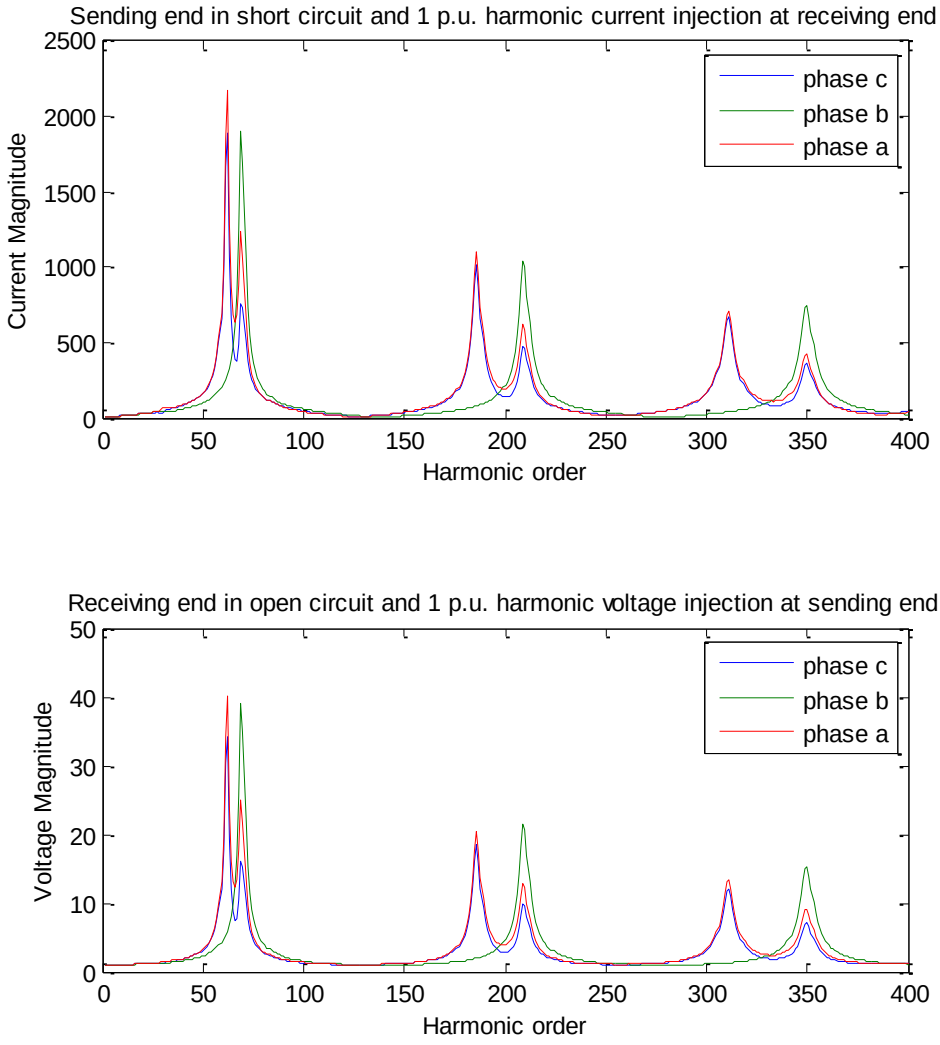

Figure 4.22 5km long cable with first resonant peak to appear at h = 70, NH = 400, freq. = 50 Hz.

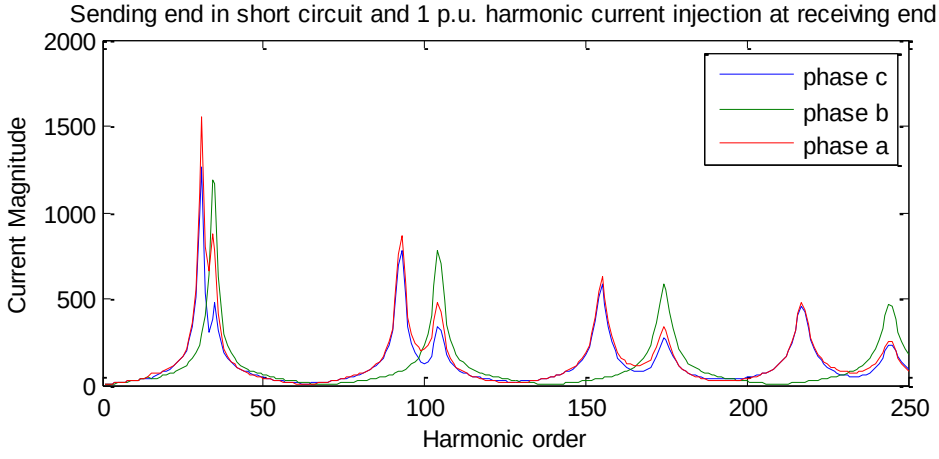

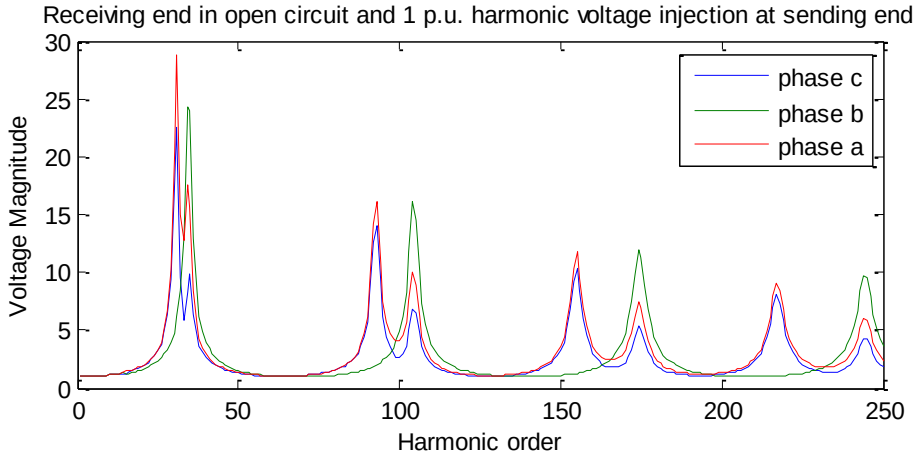

Figure 4.23 10km long cable with first resonant peak to appear at h = 30, NH = 250 freq. = 50 Hz.

The above simulations results highlight that two elements are required to create a resonant condition. These are, (1) an excitation source of harmonic current, and (2) an excitation source of harmonic voltage. With full or even partial resonance, voltage distortion can multiply many times the normal system impedance generating harmonic voltage. For resonance to occur, the system must have a substantial percentage of capacitance. In general, parallel resonance in a system is present at a frequency where impedance has very high value. From the above simulation results Fig. 4.21 to Fig. 4.23, it can be seen that there are several frequencies where resonance occurs in the system: Fig. 4.21 manifest only one resonance at with 3^{rd} harmonic voltage. While Fig. 4.22 exhibit 5^{th} harmonic voltage injection with 40% peak voltage. Also, Fig. 4.23 shows 5^{th} and 7^{th} harmonic voltage excitation with 28% peak voltage.

4.7. **Bessel Function Concept Cable Model**

The key to determining the skin effect in underground or subsea cables is to develop and use equations for impedances of multi-layer cylinders. These equations are well established but they need to be modified according to the underground or subsea cable structure and the physical arrangement under consideration in order to evaluate accurately the impact of the skin effect. The general equation for magnetic potential from Faraday's law with flux linkage can be expressed by Maxwell's equations [58][59]. The magnetic and electric fields obtained from Maxwell's equation for a cylindrical conductor are given as follows:

$$\nabla^2 \cdot \mathbf{A} = \mu \cdot \mathbf{J} \quad (4.58)$$

$$\mathbf{J} = \frac{j\omega}{\rho} \cdot \mathbf{A} \quad (4.59)$$

where, **A** is magnetic vector potential; **J** is the current density; μ is the corresponding permeability; ρ is the corresponding resistivity and ω is the angular velocity. Using cylindrical coordinates:

$$\frac{\partial^2 \mathrm{A}}{\partial r^2} + \frac{1}{r}\frac{\partial \mathrm{A}}{\partial r} + \frac{1}{r^2}\frac{\partial^2 \mathrm{A}}{\partial \theta^2} - j\frac{\mu\omega}{\rho}\mathrm{A} = 0 \quad (4.60)$$

The solutions of the Bessel's equation are combinations of modified Bessel functions given as:

$$\mathrm{A}(r,\theta) = \sum_{n=0}^{\infty}\left[A_n I_n(mr) + B_n K_n(mr)\right]\cos(n\theta) \quad (4.61)$$

where, I_n is the modified Bessel function of the first kind order n and K_n is the modified Bessel function of the second kind order n; A_n and B_n are constants need to be determined using the boundary condition:

$$m = \sqrt{\frac{j\mu\omega}{\rho}} \quad (4.62)$$

While considering the vector potential within the material conducting layer such as conductor, sheath and armour. Use the Bessel's equation (4.61) to derive the impedance [58]:

$$E(r,\theta) = Z \cdot I = \rho \cdot J(r,\theta) \quad (4.63)$$

$$Z = \rho\left[A_0 I_0(mr) + B_0 K_0(mr)\right] + \rho\sum_{n=1}^{\infty}\left(\frac{s}{r}\right)^n \left[A_n I_n(mr) + B_n K_n(mr)\right] \quad (4.64)$$

In this formula, the first term of the right hand side is due to the skin effect while the second term is due to the proximity effect. Where, *s* is the distance between conductors and the constants A_0, B_0, A_n and B_n [58].

4.7.1. **The Impedance (Z) of Three-Layer Conductor**

An equivalent circuit for impedance of a single-core coaxial cable consisting of a core, sheath and armour is as shown in Fig. 4.24. Currents flowing into the core, sheath, armour and outer medium (earth) are through I_c, I_s, I_a and I_e at x.

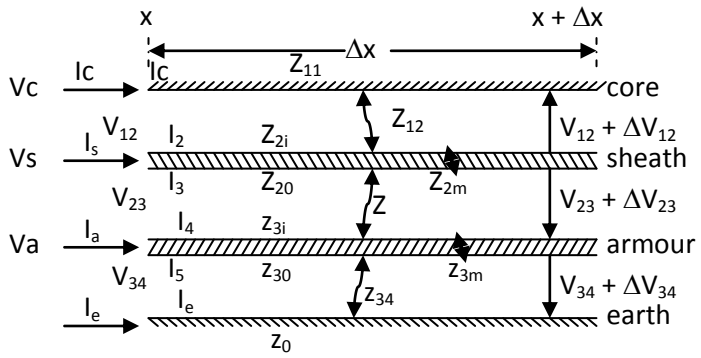

Figure 4.24An equivalent circuit for impedances of single-core cables (SC cable)

The self-impedance diagonal matrix of an SC cable is given as

$$Zij = \begin{bmatrix} Z_{cc} & Z_{cs} & Z_{ca} \\ Z_{cs} & Z_{ss} & Z_{sa} \\ Z_{ca} & Z_{sa} & Z_{aa} \end{bmatrix}$$

$$d(V)/dx = -[Z].(I) \quad (4.65)$$

$$[Z] = [Zi] + [Zo] \quad (4.66)$$

where
[Zi] is internal impedance matrix
[Zo] is earth or sea return impedance

Impedance matrix of core, sheath and armour of a cable:

$$[Z_i] = \begin{bmatrix} Z_{i1} & 0 & 0 \\ 0 & Z_{i2} & 0 \\ 0 & 0 & Z_{i3} \end{bmatrix} \quad (4.67)$$

$$[Z_o] = \begin{bmatrix} Z_{Earth} & Z_{Earth} & Z_{Earth} \\ Z_{Earth} & Z_{Earth} & Z_{Earth} \\ Z_{Earth} & Z_{Earth} & Z_{Earth} \end{bmatrix} \quad (4.68)$$

Also the inner and outer surface currents of the sheath and armour are I_2, I_3, I_4, and I_5 as shown in Fig. 4.24. The voltage between the core, sheath, armour and outer medium are V_{12}, V_{23}, and V_{34} at x and voltage at x + Δx are $V_{12} + \Delta V_{12}$, $V_{23} + \Delta V_{23}$ and $V_{34} + \Delta V_{34}$ [45].

When the single-core cable consists of a core, sheath and armour, the self-impedance is given by:

$$\left[Z_{ij}\right] = \begin{bmatrix} Z_{ccj} & Z_{csj} & Z_{caj} \\ Z_{csj} & Z_{ssj} & Z_{saj} \\ Z_{caj} & Z_{saj} & Z_{aaj} \end{bmatrix} \quad (4.69)$$

where

Z_{ccj} = core self-impedance
$= Z_{cs} + Z_{sa} + Z_{c4} - 2Z_{2m} - 2Z_{3m}$

Z_{ssj} = Sheath self-impedance
$= Z_{saj} + Z_{c4} - 2Z_{3m}$

Z_{aaj} = armour self-impedance
$= Z_{c4}$

Z_{csj}= mutual impedance between the core and sheath
$= Z_{sa} + Z_{c4} - Z_{2m} - 2Z_{3m}$

Z_{caj} = mutual impedance between the core and armour
$= Z_{c4} - Z_{3m}$

Z_{saj} = mutual impedance between the sheath and armour
$= Z_{caj}$

$Z_{cs} = z_{11} + z_{12} + z_{2i}$

$Z_{sa} = z_{20} + z_{23} + z_{3i}$

$Z_{c4} = z_{30} + z_{34}$

4.7.2. **The Component Impedance**

The component impedances per unit length are given in the following equations for a single core cable;

Z_{11}: Internal impedance of core outer surface

$$Z_{11} = \left(\frac{s\mu_0\mu_1}{2\pi}\right)\left(\frac{1}{x_2 D_1}\right).\{I_0(x_2).K_1(x_1) + K_0(x_2).I_1(x_1)\} \quad (4.70)$$

Z_{12}: Core outer insulator impedance

$$Z_{12} = \left(\frac{s\mu_0\mu_1}{2\pi}\right).\ln\left(\frac{r_3}{r_2}\right) \quad (4.71)$$

Z_{2i} : Internal impedance of sheath inner surface

$$Z_{2i} = \left(\frac{s\mu_0\mu_2}{2\pi}\right)\left(\frac{1}{x_3 D_2}\right).\{I_0(x_3).K_1(x_4) + K_0(x_3).I_1(x_4)\} \quad (4.72)$$

Z_{2m}: Sheath mutual impedance

$$Z_{2m} = \frac{\rho_2}{2\pi r_3 r_4 D_2} \quad (4.73)$$

Z_{20}: Internal impedance of sheath outer surface

$$Z_{20} = \left(\frac{s\mu_0\mu_2}{2\pi}\right)\left(\frac{1}{x_4 D_2}\right).\{I_0(x_4).K_1(x_3) + K_0(x_4).I_1(x_3)\} \quad (4.74)$$

Z_{23}: Sheath outer insulation impedance

$$Z_{23} = \left(\frac{s\mu_0\mu_{i2}}{2\pi}\right).\ln\left(\frac{r_5}{r_4}\right) \quad (4.75)$$

Z_{3i}: Internal impedance of armour inner surface

$$Z_{3i} = \left(\frac{s\mu_0\mu_3}{2\pi}\right)\left(\frac{1}{x_5 D_3}\right).\{I_0(x_5).K_1(x_6) + K_0(x_5).I_1(x_6)\} \quad (4.76)$$

Z_{3m}: Armour mutual impedance

$$Z_{3m} = \frac{\rho_3}{2\pi r_5 r_6 D_3} \quad (4.77)$$

Z_{30}: Internal impedance of armour outer surface

$$Z_{30} = \left(\frac{s\mu_0\mu_3}{2\pi}\right)\left(\frac{1}{x_6 D_3}\right).\{I_0(x_6).K_1(x_5) + K_0(x_6).I_1(x_5)\} \quad (4.78)$$

Z_{34}: Armour outer insulator impedance

$$Z_{34} = \left(\frac{s\mu_0\mu_{i3}}{2\pi}\right).\ln\left(\frac{r_7}{r_6}\right) \quad (4.79)$$

where

$D_1 = I_1(x_2)\, K_1(x_1) - I_1(x_1)\, K_1(x_2)$

$D_2 = I_1(x_4)\, K_1(x_3) - I_1(x_3)\, K_1(x_4)$

$D_3 = I_1(x_6)\, K_1(x_5) - I_1(x_5)\, K_1(x_6)$

$$x_k = \beta_k \sqrt{s}$$

$$\beta_m = r_m \sqrt{\frac{\mu_0 \mu_n}{\rho_n}}$$ where n = 1, 2, 3, 4, 5,.....

and m = 2, 3, 4,.....

and $I_n(x)$, $K_n(x)$ are modified Bessel function of order n.

4.7.3. **The Admittance (Y) of a Cable**

An equivalent circuit of a single-core coaxial cable showing the capacitive effects, consisting of a core, sheath and armour, is as shown in Fig. 4.25 [45].

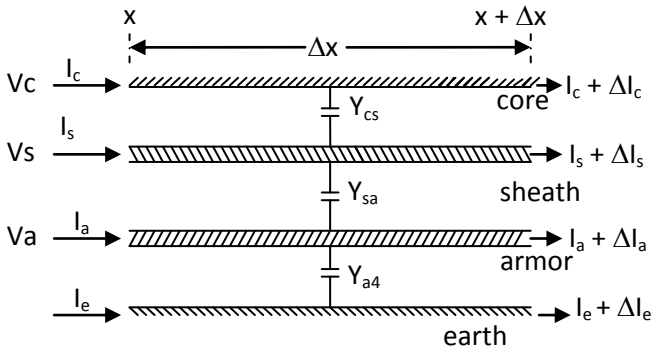

Figure 4.25 An equivalent circuit for admittances of single- core coaxial cables (SC cable)

From Figure 4.28, we that

$$\begin{aligned} I_c &= ycs\Delta x(V_c - V_s) + I_c + \Delta I_c \\ I_s &= ycs\Delta x(V_s - V_c) + ysa\Delta x(V_s - V_a) + I_s + \Delta I_s \\ I_a &= ysa\Delta x(V_a - V_s) + ya4\Delta x V_a + I_a + \Delta I_a \end{aligned} \quad (4.80)$$

Equation 4.114 can be rewritten as

$$\begin{aligned} -\Delta I_c/\Delta x &= ycsV_c - ycsV_s \\ -\Delta I_s/\Delta x &= -ycsV_c + (ycs + ysa)V_s - ysaV_a \\ -\Delta I_a/\Delta x &= -ysaV_s + (ysa + ya4)V_a \end{aligned} \quad (4.81)$$

If $x \longrightarrow 0$

then we have the admittance matrix as,

$$\begin{bmatrix} I_c \\ I_s \\ I_a \end{bmatrix} = \begin{bmatrix} ycs & -ycs & 0 \\ -ycs & (ycs + ysa) & -ysa \\ 0 & -ysa & (ysa + ya4) \end{bmatrix} \begin{bmatrix} V_c \\ V_s \\ V_a \end{bmatrix}$$

$$I = [Yi](V) \qquad (4.82)$$

4.7.4. **The Potential Coefficient (P) of a Cable**

The potential coefficient is inversely related to the admittance;

$$[P_i] = \begin{bmatrix} P_c + P_s + P_a & P_s + P_a & P_a \\ P_s + P_a & P_s + P_a & P_a \\ P_a & P_a & P_a \end{bmatrix} \qquad (4.83)$$

where
P_c = s/ycs, P_s = s/ysa, P_a = s/ya

4.8. **Test Case 3**

The Bessel function concept model analyzed above is applied in MATLAB software to demonstrate the ability of identifying the resonance condition, as well as harmonic response to a voltage and current excitation. The cable structure used is shown in Fig. A2.4. According to design standards: BS 6622 and BS 7835, this cable can be operated at voltages that do not exceed the voltage grade of 19/33kV single core armoured copper conductors. The cable is 100% insulated and solidly earthed.

The main technical datas of this approximation cable model are given in Table A2.3.

Balanced three-phase voltage source = [1 -1/2-j $\sqrt{\frac{3}{2}}$ -1/2+j $\sqrt{\frac{3}{2}}$]

Bessel function First Kind are generated as

J0 =
0 - 0.3058i 0 - 0.3058i 0 - 0.3058i

J1 =
2.2500 - 1.2231i 2.2500 - 1.2231i 2.2500 - 1.2231i

Modified Bessel first order are generated as

I0 =
-0.0183 + 0.0183i - 0.0183 + 0.0183i - 0.0183 + 0.0183i

I1 =

```
   0 + 0.9174i   0 + 0.9174i   0 + 0.9174i
```

I2 =

```
   0 + 0.1654i   0 + 0.1654i   0 + 0.1654i
```

Modified Bessel second order are generated as

K0 =

```
  0.0205 + 0.0891i   0.0205 + 0.0891i   0.0205 + 0.0891i
```

K1 =

```
  0.7205 - 0.6426i   0.7205 - 0.6426i   0.7205 - 0.6426i
```

K2 =

```
  0.1299 + 0.0258i   0.1299 + 0.0258i   0.1299 + 0.0258i
```

Internal Impedance are generated as

z11 =

```
 -9.1126e-004 -2.8291e-004i
```

z12 =

```
   0 - 0.0014i
```

Zi =

```
  -0.0009 - 0.0017i        0                0
        0          -0.0009 - 0.0017i        0
        0                0          -0.0009 - 0.0017i
```

Skin Effect is is generated as

Zsf =

```
   0.7039 + 0.0000i        0                0
        0           0.7039 + 0.0000i        0
        0                0           0.7039 + 0.0000i
```

Potential Coefficients is generated as

P =

```
    0.6164         0         0
         0    0.6164         0
         0         0    0.6164
```

The distributed parameter of the cable are generated as

A =

0.5711 - 0.9960i -0.0063 - 1.0067i -0.4342 - 0.9971i

-0.0063 - 1.0067i 0.1713 - 1.1532i -0.0063 - 1.0067i

-0.4342 - 0.9971i -0.0063 - 1.0067i 0.5711 - 0.9960i

B =

1.0e+002 *

-0.0156 - 1.1277i -0.0385 - 0.9454i -0.0714 - 1.1331i

-0.0385 - 0.9454i -0.0275 - 1.4730i -0.0385 - 0.9454i

-0.0714 - 1.1331i -0.0385 - 0.9454i -0.0156 - 1.1277i

C =

0.0022 - 0.0137i 0.0011 - 0.0037i 0.0003 - 0.0139i

0.0011 - 0.0037i 0.0017 - 0.0246i 0.0011 - 0.0037i

0.0003 - 0.0139i 0.0011 - 0.0037i 0.0022 - 0.0137i

D =

0.5711 - 0.9960i -0.0063 - 1.0067i -0.4342 - 0.9971i

-0.0063 - 1.0067i 0.1713 - 1.1532i -0.0063 - 1.0067i

-0.4342 - 0.9971i -0.0063 - 1.0067i 0.5711 - 0.9960i

Zseries =

1.0e+002 *

-0.0156 - 1.1277i -0.0385 - 0.9454i -0.0714 - 1.1331i

-0.0385 - 0.9454i -0.0275 - 1.4730i -0.0385 - 0.9454i

-0.0714 - 1.1331i -0.0385 - 0.9454i -0.0156 - 1.1277i

Yshunt =

0.0077 - 0.0077i 0.0052 + 0.0104i 0.0058 - 0.0079i

0.0052 + 0.0104i 0.0089 - 0.0242i 0.0052 + 0.0104i

0.0058 - 0.0079i 0.0052 + 0.0104i 0.0077 - 0.0077

4.8.1. **Simulation Results**

The investigation of the transmission cable in frequency domain using single-core flat formation structure does not consider the proximity effect, because its effect is insignificant. However, harmonic resonant behaviour in cable system can be obtained

and the results reveal that the inclusion of the skin effect is absolutely necessary. The per-unit frequency is based on the fundamental frequency and is equal to harmonic number. The impedance matrix is three-phase with three deriving points impedance in the system where harmonic resonance could be excited or observed. Thus the peak magnitude of each harmonic resonant is reduced drastically as the length of the cable increases as shown in Fig. 4.26 to Fig. 4.28.

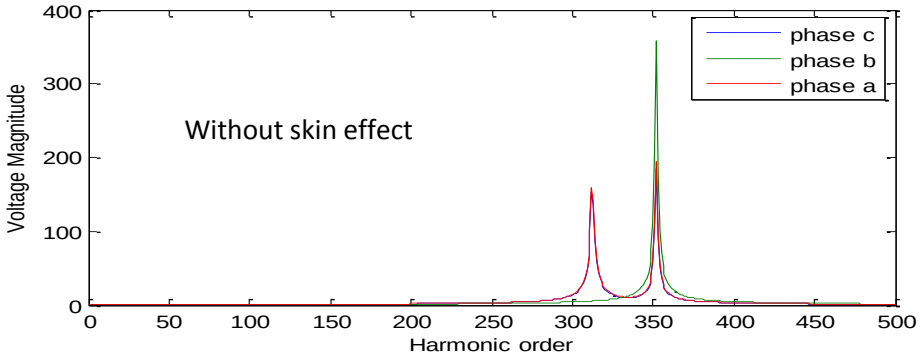

(a)

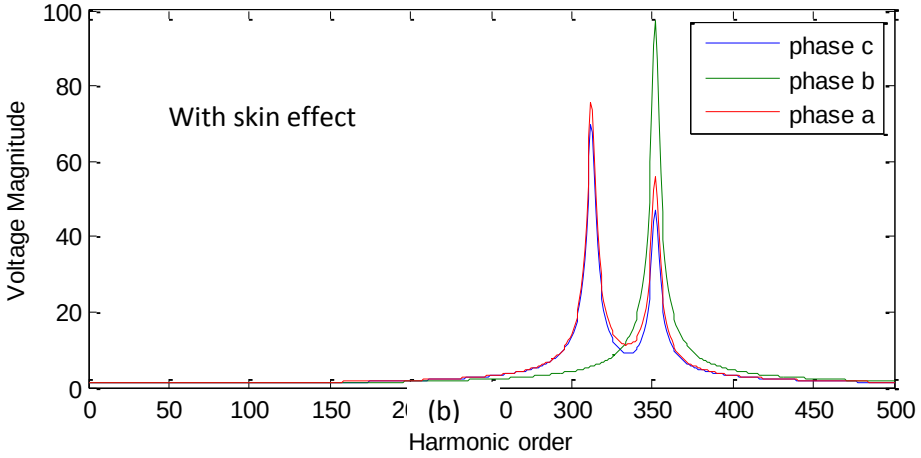

(b)

Figure 4.26. Receiving end open circuit and 1 p.u. harmonic voltage injection 1km long at sending end with first resonant peak to appear at h = 350, NH = 500, freq. = 50 Hz.

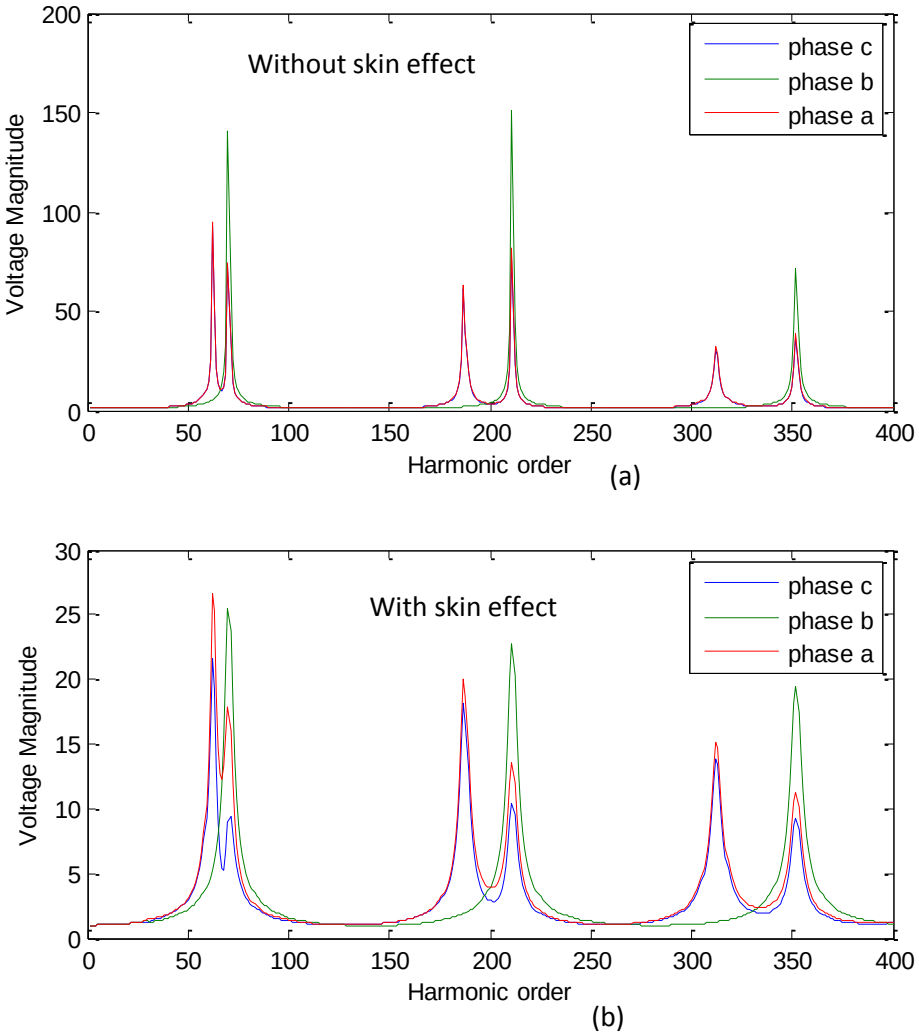

Figure 4.27. Receiving end in open circuit and 1 p.u. harmonic voltage injection 5km long at sending end with first resonant peak to appear at h = 70, NH = 400, freq. = 50 Hz.

Fig. 4.26 shows the frequency scan results when 1km long cable is injected with balanced three-phase voltage source. The results reveal that the resonance phenomenon can be observed at all three point's impedance with one resonant peak. Fig. 4.26a shown result without skin effect, as consequence resonant with high magnitude appears. Also, Fig. 4.26b shown result with skin effect, as seen there is great reduction in the resonance magnitude.

The cable length was elongated to 5km as shown in Fig. 4.27. As depicted there appeared three resonant peaks at harmonic frequency 70 Hz, 200 Hz and 350 Hz. The voltage magnitude is more reduced comparable to 1km cable length.

Investigation on the open circuit 5 km cables correspond to a low capacitance value at high frequencies up to 350 Hz and correspond to a high capacitance value at low frequencies down to 70 Hz. The increased in number of resonant mode is due to capacitive elements presence at various points along the cable length.

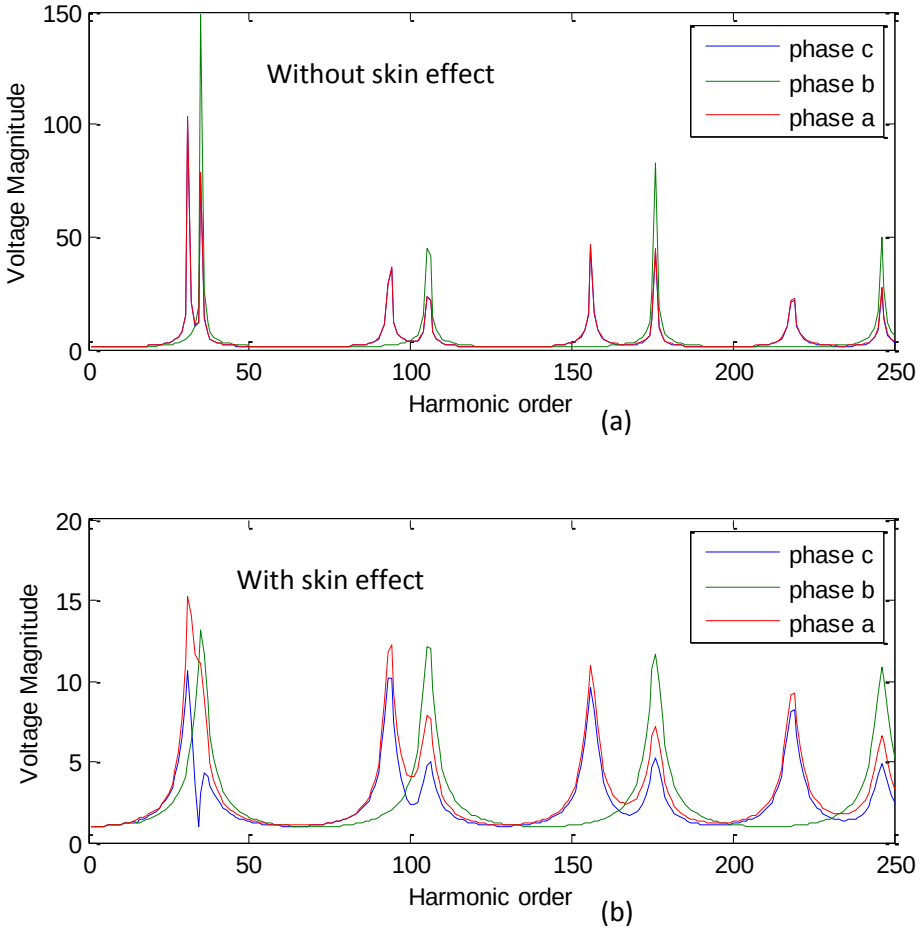

Figure 4.28. Receiving end in open circuit and 1 p.u. harmonic voltage injection 10km long at sending end cable with first resonant peak to appear at h = 30, NH = 250

The 5 km cable length was extended to 10km as shown in Fig. 4.28. As observed there appeared four resonant peaks at harmonic frequency 30 Hz, 100 Hz, 170 Hz and 250 Hz. The voltage magnitude is more reduced comparable to 5km cable length. To achieve resonance the capacitive reactance has to be equal the inductive reactance (high voltage reactor). Once resonance has been achieved only the real losses (I^2R losses in the high voltage reactor and losses in the apparatus) have to be supplied by the mains. The output voltage and the power drawn from the mains is a function of the "Q" or

quality factor of the circuit. The Q apparatus and the Q of the high voltage reactor determine the Q of the system under investigation (Q System).

In order to limit input power requirements a resonant investigation system requires a capacitive model and a variable core (variable reactor). A resonant investigation system required inductance to precisely compensate for the capacitance in the high voltage circuit thereby tuning the system to resonance. The main advantage to this is that very low (real) input power is required for large output (reactive) power.

4.9. **Conclusions**

Both harmonic voltage excitation at the sending end and harmonic current excitation at the receiving end of the line indicate that they hold the potential to characterize the excitability of the right resonance mode while cancelling the left resonance mode. This excitability has been proven as a controllability measure to inject voltage and current into the transmission system to cancel harmonics resonance mode.

On the basis of the present simulation results of the comparison of the various resonance investigation techniques, the suitability of the harmonic voltage and current for investigating resonance conditions is evaluated. The approximation model shows significant differences for cable length greater than 5km, while Bessel function approach shows more accurate results from 1km cable length. The approximation approach which is valid only within certain limits, or suffers from numerical efficiency, prohibits their generalized application.

The preliminary results show that harmonic resonances in underground cable take place at a much lower harmonic order than in comparable overhead transmission lines, owing to the strong influence of the ground mode and the increased capacitive effects introduced by the cable's insulation.

It is difficult to identify the significance of each line at resonance condition. It should be reiterated that the harmonic voltages at the point of current harmonic injection follow the same pattern as those of the line with harmonic voltage excitation. Hence, it provides the information for most potential ways for injecting signals for harmonics cancellations.

4.10. **References**

[1] N.Hatziargyriou, and A.Zervos, "Wind Power Development in Europe". Proceedings of the *IEEE*, VOL. 89, NO. 12, December 2001.

[2] "Europe's Onshore and Offshore Wind Energy Potential an Assessment of Environmental and Economic Constraints" EEA Technical report series: ISSN 1725-2237

[3] T. Ackermann, N. Barberis Negra, J. Todorovic, and L. Lazaridis," Evaluation of Electrical Transmission Concepts for Large Offshore Wind Farms",

[4] H. Brakelmann, "Efficiency of HVAC Power Transmission from Offshore-Windmills to the Grid", *IEEE* Bologna PowerTech Conference, Bologna, Italy, June 23-26, 2003.

[5] Q. Zhong, Y.Zhang, L.Lin, and Q.Chen,"Study of HVDC Light for its Enhancement of AC/DC Interconnected Transmission Systems", Power and Energy Society General Meeting - Conversion and Delivery of Electrical Energy in the 21st Century, 2008 *IEEE* .

[6] Y.P. Li, D.G. Wang, A.P. Hu, W. Wang,. "Real-time Simulation Study on HVDC Control and Protection", Power System Technology (POWERCON), 2010 International Conference on Oct. 2010 *IEEE*.

[7] D.Retzmann, and K.Uecker, "Benefits of HVDC and FACTS for Sustainability and Security of Power Supply", Power Engineering Society *IEEE* July 2007. South Africa.

[8] F. F.Silva, C.L.Bak, W.T.Wiechowski, "Study of High Voltage AC Underground Cable Systems", Modelling and Validation of Electrical Components and Systems 2010 in Fredericia, Denmark, February, 2010.

[9] X.Wilsun, H. Zhenyu Huang, Y. Cui, and H.Wang, "Harmonic Resonance Mode Analysis", *IEEE* Transactions on Power Delivery, Vol. 20, No. 2, April 2005.

[10] C. Amornvipas, and L. Hofmann, "Resonance Analysis in Transmission Systems: Experience in Germany", 2010 *IEEE*.

[11] H.W. Dommel, "Overhead Line Parameters from Handbook Formulas and Computer Programs" *IEEE* Trans. On Power Apparatus and Systems, vol. PAS-104, No.2, February 1985, pp. 366-372.

[12] M.Kane and P. Auriol, "Analytical Modelling of Frequency Parameters of Lines", Center de Genie Electrique de Lyon – ECL France.

[13] R.G. Olson and T.A. Pankaskie, "On the Exact, Carson and Image Theories fot Wire at or above the Earth's Interface". IEEE Transactions on Power Apparatus and Systems, vol. PAS -102,1983, pp, 769-777.

[14] D. Woodhouse, "On the theoretical basis of Carson's equations", Power System Technology (POWERCON), 2012 *IEEE* International Conference on Oct. 30 2012-Nov. 2 2012.

[15] J. Paul, C. Christopoulos, and D.W.P.Thomas, "Time-domain simulation of wave propagation in an overhead wire with a lossy ground return," Computational Electromagnetics in Time-Domain, 2005. CEM-TD 2005. Workshop on September 12 - 14 , 2005.

[16] J.R. Wait,"Theory of Wave Propagation along a Thin Wire Parallel to an Interface" Radio Science, vol. 7, June 1972, pp, 675-679.

[17] L.M.Wedepohl, A.E.Efthymiadis, "Wave Propagation in Transmission Lines Over Lossy Ground: A New, Complete Field Solution", Proceedings of the IEE, Vol. 125, No. 6, June 1978, pp. 505-510.

[18] L.M.Wedepohl, A.E.Efthymiadis, "Wave Propagation in Transmission Lines Over Lossy Ground: A New, Complete Field Solution", Proceedings of the IEE, Vol. 125, No. 6, June 1978, pp. 505-510..

[19] L.M.Wedepohl, "Application of Matrix Methods to the Solution Travelling Wave Phenomena in Poly-Phase Systems", Proceeding of the IEE, vol. 110, No. 12 1963, pp. 2200-2212.

[20] M.M. Ney," Striction and skin effects on the internal impedance value of flat conductors", Electromagnetic Compatibility, *IEEE* Transactions on Vol. 33, Nov 1991.

[21] L.J.Giacoletto, "Frequency- and time-domain analysis of skin effects", Magnetics, *IEEE* Transactions on Vol. 32, Jan 1996.

[22] H.G.Brachtendorf, R. Laur, "Simulation of skin effects and hysteresis phenomena in the time domain", Magnetics, *IEEE* Transactions on Vol.37, Sept; 2001.

[23] S.L.M. Berleze, and R. Robert, "Skin and proximity effects in nonmagnetic conductors", Education, *IEEE* Transactions on Vol.:46, Aug. 2003.

[24] N. Kondrath, and M.K. Kazimierczuk, " Inductor winding loss owing to skin and proximity effects including harmonics in non-isolated pulse-width modulated dc-dc converters operating in continuous conduction mode", Power Electronics, IET Vol. 3, Nov. 2010.

[25] K. Kopsidas, S.M. Rowland, "A Performance Analysis of Reconductoring an Overhead Line Structure", Power Delivery, *IEEE* Transactions on Vol. 24, Oct. 2009

[26] V.T. Morgan, and R.D. Findlay,"The effect of frequency on the resistance and internal inductance of bare ACSR conductors", Power Delivery, *IEEE* Transactions on Vol. 6 Jul 1991

[27] S.T.Sobral, J.A. Barbosa, J.V.C. Nunes,; and E. Chinelli, "Ground potential rise characteristics of urban step-down substations fed by power cables-a practical example", Power Delivery, *IEEE* Transactions on Vol. 3, Oct 1988.

[28] M.Nakagawa, "Further Studies on Wave Propagatioin along Overhead Transmission Lines: Effects of Admittance Correction," *Power Apparatus and Systems, IEEE Transactions on Vol.PAS-100, July 1981.*

[29] W.Horst,"An application of equivalent transformations for analysis of nonuniform transmission lines," *Circuits and Systems, 1988., IEEE International Symposium on 7-9 Jun 1988.*

[30] C.H.Chien, and R. W.G.Bucknall, "Harmonic Calculations of Proximity Effect on Impedance Characteristics in Subsea Power Transmission Cables," *IEEE Transactions on Power Delivery, Vol. 24, October 2009.*

[31] Z. Xu, H. Liu. "The Harmonic Model and Its Algorithm for Coupled Multiphase Transmission Line". Proceedings of the 9th International Conference on Harmonics and Quality of Power (ICHQP). October 1-4, 2000, Orlando, Florida, USA.

[32] A.B. Fernandes, W.L.A. Neves, "Phase-domain transmission line models considering frequency-dependent transformation matrices," *Power Delivery, IEEE Transactions on Vol.19, April 2004.*

[33] M. V. Escudero, and M. Redfern, "Effects of Transmission Line Construction on Resonance in Shunt Compensated EHV Lines," Conference on Power Systems Transients (IPST'05) in Montreal, Canada on June 19-23, 2005.

[34] A.B. Femandes, W.L.A. Neves, E.G.Costa, and M.N. Cavalcanti, "Transmission Line Shunt Conductance from Measurement," *Power Delivery, IEEE Transactions on Vol.19, April 2004.*

[35] H. Oraizi and M. Afsahi, **"**Analysis Of Planar Dielectric Multilayers as FSS By Transmission Line Transfer Matrix Method (Tltmm)," *Progress In Electromagnetics Research, PIER 74, 217–240, 2007*

[36] L.M.Wedepohl, "Application of Matrix Methods to the Solution Travelling Wave Phenomena in Poly-Phase Systems", *Proceeding of the IEE, vol. 110, No. 12 1963, pp. 2200-2212.*

[37] J.A. Parle, "Phase Domain Transmission Line Modelling for EMTP-Type Studies with Application to Real-Time Digital Simulation", 2000.

[38] M. Kruger, "Measurement of overhead line and cable impedance values, earth impedance of large substations and electromagnetic interference between overhead lines and signal cables, using a new technology*," Developments in Power System Protection, 2004. Eighth IEE International Conference on Vol.1, April 2004*

[39] F.A. Uribe, "Calculating Mutual Ground Impedances between Overhead and Buried Cables," *Electromagnetic Compatibility, IEEE Transactions on Vol.:50 Feb. 2008*

[40] R. Ebrahimi, A. Babaee, M. Hoseynpoor, "Evaluation and Calculation of Overhead Line Impedance in Distribution Networks" Journal of Applied Sciences Research;Aug2011, Vol. 7, August 2011

[41] C.Jong-kee, L. Won-kyo, K. Ju-sik, E.B. Shim, G.C. Hwang, "Analysis of Zero Sequence Impedance of Single-Point Bonded Cable Systems using ATP/EMTP," The International Conference on Electrical Engineering 2008

[42] M. Vinţan,P.I. Mihu, and I. Borlea , "AC Power Lines Impedances Computational Methods," Journal of Sustenable Energy, Vol. 1, No. 2, June, 2010

[43] K..N. Hasan, K, Rauma, P.Rodriguez, J. I. Candela, R.S. Munoz-Aguilar and A. Luna, "An Overview of Harmonic Analysis and Resonances of Large Wind Power Plant". *2011 IEEE.*

[44] J.R. Harries and J.I. Randall, "Harmonic Resonance on Parallel High Voltage Transmission Lines". *IEEE Power Engineering Review, January 1997.*

[45] A.Ametani, "A General Formulation of Impedance and Admittance of Cables", *IEEE Transactions on Power Apparatus and Systems, Vol. PAS-99,No. 3 May/June 1980.*

[46] M. Kane, A. Ahmad, and P. Auriol, "Multiwire Shielded Cable Parameter Computation," *IEEE Transactions on Magnetics Vol. 31, May 1995.*

[47] G. Mugala, and R. Eriksson, "Dependence of XLPE Insulated Power Cable Wave Propagation Characteristics on Design Parameters," *IEEE Transactions on Dielectrics and Electrical Insulation, Vol. 14, April 2007.*

[48] N. Nagaoka, and A. Ametani, "Modelling of Frequency-Dependent Lines and Cables by Means of Algebra Processing Program," *2000 IEEE.*

[49] C.H Chien,and R.W.G. Bucknall, "Analysis of Harmonics in Subsea Power Transmission Cables Used in VSC-HVDC Transmission Systems Operating Under Steady-State Conditions," *IEEE Transaction on Power Delivery. Vol.22. No. 4 October 2007.*

[50] F.L.Alvarado, R. Betancourt, "An accurate closed-form approximation for ground return impedance calculations," *Proc. IEEE*, **71**(2):279-280. PROC.1983.

[51] A.Ametani,"Approximate Method for Calculating the Impedances of Multiconductors with Cross Sections of Arbitrary Shapes," *Electrical Engineering in Japan, Vol. 111, 1992.*

[52] G. K. Papagiannis, D. A. Tsiamitros, G. T. Andreou, and D. P. Labridis, and P. S. Dokopoulos, "Earth Return Path Impedances of Underground Cables for the multi-layer case - A Finite Element approach," *2003 IEEE Bologna Power Tech Conference, June 23-26, Italy.*

[53] P. Pettersson, "Image Representation of Wave Propagation on Wire Above on and under Ground," IEEE Trans. PWRD. Vol. 9. Pp. 1049-10555, 1994.

[54] O.I. Gilbertson, "Electrical Cables for Power and Signal Transmission," John Wiley & Sons INC, USA, 2000.

[55] K. Ferkal and E.Dorisoni, "Proximity Effect and Eddy Current Losses in Insulated Cables," *IEEE Transactions on Power Delivery, Vol. 11, July 1996, pp. 1171-1178.*

[56] U.S.Gudmundsdottir, B. Gustavsen, C.L, Bak, W.Wiechowski and F.F.de Silva, "Wave propagation and benchmark measurements for cable model validation". *IEEE Transactions on Power Delivery, November 2009.*

[57] G., B."A study of overvoltages in high voltage cables with emphasis on sheath overvoltages," *Trondheim; NTH, Norges Tekniske Hogskole,. 1993.*

[58] M. Hasheminezhad and M. Vakilian, "Direct Introduction of Semicon Layers in a Cable Model". *Scientia Iranica, Vol. 15, No. 2, pp203-210*

[59] M.Hasheminezhad, M.Vakilian, T.R.Blackburn, and B.T.Phung, "Direct Introductionof Semicon Layer in XLPE Cable Model". *International Conference on Power System Technology. 2006 IEEE.*

Chapter 5

5. Modular Multi-Level Voltage Source Converters for HVDC Applications

5.1. Introduction

The trend to multi-terminal oil and gas platforms in future production will increase the demand for advanced power electronic systems. For this application field modular multilevel converters (MMC) with a high number of voltage levels seem to be the most suitable tools, because of the reliability of high power quality and need for low voltage distortion on the line side [1][2].

Modular multilevel converters (MMC) belong to the family of multilevel VSC topology, owing to its structure and cascade connection of VSCs sub-modules (SM) [3]. The MMC requirement is to synthesize a desired ac voltage from several levels of DC voltages. For this reason, MMC converters are suitable for connecting an AC grid with renewable energy sources either in series or parallel. In addition to its application, MMCs are used for harmonic cancellation [4]-[6]. An important feature of the MMC topology is that it generates a high voltage waveform using low voltage devices and reduction of harmonic contents [7]. An MMC is more harmonic reduction driven compared to conventional n-level VSC converters due to its ability to accommodate hundreds of converter sub-modules [8]. The most used modular multilevel converter topologies include the neutral-point clamped, cascaded H-bridge, and flying-capacitor converters.

Most of the MMC topologies presented in literature are developed using a single-phase half-bridge submodule or single-phase full-bridge submodule [9-17]. In the former, its capacitors values must be sufficiently large enough to ensure that the voltage potential remains unchanged during operation of the circuit. As revealed not all odd harmonics are cancelled and the fact that the converter cannot control the rms value of the output voltage waveform at fundamental frequency is also a limitation. When the latter is employed, being a single phase system, third harmonic is always present; also its output waveform is accompanied with high ripple. These harmonics when reflected back to the DC side source include even harmonics. Therefore, a new three-phase modular

multilevel converters using three-phase full-bridge submodule which is capable of producing multilevel waveforms plus reduction of all harmonics is investigated. The new MMC is based on solid state voltage source converters (VSCs), which enable independent, fast control of active and reactive powers, plus high harmonic reductions. In addition, ripple cancellation can also be achieved [18-19].

The proposed model is aimed at achieving high quality voltage and current waveforms and reducing harmonic content to a minimum. The aforementioned features suggested that, the MMC structure can easily realize the phase shifted PWM waveforms. The MMC topology proposed in this project can accommodate hundreds of submodules made of IGBTs switches. The required numbers of SMs are series cascaded and in phase to develop a dc operating voltage. With this arrangement and the use of a phase-shifted algorithm, balancing of capacitor voltages is achieved. The system has significant lower switching losses compared to conventional VSCs topology and also, the probability of dc bus short circuits is reduced [10].

The MMCs output voltage waveforms improve power quality as the number of levels increases, reducing the harmonic distortion of the output voltage waveforms. These features make MMCs very attractive to the oil and gas industry. The actual improvement of the harmonic spectrum depends on the control technique employed. This topology at present uses insulated gate bipolar transistor (IGBT) valves and pulse width modulation (PWM) with unipolar control techniques [20]. PWM switching control opposes the fundamental frequency switching strategy preferred in FACTs applications [21]. PWM is promising in VSCs due to its relatively low power application. In PWM with unipolar voltage control, the switches in the four legs cascaded converter are switched separately. With PWM unipolar voltage switching, the dominant harmonic voltages centred on frequency modulation ratio disappear, most importantly achieving harmonic spectrum with very low harmonic content. The waveforms produced by PWM control are phase shifted to obtain the balanced three-phase output voltages in a three-phase VSC PWM-unipolar converter.

To reduce the neutral ripple, it must be ensured that not all three line ripples are of the same sign at a given instant. This is easily achieved by using three transformers phase shifted by 120^{o} at the carrier frequency. There is significant reduction in the neutral ripple when phase-shifted is employed. The effect of using phase-shifted transformer on the single phase line ripple is unrealistic.

Since the main focus has been on minimizing the harmonic distortion in the network, the single-carrier PWM has been found unsuccessful. However, the three-carrier PWM is seen to be more effective than the single-carrier PWM in terms of three phase neutral harmonic distortion cancellations [22-26].

5.1.1. Three-Phase Full-Bridge VSC and Operating Principle

The three-phase full bridge VSC topology which is capable of generating two-level output voltage waveforms is as showed in Fig. 5.1 [27-33]. It consists of six switches devices (T_{A1+}, T_{A1-}, T_{A2+}, T_{A2-}, T_{A3+}, and T_{A3},) with six antiparallel diode (D_{A1+}, D_{A1-}, D_{A2+}, D_{A2-}, D_{A3+}, and D_{A3-},). The switching functions $S_a(t)$, $S_b(t)$ and $S_c(t)$ are obtained by comparing the three reference signals with carrier signal (V_r). The reference signals V_{sa}, V_{sb} and V_{sc} of the phase voltages are sinusoidal in the steady state, forming a symmetrical three-phase system as shown in Figure 5.1.

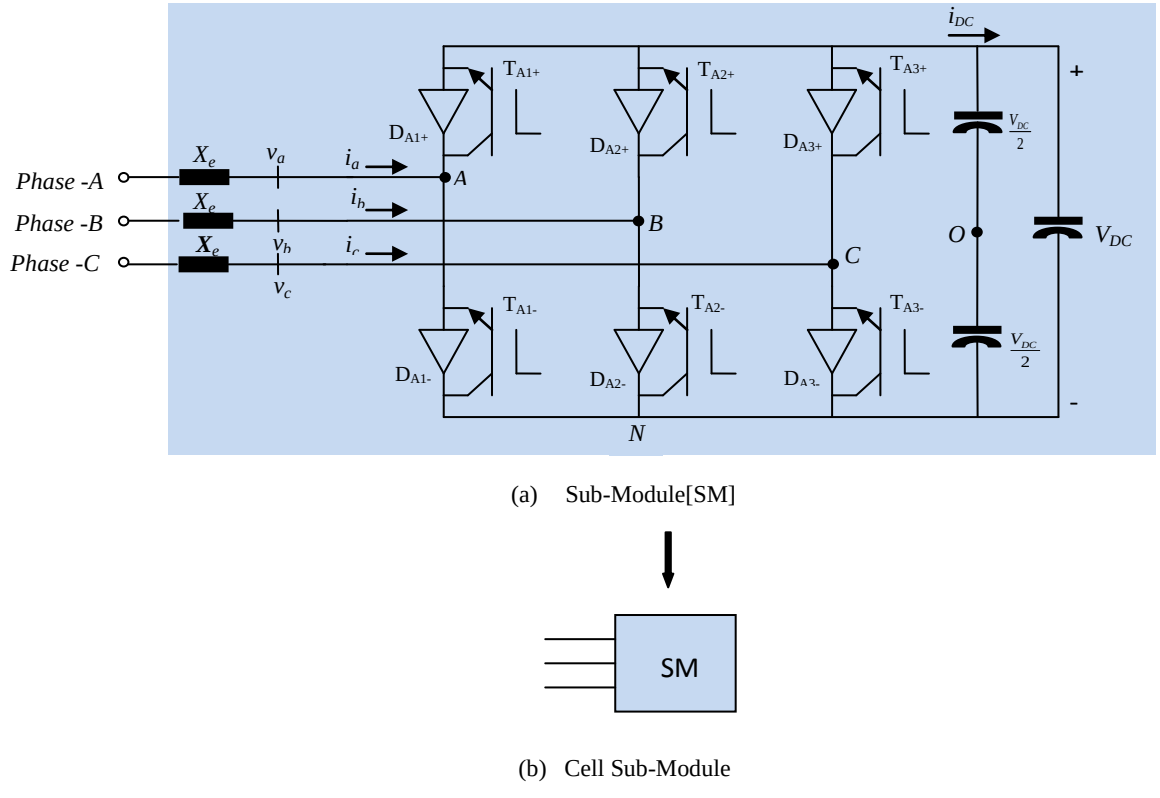

(a) Sub-Module[SM]

(b) Cell Sub-Module

Figure 5.1 Two-Level Three-Phase VSC

All switches waveforms take a value of one when:

$V_{sa} > |V_r|$, $V_{sb} > |V_r|$ and $V_{sc} > |V_r|$ and zero otherwise.

The three legs are controlled with a phase-shift of 120^o between them, and each phase has two switching functions. The six switches are paired one parallel to each other and are turned on for half of the period (180^o). With STPWM (sine-triangle pulse width modulation) control, the switches of the converter are controlled by comparing a sinusoidal control signal and triangular switching signal as shown in Fig. 5.2 [34].

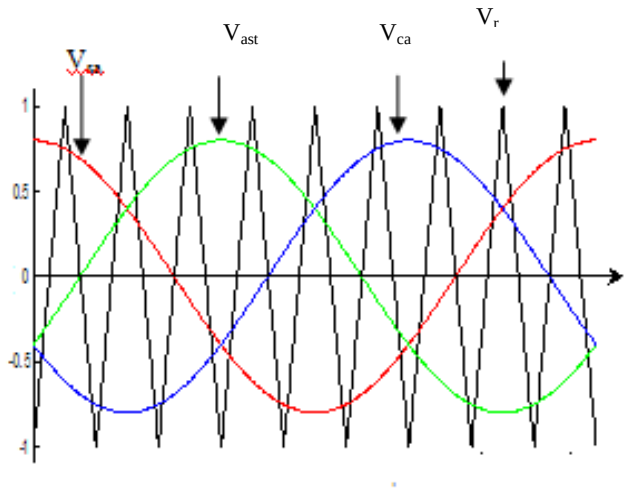

Figure 5.2 Reference signals and carrier signal

The ratio of the triangular wave frequency and the sinusoid frequency sets the modulation frequency ratio. In theory, PWM with unipolar voltage switching, the six switches in Fig. 5.1 are not switched simultaneously; the legs A, B and C are controlled separately by comparing $v_{control}$, and $-v_{control}$ with $v_{triangle}$, respectively. Therefore, the voltages v_{AN}, v_{BN} and v_{CN} fluctuate between V_{DC} and 0. The switching patterns are as follows:

$$v_{control} > v_{triangle}: T_{A1+} \text{ on and } v_{AN} = V_{DC}$$
$$v_{control} < v_{triangle}: T_{A1-} \text{ on and } v_{AN} = 0 \quad (5.1)$$
$$v_{control} > v_{triangle}: T_{A2+} \text{ on and } v_{BN} = V_{DC}$$
$$v_{control} < v_{triangle}: T_{A2-} \text{ on and } v_{BN} = 0 \quad (5.2)$$
$$v_{control} > v_{triangle}: T_{A3+} \text{ on and } v_{CN} = V_{DC}$$
$$v_{control} < v_{triangle}: T_{A3-} \text{ on and } v_{CN} = 0 \quad (5.3)$$

Line switching function are determined by:

$$v_{AB} = v_{AN} - v_{BN} \;;\; v_{BC} = v_{BN} - v_{CN} \;;\; v_{CA} = v_{CN} - v_{AN} \tag{5.4}$$

Each phase has two switching functions such as:

$SF_{A1+} = v_{control(phase\text{-}a+)} > v_{triangle}$, T_{A1+} is ON
$SF_{A1-} = v_{control(phase\text{-}a-)} < v_{triangle}$, T_{A1-} is ON

$SF_{A2+} = v_{control(phase\text{-}b+)} > v_{triangle}$, T_{A2+} is ON
$SF_{A2-} = v_{control(phase\text{-}b-)} < v_{triangle}$, T_{A2-} is ON

$SF_{A3+} = v_{control(phase\text{-}c+)} > v_{triangle}$, T_{A3+} is ON
$SF_{A3-} = v_{control(phase\text{-}c-)} < v_{triangle}$, T_{A3-} is ON

Using the switching function, $v_{control(phase\text{-}A,B,C)}$ the V_{A0}, V_{B0} and V_{C0} can be obtained as:

The output voltage of converter leg A with respect to the DC bus *0*

$$V_{A0} = \frac{V_{DC}}{2} * SF_{A1+} = \frac{V_{DC}}{2} * \sum_{n=1}^{\infty} A_n \sin(n\omega t) \tag{5.5}$$

The output voltage of converter leg B with respect to the DC bus *0*

$$V_{B0} = \frac{V_{DC}}{2} * SF_{A2+} = \frac{V_{DC}}{2} * \sum_{n=1}^{\infty} A_n \sin n(\omega t + \theta) \tag{5.6}$$

The output voltage of converter leg C with respect to the DC bus *0*

$$V_{C0} = \frac{V_{DC}}{2} * SF_{A3+} = \frac{V_{DC}}{2} * \sum_{n=1}^{\infty} A_n \sin n(\omega t - \theta) \tag{5.7}$$

where

$$A_n = \frac{\sin(n\delta)}{n\pi}$$

δ = half the on-period of the switch
n = is an integer
θ = phase shift switching function relative to SF(t)

$$V_{N0} = \frac{1}{3}(V_{A0} + V_{B0} + V_{C0}) \text{ -- Natural phase voltage} \tag{5.8}$$

The phase voltages are obtained as:

$$V_{AN} = V_{A0} - V_{N0} \;;\; V_{BN} = V_{B0} - V_{N0} \;;\; V_{CN} = V_{C0} - V_{N0} \tag{5.9}$$

Then, the converter line-to-line voltage (V_{AB}, V_{BC}, V_{CA}) can be simulated by:

$$V_{AB} = V_{A0} - V_{B0} = \frac{\sqrt{3}V_{DC}}{2} * \sum_{n=1}^{\infty} A_n \sin n(\omega t + 30^0) \tag{5.10}$$

$$V_{BC} = V_{B0} - V_{C0} = \frac{\sqrt{3}V_{DC}}{2} * \sum_{n=1}^{\infty} A_n \sin n(\omega t - 90^0) \quad (5.12)$$

$$V_{CA} = V_{C0} - V_{A0} = \frac{\sqrt{3}V_{DC}}{2} * \sum_{n=1}^{\infty} A_n \sin n(\omega t + 150^0) \quad (5.13)$$

For the SPWM technique in Fig. 5.2, a triangular carrier waveform (V_{tri}) is compared with the reference sinusoidal waveform (V_{mod}) at the fundamental frequency of the output voltage. Then, the switching pulses are (SF_{A1+}; SF_{A1-}), (SF_{A2+}; SF_{A2-}), and (SF_{A3+}; SF_{A3-}), for phase A, phase B and phase C respectively. With these modulated waveforms, the two-level switching functions ($S_a(t)$; $S_b(t)$; $S_c(t)$) for each leg of the AC/DC converter shown in Fig. 5.3 can be expressed as:

$$S_a(t) = \frac{1}{2}(SF_{A1+} - SF_{A1-}) \quad (5.14)$$

$$S_b(t) = \frac{1}{2}(SF_{A2+} - SF_{A2-}) \quad (5.15)$$

$$S_c(t) = \frac{1}{2}(SF_{A3+} - SF_{A3-}) \quad (5.16)$$

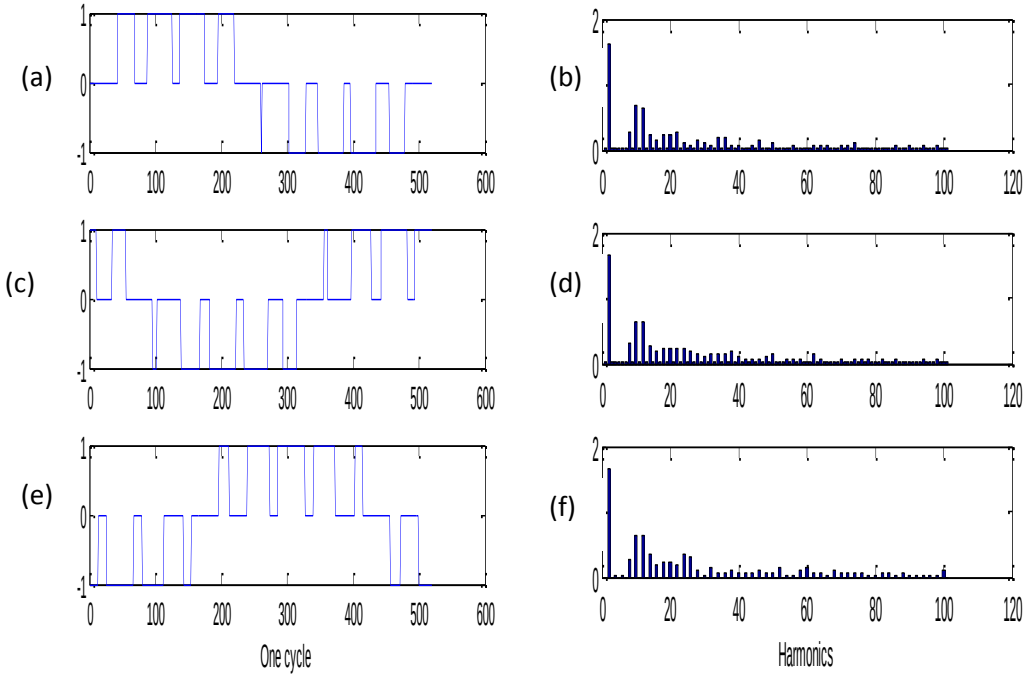

Figure 5.3. Two-level Phase Switching Function of a VSC one Unipolar PWM Converter (a)Output voltage of phase a and phase b; (b) The amplitude of all harmonic spectrum for the output voltage of phase a and phase b; (c) Output voltage of phase b and phase c; (d) The amplitude of all harmonic spectrum for the output voltage of phase b and phase c; (e) Output voltage of phase c and phase a; (f) The amplitude of all harmonic spectrum for the output voltage of phase c and phase a

A PWM switching waveform, using a signal carrier based control method with an average valve switching frequency of 1250 Hz, also with no voltage ripple in the DC capacitor (ie an infinite capacitance) is shown in Figure 5.3 (a,c,e), each waveform takes three values (V_{DC}, 0, - V_{DC}) and there is a 120^o phase-shift between them. In order to improve the quality of the output waveform, the converter is typically controlled using PWM-unipolar, resulting in the output waveform with significant high-order harmonics. When the waveforms are zero for each half of the period, they will have a 60^o interval in between them and a total of 120^o per period. The ratio of the amplitude of the sinusoidal waveforms with respect to the amplitude of the triangular wave sets the amplitude modulation ratio. For a system in which the converter sources have impedance loads and antiparallel diode, in such case the converter operates in all the four quadrants. Each leg can handle current in both directions at any time, since either the turned on switch or the antiparallel diode of the other switch can be the conducting element depending upon the polarity of the output line current. The DC bus capacitor provides the required energy such that power flow can be controlled and DC harmonics carefully eliminated. The harmonic spectrums in a 1kHz system associated with the switching function of

each converter leg are as presented in Figure 5.3 (b,d,f). Each phase-leg of the converter is connected through a star delta transformer to the AC systems. As represented the voltage waveforms contain all harmonics, and this is confirmed with the harmonic spectrum of the phase-to-phase that all harmonics are reduced.

5.2. **Design of the DC Capacitor**

The voltage in the DC side of Fig. 5.1 is given by the voltage in the capacitor as a function of the switching functions, and is given by the equation

$$v_{dc}(t) = v_{cap}(t) = \frac{1}{C}\int_{0}^{t} i_{cap}(t)dt + v_{cap}(0^{+}) \tag{5.17}$$

where,

$$v_{cap}(0^{+}) = \frac{1}{C}\int_{-\infty}^{0^{+}} i_{cap}(t)dt \tag{5.18}$$

Equation (5.18) is the voltage evaluated at t = 0^{+} due to charging from an earlier period.

The steady state changes in the instantaneous power absorbed by the load generate voltage fluctuations across the dc capacitor. For this reason the voltage across the dc capacitor produces a little harmonic distortion. The magnitude of these voltage fluctuations can be controlled effectively with an appropriate dc capacitor value.

$$C = \frac{1}{v_{cap}}\int_{0}^{t} i_{cap}(t)dt \tag{5.19}$$

Equation (5.19) represents the value of the dc capacitor, *C*, that will maintain the dc voltage above harmonic distortion.

the voltage on the DC side is

$$v_{dc}(t) = v_{cap}(t) \tag{5.20}$$

The line voltages on the AC side and on the DC side are related to each other by:

$$v_{ab} = s_{ab}(t)v_{dc}(t) \tag{5.21}$$

$$v_{bc} = s_{bc}(t)v_{dc}(t) \tag{5.22}$$

$$v_{ca} = s_{ca}(t)v_{dc}(t) \tag{5.23}$$

The expression that relates the AC side and DC side current

$$i_{DC}(t) = S_{ab}(t)\, i_{ab}(t) + S_{bc}(t)\, i_{bc}(t) + S_{ca}(t)\, i_{ca}(t) \tag{5.24}$$

In the harmonic domain Equ (5.14) may be represented as

$$\mathbf{V}_{cap} = \frac{1}{C}\mathbf{D}^{-1}(jh\omega_0)\mathbf{I}_{dc} + \mathbf{E}_{dc} \tag{5.25}$$

where

$\mathbf{V}_{cap}$ is assembled with the harmonic content of $v_{cap}(t)$

$\mathbf{I}_{dc}$ is assembled with the harmonic content of $i_{dc}(t)$

$\mathbf{E}_{dc}$ contains only a DC term, i.e.

$$\mathbf{E}_{dc} = [0 \ \cdots \ 0 \ v_{cap}(0^+) \ 0 \ \cdots \ 0]^T$$

The equivalent impedance of the capacitor on the DC side is given as

$$\mathbf{Z}_{cap} = \frac{1}{C}\mathbf{D}^{-1}(jh\omega_0) \tag{5.26}$$

Therefore, (5.25) can be represented as

$$\mathbf{V}_{cap} = \mathbf{Z}_{cap}\,\mathbf{I}_{dc} + \mathbf{E}_{dc} \tag{5.27}$$

Also, (5.20) and (5.21) the voltage on the DC side and its relationship to the AC phase voltages may be represented in the harmonic domain as

$$\mathbf{V}_{dc} = \mathbf{V}_{cap} \tag{5.28}$$

$$\mathbf{V}_a = \mathbf{S}_{ab}\,\mathbf{V}_{dc}$$

$$\mathbf{V}_b = \mathbf{S}_{bc}\,\mathbf{V}_{dc} \tag{5.29}$$

$$\mathbf{V}_c = \mathbf{S}_{ca}\,\mathbf{V}_{dc}$$

Similarly, the relationship between the line currents and the DC is represented in harmonics domain as

$$\mathbf{I}_{dc} = \mathbf{S}_{ab}\,\mathbf{I}_a + \mathbf{S}_{bc}\,\mathbf{I}_b + \mathbf{S}_{ca}\,\mathbf{I}_c \tag{5.30}$$

5.3. **Modular Multi-Level VSC with PWM-Unipolar**

Multilevel converter technology has experienced increasing attention in the last decade, and several topologies have been reported [35][36]. From the traditional topology of H-bridge converter, a new topology named modular multi-level converter **(**MMC) is developed, which has the capability of generating multi-level output voltage waveforms. By using two or more sub-modules cascaded connection with additional DC capacitors, a flexible three-phase cascaded H-bridge VSC is formed. This H-bridge converter is expanded to develop three legs per phase connected to three-phase electromagnetic interface without any filter equipment. As shown each arm is composed of three or

more sub-modules with additional central capacitive energy storage at the DC side. The proposed model has the capability of generating multi-levels (two-level, four-level and six-level, etc) voltage waveforms. Each sub-module of the converter consists of three legs similar to the conventional three-phase VSC, which is minimum power unit of MMC. In which D_{A1+}, D_{A1-}, D_{A2+}, D_{A2-}, D_{A3+}, and D_{A3-} are the diodes of IGBTs. This IGBT valve consists of IGBT module with its freewheeling diode (FWD) and auxiliary's snubbed circuit. The cascaded connected SM is aimed at increasing the output voltage waveforms and power quality operational characteristics, which can be termed as the expansion of three phase IGBT module [37][38]. Though MMC valves are not only used to increasing voltage levels but also has good driver and controller attributes. This sophisticated topology opens doors for more cancellation of harmonics with proper phase-shifting comparable to conventional VSCs. With this configuration, the harmonic content of the output voltage is reduced and the harmonic elimination at the magnetic interface level can be achieved without increasing the switching frequencies in the PWM control system.

Phase shifting is an important parameter for the control of modular converters in order to achieve high quality output voltage waveforms. It magnetically cancels lower order harmonics such 5^{th} and 7^{th}, even if they are not equal in magnitude. Each cascaded three-phase MMC converter uses PWM uni-polar voltage switching. The number of levels per phase half cycle of the switching function $s_{ni}(t)$, where SM_{ni} is the cell sub-module, is given by the frequency modulation ratio m_f,

$$m_f = \frac{f_r}{f_s} \tag{5.31}$$

where,

f_r = triangular frequency and f_s = sinusoidal

the harmonics generated by the voltage converter i are given by

$$h = 2jm_f \pm k \qquad \text{where} \quad j,k = 1,2,3,... \tag{5.32}$$

h are the harmonics of $s_{ni}(t)$

The shifted angles for the cell sub-module (SM_{ni}) carrier signal are given by

$$\delta_{ri} = 2\pi(i-1)/n_i \tag{5.33}$$

By using cell sub-module MMC-PWM converters in parallel, the harmonics generated by the VSC-MMC are given as

$$h = 2jm_f \pm k \qquad \text{where} \quad j,k = 1,2,3,... \tag{5.34}$$

the magnitudes of the harmonics are given as

$$S_{MMC} = \frac{SM_{a1} + SM_{a2} + SM_{a3} + \cdots + SM_{an}}{ni} \tag{5.35}$$

where the magnitude of the fundamental frequency component has a value of modulation index (m).

It should be noted that an increase in the voltage ratings (which is imposed by the application) has a direct impact in the Cascaded H-Bridge (CHB) MMC power quality, due to the increase in the number of the output voltage levels and the increase of the number of input-current pulses, both leading to output- and input-quality improvements, respectively

The topology of MMCs with three-phase cascaded H-bridge (CHB) per phase is as depicted in Fig. 5.4. This topology is suitable for MV high-power drives and high voltage applications (HV), due to its modular structure and power-quality operational characteristics and could gain popularity in the future. One advantage of this topology is that, there is no need for a voltage balancing stabilizer. Owing to the fact that, the input transformer has the provision for independent and isolated DC sources at the secondary windings side. The capacitor voltage does not required huge initialization. The configuration of CHB MMC permits series connection to achieve high voltage levels for high power application, used in oil and gas exploration and production fields. The topology offers very high power voltage waveforms and lower switching losses, because the high power sub-modules only commutate at fundamental switching frequency. The CHB can be more adapted to operate under internal fault conditions. In a case where one of the sub-modules is reported to be faulty, a simply bypassing faulty cell can be employed with ease to enhance operation. The model uses phase shifted transformer with PWM control technique to cancel more harmonics, even at a low frequency. Each PWM converter (sub-module) is capable of generating more than two-level voltage waveform across the three mid-point legs.

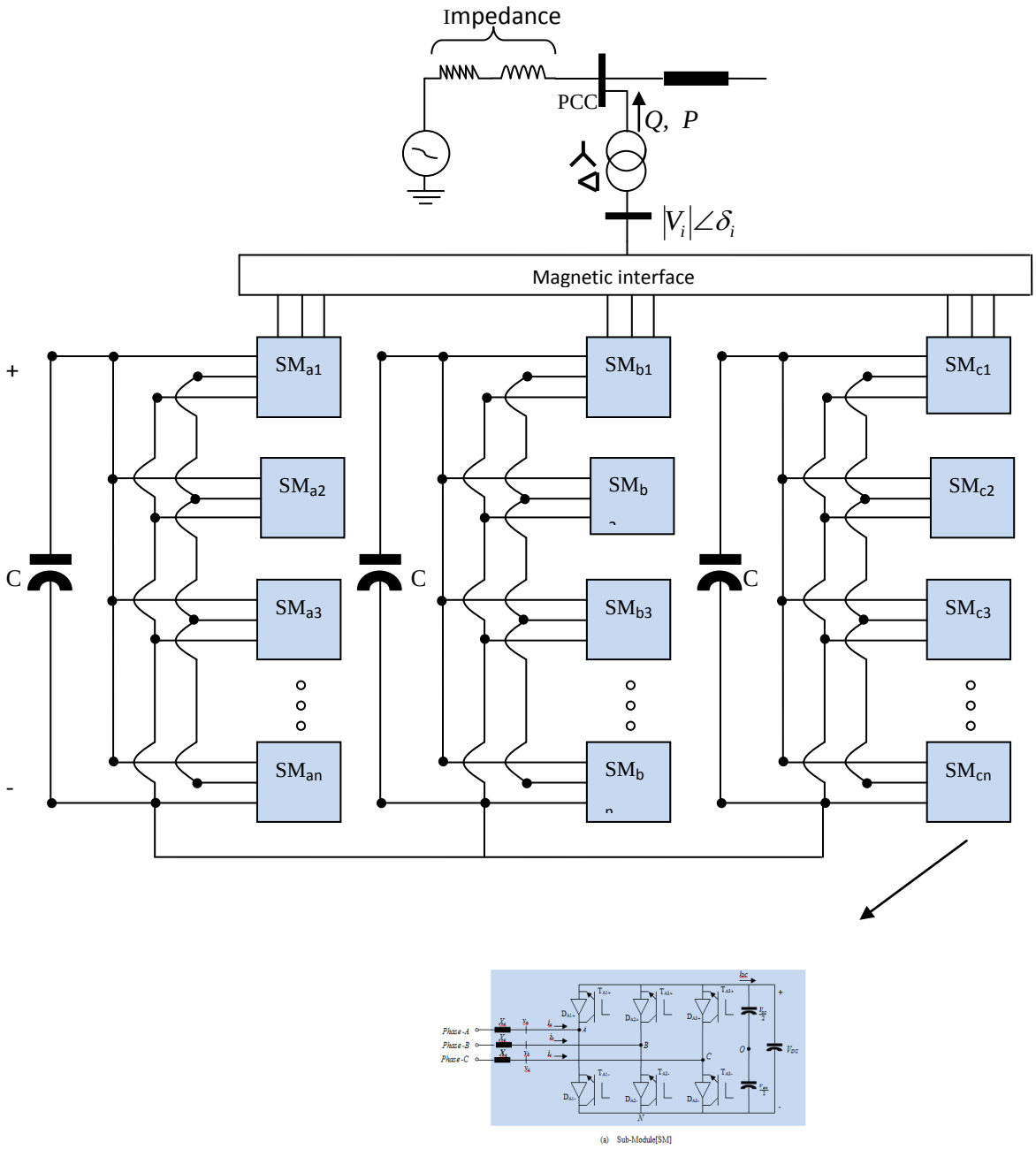

Figure 5.4: Modular Multi-Level Three-Phase VSC

5.4. **Multilevel Output-Voltage Generation**

Consider the topology of the power sub-modules presented in Fig. 5.4. The switching state of one sub-module *SMa* is determined by the logical value of three signals (T_{A1+},

T_{A2+}, and T_{A3+}), which can be "1" and "0" representing the "ON" and "OFF" state of each switch, respectively. This leads to six different binary combinations that generate three different output voltages $+V$dc, 0 and $-V$dc. Considering the nature of the converter phase leg, the phase voltage will be the sum of all converter voltages as follows:

$$v_{AN} = SM_{a1} + SM_{a2} + SM_{a3} + \cdots + SM_{an} \tag{5.36}$$

The different output-voltage levels can be determined by increasing the number of the *SM* in ascending order. An example for one phase of a two-*SM* MMC CHB converter is presented as

$$v_{AN} = SM_{a1} + SM_{a2} \tag{5.37}$$

The phase voltage v_{AN} will have a total of four-levels plus the zero level (overall five-level converters). The voltage v_{AN} will have values of $2V_{dc}$, V_{dc}, 0 and $-V_{dc}$, $-2V_{dc}$, as shown in Fig. 5.5

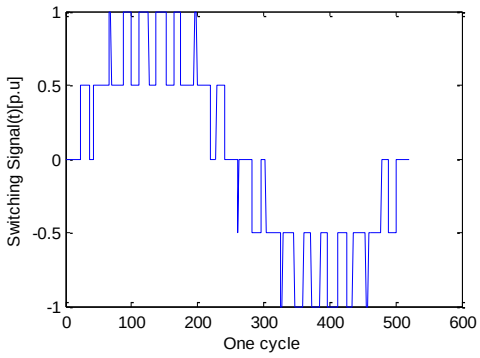

a

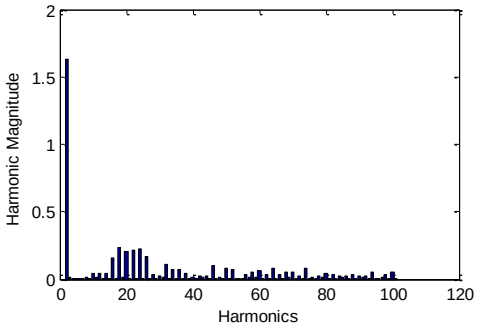

b

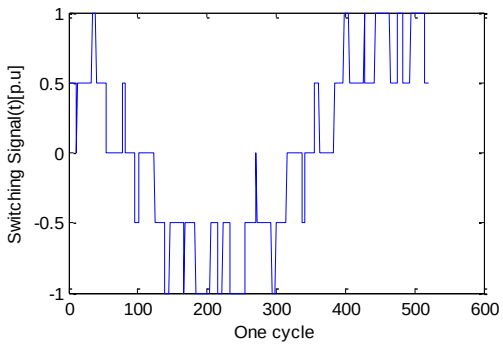

c

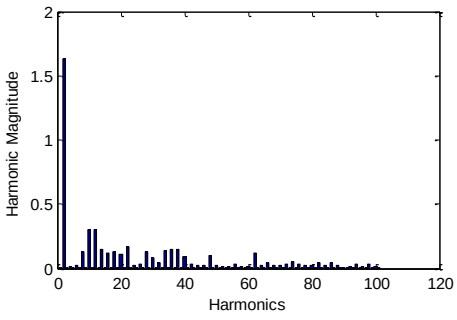

d

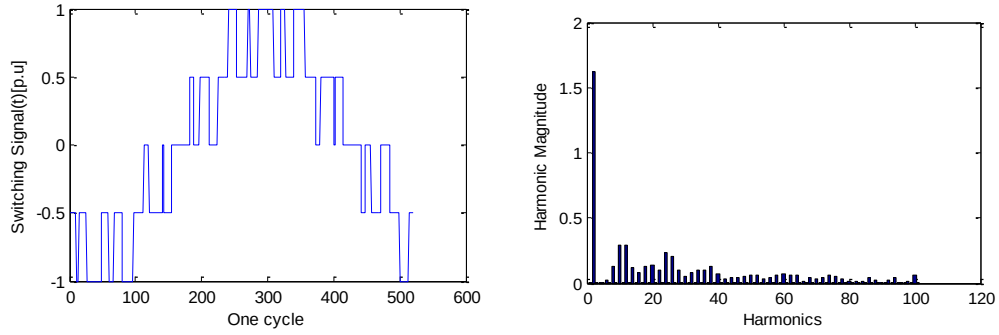

e f

Figure 5.5 Five-level Phase Switching Function of a two VSC Unipolar PWM Converters (a)Output voltage of phase a and phase b; (b) The amplitude of all harmonics for the output voltage of phase a and phase b; (c) Output voltage of phase b and phase c; (d) The amplitude of all harmonics for the output voltage of phase b and phase c; (e) Output voltage of phase c and phase a; (f) The amplitude of all harmonics for the output voltage of phase c and phase a

The line-to-line voltage waveform will have a higher number of levels, as represented in Fig. 5.6. Note that there is more than one switching state for some voltage levels (this is called converter-output level redundancy), and this redundancy increases proportionally with the number of levels. These extra degrees of freedom can be used for control purposes.

More recently, CHB multilevel converter with unequal dc source, also known as hybrid or asymmetric CHB converter has been introduced [39]–[42]. Basically, the power circuit is very similar to the MMCHB shown in Fig. 5.4, the difference is that the isolated dc sources have different values.

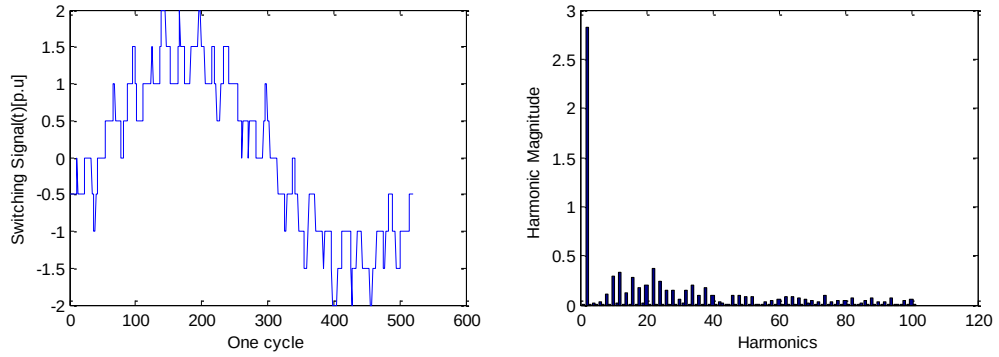

a b

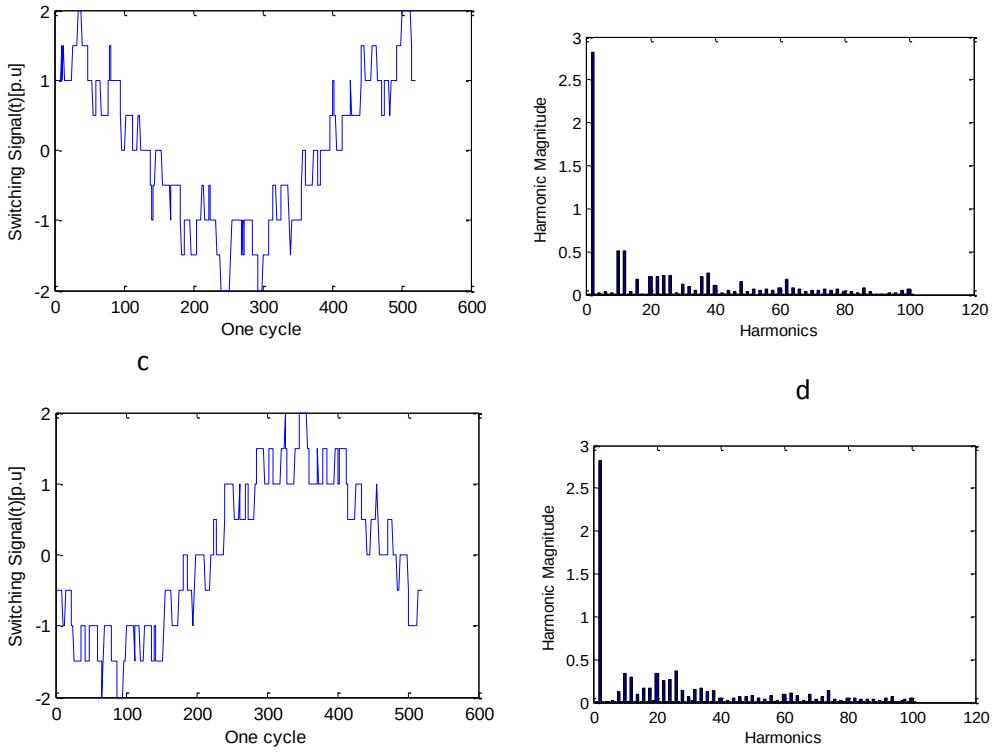

Figure 5.6 Five-level line-to-line Switching Function of a two VSC Unipolar PWM Converters Output voltage of phase a and phase b; (b) The amplitude of all harmonics for the output voltage of phase a and phase b; (c) Output voltage of phase b and phase c; (d) The amplitude of all harmonics for the output voltage of phase b and phase c; (e) Output voltage of phase c and phase a; (f) The amplitude of all harmonics for the output voltage of phase c

When choosing unequal dc sources, some switching-state redundancies are avoided, and more different output-voltage levels are generated with the same amount of power cells. This reduces the size and cost of the converter and improves reliability since few semiconductors and capacitors are employed. An additional advantage is that the converter can be controlled appropriately to reduce the switching losses, which is very important in high-power applications. The main drawback is the fact that the modularity of the converter is lost; since the different power ratings of the cells force special design for each power cell (even different power-device families could be needed). In addition, no input-current harmonic cancellation can be achieved like in the equally fed case, since the power asymmetry disables the multi-pulse rectifier and transformer function.

5.5. **Modulation Method and Simulations Results**

Phase-shifted PWM (PS-PWM) is the natural PWM method for CHB [43], mainly due to the modularity of this topology. Each cell is modulated independently using unipolar PWM with the same reference signal. A phase shift is introduced across all the carrier signals of each SM in order to produce the stepped multilevel waveform. The lowest output-voltage distortion is achieved with $180^{o}/n$ phase shifts between the carriers, for a *k*-SM converter. This operating principle is shown for a three SM seven level in Fig. 5.7. Note how the converter-output voltage has *k* times the fundamental component of each SM. In addition, the frequency of the converter-output-voltage switching pattern is *k* times the SM switching frequency, since the phase shift introduces a multiplicative effect. This is very useful, since the device switching frequency (hence, the switching losses) is *k* times lower than the apparent switching frequency perceived by the load. This means that, for the same output switching frequency, phase-shifted produces *k* times less switching losses as compared to level-shifted. However, level-shifted leads to less distorted line voltages since all the carriers are in phase [44].

Since all the SMs are controlled with the same reference and the same carrier frequency, the power is evenly distributed among the SMs, achieving input-current harmonic reduction owing to the multi-pulse transformer–rectifier system [43].

For low-switching-frequency applications, the staircase modulation is used. The basic idea of this technique is to connect each SM of the converter at specific angles to generate the multilevel output waveform, producing only a minimum of necessary commutations [44].

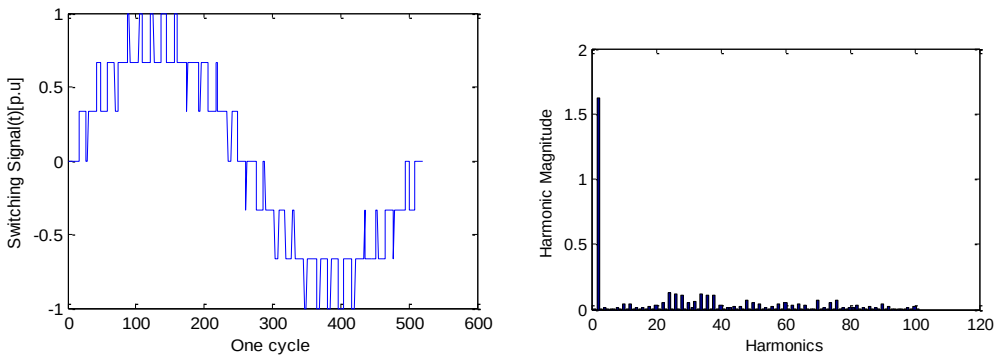

a b

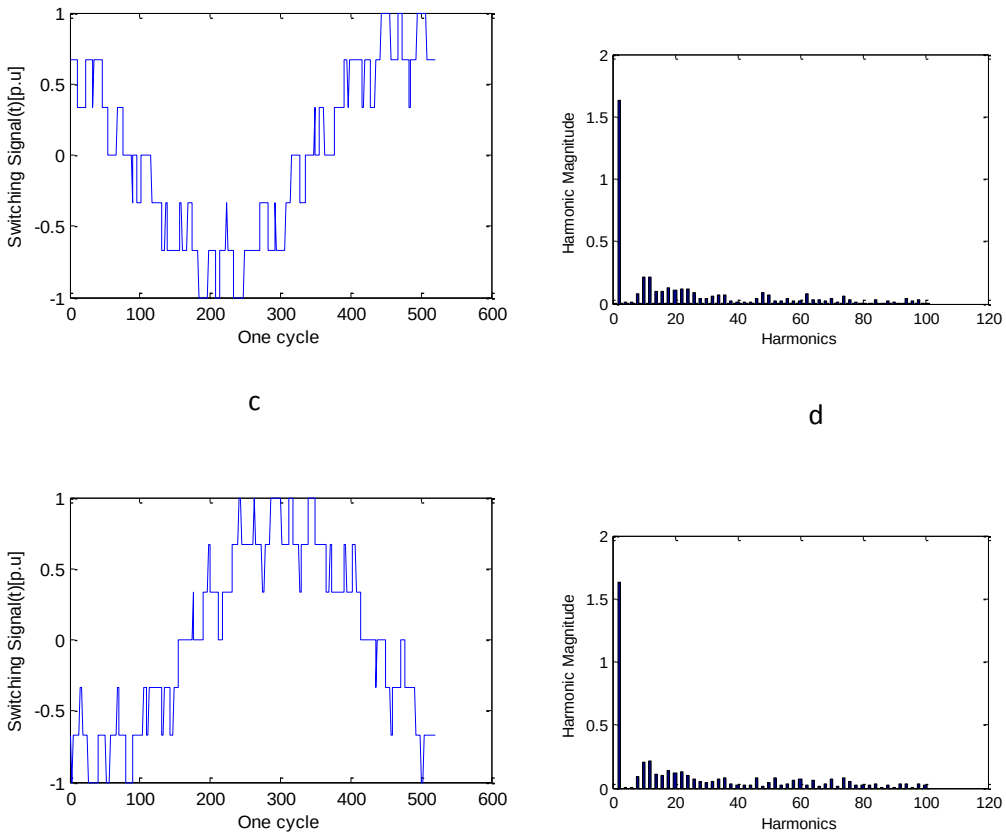

Figure 5.7 Seven-level Phase Switching Function of a three VSC Unipolar PWM Converters Output voltage of phase a and phase b; (b) The amplitude of all harmonics for the output voltage of phase a and phase b; (c) Output voltage of phase b and phase c; (d) The amplitude of all harmonics for the output voltage of phase b and phase c; (e) Output voltage of phase c and phase a; (f) The amplitude of all harmonics for the output voltage of phase c and phase a

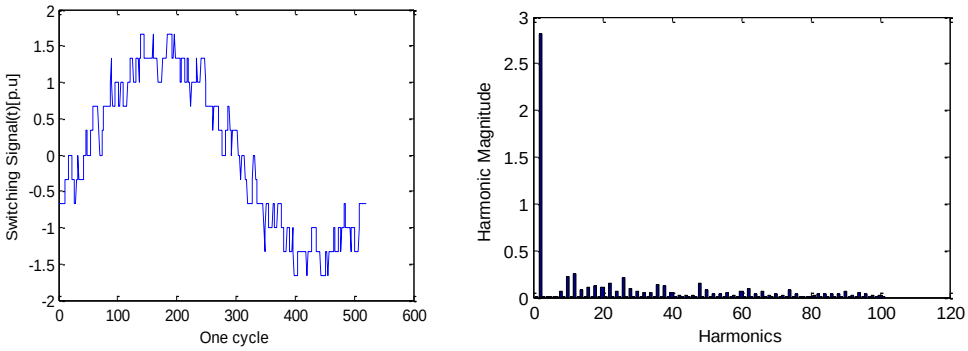

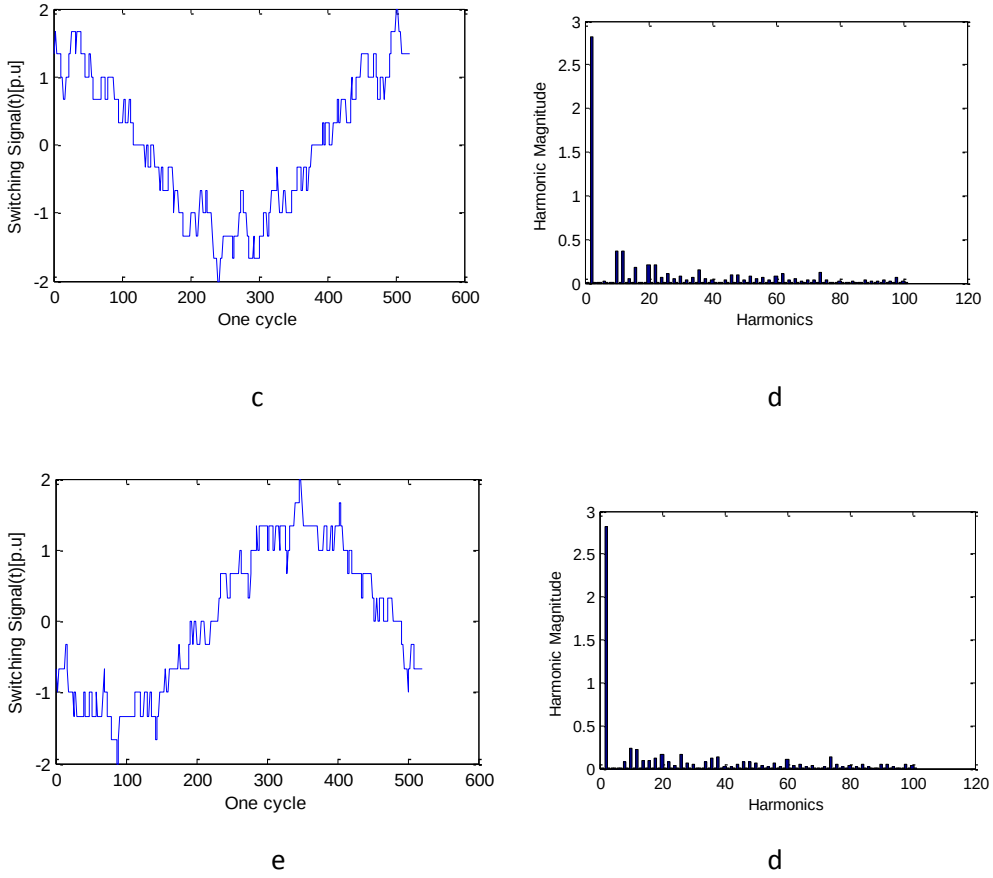

Figure 5.8 Seven-level line-to-line Switching Function of a three VSC Unipolar PWM Converters. Output voltage of phase a and phase b; (b) The amplitude of all harmonics for the output voltage of phase a and phase b; (c) Output voltage of phase b and phase c; (d) The amplitude of all harmonics for the output voltage of phase b and phase c; (e) Output voltage of phase c and phase a; (f) The amplitude of all harmonics for the output voltage of phase c

The operating principle is shown in Fig. 5.6 and Fig. 5.7; note that only one angle needs to be determined per power cell. These angles can be computed using the same principles of selective harmonic elimination (SHE). The output voltage, for the n-level case shown can be expressed in Fourier series as

$$v_{AN} = \frac{4V_{dc}}{\pi}\sum_{n=1}^{\infty}\frac{1}{n}\times\left\{\cos(n\alpha_1)+\cos(n\alpha_2)+\cos(n\alpha_3)\right\}\sin(n\omega t) \qquad (5.38)$$

where

n = 3, 5, 7, 9,...

n is uneven, and $0 \le \alpha 3 < \alpha 2 < \alpha 1 \le \pi/2$.

The three coefficients of the Fourier series (5.38) can be forced to a desired value; naturally, the first coefficient corresponds to the fundamental component and is set to the desired modulation index while, usually, the fifth and seventh coefficient are set to zero to eliminate 5th and 7th harmonics as follows

$$\begin{aligned} M\frac{\pi}{4} &= \cos(\alpha_1)+\cos(\alpha_2)+\cos(\alpha_3) \\ 0 &= \cos(5\alpha_1)+\cos(5\alpha_2)+\cos(5\alpha_3) \\ 0 &= \cos(7\alpha_1)+\cos(7\alpha_2)+\cos(7\alpha_3) \end{aligned} \tag{5.39}$$

where

$M = \frac{v_{AN}}{kV_{dc}}$ is the modulation index, defined by the desired peak amplitude for the fundamental component of the output voltage (v_{AN}) and

k = 1,2,3,... is the number of SM cells

The main advantage of MMCHB, is that the converter switches very few times per cycle, reducing the switching losses to a minimum. In addition, there is a reduction in all harmonics as the number of SM cells increases, therefore facilitating the output-filter design.

The hybrid modulation is particularly conceived for the MMCHB with unequal dc sources. The basic idea is to take advantage of the different power ratings among the cells to reduce switching losses and improve the converter efficiency. For example, from Fig. 5.9 and Fig. 5.10, it is shown that the high-power cell will turn on and off only one time during a half reference cycle. The un-modulated part left by the square shape of the high-power cell output is then generated by the next power cell and so on, until the final un-modulated parts of the reference are modulated at high switching frequency (with unipolar sinusoidal PWM) by the smallest power cell. This completes the generation of a multilevel stepped waveform with a high-frequency component (similar to multicarrier based PWM) but with the difference that fewer switching losses are produced to achieve it.

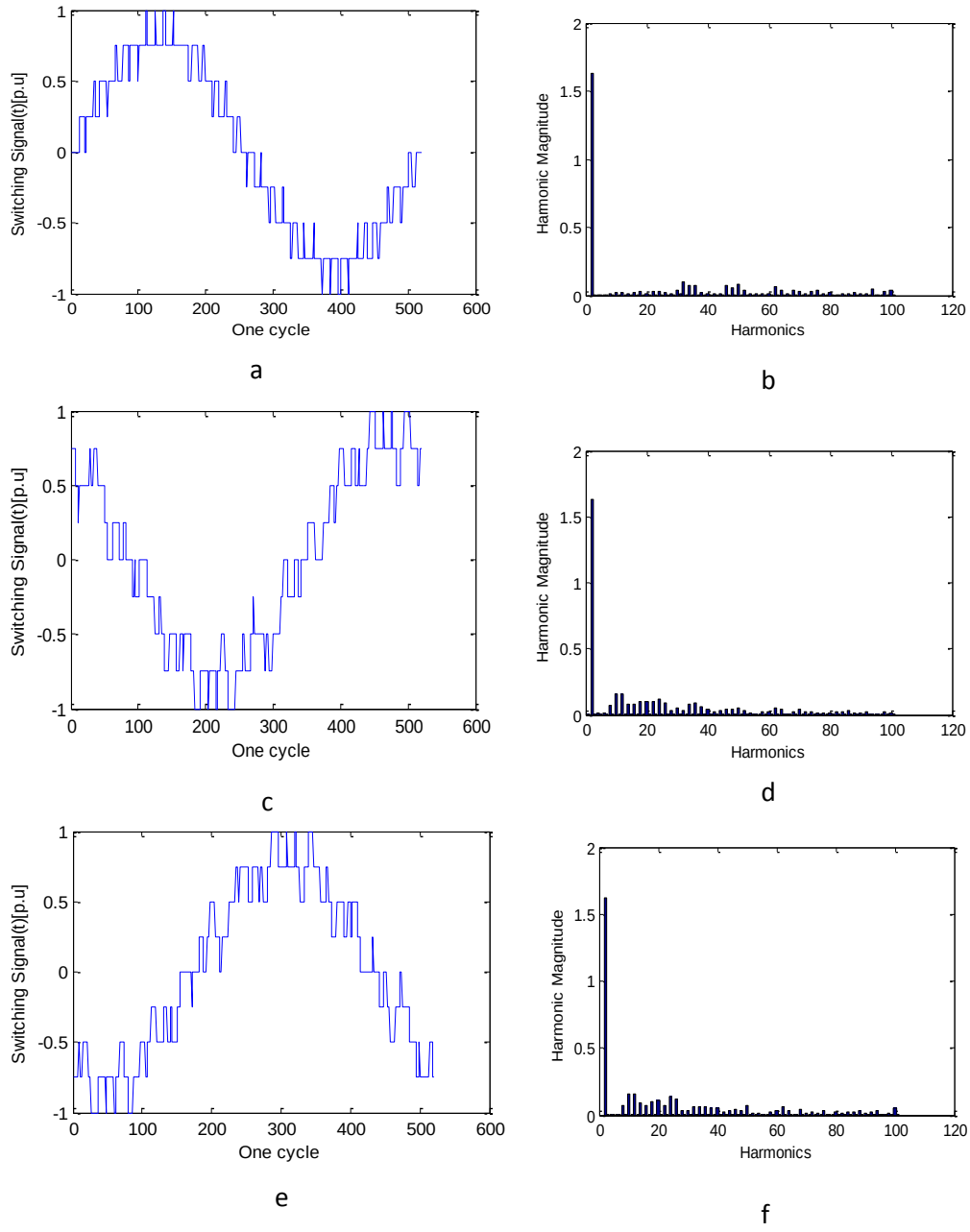

Figure 5.9 Nine-level Phase Switching Function of a fourVSC Unipolar PWM Converters. Output voltage of phase a and phase b; (b) The amplitude of all harmonics for the output voltage of phase a and phase b; (c) Output voltage of phase b and phase c; (d) The amplitude of all harmonics for the output voltage of phase b and phase c; (e) Output voltage of phase c and phase a; (f) The amplitude of all harmonics for the output voltage of phase c and phase a

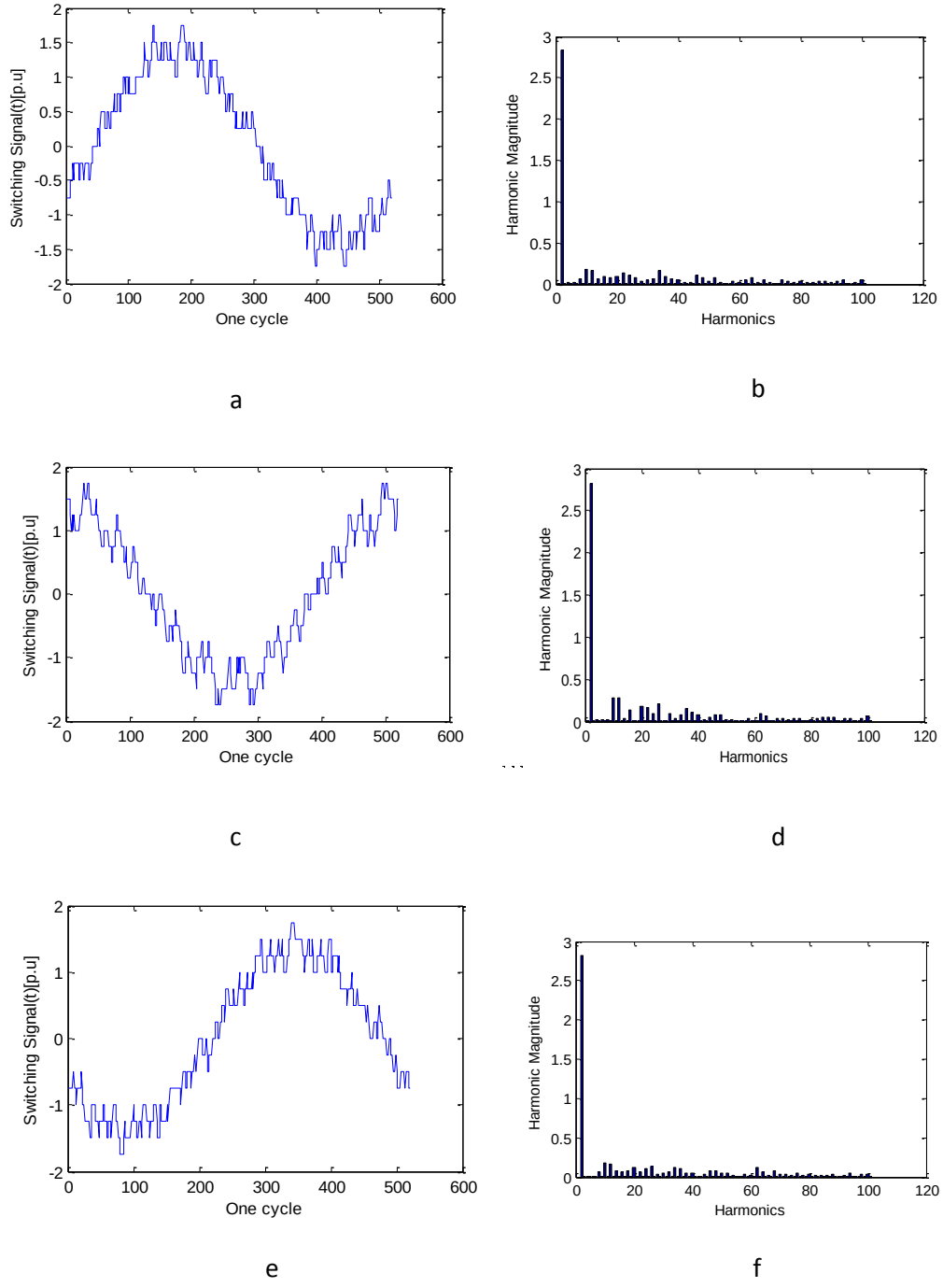

Figure 5.10 Nine-level line-to-line Switching Function of a four VSC Unipolar PWM Converters. Output voltage of phase a and phase b; (b) The amplitude of all harmonics for the output voltage of phase a and phase b; (c) Output voltage of phase b and phase c; (d) The amplitude of all harmonics for the output voltage of phase b and phase c; (e) Output voltage of phase c and phase a; (f) The amplitude of all harmonics for the output voltage of phase c

It should be noted that the high-voltage cell commutates when the reference reaches a specific voltage level $\pm h$n. This level needs to be selected in such a way that the un-modulated part can be generated by the lower power cells to avoid over-modulation. If we consider that the maximum amplitude that can be generated by the converter as shown in Fig. 5.9 and Fig. 5.10 are $V1 + V2 + V3 + V4$ 0 $-V1 -V2 -V3-V4$ the only possibility to avoid over-modulation is that the un-modulated part does not exceed the total voltage left for the low-power cells of the converter, i.e., $h4 = V1 + V2 + V3 + V4$. Hence, must be $h3 = V1 + V2 + V3$ for the third power cell with traditional unipolar PWM.

The distortion of the voltage waveforms, harmonic losses in the power converter and the load are due to the operation in the switching mode. These highlight the comparison of power qualities of the different output voltage levels with the PWM-unipolar control method. The simulations of individual frequency components to a voltage waveform are expressed in a harmonic voltage spectrum, which give more detailed harmonic description than the output voltage waveform as shown in Fig. 5.11 and Fig. 5.12. The simulations data are as follows: *h* = 100; % h is the number of harmonics to be calculated. *E* = 1.2; % E is the DC capacitor voltage. *C* = 10^-3; % C is the capacitor in the DC side, farads. *f* = 1000; % *f* is the frequency in Hz. w = 2*pi**f*; % angular frequency. *hr* = 5; % is the harmonic frequency of the carrier signal. *mf* = 5 ;% freq modulation index = triangular frequency (250)/sinusoidal frequency(50) . *ma* = 0.8; % ma is the voltage modulation index = sinusoidal amplitude/triangular amplitude. *nc* = 4; % Number of converter.

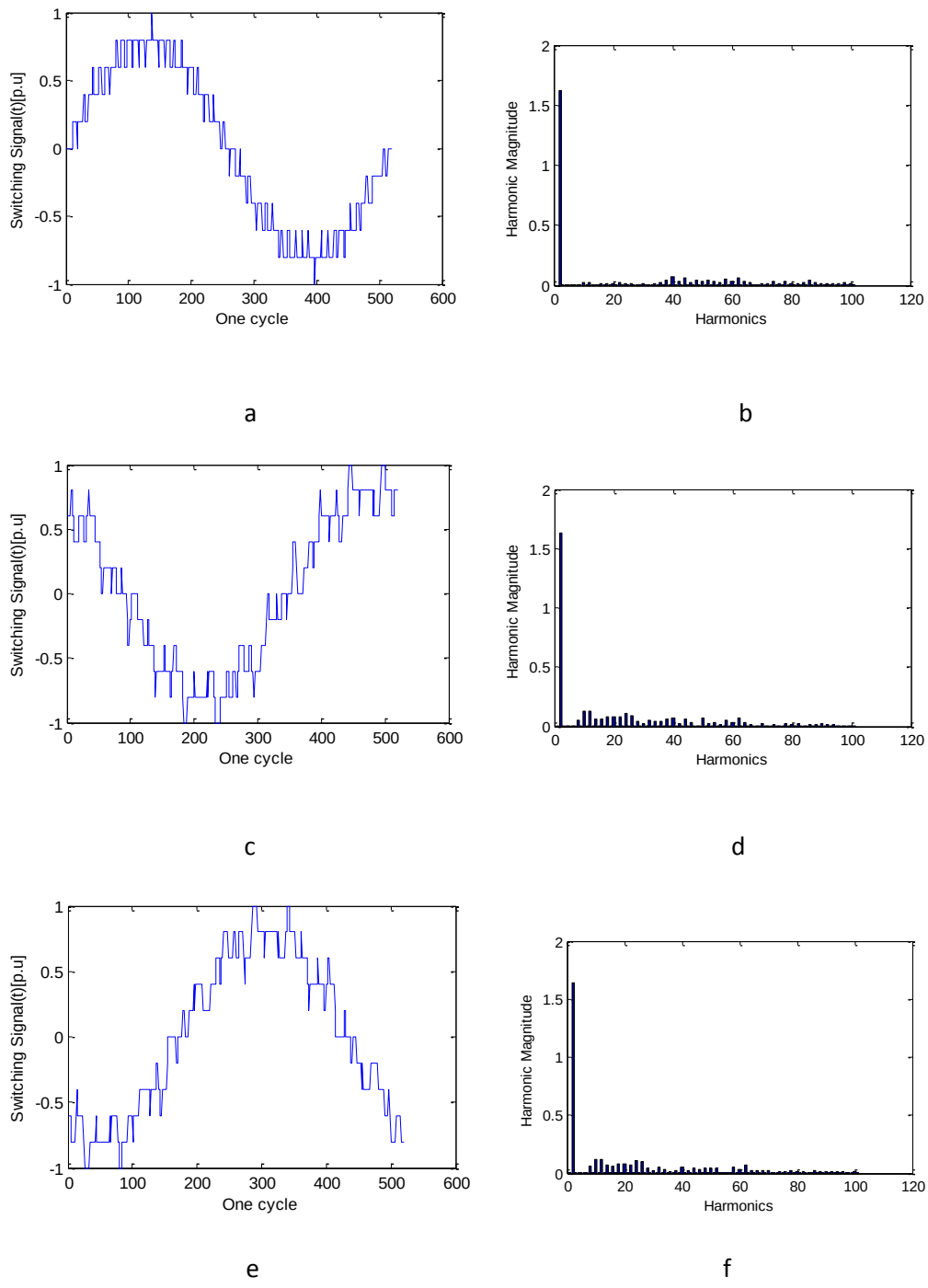

Figure 5.11. Eleven-level Phase Switching Function of a five VSC Unipolar PWM Converters Output voltage of phase a and phase b; (b) The amplitude of all harmonics for the output voltage of phase a and phase b; (c) Output voltage of phase b and phase c; (d) The amplitude of all harmonics for the output voltage of phase b and phase c; (e) Output voltage of phase c and phase a; (f) The amplitude of all harmonics for the output voltage of phase c and phase a

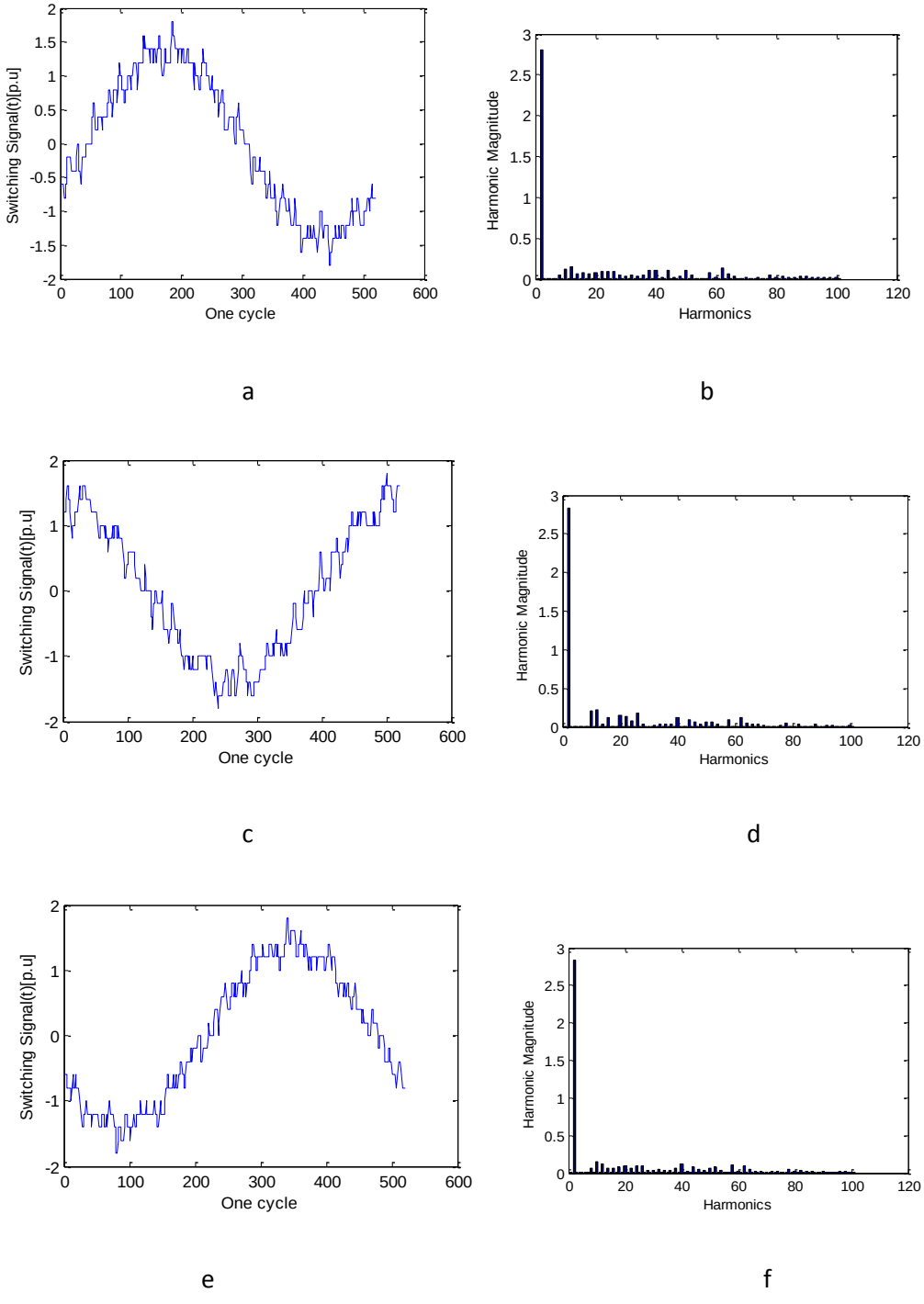

Figure 5.12. Eleven-level line-to-line Switching Function of a five VSC Unipolar PWM Converters Output voltage of phase a and phase b; (b) The amplitude of all harmonics for the output voltage of phase a and phase b; (c) Output voltage of phase b and phase c; (d) The amplitude of all harmonics for the output voltage of phase b and phase c; (e) Output voltage of phase c and phase a; (f) The amplitude of all harmonics for the output voltage of phase c

The number of output phase voltage levels in a cascade multilevel converter is then 2s +1, where s is the number of dc sources. Simulated phase voltage waveform for an 11-level cascaded multilevel converter with five separate dc sources SDSCs (s = 5) and five full bridges is shown in Fig. 5.18. The output phase voltage is given by

$$v_{an} = V1 + V2 + V3 + V4 + V5 \quad (5.40)$$

With enough levels and an appropriate switching algorithm, the multilevel converter results in an output voltage that is almost sinusoidal as shown in Fig. 5.12.

As observed the phase output voltage has better output power quality as shown in Fig. 5.11 comparable to the line-to-line output voltage waveform as shown in Fig. 5.12. By increasing number of the SM of the network reduces all harmonics to a minimum and also improves voltage profiles and reduces power system losses. Lower harmonic contents require a higher current flow for a given load. Increase in the line current results in a high voltage distortion at the converter output. With a reduction in the harmonic content, the voltage distortion is reduced.

When the converters are in operation they produce electromagnetic interference with harmonic content, thus reducing power quality. On this scenario, PWM-unipolar can be used to eliminate harmonic contents and permit additional submodules to be added to an existing facility and also, provide high power drives at electromagnetic interface to high voltage network. The achievement of power quality using PWM-unipolar control could become an important issue to transmission and distribution engineers.

The reduction in switching function losses vary from lower number of submodules to higher number submodules of the total PWM-unipolar converters. The financial benefit from switching loss reduction is enough to justify the MMC PWM-unipolar technique. The switching functions losses are proportional to the voltage and current output waveforms reduced harmonic distortion.

From the harmonic spectrum the harmonics occur as side bands of $2m_f$ and its integral multiple. As identified the frequencies of the harmonics are doubled, owing to the utilization of a unipolar switching scheme. This results in a reduction in the lower order

harmonics. This order of harmonics is as given by (5.29). It should be noted here that the fundamental component has a peak value equal to m_a times the source voltage.

In this type of converter, the only states that have no redundant configurations are the two states that generate the maximum positive and negative voltages, + $V_{DC}/2$ and – $V_{DC}/2$. For generating the other levels, IGBT-PWM is the possible switching configuration that keeps the capacitor voltages balanced. The switching sequence is controlled such that at each instant only SM_{an}s (i.e. half of the $2SM_{an}$s of a phase leg) are in the on-state. The upper arm SMs from SM_{a1} to SM_{an} are in the on-state, in the lower arm only SM_{a2} to SMan will be in on-state. It is clear that there are several possible switching configurations. Equal voltage sharing among the capacitor of each arm was achieved by unipolar algorithm of inserted SM_{an}s during each sampling period of the control system.

5.6. **Conclusions**

A new topology, modular multi-level converter using PWM-unipolar switching technique for harmonic reduction is developed. The output voltage waveforms of the IGBTs are controlled using a PWM-unipolar technique to achieve the minimum harmonic reduction.

The MMC is suitable for reducing wave power harmonic voltage to a minimum level, and has the capability for stabilization of the voltage and current in the high voltage oil and gas network exploration and production

The line-to-line voltage is able to synthesize more levels compared to the phase voltage, thus resembling a more desirable sinusoidal waveform. Besides that, the phase voltage yields better spectral performance, hence reducing the need of an output filter.

The number of output waveform levels is higher than the level of the converters, hence leads to output power quality improvement.

The switching functions, based on Complex Fourier Series, are used effectively to demonstrate the operation of the MMC. The optimum harmonic reductions of this developed model are proportional to the increase in the number of VSC sub-modules.

5.7. **References**

[1] J.S.Lai, and F.Z.Peng,"Multilevel Converters – A new breed of power converters", *IEEE Trans. Ind. Applicat., vol. 32, pp 509-517, May./June. 1996*

[2] J. Rodriguez, J.Sheng. Lai, F. Z. Peng, "Multilevel Inverters: A survey of topologies, controls, and applications", *IEEE Trans. Ind. Electr., vol. 49, pp 724-738, Aug. 2002*

[3] H. Akagi, "Classification, Terminology, and Application of the Modular MultilevelCascade Converter (MMCC)". *IEEE International Power Electronics Conference, 2010*.

[4] F.Z.Peng, J. W. McKeever, D. J. Adams,"Cascade Multilevel Inverters for Utility Applications." *IEEE Industrial Electronics, Control and Instrumentation Conference (IECON), 1997.*

[5] F.Z. Peng. J. S. Lai, "Dynamic Performance and Control of a Static Var Generator using Multilevel Inverters." *IEEE Transactions on Industrial Applications, vol. 33, May/June 1997*.

[6] L.M. Tolbert and F. Z. Peng, "Multilevel Converters as a Utility Interface for Renewable Energy Systems." *IEEE 2000.*

[7] S. Sirisukprasert, A.Q. Huang and J.S. Lai, " Modelling, Analysis and Control of Cascaded-Multilevel Converter-Based STATCOM". *IEEE 2003.*

[8] J. Rodriguez, J.-S. Lai, and F.Z. Peng, "Multilevel Inverters: A Survey of Topologies, Controls, and Applications." *IEEE Trans. Ind. Electronics, vol. 49, Aug. 2002*.

[9] Q. Tu, Z. Xu, H. Huang and J. Zhang, "Parameter Design Principle of the Arm Induction in Modular Multilevel Converter based HVDC". International Conference on Power System Technolgy, *2010 IEEE*.

[10] A.L.P. de Oliveira, C.E. Tiburcio, M.N. Lemes and D. Retzmann, "Prospects of Voltage-Sourced Converters (VSC) Application in Power Transmission Systems". *IEEE ANDESCON 2010.*

[11] A. Lesnicar and R. Marquardt, "An Innovative Modular Multilevel Converter Topology Suitable for a Wide Power Range". *PowerTech Conference. 2003 IEEE* .

[12] K.Li and C.Zhao, "New Technologies of Modular Multilevel Converter for VSC-HVDC Application". *2010 IEEE*.

[13] A. Rasic, U. Krebs and H. Leu, "Optimization of the Modular Multilevel Converters Performance using the Second Harmonic of the Module Current". URL: http://www.siemens.com

[14] X. Luo, G.F. Tang, K.P. Zha, Z.Y. He, and Y.N. Wu, "Study on the Design and Equivalence Test Methods of VSC-HVDC Valves". *International Conference on Power System Technolgy, 2010 IEEE.*

[15] J. Rodrigues, S. Bernet, B. Wu, J. O. Pontt and S. Kouro, " Multilevel Voltage-Source-Converter Topologies for Industrial Medium-Voltage Drives". *IEEE Transactions on Industrial Electronics, VOL. 54. 2007.*

[16] M. Saeedifard and R. Iravani, "Dynamic Performance of a Modular Multilevel Back-to-Back HVDC System". *IEEE Transactions on Power Delivery, VOL. 25. 2010*

[17] J.S. Lai, F. Z. Peng, "Multilevel Converter-A New Breed of Power Converter". *IEEE Transactions on Industrial Applications. Vol. 32. 1996.*

[18] C. Casablanca and J. Sun, "Interleaving and Harmonic Cancellation Effects in Modular Three-Phase Voltage-Sourced Converters". *IEEE COMPEL Workshop, July 16-19, 2006.*

[19] U.N.Gnanarathna, S.K.Chaudhary, A.M. Gole, and R. Teodrescu." Modular Multi-level Converter Based HVDC System for Grid Connection of Offshore Wind Power Plant".

[20] G.Carrara, S. Gardella and M. Marchesoni,"A New Multilevel PWM Method: A Theoretical Analysis". *IEEE Transactions on Power Electronics, VOL. 3. July 1992.*

[21] M. Calais, V.G. Agelidis and M. Meinhardt, "Multilevel Conveters for Single-Phase Grid Connected Photovoltaic Systems: An Overview". Solar Energy vol. 66, 1999.

[22] J.Kim, S. Sul, "A Carrier-Based PWM Method for Three-Phase Four-Leg Voltage Source Converter". *IEEE* Transactions on Power Electronics, VOL. 19. January 2004.

[23] O. A. Sadaba, P. S. Girpide, J. L. Taberna, I. M. Morales, and L. M. Palomo, "Voltage harmonics generated by 3-level converters using PWM natural sampling," in *Proc. IEEE Power Electronics Specialist Conf. (PESC)*, Jun. 2001, vol. 2, pp. 1561–1565.

[24] J. Hamman and F. S. Van Der Merwe, "Voltage harmonics generated by voltage-fed inverters using PWM natural sampling," *IEEE Trans. Power Electron.*, vol. 3, no. 3, pp. 297–302, Jul. 1988.

[25] R.Ghosh and G.Narayanan, "Control of Three-Phase, Four-Wire PWM Rectifier", *IEEE Transactions on Power Electronics*, vol. 23, No. 1, January 2008

[26] P.H.Zope,P.G.Bhangale, P.Sonare and S.R.Suralkar,"Design and Implementation of carrier based Sinusoidal PWM Inverter", *International Journal of Advanced Research in Electrical, Electronics and Instrumentation Engineering, Vol. 1, Issue 4, October 2012.*

[27] B.Ismail,"Development of a Single Phase SPWM Microcontroler -Based Inverter, *First International Power and Energy Conference PEC pp. 437. Putra jaya, Malaysia: IEEE, November 2006.*

[28] R. Teichmann and S. Bernet, "A comparison of three-level converters versus two-level converters for low-voltage drives, traction, and utility applications," *IEEE Trans. Ind. Appl., vol. 41, pp. 855–865, May–June 2005.*

[29] D. M. Mohan, B. Singh and B. K. Panigrahi, "A Two-Level, 48-Pulse Voltage Source Converter for HVDC Systems", Fifteenth National Power Systems Conference (NPSC), IIT Bombay, December 2008.

[30] P.W. Lehn, "Direct Harmonic Analysis of the Voltage Source Converter", *IEEE Transactions on Power Delivery, Vol. 18, No. 3, July 2003*

[31] M.Madrigal and E. Acha, "Modelling of custom power equipment using harmonic domain techniques," vol. 1, pp. 264–269, 2000.

[32] P. Lehn, "Exact Modelling of the Voltage Source Converter," *IEEE Trans.Power Delivery, vol. 17, pp. 217–222, Jan. 2002.*

[33] H. Visser and P. van den Bosch, "Modelling of periodically switched networks," in *IEEE Power Electron. Specialists Conf.*, 1991, pp. 67–73.

[34] E. Acha and M. Madrigal, "Harmonic Modelling of Voltage Source Converters for HVDC Station". AC-DC Power Transmission, Conference Publication. *IEE 2001.*

[35] J.Rodriguez, S.L a i j and F.Z. Peng, "Multilevel inverters: a survey of topologies, controls, and applications", *IEEE Trans.Ind. Electron.*, 49 (2002), No. 4, 724-738

[36] Z. F. Peng, "A Generalized Multilevel Inverter Topology with Self Voltage Balancing", Oak Ridge National Laboratory, Oak Ridge, Tennessee 37831-8038

[37] J. Rodríguez, J. Dixon, J. Espinoza, J. Pontt, and P. Lezana, "PWM regenerative rectifiers: State of the art," *IEEE Trans. Ind. Electron.*, vol. 52, no. 1, pp. 5–22, Feb. 2005.

[38] P. Lezana, C. A. Silva, J. Rodriguez, and M. A. Perez, "Zero-steadystate-error input-current controller for regenerative multilevel converters based on single-phase cells," *IEEE Trans. Ind. Electron.*, vol. 54, no. 2, pp. 733–740, Apr. 2007.

[39] O. M. Mueller and J. N. Park, "Quasi-linear IGBT inverter topologies," in *Proc. APEC*, Feb. 1994, pp. 253–259.

[40] S. Mariethoz and A. Rufer, "Design and control of asymmetrical multi-level inverters," in *Proc. IECON*, Sevilla, Spain, Nov. 2002, pp. 840–845.

[41] C. Rech and J. R. Pinheiro, "Line current harmonics reduction in multipulse connection of asymmetrically loaded rectifiers," *IEEE Trans. Ind. Electron.*, vol. 52, no. 3, pp. 640–652, Jun. 2005.

[42] C. Rech and J. R. Pinheiro, "Hybrid multilevel converters: Unified analysis and design considerations," *IEEE Trans. Ind. Electron.*, vol. 54, no. 2, pp. 1092–1104, Apr. 2007.

[43] P. Hammond, "A new approach to enhance power quality for medium voltage AC drives," *IEEE Trans. Ind. Appl.*, vol. 33, no. 1, pp. 202–208, Jan./Feb. 1997.

[44] D.G. Holmes and T. Lipo,"PulseWidth Modulation for Power Converters: Principles and Practice". *Piscataway, NJ: IEEE Press, 2003.*

[45] B. Wu, "High-Power Converters and AC Drives". *Piscataway, NJ: IEEE Press, 2006*

Chapter 6

6. Harmonic Analysis of Wind Energy Generator with Voltage Source Converter Based HVDC Powering Oil and Gas Operations

6.1. Introduction

Harmonics are one of the main concerns as the number of grid connected wind power farms (WPF) increases, the results possibly causing harmful effects on the oil and gas network [1-2]. Integration of a large number of power electronics equipment such as VSCs, static var compensators (SVC), variable frequency drive (VFD) contribute to the emission of harmonics [3-4]. Since each WPF comprises of a great number of both inductive sources and capacitive elements coming from large capacities of wind turbines, induction generators, induction motors, transmission lines such as long underground/subsea cables, reactive power compensation equipment and other passive elements in the network, the need of resonance analysis is essential [5]. These impedances may resonate near a harmonic frequency. This resonance can aggravate the harmonic voltage or current [6]. Basically, a resonance will cause an increase of voltage distortion due to parallel resonance or result in high harmonic current due to series resonance at the resonance frequency.

The resonance analysis in this chapter studies the impact of several conditions in WPF mainly using the impedance scan in MATLAB, including the impact of capacitor bank, VFD, active filters and SVC in the network. The harmonic current that flow through SVC is expected to be purely reactive. Thus, the determination of harmonic voltage developed across the fundamental frequency impedance (Z_h) by harmonic current (I_h) is of paramount important in harmonic studies. The expected result paves way for the application of total harmonic voltage distortion (THD_V), which is helpful to determine whether any generality can be achieved.

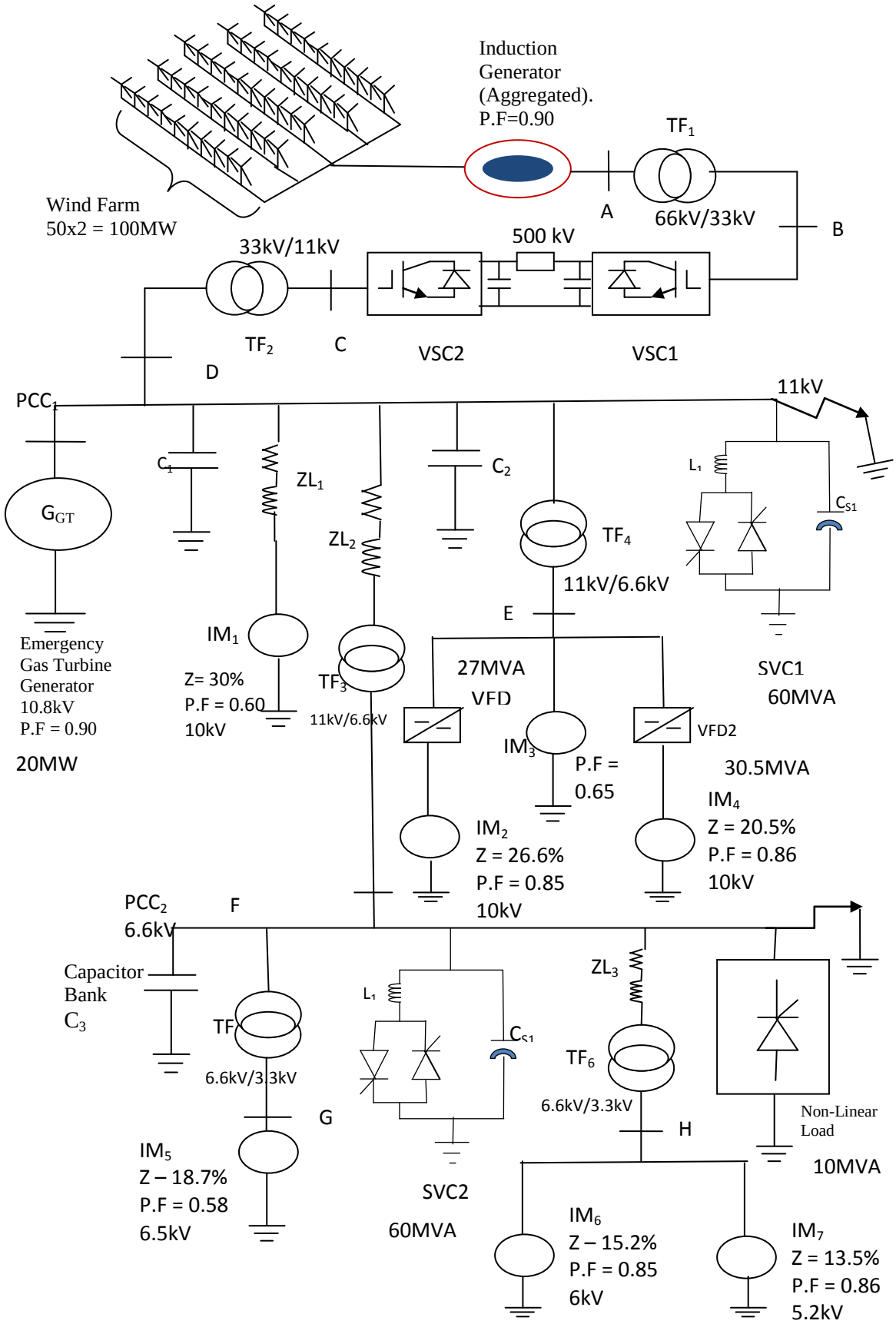

Figure 6.1. Schematic of Wind Farm Fed Oil Platform

The harmonic analysis in this chapter will be performed on a 100 MW aggregated WPF model as depicted in Fig. 6.1, it is based on an offshore WPF. The entire component parameters are modelled as impedance equivalent at 66 kV-base. The turbines of the wind power plant are modelled as five aggregated turbines (10 turbines each), where each one of them representing a power of 2 MW. The wind turbines are modelled as ideal harmonic current sources which implement VSC topology [7].

Each wind turbine is connected to an induction generator through two winding transformers. The 2MW from the wind turbine passes into the generator through its shaft. Operating wind turbines with fixed speed induction generators that are very reliable, rugged, and low cost, requires reactive power from the grid at all times. Thus, there is need to compensate reactive power locally at the wind turbine and at the point of common coupling where the wind farm interfaces with the oil and gas platforms. The generator stator windings are connected through excitation capacitor, which provide reactive power to the three-phase power network. Being a squirrel-cage rotor generator, the stator connection also provides the route by which generated power is transferred into the network and is called self excited induction generator (SEIG) [7-8].
A self-excited induction generator with its stator connected to the utility grid through a 100 km long 500kV back-to-back VSC-HVDC is as represented in Fig. 6.1. The main advantage of this system lies in the simple and robust structure of the squirrel-cage induction generator.

The output power of the SEIG is rectified using the VSC rectifier and the dc power is transferred to the load through a VSC inverter [7]. The requirement for smoothing series inductor and passive filters are unnecessary, since both VSC rectifier and inverter act as an active filter and can reduce the voltage ripple within the required limits. The active power filter solution injects harmonic and reactive current to limit the harmonic distortion, and improves the displacement power factor for electrical distribution systems. It measures the entire load current, removes the fundamental frequency component, and injects the inverse of the remaining waveform for nearly complete cancellation of harmonic current. The filter is not focused on specific frequencies; rather it creates the required waveform based upon the input of its sensing circuitry by monitoring the load through current transformers mounted on the AC side [9-10].
All the cables are modelled as nominal π-models. The transformers have YNdd-configuration that eliminates the zero sequence harmonics. The single output harmonic

mitigating isolation transformer is modelled as inductances to reduce the voltage distortion created by the 3rd and other triplen harmonic currents. That is, 3rd, 9th and 15th harmonics and other zero sequence currents shall be treated within the secondary windings through cancellation of the zero sequence fluxes. For 5th, 7th, 11th, 17th and 19th harmonics, provided an appropriate phase shift transformer is in place, these harmonics can be cancelled with those of other loads fed from the same primary supply.

When determining the harmonic impedances of an oil and gas field network, or performing harmonic penetration studies from a given harmonic current injections, the transformers are rarely represented as harmonic sources, i.e. their inherent magnetisation non-linearity is ignored on the assumption that the transformers have been designed to operate within the linear region of the magnetising characteristics [11-12]. Such an assumption may have been reasonable in earlier less competitive times. Recent transformer designs tend to operate very close to the limit of the linear characteristics and, even under small over-excitation; their contribution to the harmonic content cannot be ignored [13].

In the event of determining the network harmonic admittances the transformers and induction generators may be modelled as series impedances (i.e. series combination of resistance and inductive). In such a case, a frequency dependent multiplying factor can be required at the reactance sides to account for skin effect [6].

Induction motors constitute 50% of the platform loads, some are driven by variable frequency drive (VFD). The motor is modelled as series impedances, with the magnetizing impedance ignored. This motor type is selected due to its simple maintenance and robustness to industrial operations. Since the motor is supplied from a source of harmonic voltages the impedance elements in the circuit need to be modified to account for the frequency of each harmonic that is present. The triplen harmonics can be ignored because the motor has a star-wound stator winding, therefore only non-triplen harmonics are considered [14-16].

The network analysis of Fig. 6.1 can be performed using the per unit (p.u) method. This technique is selected because it is a strong tool for systems studies where several different voltage levels exist. The impedances of the electric apparatus are usually given

in p.u or %. In this study, the base voltage is taken as the nominal system voltage, which is the voltage rating of the induction generator in kVA [17].

6.2. **Offshore Operation of Wind Turbine Feeding Oil Platform**

A hypothetical configuration of a schematic diagram of wind turbine feeding oil platform is as shown in Fig. 6.1. It consists of a wind farm connected to an oil platform through a PWM VSC-HVDC. The electric energy on oil platforms is weaker comparable to onshore grid; as such wind power integration could contribute to a more stable operation on the platform. The main motivation of modelling the dynamics of this system is to obtain a harmonic behaviour that fulfils a set of given requirements.

The wind farm extracts kinetic energy from the wind and converts it to electrical energy. First is the interaction between the wind and the rotor blades. This requires an aerodynamic model of the blades, follow by the process of converting the mechanical energy to electrical. This is performed through the generator. The generator is connected to a point-to-point/back-to-back voltage source converter, and the control strategies are developed based on maximum power extraction. The oil platform consists of a wind farm with a gas turbine. The gas turbine generator has to provide the load power when the wind speed is low, and it also compensates for the variable power output in the wind.

6.2.1. Wind Turbine Model

The variable speed wind turbine model is based on the steady-state power characteristics. Investigating the behaviour of the wind turbine required the torque that it exerts on the mechanical shaft that must be verified. This torque is as define in (6.1)

$$T_{turbine} = \frac{P_m}{\omega_w} \tag{6.1}$$

where P_w is the output power of the turbine (mechanical power extracted from the wind) given by the following:

$$P_m = \frac{1}{2}\rho\pi R^2 v^3 C_p(\theta, \lambda) \tag{6.2}$$

Where P_m is the mechanical output power of the wind turbine (Watt), ρ is the Air density (Kg/m3) = 1.29kg/m^3, R is the blade radius (m) , Cp is the power coefficient of the wind turbine and υ is the wind speed (m/second). Consequently, the output energy is determined by the power coefficient (C_p) of wind turbine if the swept area, air density, and wind speed are assumed to be constant. λ is the tip speed ratio (the rotor blade tip speed to wind speed). C_p is function in tip speed ratio (λ) and pitch angle (θ) in degree. If θ is equal zero, in this case C_p is only function in λ as shown in (6.2), and λ is function of rotor mechanical speed, rotor radius of blade and wind speed as indicated in (6.4).

Mechanical speed of the turbine ω_w (rad/sec) is define as

$$\omega_w = \frac{\lambda v}{R} \tag{6.3}$$

The power coefficient C_p characteristics of different values of the pitch angle θ are illustrated Fig. 6.2 below. It should be note here that the maximum value of the performance coefficient C_p ($C_{p\text{-}max}$ = 0.48) is achieved for blade pitch angle θ = 0^o and for a tip-speed ratio value $\lambda_{\max}$ = 8.0. This value is defined as the nominal value. The power coefficient expression, based on the modelling wind turbine characteristics is obtained using a generic equation given by

$$C_{p(\lambda,\theta)} = c_1\left(\frac{c_2}{\lambda_1} - c_3\theta - c_4\theta^{2.14} - c_5\right)e^{\frac{-c_6}{\lambda_1}} \tag{6.4}$$

where

$$\frac{1}{\lambda_1} = \frac{1}{\lambda - 0.02\theta} - \frac{0.003}{\theta^3 - 1}$$

The theoretical limit for C_P is 0.59 according to Betz's Law, but its practical range of variation is 0.2-0.5. [18-21]

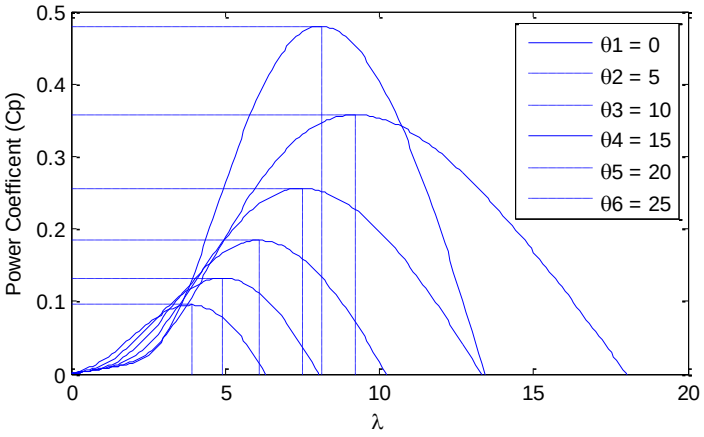

Figure 6.2. Wind generator power curves at various wind speed

Figure 6.2 indicates the mechanical power generated by the turbine as a function of rotor speeds for different wind speeds. The maximum power extraction within the allowable range can be achieved if the controller can properly follow the optimum curve with variation of wind speed. The generator side converter (a single switch three phase mode rectifier) is controlled to extract maximum power from available wind turbine power. Hence, the wind turbine can produce maximum power when the turbine operates at an optimum value of C_p (C_p-opt). So it is necessary to adjust the rotor speed at optimum value of the tip speed ratio (λ_{opt}).

The wind turbine power curves for various wind speeds can be obtained as

$$P_{\max} = k\omega_w^3 \tag{6.5}$$

where

$$k = \frac{1}{2}\rho\pi R^5 \frac{C_{P-\max}}{\lambda_{\max}^3}$$

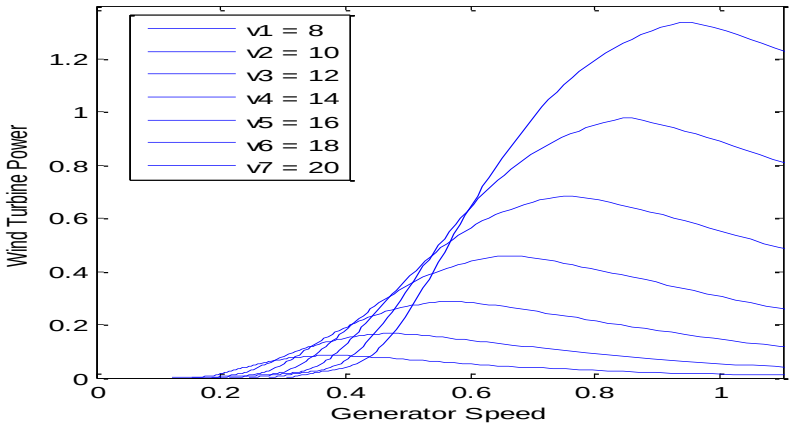

Figure 6.3. Wind turbine rotor mechanical power

Thus knowing the wind speed, the angular speed of the wind turbine and the blade pitch angle, then the wind turbine rotor mechanical power can be easily computed as shown in Fig. 6.3.

Therefore, wind turbine data can be represented as follows:

Number of blades = 3

Blade radius (m) = 24

Nominal rotational speed N_m = 25 rpm

Air density (kg/m^3) = 1.29kg/m^3

Optimal lambda (λ) = 8.0

Performance coefficient C_p = 0.48

Selecting the operating speed of the generator and controlling it with changing wind speed must be determined early in the system design. This is important, as it determines all major components and their ratings. The alternative strategies and the corresponding speed control methods fall in the following categories. That is fixed-speed drive and variable-speed using power electronics.

The fixed-speed operation of the generator naturally fits well with the induction generator, which is inherently a fixed-speed machine. But, the turbine speed is generally low, while the electrical generator works effectively at high speed. Thus, the equal speed between the two is obtained through a mechanical gearbox. The gearbox decreases the speed and increases the torque, thereby improving the rotor power coefficient C_P.

The major disadvantage of fixed-speed is that it almost never captures the wind energy at the peak efficiency in terms of the rotor power coefficient C_P. The wind energy is wasted when the wind speed is higher or lower than the certain value selected as the optimum. The two-speed machine increases the energy capture, reduces the electrical loss in the rotor and reduces the gear noise. The speed is change by changing the gear ratio. A gear ratio is the relationship between the numbers of teeth on two or more gears that are meshed [22]. The turbine torque varies with the gear ratio and the turbine wind velocity as depicts in Fig. 6.4.

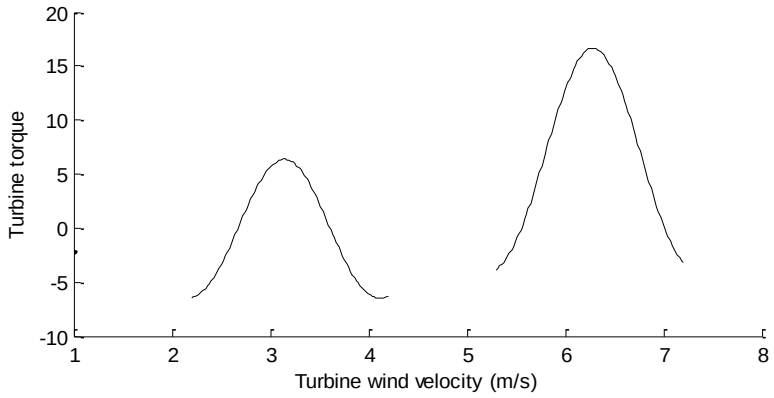

Figure 6.4 speed characteristic of wind turbine with low and high gear ratios.

The system is operated on the low-gear ratio for wind speed below 4 m/s and on the high-gear ratio for wind speed above 4 m/s. The gear ratio is changed at 4 m/s, the generator however operates with only one-speed ratio of 100:1. Self-excitation can occur in a fixed-speed wind turbine equipped with an induction generator. Fixed capacitors supplies reactive power compensation in a fixed-speed wind turbine. Induction generators alone cannot self excite. It requires reactive power from the grid to operate normally. The grid dictates the voltage and frequency of the induction generator.

When the generator reaches its rated power, the turbines must limit the magnitude of mechanical power delivered to the generator. As shown in Fig. 6.4, the generator reaches its rated power at wind speeds of 3 m/s to 6 m/s, and thus, must decrease in energy collection at higher wind speeds. This energy collection control is achieved by either stall, pitch, or a combination of them both, called active stall. There are no moving parts in stall-controlled blades, and the challenge in this control technique is proper blade construction to avoid vibration and permit a gradual stalling. The pitch

function provides full control over the mechanical power. The pitch angle is controlled to keep the generator at the rated power by reducing the angle of the blades. By actuating the blade angle to be at the limit of the stalling, fast torque changes in the wind speed can be tolerated [23-24].

6.3. Induction Generator Modelling for Offshore Wind Turbine

The invention of induction generators completed the ac system of electrical power production, transmission, and utilization. Induction generators require no electrical connection to the rotor windings. Instead, the rotor winding are short-circuited. The magnetic flux flowing across the air gap links these closed rotor circuits.

The stator of the induction generators (IGs) is made of numerous coils with three phases, and is supplied with three phase current. The three coils are physically distributed around the stator area with out of time-phase currents, which produces a rotating magnetic field. Induction generators are asynchronous speed machines, operating speed is slightly less than synchronous speed in the motor mode and slightly greater than synchronous speed in the generator mode. Induction machines are sometimes operated in the motor mode, so they are usually called induction motors [25-26].

Induction generators have relatively advantageous features over conventional synchronous generators. These features are brushless and rugged construction, low cost, maintenance and operational simplicity, self-protection against faults, and good dynamic response. Induction generators have the capability of generating power at varying speed; this facilitates the induction generator operation in a stand-alone or isolated mode to supply remote areas where grid extension is not economically viable, in conjunction with the synchronous generator to fulfil the increased local power demand of the grid by integrating power from resources located at different sites. The disadvantage found in induction generator is the reactive power requirement. The reactive power can be supplied from the grid and capacitor compensator [27-34].

6.3.1. SEIG with External Capacitor

Since the excitation current is mainly reactive, a stand-alone system is self-excited by shunt capacitors. In grid-connected operation, it draws excitation power from the

network, and its output frequency and voltage values are dictated by the grid. Where the grid capacity of supplying the reactive power is limited, local capacitors can be used to partly supply the needed reactive power [35-40].

Self-excited induction generator (SEIG) works in the saturation region and it has excitation capacitors connected across its stator terminals as shown in Fig. 6.5. These generators are an ideal choice for electricity generation in stand-alone variable speed wind energy systems, where reactive power from the grid is not available. The induction generator will self-excite, using the external capacitor, only if the rotor has an adequate remnant magnetic field. In the self-excited mode, the generator output frequency and voltage are affected by the speed, the load, and the capacitance value in Farads [41-42].

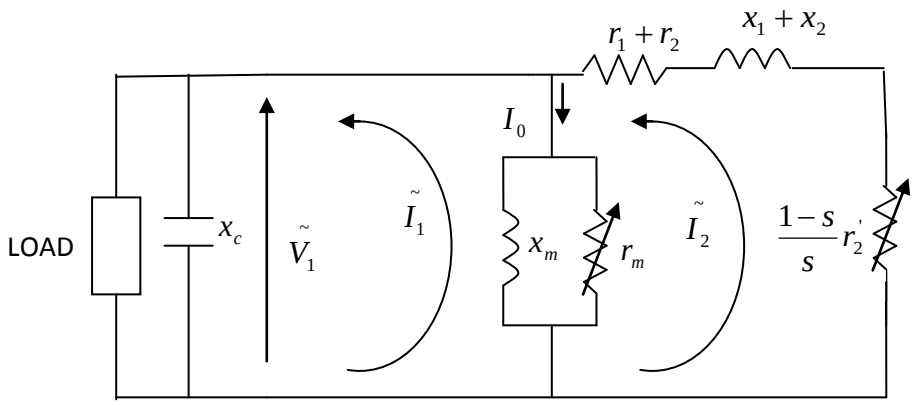

Figure 6.5. Self-excited induction generator with external capacitor.

Steady-state analysis of induction generators is of interest both from the design and operational points of view. Knowing the parameters of the machine, it is possible to determine the performance of the machine at a given speed, capacitance and load conditions.

Loop impedance and nodal admittance methods used for the analysis of SEIG are both based on per phase steady-state equivalent circuit of the induction machine as represented in Fig. 6.5, modified for the self-excitation case. This structure is very effective in calculating the minimum value of capacitance needed for guaranteeing self-excitation of the induction generator. For stable operation, the excitation capacitance must be slightly higher than the minimum value. Also there is a speed threshold, below which no excitation is possible, i.e.
the cutoff speed of the machine [43-45].

The mutual inductance (X_M) is related to the voltage $\left(\frac{V_g}{F}\right)$ across it by the following equation

$$X_M = \frac{\left(K_1 - \frac{V_g}{F}\right)}{K_2} \tag{6.6}$$

$$V_g = V_T\left(\frac{Z_L + Z_S}{Z_L}\right) \tag{6.7}$$

where

K_1 and K_2 depend on the design of the machine

The capacitors compensators of the wind turbine are switched capacitors. Manufacturer usually set the wind turbine with only a few hundred kVAR for reactive power compensation. The wind turbine is compensated at different levels of compensation depending on the level of generation. In the event of losses in the capacitor, a resistor may be included in series with the capacitance. The losses in the capacitors are usually very small for high quality capacitors [46].

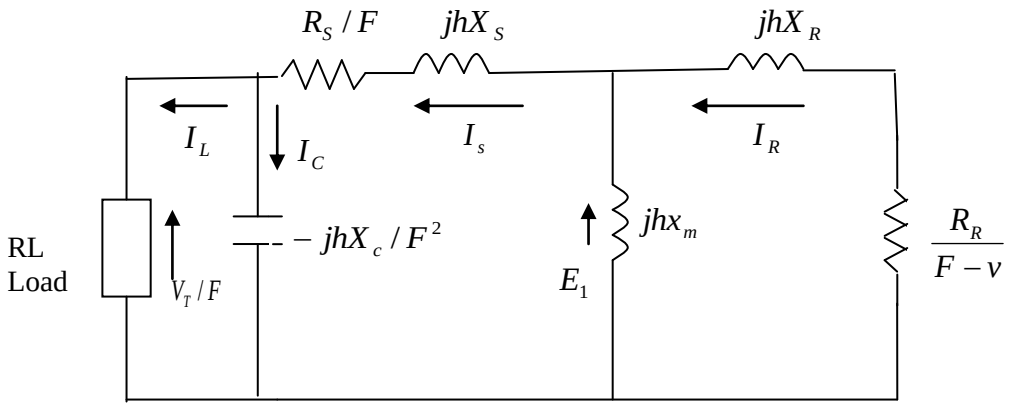

Figure 6.6. Equivalent circuit of self-excited induction generator with R-L Load.

where
Rs, Rr, R : p.u. per-phase stator, rotor (referred to stator) and load resistance respectively.
Xls, Xlr, X, Xm : p.u. per-phase stator leakage, rotor leakage (referred to stator), load and magnetizing reactances (at base frequency), respectively.
Xsmax : p.u. maximum saturated magnetizing reactance.
C : per-phase terminal-excitation capacitance.

Xc : p.u. per-phase capacitive reactance (at base frequency) of the terminal excitation capacitor.
f, v : p.u. frequency and speed, respectively.
N : base speed in rev/min
Zb : per-phase base impedance
fb : base frequency
Vg, V0 : per-phase air gap and output voltages, respectively.
h is odd harmonics order (h = 5,7,11,13...)

In wind turbine applications, the induction generator, transformer, and capacitors are three phases connected either in Wye or Delta. The even harmonics, 3rd and its multiples do not exist in wind turbine operations. The only harmonics present are non-multiple of 3 as represented in Table 6.1. Harmonic representation of a per phase equivalent circuit is as shown in Fig. 6.6, h in this circuit indicate the higher harmonics multiples of 50 Hz, i.e. for h = 5 indicates the 5th harmonic (250 Hz) [47-48].

For the purpose of determining the circuit harmonic impedance the induction generator can be modelled as a series combination of resistance and inductive reactance [6], i.e.

$$Z_h = R_L\sqrt{h} + jX_L^{''}h \tag{6.8}$$

The equivalent harmonic admittance is determined as

$$Y_h = \frac{1}{Z_h} \tag{6.9}$$

where

R_L is derived from the generator power loss

$X_L^{''}$ is the generator sub-transient reactance

h is the harmonic order

Table 6.1: Planning Levels for Harmonics Voltage

Odd harmonics (Non-multiple of 3)		Odd harmonics (Multiple of 3)		Even harmonics	
Order 'h'	Harmonic Voltage (%)	Order 'h'	Harmonic Voltage (%)	Order 'h'	Harmonic Voltage (%)
5	2.0	3	1.5	2	1.0
7	1.5	9	0.5	4	0.8
11	1.0	15	0.3	6	0.5
13	1.0	21	0.2	8	0.4
17	0.5	>21		10	0.4
19	0.5			12	0.2
23	0.5			>12	
25	0.5				
29	0.5				
31	0.5				
>31	0.2+0.3(31/h)				

A frequency dependent multiplying factor can be added to the reactance terms to account for skin effect. A typical variation of the inductive load of an induction generator with rotor speed is shown in Fig. 6.6 [6].

Loop equation in terms of stator current is obtained using equivalent circuit represented in Fig. 6.5 as follows,

$$I_S\left(Z_L + Z_S + Z_R\right) = Z_{LSR} I_s = 0 \tag{6.10}$$

where

$$Z_L = \frac{R_L}{F} // \frac{-jhX_c}{F^2}$$

$$Z_S = \frac{R_S}{F} + jhX_S$$

$$Z_R = jhX_m // \left(\frac{R_R}{F-v} + jhX_R\right)$$

$$Z_{LSR} = \frac{-jhX_c R_L}{(R_L F^2 - jhX_c F)} + \left(\frac{R_S}{F} + jhX_S\right) + \frac{jhX_m\left[R_R + j(F-v)hX_R\right]}{R_R + j(F-v)(hX_m - hX_R)}$$

(6.11)

where

$$F_{\max} = v - \frac{v}{2}\left\{\frac{1-\sqrt{1-\left(\frac{v_c}{v}\right)^2}}{1+\frac{R_s}{R_r}\left(1+\frac{X_r}{X_m}\right)^2}\right\}$$ is the self-excited frequency

$$v_c = \frac{2R_s}{X_m}\sqrt{\frac{R_r}{R_s}+\left(1+\frac{X_r}{X_m}\right)^2}$$

v is the rotor speed $\left(\omega_r = (1-s)\omega_s\right)$

Under steady state operation of SEIG, $I_S \neq 0$, therefore

The value of stator current is

$$I_S = \frac{\left(\frac{V_g}{F}\right)}{(Z_L + Z_S)} \tag{6.12}$$

The value of the rotor current

$$I_R = \frac{\left(-\frac{V_g}{F}\right)}{\left(\frac{R_R}{(F-v)+ jhX_R}\right)} \tag{6.13}$$

The value of the load current

$$I_L = \frac{-jhX_C I_S}{R_L F - jhX_C} \tag{6.14}$$

The value of the terminal voltage

$$V_T = I_L * R_L \tag{6.15}$$

The value of the output power

$$P_{in} = \frac{|I_R|^2 R_R F}{(F-v)} \tag{6.16}$$

$$P_{out} = |I_L|^2 R_L \tag{6.17}$$

$$Z_{LSR} = 0 \tag{6.18}$$

In appeandix A4, Equ. (A4.21) has real and imaginary parts as follows

$\mathrm{Re}\{Z_{LSR}\}$ = 0

$$\text{Im}\{Z_{LSR}\} = 0 \tag{6.19}$$

In stable operating condition of an SEIG, (6.13) and (6.19) must be satisfied.

Equation (6.16) and (6.19) may be solved using optimization technique to determine the excitation capacitance and generated frequency for the desired terminal voltage.

The operations of the real part can be obtained as

$$C_4F^4 + C_3F^3 + C_2F^2 + C_1F + C_0 = 0 \tag{6.20}$$

where

$$C_0 = (R_L + R_S)R_LR_S(R_r + v + I_2)^2$$

$$C_1 = R_L^2R_rv(I_1 - I_2I_3) - 2R_LR_SI_2^2v(R_L + R_S) + 2R_LR_SR_rv(I_1 - I_2I_3)$$

$$C_2 = R_L^2(R_SI_2^2 - R_rI_1 + R_rI_2I_3) + hX_L^2R_S(R_r + I_2v)^2 + 2R_LR_rR_S(I_2I_3 - I_1) + R_L(I_1^2v^2 + R_r^2I_3 + R_S^2I_2^2)$$

$$C_3 = hX_L^2R_rv(I_1 - I_2I_3) - 2(hX_L^2R_S^2I_2^2 + R_LI_1^2)v$$

$$C_4 = X_L^2R_r(I_2I_3 - I_1) + X_L^2R_SI_2^2 + R_LI_1^2$$

$$I_1 = hX_S(X_R + hX_M) + X_RX_Mh$$

$$I_2 = X_R + hX_M$$

$$I_3 = h(X_M + X_S)$$

$h =$ harmonic of the order of 5,7,11,13,17,19,23,25,...

Its imaginary part contains information for maximum value of terminal capacitor and is obtained as follows

$$C_{\max} = \frac{1}{2\pi}\left(\frac{X_LF}{Y_3} + \frac{Y_4}{Y_1^2 + Y_2^2}\right) \tag{6.21}$$

where

$$Y_1 = R_SR_r - FI_1(F - v)$$

$$Y_2 = R_rFI_3 + R_S(F - v)I_2$$

$$Y_3 = (R_L + hX_LF)^2$$

$$Y_4 = R_rY_2 - I_2FY_1(F - v)$$

6.3.2. Test Case Impact of Harmonic Injection Stabilizer and Capacitor Excitation

It should be reiterated here that (6.20) contained four possible real roots that ignite self-excitation and it has only physical meaning. The Fig. 6.7 to Fig. 6.14 illustrates the impact of harmonic injection stabilizer and capacitor excitation to stabilize an induction generator in a wind turbine. As shown in Fig. 6.7 is injection of 5th harmonic at fixed resistive load with variable inductive load, as observed capacitor self-excitation occurs between 50% and 100% inductive load. There is under excitation when inductive load is 0%, hence the capacitance collapses after hitting its maximum.

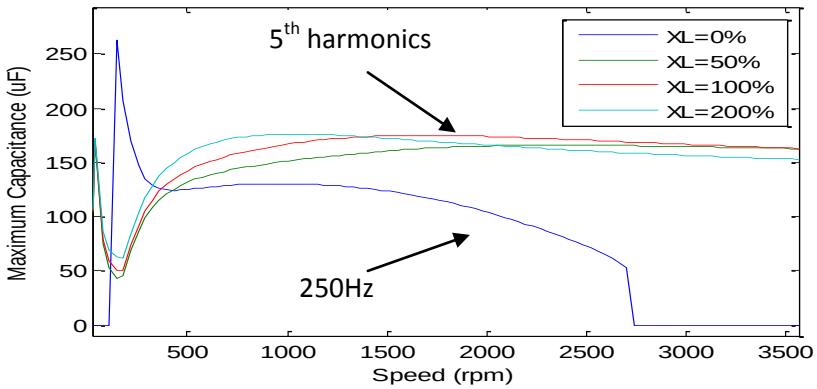

Figure 6.7. Maximum capacitance at 5th harmonic

A large variation in the capacitor profile is recorded when the value of the inductive load is increased from an initial value 0% to 50%. The 50% and 100% values stabilize at maximum capacitance excitation of 170 μF with 100% value recording overshoot of 5 μF. The 200% recorded lower settling value of 152 μF but have high overshoot capacitor value of 30 μF.

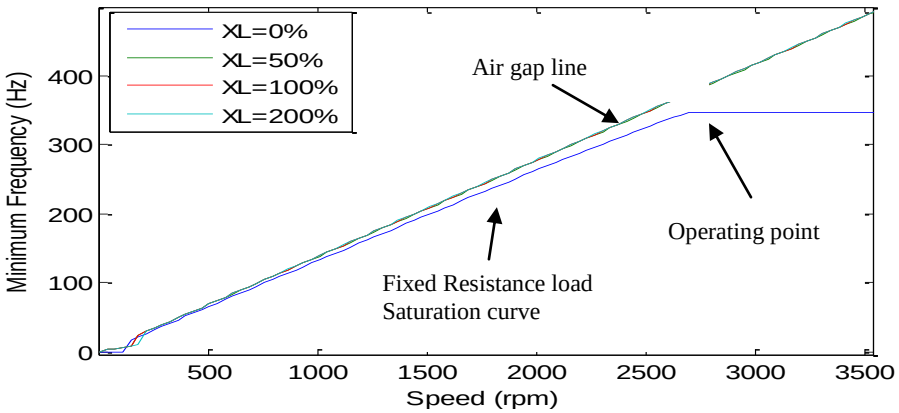

Figure 6.8. Exciter load-saturation curve at 5th harmonic

As observed the 5th harmonic will induces a 250Hz component in the torque.
The air-gap line in Fig. 6.8 is a tangent to the fixed resistive load saturation curve. The operating point denotes the departure of the load saturation curve from the air-gap line.

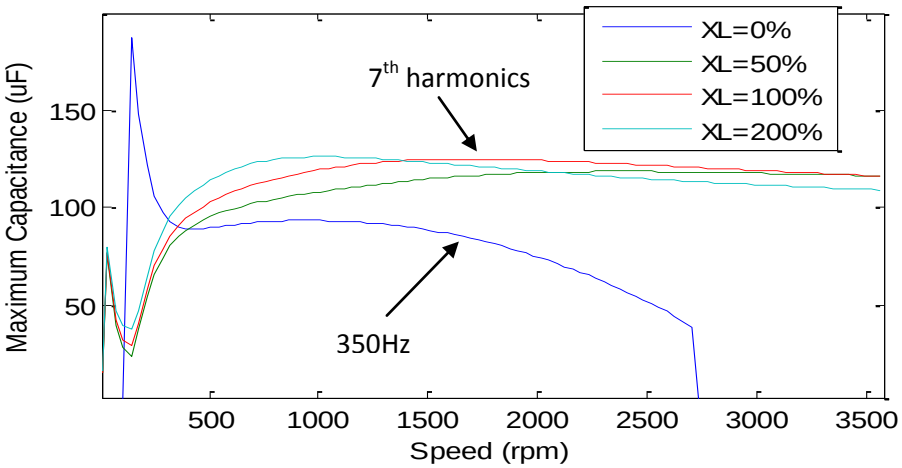

Figure 6.9. Maximum capacitance at 7th harmonics

Injecting 7th harmonic produces Fig. 6.9 with reduction of capacitance value from 170µF to 140 µF . Also, injecting 13th harmonic produces Fig. 6.11 with reduction of capacitance value from 140µF to 62 µF. Injecting 29th harmonic produces Fig. 6.117 with reduction of capacitance value from 62µF to 29 µF. These results have proven that harmonic injection into the excitation systems is essential for the assessment of desired performance requirement for the design and coordination of supplementary control and protective of wind turbine model for harmonic and stability studies.

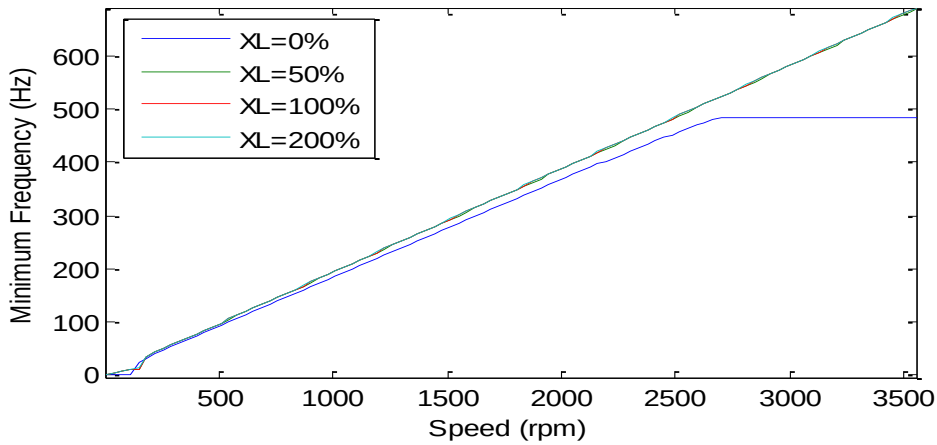

Figure 6.10 Exciter load-saturation curve at 7th harmonic

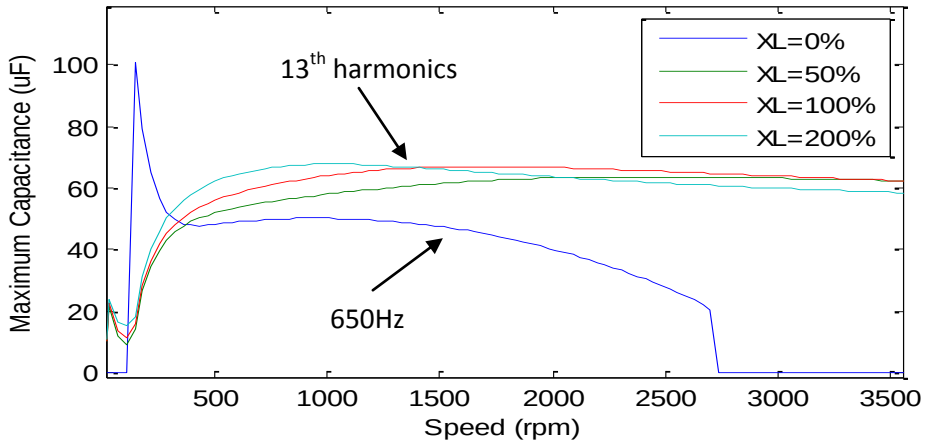

Figure 6.11 Maximum capacitance at 13th harmonic

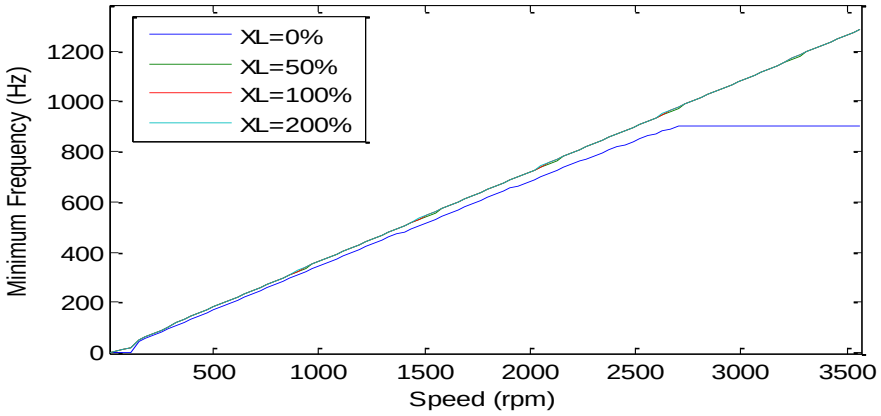

Figure 6.12 Exciter load-saturation curve at 13th harmonic

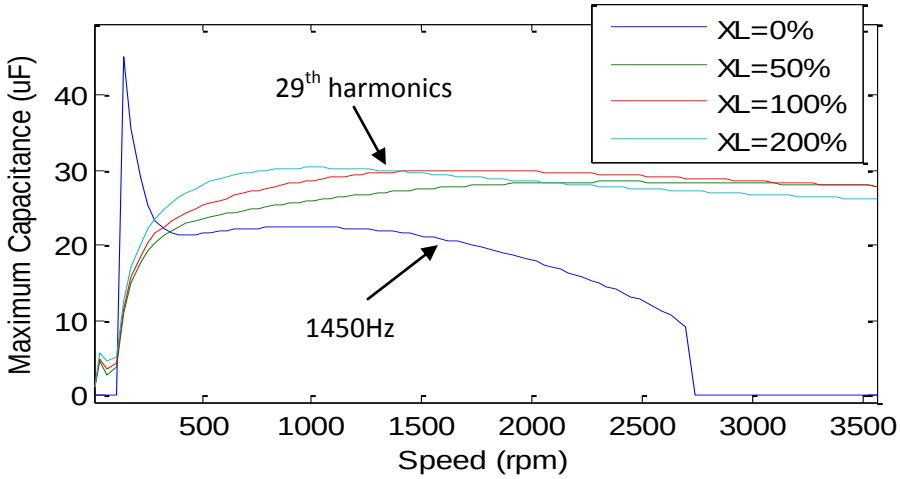

Figure 6.13. Maximum capacitance at 29th harmonic

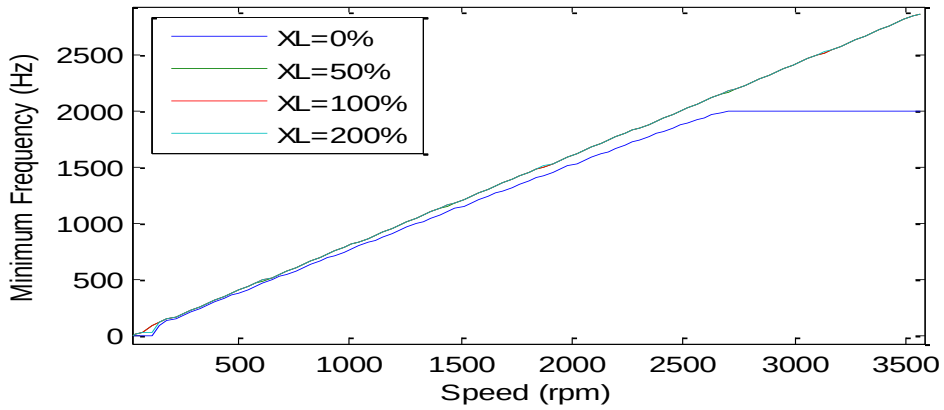

Figure 6.14. Exciter load-saturation curve at 29th harmonic

Injection of high odd harmonics as shown in Fig. 6.13 generates low capacitance value. When the capacitance is large it takes a longer time to reach its steady state value. If the capacitance is too small there will not be enough exciting current and as a result there will not be voltage build up. As observed in the figures under considerations the inductive load must be kept low to achieve stabilized capacitance value, since large inductive load will introduce unstable behaviour.

Examining these figures reveals the following remarks:

- For all harmonics components, gives good estimates for the capacitance magnitudes due to odd harmonic injection.
- As the non-multiple of 3rd harmonics increases, relatively low capacitance magnitudes are achieved.
- At a low non-multiple of 3rd harmonics, the simulation produces high magnitude.
- The critical capacitance value is 10 μF of the initial region of capacitor curve. If the capacitance is chosen below the critical capacitance 10 μF, the voltages will never build-up and excitation fails initially.
- The minimum capacitance required to generate the rated voltage is 28 μF. If we choose below this value, the rated voltage will not be generated.
- The maximum value of capacitance required should not exceed 30 μF. If the capacitance exceeds the maximum value, the current flow will be more than the rated value. This may lead to heating of stator core.

6.4. Steady-State Harmonic Model of the VSC-HVDC

The principles of operation and steady-state operation of the VSC have been dealt with in Chapter 5. The steady-state model of the VSC for harmonic study is derived from the harmonic domain (HD) technique detailed in Appendix B. One SM as explained in the previous chapter may be represented for harmonic domain modelling as shown in Fig. 6.15, which includes current injection in the DC side. This current permit active power exchange between the DC and AC systems in steady-state operation [49].

The voltage across the capacitor in harmonic domain may be represented as

$$\mathbf{V}_{cap} = \frac{1}{C}\mathbf{D}^{-1}(jh\omega_0)\,\mathrm{I}_{cap} + \mathbf{V}_0 \tag{6.22}$$

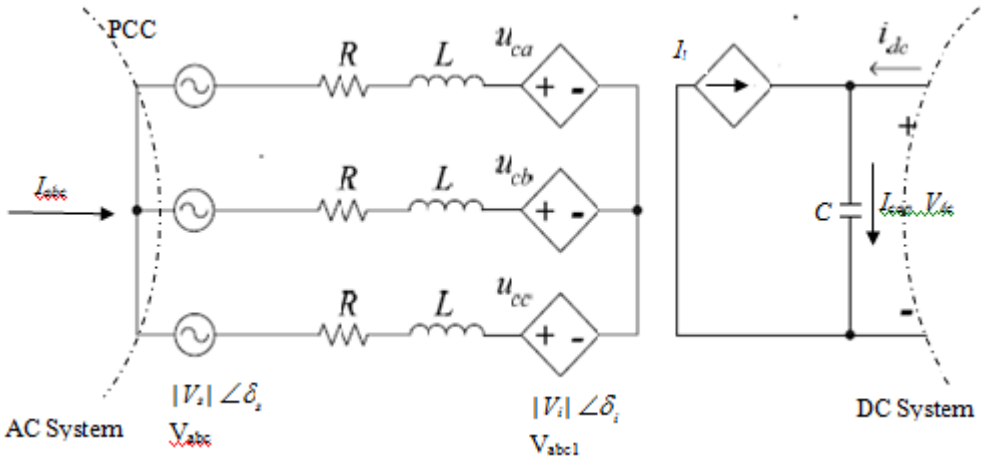

Figure 6.15 Voltage source converter equivalent model

In Figure 6.16 voltage at $\mathbf{V}_0$ may be assumed to be constant, meaning that the capacitor is not charging, on this condition the DC-term of $I_{cap}(t)$ is zero. Therefore it is not possible to exchange active power in the steady state with the AC system. It should be noted here that the value of the resistance must be kept at minimum to obtain maximum capacitor charge.

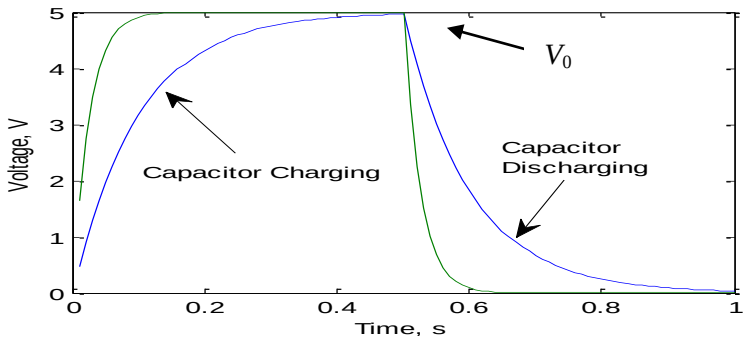

Figure 6.16 shows the charging and discharging curves

Maintaining the required DC capacitor voltage has to correspond to the active power supplied by the DC side. This has to be equal to the active power absorbed by the AC side with the losses of the VSC, which include the switching losses and capacitor losses in the converter.

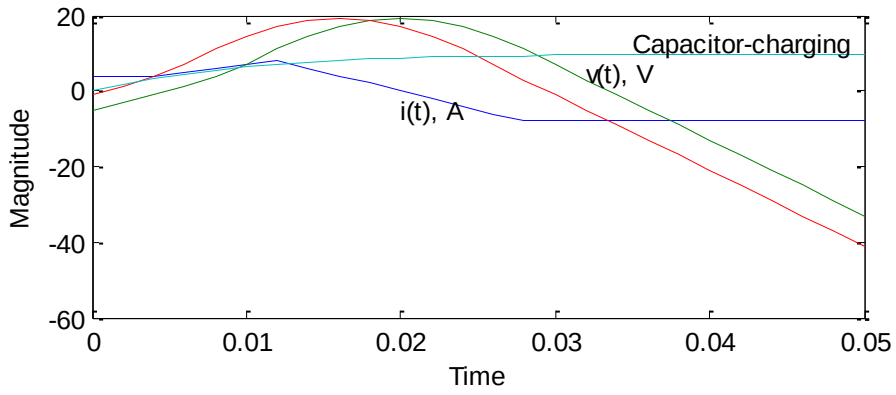

Figure 6.17. Voltage and current of DC capacitor

On any scenario that the active power is greater than the AC side will result in converter losses, the excess quantity will be absorbed by the VSC resulting in DC capacitor voltage increase. In the reverse, if the active power is less than the AC side requirement with the converter losses, the DC capacitor voltage will decrease as shown in Fig. 6.17.

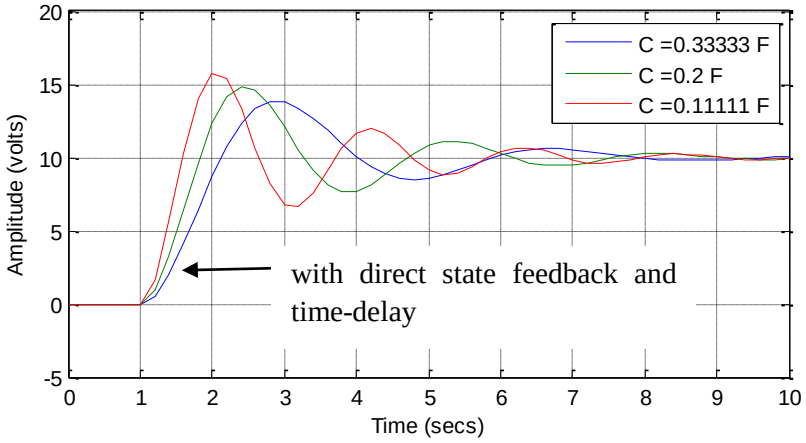

Figure 6.18. PI controller design and responses

In order to maintain a constant DC voltage, a PI controller is employed to regulate the DC capacitor voltage. With the designed controller (Kp, Ti), the closed-loop step response of the system is shown in Fig. 6.18. Clearly, the PI design for time delay element gives a satisfactory result. The basic idea of this controller is the error between a voltage reference and the actual DC voltage as a feedback signal. This indicates that it is possible to comment further on the constant voltage V_0 in the steady-state.

Hence the voltage on the DC side and its relationship to the AC phase voltages may expressed in harmonic domain as,

$$\mathbf{V}_{abc} = \mathbf{P}_s \mathbf{V}_{cap} \tag{6.23}$$

and, the relationship between the line currents and the DC current is given as follows

$$\mathbf{I}_{cap} = \mathbf{Q}_s \mathbf{I}_{abc} \tag{6.24}$$

the transformation matrices $\mathbf{P}_s$ and $\mathbf{Q}\ [50]_s$ are given as

$$\mathbf{P}_s = \begin{bmatrix} S_{ab} \\ S_{bc} \\ S_{ca} \end{bmatrix} \tag{6.25}$$

$$\mathbf{Q}_s = \begin{bmatrix} S_{ab} & S_{bc} & S_{ca} \end{bmatrix} \tag{6.26}$$

where, $S_{ab,}$ S_{bc}, and S_{ca} are Toeplitz matrices of the form

$$\mathbf{Z} = \begin{bmatrix} Z_0 & Z_{-1} & \cdots & Z_{-h} & & & \\ Z_1 & \ddots & \ddots & \ddots & \ddots & & \\ \vdots & \ddots & Z_0 & Z_{-1} & \ddots & \ddots & \\ Z_h & \ddots & Z_1 & Z_0 & Z_{-1} & \ddots & Z_{-h} \\ & \ddots & \ddots & Z_1 & Z_0 & \ddots & \vdots \\ & & \ddots & \ddots & \ddots & \ddots & Z_{-1} \\ & & & Z_h & \cdots & Z_1 & Z_0 \end{bmatrix} \tag{6.27}$$

The output voltage (ie $\mathbf{V}_{abc1}$) is given as

$$\mathbf{V}_{abc1} = \mathbf{P}_s\mathbf{V}_{dc} \tag{6.28}$$

while the voltage (ie $\mathbf{V}_{abc}$) in AC system side is

$$\mathbf{V}_{abc} = \mathbf{Z}_e\mathbf{I}_{abc} + \mathbf{V}_{abc1} \tag{6.29}$$

where

$\mathbf{Z}_e = R_e\mathbf{U_1} + L_e\mathrm{D}(jh\omega_0)$, R_e and L_e are the equivalent resistance and inductance of the coupling transformer. $\mathbf{U_1}$ is the identity matrix.

The current in the DC side of the VSC is given by

$$\mathbf{I}_1 = \mathbf{Q}_s\mathbf{I}_{abc} \tag{6.30}$$

also, the voltage in the DC side is given as

$$\mathbf{V}_{dc} = \mathbf{Z}_{cap}\mathbf{I}_{cap} + \mathbf{V}_0 \tag{6.31}$$

where $\mathbf{I}_{cap} = \mathbf{I}_1 + \mathbf{I}_{dc}$ (6.32)

Solving for $\mathbf{V}_{abc}$ and $\mathbf{V}_{dc}$ the following equation is obtained,

$$\begin{bmatrix} V_{abc} \\ V_{dc} \end{bmatrix} = \begin{bmatrix} Z_e + P_s Z_{cap} Q_s & P_s Z_{cap} \\ Z_{cap} Q_s & Z_{cap} \end{bmatrix} \begin{bmatrix} I_{abc} \\ I_{dc} \end{bmatrix} + \begin{bmatrix} P_s V_0 \\ V_0 \end{bmatrix} \tag{6.33}$$

Equation (6.10) can be represented in more compact form as

$$\begin{bmatrix} V_{abcT} \\ V_{dcT} \end{bmatrix} = \begin{bmatrix} A & B \\ C & D \end{bmatrix} \begin{bmatrix} I_{abc} \\ I_{dc} \end{bmatrix} \tag{6.34}$$

where

$\mathrm{V}_{abcT} = V_{abc} - \mathrm{P}_s V_0$; $\mathrm{V}_{dcT} = V_{dc} - V_0$

$\mathrm{A} = Z_e + P_s Z_{cap} Q_s$; $\mathrm{B} = P_s Z_{cap}$; $\mathrm{C} = Z_{cap} Q_s$; $\mathrm{D} = Z_{cap}$

The VSC DC voltage and current responses are as shown in Fig. 6.19, the DC voltage contains three different values i.e. -2, 0, and 2, while the DC current contain no DC-term i.e. DC-term = 0. This indicates that there is no active power exchange between the two systems. The zero active power balance between the systems is achieved by using

proper phase shift angle of the PWM modulation signal resulting in a VSC DC voltage output. This condition gives a 120^{o} phase shift angle of $i_a(t)$ with respect to the voltage.

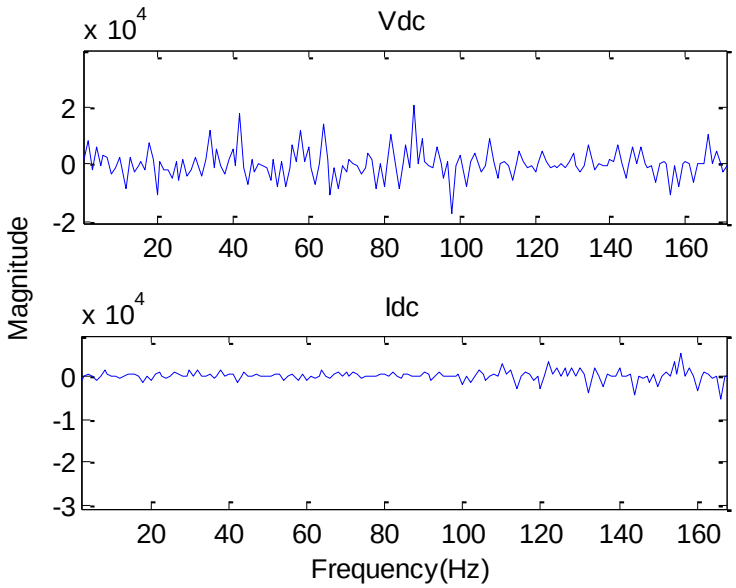

Figure 6.19. Voltage and current in the DC side

The frequency content of the DC voltage signal is as shown in Fig. 6.20 and its complex conjugate is as represented in Fig. 6.21, which determine the real harmonic magnitude in the DC voltage signal. As observed in the harmonic spectrum, one dominant harmonic content appears which has no significant effect in the DC voltage signal.

The Fast Fourier Transform (FFT) of Fig. 6.19 (i.e Vdc) is represented in Fig. 6.20 and real part of this signal is as shown in Fig. 6.21. The FFT algorithm applied here comprises a number of elements which is equal to 2^n (e.g. $2^8 = 256$, $2^{10} = 1024$ etc). Its main advantage is that it significantly reduces the computational time by a factor of the order $n/\log_2 n$, i.e. more than 100 times for a sample of 1024 elements.

The number of FFT elements is equal to the size of the time sample which contains complex conjugates and does not carry any new information. All the components of the harmonic spectrum produce the correct estimate of the voltage magnitude of Fig. 6.19.

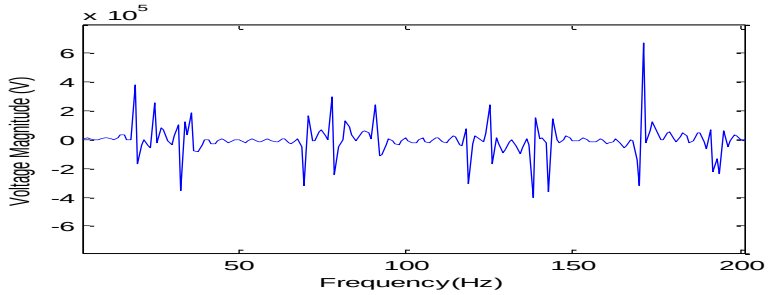

Figure 6.20. Frequency Contents of Vdc

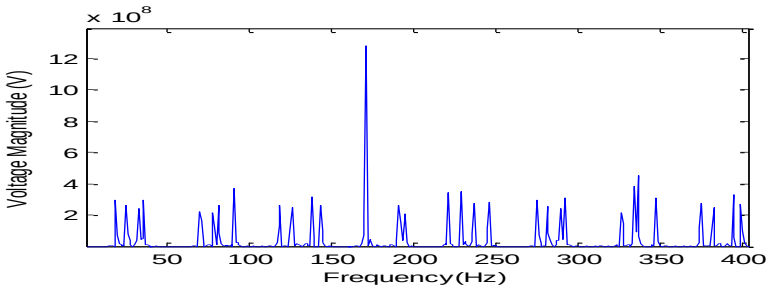

Figure 6.21. Frequency Content of Vdc with its complex conjugate

6.4.1. VSC-HVDC Steady State Model

A typical basic structure of a bi-terminal HVDC-VSC is shown in Fig. 6.1. Its generator supply voltage is fixed with generated active and reactive power. The generator voltage is determined by

$$V_g = V + (R + jX)I \tag{6.35}$$

V is the output voltage at the wind speed side; I input current of the rectifier and $(R + jX)$ is the line impedance

The grid-side converter can be controlled to inject the active power and reactive power into the grid by regulating the DC current. The generator side converter works as a DC voltage regulator. Thus, the wind system is capable of providing reactive power support, if required.

The current I will be in phase with the generator voltage, therefore I is given in harmonic domain by

$$I = S_{ab}I_a + S_{bc}I_b + S_{ca}I_c \tag{6.36}$$

where

S_{ab}, S_{bc} and S_{ca} are Phase switching function
I_a, I_b and I_c are line currents

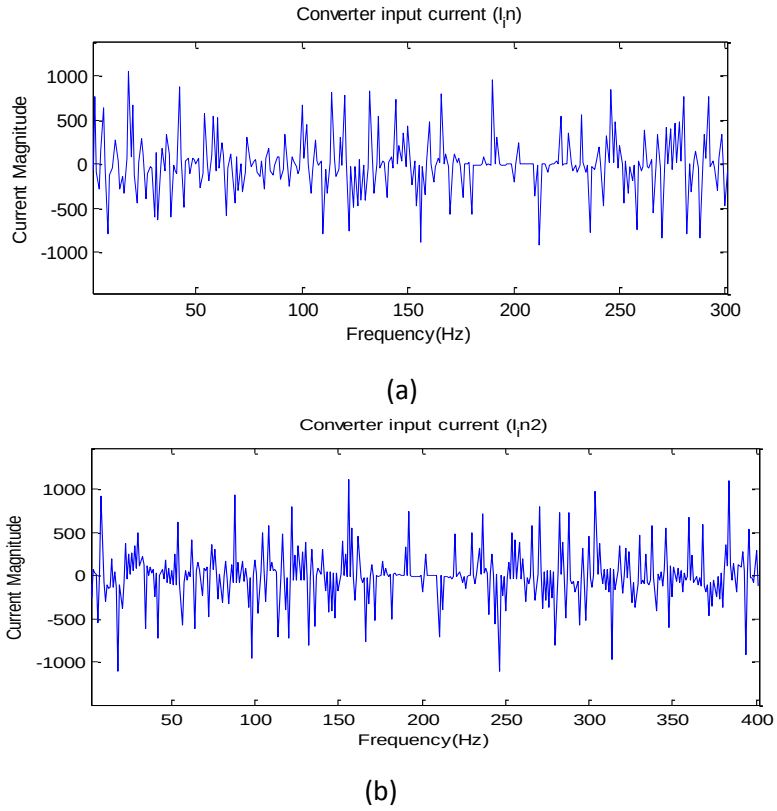

Figure 6.22. Input current of the (a) rectifier and (b) inverter

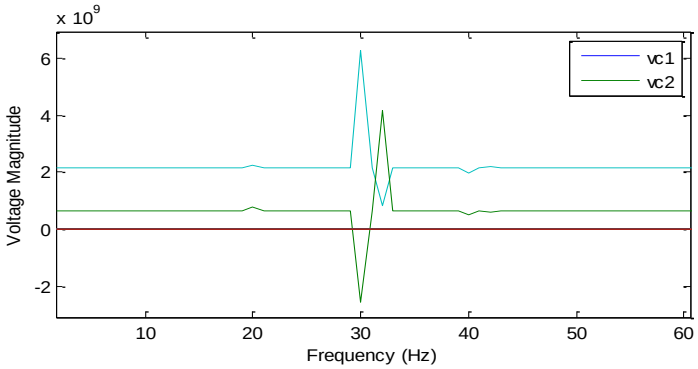

Figure 6.23. Output voltage of wind speed side and AC output voltage of the platform side

The input current of the rectifier is represented in Fig. 6.22a, while in the inverter side is as depicted in Fig. 6.22b. The AC output voltage of the generator side and the platform side are represented in Fig. 6.23.

6.4.2. Sending and Received Voltage in Terms of Power and Reactive Power

The steady state model of the generator side is deduced as follows:
Power flowing through the VSC1 is the product of voltage and current across the capacitor

$$P_{c1} = V_{cap1} I_{cap} \tag{6.37}$$

The relationship between the AC output voltage V_{c1} and the DC voltage V_{dc} can be expressed as

$$V_{c1} = \frac{maV_{cap1}}{\sqrt{2}} \tag{6.38}$$

where,

ma is the voltage modulation index = sinusoidal amplitude/triangular amplitude

According to the basic circuit relationship in Fig. 6.1, it is required to establish the equations for the source voltage, voltage across the load and the angle (δ), that is

$$V_{s1}^2 = \left(V_g + \Delta V\right)^2 + \delta V^2 \tag{6.39}$$

where

$$\Delta V = \frac{\left(PR + jQX_{eq}\right)}{V_g} h$$

$$\delta V = \frac{\left(X_{eq} P - jQR\right)}{V_g} h$$

$$P = \frac{V_g V_c}{Z \sin\theta};\ Q = \frac{V_c^{\ 2}}{Z \cos\theta};\ V_c = maV_{cap}/\sqrt{2} \tag{6.40}$$

and h = number of harmonics

If $\delta V << V_{s1}^2 = \Delta V$

$$V_{sc1}{}^2 = \left(V_g + \frac{RP + jQX}{V_g} \right)^2 \tag{6.42}$$

Also, if $R = 0$

therefore, $V_{sc}^2 - V_g = \frac{jQX}{V_g}$

Thus, voltage depends only on **Q**, if and only $PX << V_{c1}^2 + QX$, and angle of transmission δ is obtained from $\sin^{-1} \frac{\delta V}{V_{sc1}^2}$ which only depend on **P**

The load angle control can be determine using power transfer, active power **P** and reactive power **Q** between the sending and receiving end of Fig. 6.1. The quantities **S** (volt-amperes), known as the complex power, may be obtained by product of V_{c1} and the conjugate of current (I) [51]. Assuming that

$$S_G = V_{c1} I^* = V_{c1} \left(\frac{V_{c1} - V_{c2}}{Z} \right)^* \tag{6.43}$$

$$= V_{c1} e^{j\theta} \left(\frac{V_{c1} e^{-j\theta} - V_{c2}}{Z e^{-j\theta}} \right) \tag{6.44}$$

$$= \frac{V_{c1}^2}{Z} e^{j\theta} - \frac{V_{c1} V_{c2}}{Z} e^{j(\theta+\delta)} \tag{6.45}$$

$$\mathbf{P}_{\text{VSC1}} = \frac{V_{c1}^2}{Z} \cos\theta - \frac{V_{c1} V_{c2}}{Z} \cos(\theta + \delta) \text{ MW} \tag{6.46}$$

$$\mathbf{Q}_{\text{VSC1}} = \frac{V_{c1}^2}{Z} \sin\theta - \frac{V_{c1} V_{c2}}{Z} \sin(\theta + \delta) \text{ Mvar} \tag{6.47}$$

Similarly,

$$= V_{c2} \left(\frac{V_{c2} - Ve^{-j\delta}}{Z e^{-j\theta}} \right) \tag{6.48}$$

$$\mathbf{P}_{\text{VSC2}} = \frac{V_{c2}^2}{Z} \cos\theta - \frac{V_{c1} V_{c2}}{Z} \cos(\theta - \delta) \text{ MW} \tag{6.49}$$

$$\mathbf{Q}_{\text{VSC2}} = \frac{V_{c2}^2}{Z} \sin\theta - \frac{V_{c1} V_{c2}}{Z} \sin(\theta - \delta) \text{ Mvar} \tag{6.50}$$

The active and reactive powers in VSC1 and VSC2 with dc link impedance (DC resistance) are as shown in Fig. 6.24. Also, the active and reactive powers in VSC1 and VSC2 sides without dc link impedance are as represented in Fig. 6.25. As observed the system with a dc link has low active and reactive power magnitude, comparable to the system without dc link which higher magnitude as shown in Fig. 6.25.

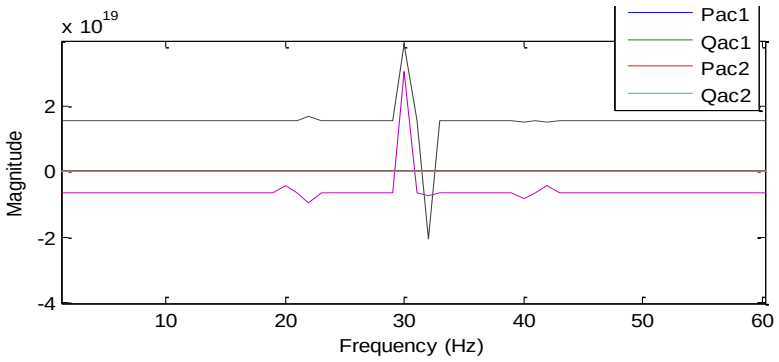

Figure 6.24. Active and reactive power of VSC1 and VSC2 with DC link impedance

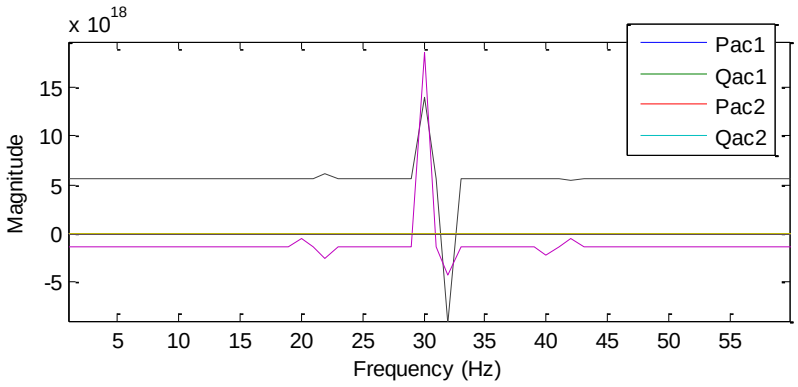

Figure 6.25. Active and reactive power of VSC1 and VSC2 without DC link impedance

The wind turbine generator and power transfer from the generator to the DC link are controlled by adjusting the magnitude and angle of the voltage at the AC terminals of the VSC1 side. The voltage magnitude, V_{R1} and angle magnitude, δ_1 required at the terminals of the generator-side VSC1 are as shown in Fig 6.26 and are obtained as follows:

$$V_{g1} = V_{s1} - \frac{Q_{s1gen} X_{gen}}{V_{s1}} \tag{6.51}$$

and

$$\delta_1 = \frac{P_{s1gen} X_{gen}}{V_{c1} V_{s1}} \tag{6.52}$$

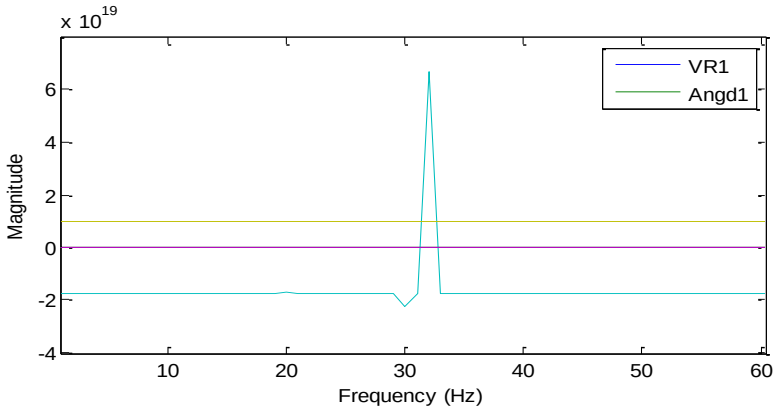

Figure 6.26. Load angle and voltage magnitude control of the generator-side converter

Similarly,

The voltage magnitude, V_{R2} and angle magnitude, δ_2 required at the terminals of the generator-side VSC2 are as shown in Fig 6.27 and are obtained as follows:

$$V_{g2} = V_{s2} + \frac{Q_{s2\,platform} X_{platform}}{V_{s2}} \tag{6.53}$$

and

$$\delta_1 = \frac{P_{2\,platform} X_{platform}}{V_{c2} V_{s2}} \tag{6.54}$$

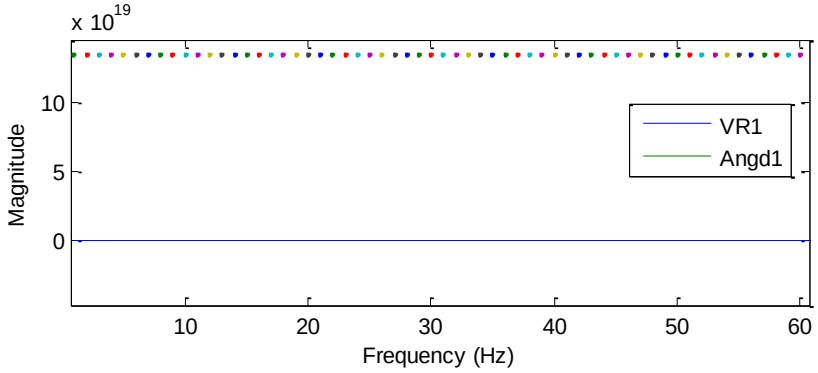

Figure 6.27. Load angle and voltage magnitude control of the platform-side converter

Figure 6.31 illustrates the implementation of the load angle and voltage magnitude control for the oil platform-side VSC2 with the reactive power exchange equal to zero with the network (i.e. $Q_{s2\,platform} = 0$ for unity power factor operation).

6.5. Harmonic Determination Needed in the Capacitor Bank

When harmonics appear to be the cause of the system problems, it is desirable to determine the system harmonic resonance point. To obtain this resonance point, the short-circuit capacity of each capacitor bank location is needed.

As it can be seen from the power distribution network Fig. 6.1, the power-factor-correction capacitor bank, which is connected on the 11 kV bus, can create a parallel resonance between the capacitors and the system source inductance.

To ascertain if harmonic considerations are required in the capacitor banks, the following equations applies,

with damping $$H_s = \sqrt{\frac{MVA_{TX}/2}{(MVA_C)(Z_{TX})} - \frac{(MW_L)^2}{(MVA_C)^2}} \quad (6.55)$$

without damping $$H_s = \sqrt{\frac{MVA_{TX}/2}{(MVA_C)(Z_{TX})}} \quad (6.56)$$

where

H_s is the series resonance point
MVA_{TX} is the transformer MVA
Z_{TX} is the transformer impedance
MW_L is the damping factor

Approximate parallel resonance point may be obtain by the equation

$$H_p = \sqrt{\frac{MVA_{SC}}{MVA_C}} \quad (6.57)$$

where

H_p is the parallel resonance point at fundamental frequency
MVA_{SC} is the short circuit capacity
MVA_C is the Mvar rating of the unfiltered capacitor bank at that location

The following test results show enforcement of harmonic considerations needed in the capacitor banks. Utilizing the system data, the following test results are obtained, Fig. 6.28a depicts resonance point close to 3rd, 5th, 7th , 9th and 11th and Fig. 6.30a depicts 15th, 19th, 23rd, 25th, and 29th possible harmonic-related problem could occur. The test results produce a solution or at least identify the cause of a harmonic problem, so that

the need for a detailed harmonic study is either reduced or the study is greatly simplified in the capacitor banks..

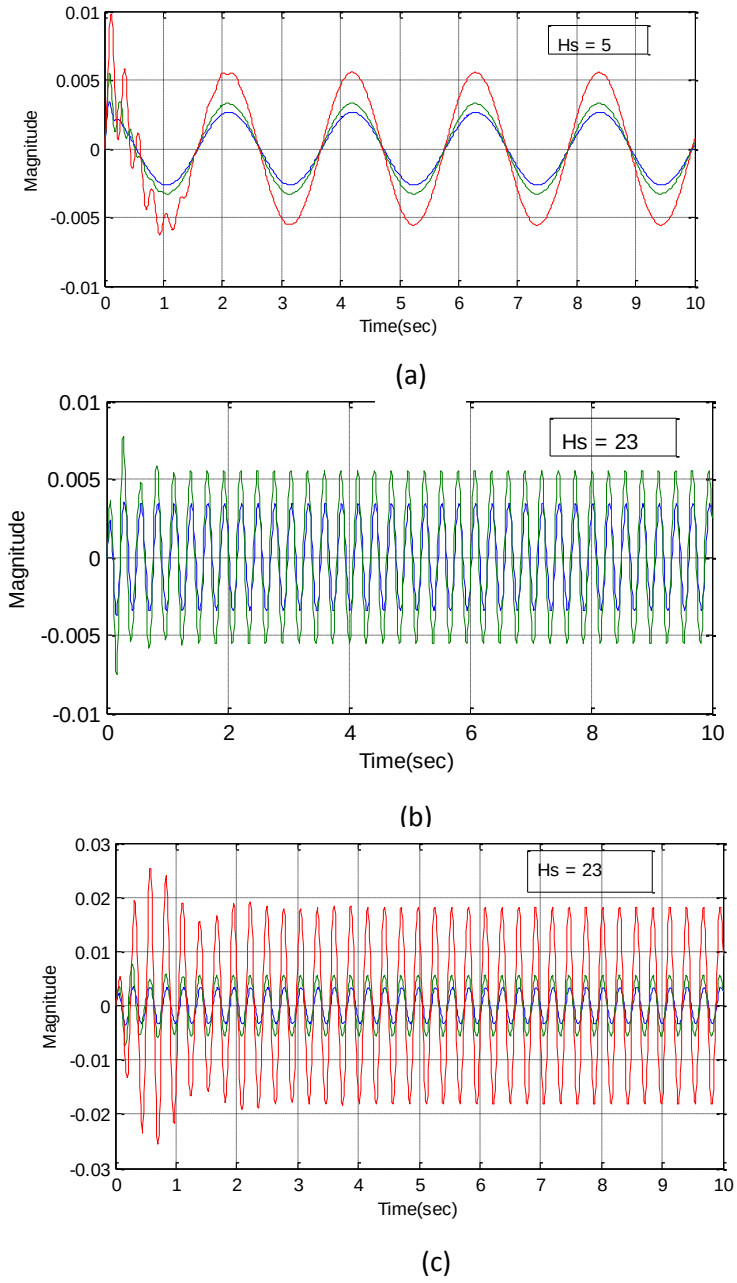

Figure 6.28. Series resonance harmonic point with damping in OG 1

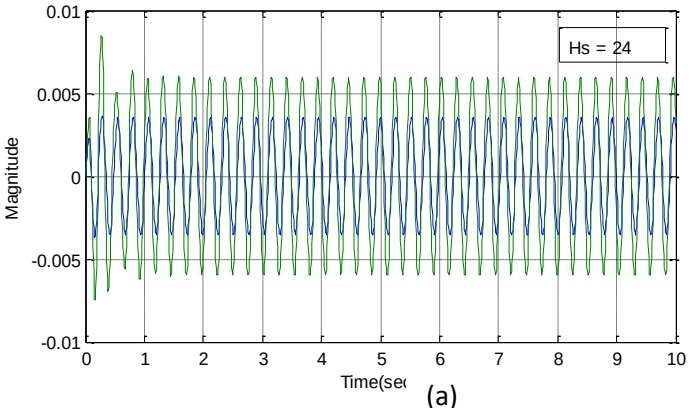

(a)

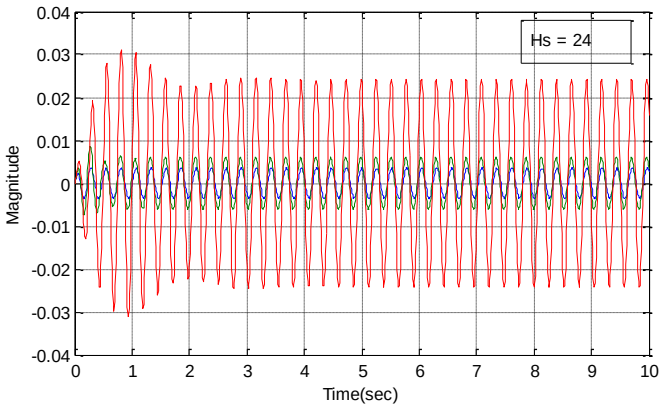

(b)

Figure 6.29. Series resonance harmonic point without damping in OG 1

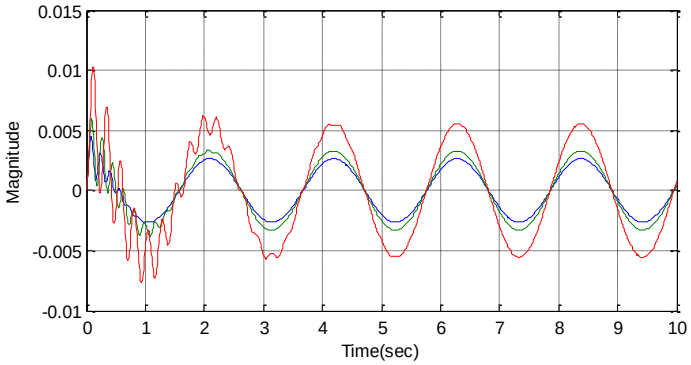

(a)

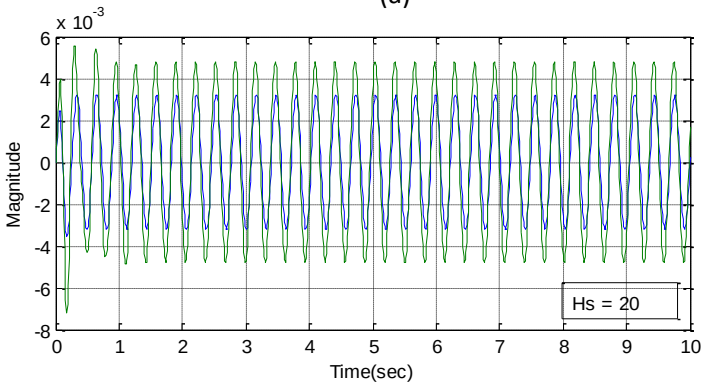

(b)

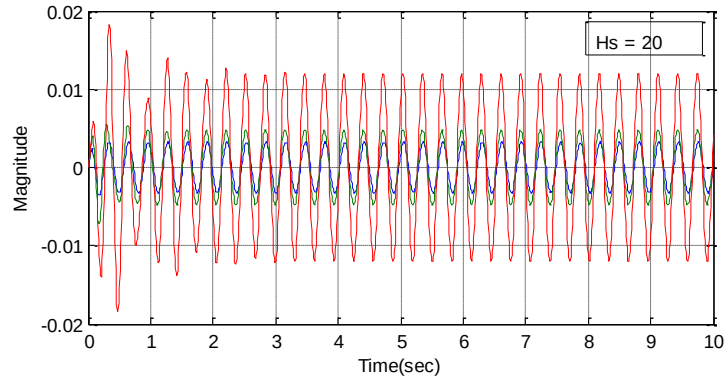

(c)

Figure 6.30. Series resonance harmonic point with damping in OG 2

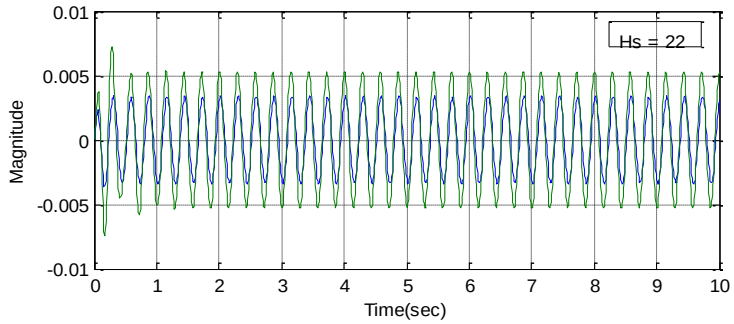

(a)

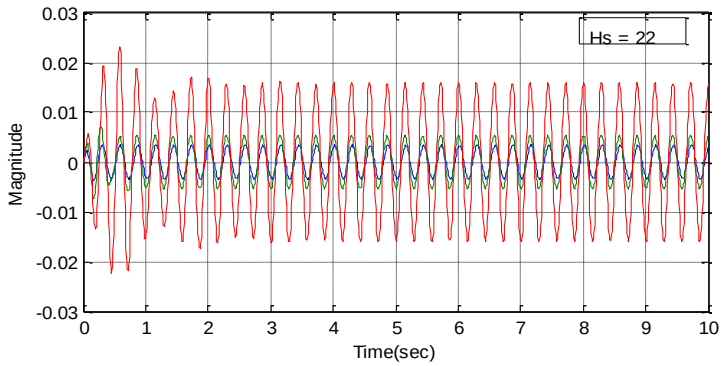

(b)

Figure 6.31. Series resonance harmonic point without damping in OG 2

It is uncommon to encounter a system where it is more practical to make a harmonic study on a system model as a diagnostic measure rather than to perform a detailed, time consuming harmonic analysis study. The results are used to obtain a harmonic spectrum as input data by which the system model is confirmed prior to performance of a detailed harmonic analysis study. In a way of confirmation, Fig. 6.28b, 6.28c and Fig. 6.29b, 6.29c depicts series resonance harmonic point with and without damping at PCC1 respectively. And Fig. 6.30b, 6.30c and Fig. 6.31b, 6.31c depicts series resonance

harmonic point with and without damping at PCC2 bus respectively. As observed no harmonic appear that can cause system problems comparable to Fig. 6.28a and Fig. 6.30a. These suggest the right input data for capacitor banks with corresponding transformers on the oil platform by which the system can operate without harmonic distortion.

6.6. Harmonic Deriving Point Impedance of Oil Platform

The impedances of the components of a oil and gas system to harmonic frequencies are determined on the basis of their values at power frequency (50 Hz or 60 Hz). The model of components of the system is as shown in Fig. 6.1. The choice of the model depends solely on the accuracy sought, the data and the range of operating frequencies.
It should be iterated here that, the complete system can never be represented in full in all harmonics studies. This will mandate the use of equivalent impedance representing its behaviour to harmonic disturbance for some components. These impedances depend on the short-circuit power of systems, the length of cable lines, the capacitor banks for reactive power compensation, the transformers, generating plant, the load levels of the system and the power electronics equipment. The software simulation method can be used to estimate these impedances.

The load on an oil and gas platform can roughly be divided in to three types of load: direct online AC motors, variable speed drives, and passive loads. The total electric power demand, and distribution between the different types of load, can vary greatly depending on the design of the platform and the operations running on the platform.
The system to be modelled is a simple radial oil and gas platform network with PCC voltage levels (11kV and 6.6 kV), fed by 100MW aggregated wind farm generators, 66kV, VSC-HVDC 500km system.

If a harmonic modelling study indicates excessive harmonic levels or a potentially harmful resonance condition, there are a number of alternative corrective measures that can be taken. Firstly, consideration can be given to implementing a rectifier with a pulse number higher than 6. As a comparison, a 6-pulse rectifier will produce in the order of 25% current THD, whereas a 12-pulse rectifier will produce about 12% current THD. An 18-pulse rectifier will produce on the order of 5% current THD. Somewhat lower harmonics can be achieved using rectifiers with a pulse number greater than 12,

however, the incremental benefit in harmonic reduction decreases while the complexity of the design increases.

If a problem is anticipated due to a power system resonance, it may be worthwhile to relocate or disconnect a small amount of power factor correction capacitance to shift a resonant frequency away from a characteristic harmonic. Harmonic filters can also be added to the system. Harmonic filters generally consist of one more tuned series LC legs which shunt specific harmonic currents away from the power system.
Harmonic tune filters have the added benefit of supplying leading KVARs and thus provide power factor correction.

A Pulse Width Modulated (PWM) rectifier is another means to reduce harmonic voltage/currents in the power system as discussed in previous chapter. Implementing PWM control of the rectifier switching devices allows elimination of a number of harmonics and compliance with IEEE Std. 519-1992. The PWM rectifier also offers the ability to improve the power factor at the input to the drive.
The Fig. 6.1 is a typical one-line diagram showing how a non-linear and linear would tie in to the oil and gas platform distribution power systems.

The component parameters were collected as follows:

Table 6.2. Platform component datas

Equipment	**Parameters**
Wind Turbine Generator (Induction Generator)	Wind Turbine power = 100MW Vg = 66kV; Xls = 0.0135; stator reactance Xlr = 0.0075; rotor reactance Rs = 0.00059; stator resistance Rr = 0.00339; rotor resistance Xm = 3.23; leakage reactance P = 4; No. of poles Xc = 30 μ F; capacitance excitation v = 1425rpm vc = 9.4917e-004 F = 1.3004e+003 Zgen = 6.3615e+006 +3.7356e+001i
Generator Transformer (TXg)	V_{TXg} = 66/33kV; X = 1.0+j10%; X/R = 10; p.f = 0.85
Transmission line (T1)	Long = 50km; V_T = 500kVA; p.f = 0.85

Grid Transformer ($TX_{platform}$)	V_{grid} = 33/11kV; X = 6%; p.f = 0.85
Capacitor Bank 1 (C1)	kvarC1 = 80Mvar; p.f = 0.85
Cable 1 (Z_{T2})	Z = 0.668+j0.115 Ω km
Transformer (TX_3)	V_{T3} = 11/6.6kV; X = 6.4%
Static VAR Compensator (SVC1)	$90^o < \alpha < 180^o$
Reactor (X_{react})	MvarX1 = 80Mvar
Motor 1(M_1)	3-Phase, 4 Pole, Y- connected, 50 Hz, Rs = 1.0 Ω, Rr = 0.76 Ω, Xls = 1.1404 Ω Xlr =1.7122 Ω, Lm = 0.114 H, J=0.1 kg·m2. Vm1 = 11kV; Pm1 = 60MVA; p.f = 0.6; p.f = 0.85
Motor2 (M_2)	Vm2 = 11kV; Pm2 = 25MVA; p.f =0.6; p.f = 0.85
Motor3 (M_3)	Vm3 = 11kV; Pm3 = 50MVA; p.f =0.6; p.f = 0.85
Motor4 (M_4)	Vm4 = 6.6kV; Pm4=30MVA; p.f =0.6; p.f = 0.85
Motor5 (M_5)	Vm5 = 6.6kV; Pm5 = 40MVA; p.f =0.6; p.f = 0.85
Motor6 (M_6)	Vm6 = 6.6kV; Pm6 = 35MVA; p.f = 0.6; p.f = 0.85
Motor7 (M_7)	Vm7 = 6.6kV; Pm7 = 20MVA; p.f = 0.6; p.f = 0.85
Motor8 (M_8)	Vm8 = 6.6kV; Pm8 = 15MVA; p.f =0.6; p.f = 0.85
Emergency Generator (Gas Turbine)	19.8kV; 20MW; P.F = 0.8; Xgastur = 0.20
Capacitor Bank 2 (C2)	MVARC2 = 80Mvar

The system consists of two buses OG1 and OG2 connected through a short circuit three-phase VSC-HVDC. The platform is fed by the wind farm power plant via a 66kV/33kV power transformer with a star-delta connection.

The long connection cables will introduce a low voltage at the point and a 80 MVAR static VAR compensator is connected on bus OG1. A line-commutated power converter is connected on the OG2 bus.

6.6.1. Determination of the Base Voltages

Power converted to motion, heat, sound, etc. is called real power and is measured in kilowatts (kW). Power that charges capacitors or builds magnetic fields is called reactive power and is measured in Kilovolts Amps Reactive (kVAR). The vector sum of the kW and the kVAR is the Total Power (energy) and is measured in Kilovolt Amperes (KVA). Power factor is the ratio of kW/KVA.

First the bases must be determined for all sections of the oil and gas network (Fig. 6.1). The bases in section A are given as the wind turbines bases as follows:

$$\text{Apparent power (S)} = \frac{\text{Actual power}}{\text{Power factor}} = \frac{100MW}{0.90} = 111MVA \quad = 111000kVA \tag{6.58}$$

$$\text{The reactive power} = \text{Actual power x } \tan(\cos^{-1}\text{P.F}) = 100MW \times \tan\left(\cos^{-1} 0.9\right) \tag{6.59}$$

$$= 48.43\ MVAR$$

$$\text{Voltage base} = 66kV$$

The current from the wind turbine generator can be obtained as follows:

$$I_A = \frac{P_A}{E_A \cos\theta} = \frac{100MW}{66kV \times 0.9} = \frac{1\times10^5}{66k \times 0.9} = 1683.50A \tag{6.60}$$

The voltage base in section B is

$$= 66\times10^3\left(\frac{33\times10^3}{66\times10^3}\right) = 33kV \tag{6.61}$$

Section D is connected to section B by

$$= 66\times10^3\left(\frac{11\times10^3}{33\times10^3}\right) = 22kV$$

Section E is connected to section D by

$$= 22\times10^3\left(\frac{6.6\times10^3}{11\times10^3}\right) = 13.2kV$$

Section F is connected to section D by

$$= 22\times10^3\left(\frac{6.6\times10^3}{11\times10^3}\right) = 13.2kV$$

Section G is connected to section F by

$$= 22\times10^3\left(\frac{3.3\times10^3}{6.6\times10^3}\right) = 11kV$$

Section H is connected to section F by

$$= 22\times10^3 \left(\frac{3.3\times10^3}{6.6\times10^3}\right) = 11kV$$

Table 6.3. The base impedances and currents

Bus	kV	Base ohms $= \frac{(kV)^2}{MVA}\ \Omega$	Base amperes $= \frac{kVA}{\sqrt{3}kV}$ Ampere
A	66	39.2400	971
B	33	9.8100	1942
C	33	9.8100	5826
D	11	1.0900	5826
E	6.6	0.3924	9710
F	6.6	0.3924	9710
G	3.3	0.0981	19420
H	3.3	0.0981	19420

Convert transformer impedances to per unit using

$$\text{Per unit } Z_2 = \text{per unit } Z_1 \times \frac{(base(kV_1))^2}{(base(kV_2))^2}\frac{base(kVA_2)}{base(kVA_1)}\text{h} \qquad (6.62)$$

Subscripts 1 refer the old base condition
Subscripts 2 refer the new base condition

Table 6.4. Convert transformer impedances to per unit

	Xh%	p.f	kV_1	kV_2	MVA	kVA_1	kVA_2
T_1	1+j10	0.87	33	33	100	100000	111000
T_2	0.8+j7	0.85	11	22	80	80000	111000
T_3	0.7+j6	0.86	6.6	13.2	30	30000	111000
T_4	0.7+j6	0.85	6.6	13.2	10	10000	111000
T_5	1+j9	0.90	3.3	11	20	20000	111000
T_6	0.6+j5.75	0.85	3.3	11	10	10000	111000

Table 6.5. Transformer Impedances

Transformer Number	Resistance p.u R_T	Reactance (p.u) jX_Th
Z_{TF1}	0.0111	0.1110ih
Z_{TF2}	0.0028	0.0243ih
Z_{TF3}	0.0065	0.0555ih
Z_{TF4}	0.0194	0.1665ih
Z_{TF5}	0.0050	0.0450ih
Z_{TF6}	0.0060	0.0574ih

Calculate line impedance in ohms using

$$\text{Per unit ohms} = \frac{\text{Actual ohms}}{\text{Base ohms}} \tag{6.63}$$

Table 6.6. Line impedance in ohms

Line Impedance Number	Resistance ohms R_T	Reactance (ohms) X_Th
Z_{L1}	0.0195	0.0124ih
Z_{L2}	0.0015	0.0019ih
Z_{L3}	0.0225	0.0031ih
Z_{L4}	0.0172	0.0021ih

Convert motor impedances to per unit using

$$\text{Per unit } Z_2 = \text{per unit } Z_1 \times \frac{\left(base\left(kV_1\right)\right)^2}{\left(base\left(kV_2\right)\right)^2} \frac{base\left(kVA_2\right)}{base\left(kVA_1\right)} \text{h} \tag{6.64}$$

Table 6.7. Convert motor impedances to per unit

Motor Number	Xh%	p.f	kV_1	kV_2	MVA	kVA_1	kVA_2
M_1	30	0.60	10.5	66	60	60000	111000
M_2	26.6	0.85	10	66	25	25000	111000
M_3	22.9	0.65	9.2	66	50	50000	111000
M_4	20.5	0.86	10	66	30	30000	111000
M_5	18.7	0.58	6.5	66	40	40000	111000
M_6	15.2	0.85	6	66	35	35000	111000
M_7	13.5	0.86	5.2	66	20	20000	111000

Table 6.8. Motor impedances

Motor Number	Resistance p.u R_M	Reactance (p.u) jXh_M
Z_{M1}	0	0.0140ih
Z_{M2}	0	0.0271ih
Z_{M3}	0	0.0099ih
Z_{M4}	0	0.0174ih
Z_{M5}	0	0.0050ih
Z_{M6}	0	0.0040ih
Z_{M7}	0	0.0047ih

Table 6.9. Harmonic currents for the variable frequency drive

VFD No.	(MVA_{base})	Apparent Short Circuit $S_{SC} = \frac{MVA_{base}}{X}$	$S_{SCphase} = \frac{S_{SC}}{3}$ (MVA)	$V_{phase} = \frac{kV_{base}}{\sqrt{3}}$ (kV)	$I_{SCphase} = \frac{S_{SCphase}}{V_{phase}}$ (A)	S_{load} (MVA)	$S_{loadphase} = \frac{S_{load}}{3}$ (MVA)	$I_{loadphase} = \frac{S_{loadphase}}{V_{phase}}$ (A)
VFD_1	111	8952	2984	38	78.53	27	9	237
VFD_2	111	8952	2984	38	78.53	30.5	10.2	268
VFD_3	111	7161	2387	38	62.82	10	3.3	87

Table 6.10. Convert generator impedance to per unit

(Generator Type)	Z h(ohms)	P.F	kV_1	kV_2	MW	$kVA_1 = \frac{MW}{p.f}$	kVA_2
G_{WT} (Wind Turbine)	6.3615e+006 +3.7356e+001i	0.90	33	66	100	117.647	111000
G_{GT} (Gas Turbine)	30%	0.90	10.8	33	20	23.529	111000

The reactive power in kvar needed in the network before the capacitor banks are added is determined by multiplying the apparent power in kVA by the sine of the power factor angle of the induction motor as follows

$$k\,\text{var} = kVA\sin\left(\cos^{-1}\theta\right) \tag{6.65}$$

$$kW = kVA \times p.f \tag{6.66}$$

Table 6.11. Generator impedance

Gas Turbine (Emergency Generator)Number	Resistance p.u R	Reactance (p.u) jXh
Z_{WT}	1.5005e+009	8.8114e+003ih
Z_{GT}	0	1.5159e+002ih

For Capacitor bank1and determined from motor1 (M1) data

Apparent power (S) = 60000 kVA

p.f = 0.60

0.60 to be improved to 0.85 by the capacitor bank1

Before adding capacitor bank 1 (C_1)

$\theta_1 = \cos^{-1}0.60 = 53.13^o$

A = 60000 kVA

B = 60000 * cos 53.13 = 36000 kW

kVA

C = sqrt($A^2 - B^2$) = 48000 kvar

After adding capacitor bank 1 (C_1)

$\theta_2 = \cos^{-1}0.85 = 31.79^o$

E = B = 36000 kW

D = 36000 / cos 31.79 = 42354

F = sqrt($D^2 - E^2$) = 22313 kvar

The rating of the capacitor = 48000 – 22313 = 25687 kvar

The capacitor bank impedances (X_{cap}) can be obtained as represented in Table 6.6

It should be reiterated here that Eqn.(6.17) remains constant before and after the capacitor banks are added.

The rating of the capacitor banks depends solely on the apparent power and power factor of the induction motors that is required to improve its power factor to 0.85 lagging.

Table 6.12: Capacitor bank impedances

Capacitor bank Number	$(kV)^2$	kvar	$X_{cap} = \frac{(kV)^2}{k\,\text{var}}$ h
C_1	66	25687	0.1700ih
C_2	66	17855	0.2440ih
C_3	66	18205	0.2393ih
C_{ACTUAL}	66	144619	0.0301h

The nodal admittance matrix of Fig. 6.1 is obtain as follows

$$Y_h = \begin{bmatrix} \frac{1}{Z_{IG}h} + \frac{1}{Z_{TF1}h} + \frac{1}{Z_{TL1}h} + \frac{1}{Z_{M1}h + Z_{L2}h} + \frac{1}{Z_{TF3}h + Z_{TL3}h} + & -\frac{1}{Z_{TL3}h + Z_{TF3}h} \\ \left(\frac{1}{Z_{TF4}h} + \left(\frac{1}{Z_{M2}h} + \frac{1}{Z_{M3}h} + \frac{1}{Z_{M3}h}\right) + \frac{1}{B_{SVC1}h} + C_1h + C_2h\right) & \\ -\frac{1}{Z_{TL3}h + Z_{TF3}h} & \frac{1}{Z_{TF_5}h + Z_{M5}h} + C_3h + \frac{1}{B_{SVC2}h} + \frac{1}{Z_{TF6h}h} + \\ & \left(\frac{1}{Z_{M6}h} + \frac{1}{Z_{M7}h}\right) \end{bmatrix}$$

(6.67)

The nodal impedance matrix at each harmonic order is obtained as follows

The nodal admittance matrix is a useful tool for the determination of the system harmonic voltage, the transfer impedance and the deriving point impedance at each frequency of the converter harmonic order. The non-linear load at PCC2 is represented by a current injection source i_f and the solution of the system is obtained by superposition of source effect.

$$Z_h = Y_h^{-1} \tag{6.68}$$

Once Z_h, is obtained at each characteristic harmonic, the voltage magnitude can be calculated at each harmonic as follows:

$$V_h = Z_h I_h \tag{6.69}$$

where

I_h = the source current at each characteristic harmonic

Further analysis can be performed using the individual harmonic voltages and currents. It may be important to investigate quantities such as the total harmonic distortion (THD), fault current, harmonic resonance, voltage dip and etc

6.6.2. Further Simulation Results

Motors draw reactive current to support their magnetic fields in order to cause rotation. Excessive reactive current is undesirable because it creates additional resistance losses and can require the use of larger transformers and wires. In addition, utilities often penalize owners for low power factor. Decreasing reactive current will increase power factor.

Typical AC motors may have a full load power factor ranging from 0.84 to 0.88. As the motor load is reduced, the power factor becomes lower. Utilities may require site power factor values ranging from 0.85 to 0.95 and impose penalties to enforce this requirement. Power factor correction capacitors can be added to reduce the reactive current measured upstream of the capacitors and increase the measured power factor. To prevent damage to the motor, power factor correction capacitors should not exceed the motor manufacturer's recommendations. In most cases, this results in maximum corrected values of 0.90 to 0.95.

A lot of motor loads are used in the oil and gas as seen in Fig. 6.1, many compensation capacitors bank have been installed to improve the power factor. Unfortunately, these capacitors have introduced serious parallel resonance problems and cause detrimental effect to the electrical facilities in the platform as represented in Fig. 6.32a.

Harmonic current components that are close to the parallel resonant frequency are amplified.

Higher order harmonic currents at the PCC1 and PCC2 are reduced because the capacitors are low impedance at these frequencies. The Fig. 6.32a below shows the effect of adding capacitors on the 11kV and 6.6kV buses for power factor correction.

This figure shows that by adding some typical sizes of power factor correction capacitors will result in the magnification of the 5^{th} and 25^{th} harmonic components, which in turns makes it even more difficult to meet the IEEE 519-1992 harmonic current standards.

More also, large harmonic voltages as observed in Fig. 6.32b and 6.32c are introduced at these harmonic resonant even though the harmonic current flow is small. To avert the harmonic resonance problem, it is necessary to install compensator equipment such as SVC or filter on the distribution network platform.

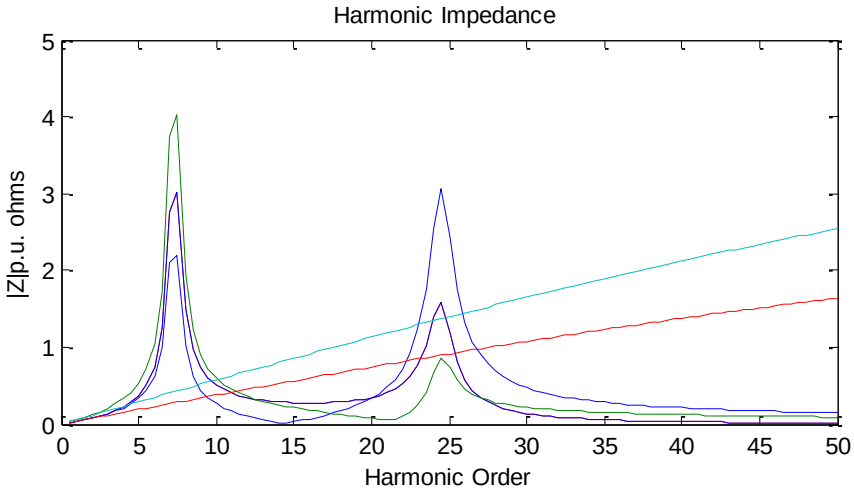

(a)

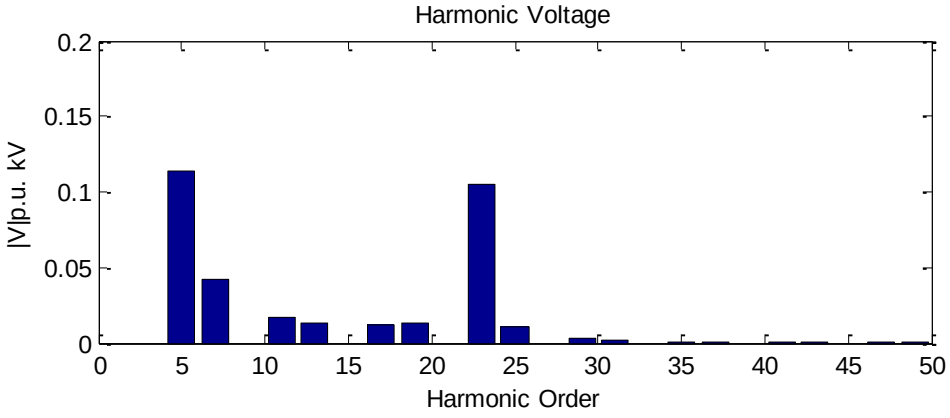

(b)

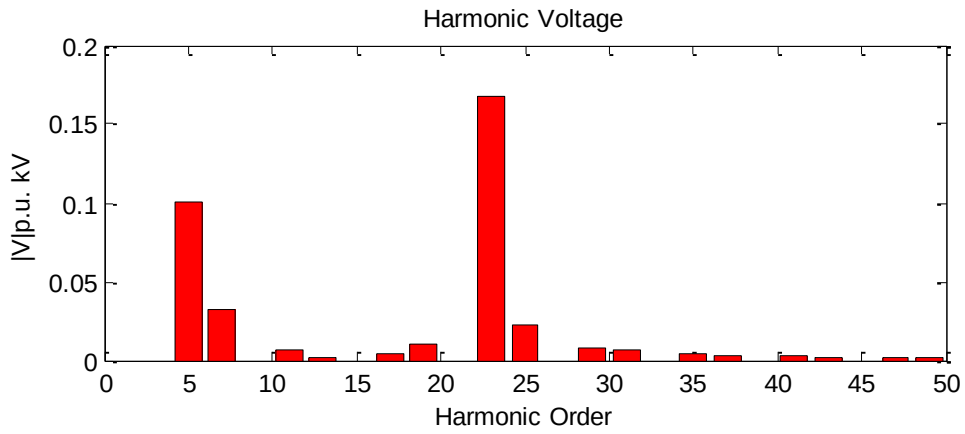

(c)

Figure 6.32. (a) Harmonic resonance impedance with capacitor bank (b) Harmonic voltage spectrum of PCC one (c) Harmonic voltage spectrum of PCC two

6.6.3. Impact of Advance Static Var Controller (ASVC)

The fixed capacitor banks are supported with ASVC represented in Fig. 6.33 of suitable rating to compensate fully for the reactive power requirement. In order to investigate the performance of ASVC on the oil platform distribution network, some choices have been made regarding the system studies. The rating of the ASVC is $\pm$ 300 Mvar and its firing angle α that would require to achieve this Mvar is obtain via carrying out sufficient Newton-Raphson iterations that will satisfy a firing angle mismatch $\Delta\alpha$ of less than $1x10^{-3}$. Where $\alpha_{TCR} = 90^{o}$ at the initial starting condition.

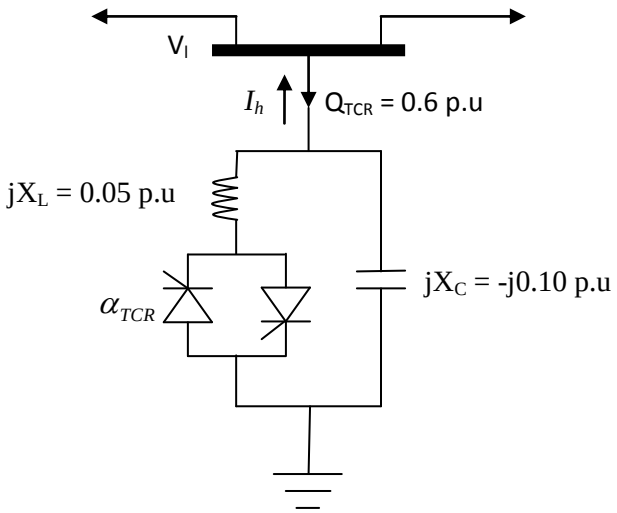

Figure 6.33. Static Var compensator

The capacitor's susceptance is:

$$jB_C = \frac{1}{-jX_C} \tag{6.70}$$

For the Thyristor-controlled reactor (TCR), we have,

$$-jB_{TCR} = \frac{2(\pi-\alpha)+\sin 2\alpha}{jX_L\pi} \tag{6.71}$$

The combined susceptance is:

$$jB_{SVC} = jB_C - jB_{TCR} \tag{6.72}$$

In more detained form:

$$jB_{SVC} = \frac{jX_L\pi - jX_C(2(\pi-\alpha)+\sin\alpha)}{X_C X_L \pi} \tag{6.73}$$

The SVC equivalent impedance at fundamental frequency, Z_{SVC} is obtained as follow

$$jZ_{SVC} = \frac{1}{jB_{SVC}} \tag{6.74}$$

The SVC current is:

$$I_{SVC} = j(Z_{SVC})V_l \tag{6.75}$$

and complex power is:

$$\begin{aligned} S_{SVC} &= V_l I_{SVC}^* \\ &= -j\left[\frac{X_L\pi - X_C(2(\pi-\alpha)+\sin 2\alpha)}{X_C X_L \pi}\right]V_l^2 \end{aligned} \tag{6.76}$$

Since the SVC under consideration contains no resistance then no active power exists in the circuit. Hence,

$$P_{SVC} = 0 \tag{6.77}$$

$$Q_{SVC} = \left[\frac{X_C(2(\pi-\alpha)+\sin 2\alpha) - X_L\pi}{X_C X_L \pi}\right]V_l^2 \tag{6.78}$$

or

$$\sin 2\alpha - 2\alpha + \pi\left[2 - \frac{X_L}{X_C} - \frac{X_L Q_{SVC}}{V_l^2}\right] = 0 \tag{6.79}$$

Using the Newton-Raphson iterative method to solve for the firing angle, using the following Equations

$$f(\alpha) = \sin 2\alpha - 2\alpha + \pi\left[2 - \frac{X_L}{X_C} - \frac{X_L Q_{SVC}}{V_l^2}\right] \tag{6.80}$$

and

$$f(\alpha) = \frac{\partial f}{\partial \alpha} = 2\cos 2\alpha - 2 \tag{6.81}$$

$$\Delta\alpha^{(0)} = -\left(\frac{\partial f}{\partial \alpha}\right)^{-1} f \tag{6.82}$$

$$\alpha^{(1`)} = \alpha^{(0)} + \Delta\alpha^{(0)} \frac{180^o}{\pi} \tag{6.83}$$

In order to enable both absorption and the injection of reactive power at the point of common coupling (PCCs), the SVC will have to changes from the inductive region to the capacitive region as the firing angle increases. In this test result the SVC generated maximum reactive power from capacitive region into the network as shown in Fig. 6.34a at $90^o < \alpha \leq 180^o$. Partial impedance appears at the bus where harmonic resonance occurs that is, partial 15^{th} harmonics, so no large harmonic voltages including 15^{th} harmonics are observed in Fig. 6.34b and 6.34c.

As illustrated in Fig. 6.34b and 6.34c the variation of reactive power with firing angle is non-linear. Also, these figures shows that the SVC generates 5^{th} ,25^{th} and 35^{th} harmonics and the three-phase SVC are delta connected to prevent the triplen harmonics from spreading to the oil platform.

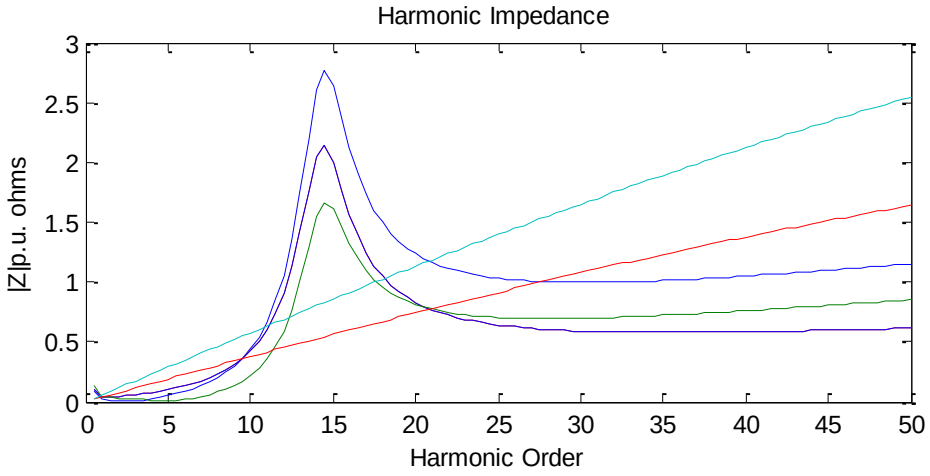

(a)

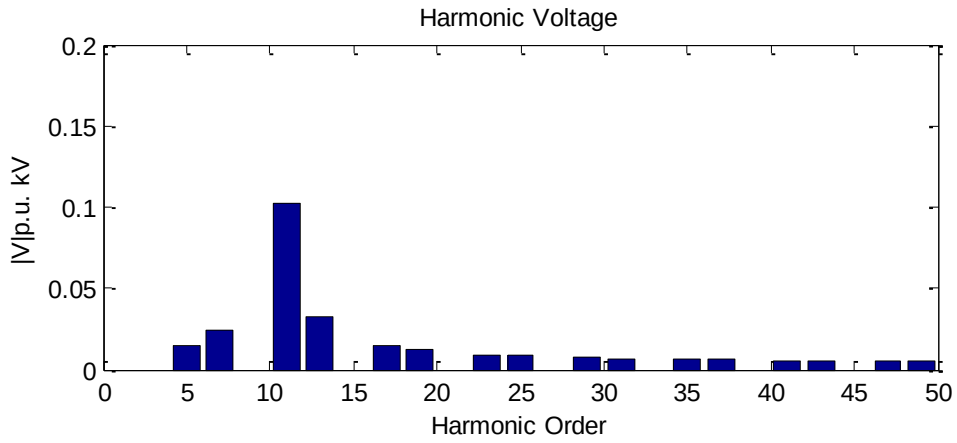

(b)

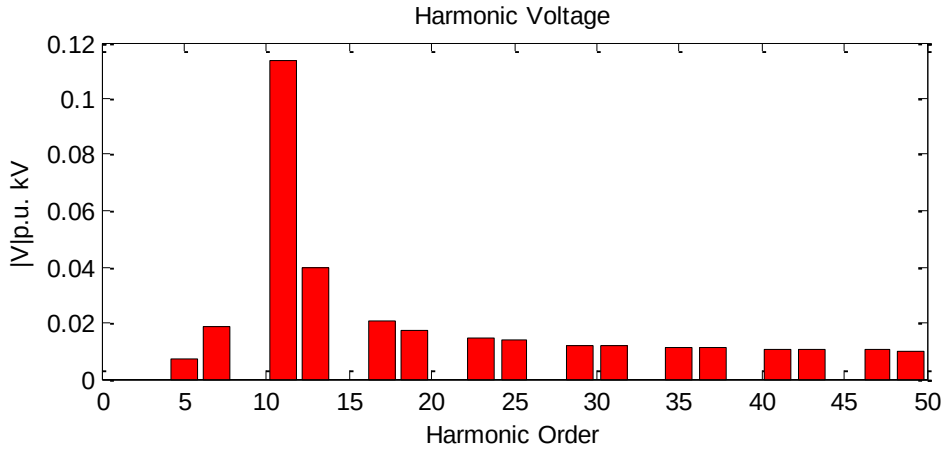

(c)

Figure 6.34. (a) Harmonic resonance impedance with SVC (b) Harmonic voltage spectrum of PCC one (c) Harmonic voltage spectrum of PCC two

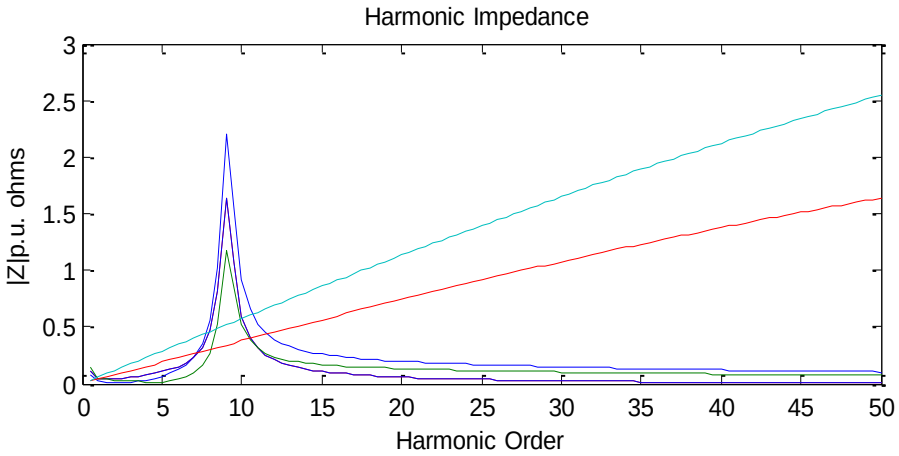

(a)

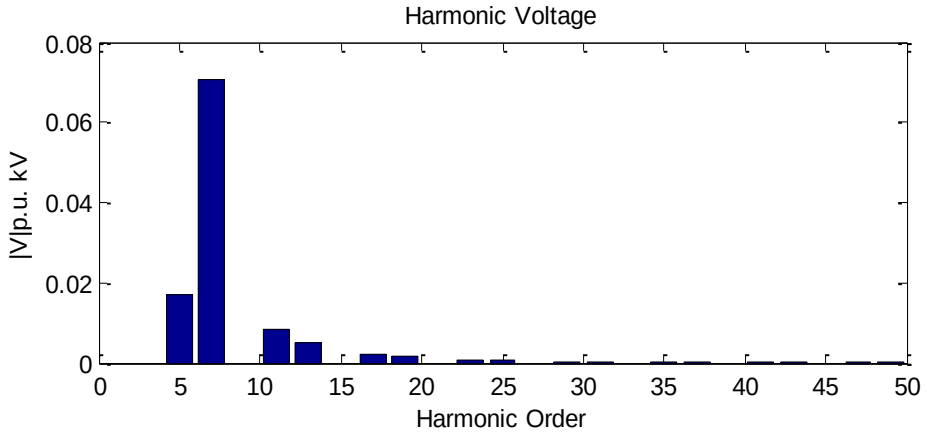

(b)

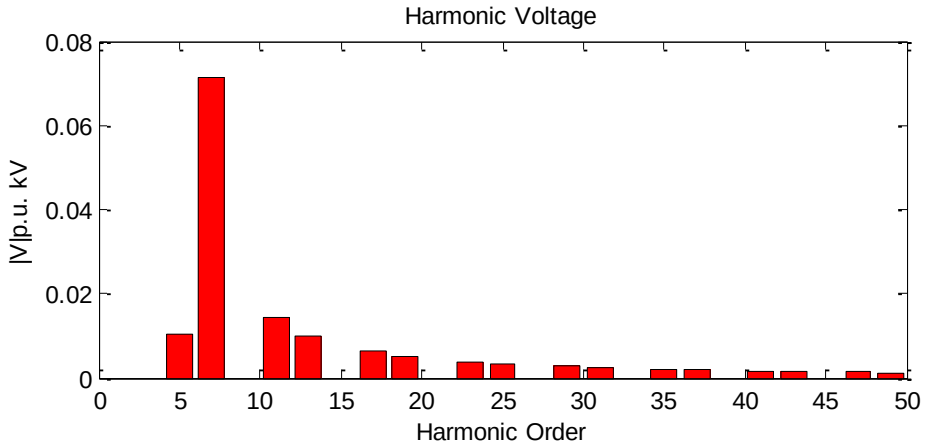

(c)

Figure 6.35. (a) Harmonic resonance impedance with SVC and capacitor bank(b) Harmonic voltage spectrum of PCC one (c) Harmonic voltage spectrum of PCC two

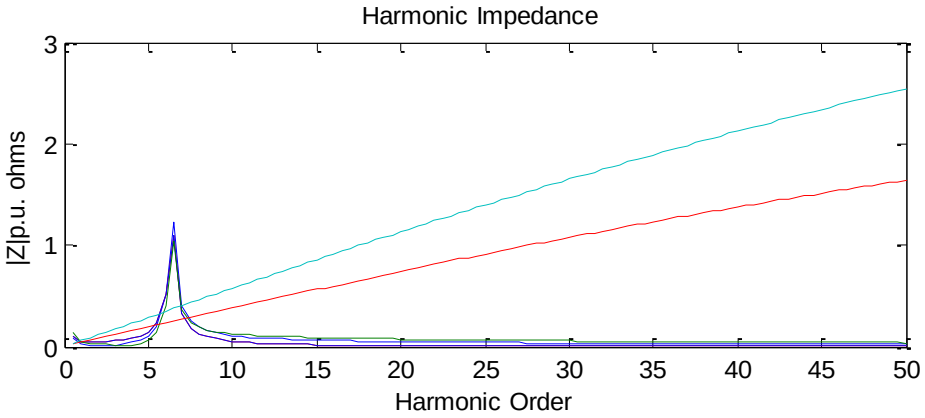

(a)

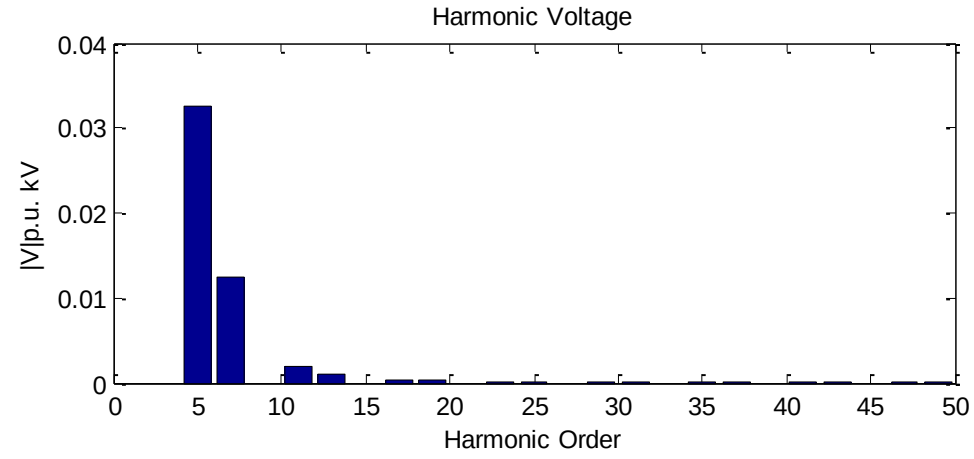

(b)

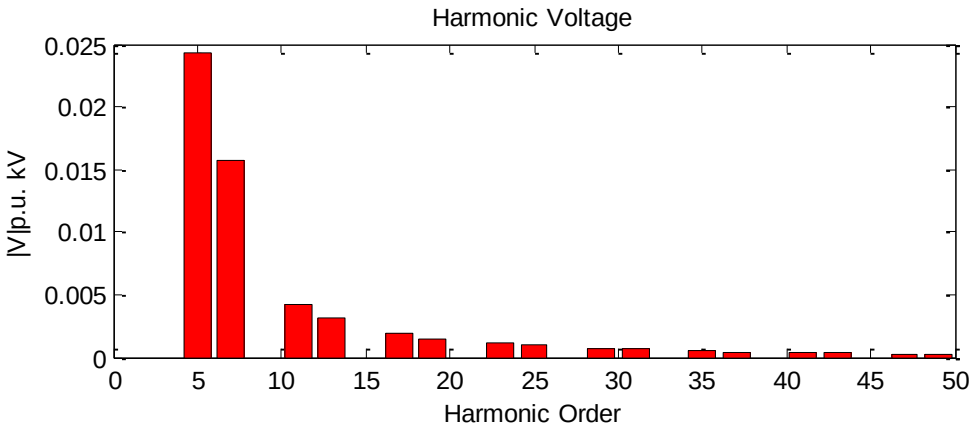

(c)

Figure 6.36. (a) Harmonic resonance impedance with motor starting (b) Harmonic voltage spectrum of PCC one (c) Harmonic voltage spectrum of PCC two

The combination of SVC and capacitor banks in the platforms resulted in reducing the magnitude of the harmonic resonanace impedance as shown in Fig. 6.35a, as observed there is no indication of odd harmonics comparable to Fig. 6.32 and 6.34. The Fig. 6.35b and Fig. 6.35c represent the harmonic voltage spectrum of PCC 1 and PCC 2 with very low magnitude of 5^{th} , 25^{th} and 35^{th} harmonics.

The lower harmonic resonanace impedance magnitude in Fig. 6.36a shows motor starting with other load interactions. Starting of high capacity induction motors is one cause of voltage dips. During start-up an induction motor demand voltage five to six times higher than nominal speed and this takes several seconds, as such voltage dips occurs.

As observed in Fig. 6.36b and 6.36c shown that harmonics that are multiples of 2 are not seen because they cancel out. The same is true for 3^{rd} order harmonics (3^{rd}, 6^{th}, 9^{th}

etc.). Because the power supply is three-phase, the third order harmonics cancel each other out in each phase. This leaves only the 5^{th}, 25^{th}, 35^{th} etc.

The magnitude of the harmonics produced by SVC and capacitor banks is greatest for the lower order harmonics (5^{th}) and drops quickly as you move into the higher order harmonics (35^{th} and greater).

6.6.4. Impact of Tuned Reactor Filter

The little harmonic resonance peak in Fig. 6.36a could be avoided by installing tuned frequency filter. In order to avoid this harmonic magnification we choose a tuned frequency less than nine. The frequency characteristic of the tuned filter at 7^{th} harmonics is shown Fig. 6.41 using the following equations.

$$L_f = \frac{1000\left(kV_{base}\right)^2 f}{2\pi\left(h_f\right)^2 kVAR_{cap}} \tag{6.84}$$

$$f_{resonance} = \frac{1}{2\pi\sqrt{L_f C}} \tag{6.85}$$

where

f – fundamental frequency (50Hz)

h_f – harmonic level frequency (e.g for 7^{th} harmonic level frequency = $7 \times 50 = 350$Hz

As it can be seen from the Fig. 6.37a harmonic resonance in the system has been removed. Moreover, there is some reduction for all the other harmonic components as shown in Fig. 6.37b and Fig. 6.37c

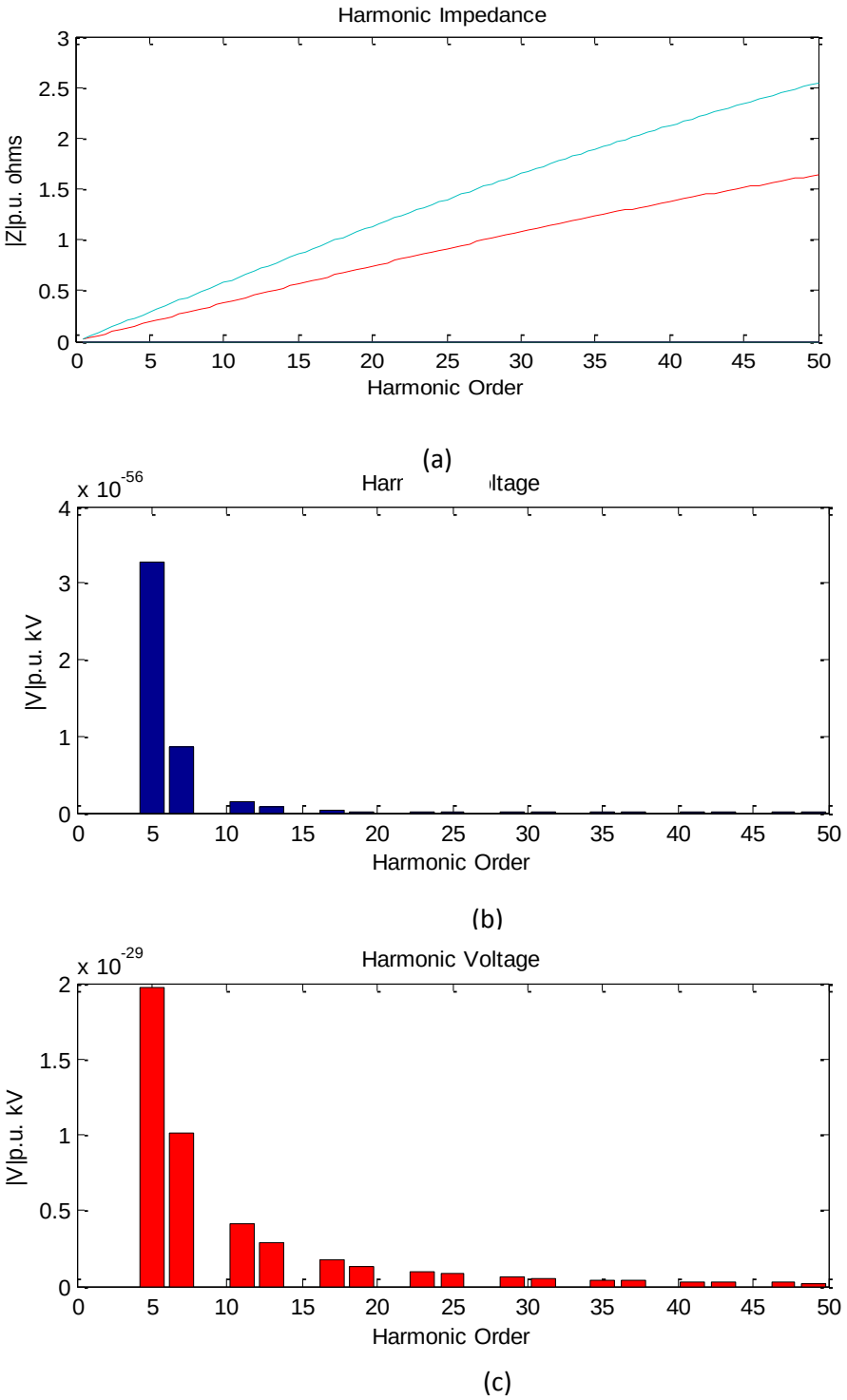

Figure 6.37. (a) Harmonic resonance with tune filter (b) Harmonic voltage spectrum of PCC one (c) Harmonic voltage spectrum of PCC two

The harmonic current of the SVC and capacitor bank can be determine using the following relations,

$$I_{SVC} = \frac{Z_{TOTAL}}{Z_{SVC}} I_h \tag{6.86}$$

$$I_C = \left(\frac{Z_{TOTAL}}{Z_C} + Z_{TOTAL} \right) I_h \tag{6.87}$$

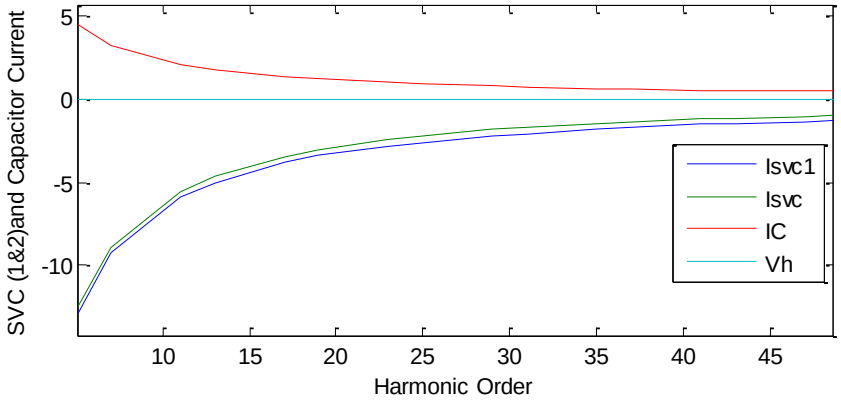

Figure 6.38. SVC current and capacitor current as afunction of system impedance

Figure 6.38shows the behaviour of the SVC and capacitor current and harmonic voltage. As observed the SVC current is absolutely reactive region, while the capacitor current is purely active region and harmonic voltage is acting from the apparent region. These indicate that the majority of the reactive power is supplied by the SVC. The harmonic currents appears not to contain lower harmonics such as 3rd, 5th, 7th and 9th (h = 2k+1, with k = 1,2,3...) harmonics.

6.7. Conclusions

It is possible to suggest that renewable energy in the form of wind energy could become economically viable within oil and gas production field in future. The large actual power MW produced by wind energy may lower harmonic distortion on the PCC voltage. The reduction of CO_2 and the fact that wind source is free presents the real possibility that wind energy might become the energy source of choice for the oil and gas industry.

The harmonic currents induce harmonic voltages at the PCC. The impedance harmonic depends on the harmonic current injection to the PCC and the resulting harmonic voltage is computed. The harmonic distortion on the PCC voltage caused by harmonic current drawn by the nonlinear loads on the oil platform, this causes the harmonic current to flow through the pure linear resistive load.

After respective computational implementation of the model, there followed a set of studies for the evaluation of a simplified power factor capacitor bank compensation, comparable to SVC. Although, the capacitor compensation improved the power factor correction of the induction motor, it also introduced harmonic resonance problem in the system. This problem could be averted using appropriate SVC as seen. The reduction of the harmonic components and harmonic resonance is mainly, by the replacement of capacitor bank or use of both.

In investigating the performance of ASVC at distribution systems network some choices have been made regarding system studies, the ASVC, and a tool for harmonic control. The radial model has been chosen as the study system. This choice has been motivated by the fact that the model has been established to provide a common reference system to researchers conducting comparative performance studies, either of component interactions or of harmonic control concepts. Some modifications of the system have been carried out to create a very weak ac system at the inverter site.

6.8. References

[1] P.E.R.Walling, and D.Mueller,"Harmonics and Resonance Issues in Wind Power". *IEEE PES General Meeting, July 26th, 2011.*

[2] M. Hacil, A. Khezzar, A.L. Nemmour and L. Louze," Harmonic current cancellation and control of a grid-connected synchronous generator entrained by a wind turbine". *Revue des Energies Renouvelables Vol. 12 N°3 (2009) 405 – 418*

[3] F. Blaabjerg and Z. Chen, "Power Electronics for Modern Wind Turbines", 1st ed. Morgan & Claypool, 2006.

[4] Ł.H.Kocewiak, J.Hjerrild, and C. L. Bak, "Harmonic Analysis of Offshore Wind Farms with Full Converter Wind Turbines".

[5] C.H.Chien, R.W.G. Bucknall,"Theoretical Aspects of the Harmonic Performance of Subsea AC Transmission Systems for Offshore Power Generation Schemes", in Proc. *Generation Transmission and Distribution*, 2006, p. 599-609.

[6] J.Arrillage, B.C.Smith, N.R.Watson, and A.R.Wood, "Power System Harmonic Analysis".*ISBN 0 471 97548 6. 1997*

[7] O.Anaya-Lara, N.Jenkins, J.Ekanayake, P.Cartwright, and M.Hughes, "Wind Energy Generation Modelling and Control". *ISBN 978-0-470-71433-1 (H/B). 2009.*

[8] W.Shepherd, and L.Zhang, "Electricity Generation using Wind Power" *ISBN 13 978-981-4304-13-9. 2011.*

[9] L. Asiminoaei, F. Blaabjerg and S. Hansen, "Evaluation of Harmonic Detection Methods for Active Power Filter Applications" Applied Power Elec. Conf. and Expo. (APEC), *Vol. 1, pp.635-641, 2005.*

[10] T.B. Soeiro, M.Schweizer, J.Linner, P.Ranstad and J.W. Kolarl, "Comparison of 2- and 3-level Active Filters with Enhanced Bridge-Leg Loss Distribution".

[11] E.Acha, J.Arrillaga,A. Medina. and A.Semlyen, "General frame of reference for analysis of distortion in system with multiple transformer nonlinearities", *Proc.IEE Pt. C, Vol. 136, No.5, September, pp. 271-278. (1989),*

[12] E.Acha, and J.J.Rico ,"Harmonic domain modelling of non-linear power plant components", *ICHPS Conference, Bologna, Italy.* (1994).

[13] S.Ganesan, "Selection of Current Transformers and Wire Sizing in Substations" ABB Inc.

[14] R.D.Henderson, and P.J.Rose,"Harmonics: The effects on Power Quality and Transformers", IEEE Trans Industry Appllication 1994, Vol 30(3), pp 528-532.

[15] S.I.Shahl, "Electrical Machines II".

[16] A.L.Sheldrake," Handbook of Electrical Engineering for Practitioners in the Oil, Gas and Petrochemical Industry" ISBN 0-471-49631-6. 2003

[17] IEEE Recommended Practice for "Power Systems Analysis", *IEEE Std. 399-1990.*

[18] Y. Goo, J. N. Jiang, and C.Y. Tang, "Nonlinear Control of Wind Power Generation Systems," 2009 IEEE Xplore.

[19] M. Liserre, R. Cardenas, M. Molinas, and J. Rodriguez, "Overview of multi-MW wind turbines and wind parks," *IEEE Trans. Ind. Electron.*, vol. 58, no. 4, pp. 1081–1095, Apr. 2011.

[20] F. Van Hulle and N. Fichaux, "Powering Europe: Wind energy and the electricity grid," Eur. Wind Energy Assoc., Brussels, Belgium, Nov. 2010.

[21] M. Tsili and S. Papathanassiou, "A review of grid code technical requirements for wind farms," *IET Renewable Power Gener.*, vol. 3, no. 3, pp. 308–332, Sep. 2009.

[22] M. Ali and B. Wu, "Comparison of stabilization methods for fixed speed wind generator systems," *IEEE Trans. Power Del.*, vol. 25, no. 1, pp. 323–331, Jan. 2010.

[23] V. Ramakrishnan, S. K. Srivatsa, "Pitch Control of Wind Turbine Generator by using New Mechanism"

[24] C.V. Nayar and J.H. Bundell, "Output Power controller for a Wind-Driven Induction Generator", IEEE Transactions on Aerospace and Electric Systems, vol. AES-23 no.3, pp. 388-400, May 1987

[25] S. M. Salameh and L. F. Kazda, "Analysis of the steady state performance of the double output induction generators," IEEE Trans. Energy Convers., vol. EC-1, pp. 26–32, 1986.

[26] J. M. Elder, J. T. Boys, and J. L. Woodward, "The process of self excitation in induction generators," Proc. Inst. Elect. Eng. B, vol. 130, no. 2, pp. 103–108, Mar. 1983.

[27] R. C. Bansal, T. S. Bhatti, and D. P. Kothari, "A bibliographical survey on induction generators for application of nonconventional energy systems," IEEE Trans. Energy Convers., vol. 18, no. 3, pp. 433–439, Sep. 2003.

[28] R. C. Bansal, D. P. Kothari, and T. S. Bhatti, "Induction generator for isolated hybrid power system applications: A review," in *Proc. 24th Nat. Renewable Energy Conversion*, Bombay, India, Nov. 30/Dec. 2, 2000, pp. 462–467.

[29] B. Singh, "Induction generator-A prospective," *Elect. Mach. Power Systems*, vol. 23, pp. 163–177, 1995.

[30] P. K. S. Khan and J. K. Chatterjee, "Three-phase induction generators: A discussion on performance," *Elect. Mach. Power Syst.*, vol. 27, pp. 813–832, 1998.

[31] L.A.R.. Fajardo, A. Univ, F. F. Blaabjerg and A.D..Hansen, "Advanced Induction Machine model in Phase Coordinates for Wind Turbine Application" Electric Machines & Drives Conference. *IEMDC '07. IEEE International. 2007.*

[32] G.Ofualagba, and E.U.Ubeku,"The Analysis and Modelling of a Self-excited Induction Generator Driven by a Variable Speed Wind Turbine", Fundamental and Advanced 250 Topics in Wind Power

[33] P.C.Sem, "Principles of Electric Machines and Power Electronics", *ISBN-13: 9781118078877. 1996.*

[34] J.A.Restrepo, U.B.Simon, P.Bowler, "Analysis of induction machine slot harmonics in the TF domain", *Devices, Circuits and Systems, 1995, Proceedings of the 1995 First IEEE International Caracas Conference on Dec 1995.*

[35] D.C.Sue," High Efficiency Double-Fed Induction Generator Applied to Wind Power Generator Technical Analyses". *Energy and Power Engineering*, 2011, 3, 253-261.

[36] *IEEE Standard Test Procedure for Polyphase Induction Motors and Generator, IEEE Std 112-2004, 2004*.

[37] W Deprez, A Dexters, J Driesen, "Energy efficiency of small induction machine. Comparison between motor and generating mode" - *ICEM 2006, 2006 - esat.kuleuven.be*

[38] E.Muljadi, J.Sallan, M,Sanz , and C.P. Butterfield," Investigation of Self-Excited Induction Generators for Wind Turbine Applications", *February 2000 . NREL/CP-500-26713.*

[39] A. K. Tandon, S. S. Murthy and G. J. Berg, "Steady State Analysis of Capacitor Self-excited Induction Generators," *IEEE Transactions on Power Application Systems,* Vols. PAS-103, no. 3, pp. 612-618, March 1984.

[40] L. Quazene and G. McPherson, "Analysis of the Isolated Induction Generator," *IEEE Transactions on Power Apparatus and Systems*, Vols. PAS-102, no. 8, pp. 2793-2798, August 1983.

[41] S. S. Murthy, O. P. Malik and A. K. Tandon, "Analysis of Self-excited Induction Generators," *IEE Proceedings C on Generation, Transmission and Distribution,* vol. 129, no. 6, pp. 260-265, November 1982.

[42] S. Rajakaruna and R. Bonert, "A Technique for the Steady-state Analysis of a Self-excited Induction Generator with Variable Speed," *IEEE Transactions on Energy Conversion,* vol. 8, no. 4, pp. 757-761, December 1993.

[43] S. S. Murthy, G. Bhuvaneswari, S. Gao and R. K. Ahuja, "Self Excited Induction Generator for Renewable Energy Applications to Supply Single-phase Loads in Remote Locations," in *IEEE International Conference on Sustainable Energy Technologies*, Kandy, December 2010.

[44] L. Wang and C. H. Lee, "A Noval Analysis of the Performance of an Isolated Self-excited Induction Generator," *IEEE Transactions on Energy Conversion,* vol. 12, no. 2, pp. 109-115, June 1997.

[45] I. Boldea and S. A. Nasar, The Induction Machine Handbook, Florida: CRC Press, 2002.

[46] A.M.Sharaf,and S.K.Murugan, "Dynamic power filter & capacitor compensator for isolated self-excited induction generator driven by a wind turbine**".**

Harmonics and Quality of Power, 2004. 11th International Conference on Sept. 2004.

[47] E. Muljadi, C.P. Butterfield, H. Romanowitz, and R. Yinger "Self Excitation and Harmonics in Wind Power Generation". November 2004 • NREL/CP-500-33138.

[48] M. Bradt, B. Badrzadeh, E. Camm, D. Mueller, J. Schoene, T. Siebert, T. Smith, M. Starke, and R. Walling, "Harmonics and Resonance Issues in Wind Power Plants". *IEEE PES Wind Plant Collector System Design.*

[49] A.V.Jacn, E.Acha, and A.Gomez, "Voltage Source Converter Modelling for Power System State Estimation: STATCOM and VSC-HVDC". *IEEE Transaction on Power Systems Vol. 23. No. 4 Nov. 2008.*

[50] P.W.Lehn, and K.L.Lian, "Frequency Coupling Matrix of a Voltage Source Converter Derived from Piecewise Linear Differential Equations". *IEEE Transaction on Power Delivery. Vol.22. July 2007.*

[51] P. W. Lehn," Direct Harmonic Analysis of the Voltage Source Converter". *IEEE Transactions on Power Delivery, Vol. 18, No. 3, July 2003*

CHAPTER 7

7. Harmonic Modelling of Multi-Terminal HVDC-VSC Oil and Gas Platforms

7.1. Introduction

The flexibility of VSC (AC-DC and DC-AC converters) technology has shown a strong competitive advantage in interconnecting different oil and gas platforms, functioning as the firewall against outages expanding and propagating [1-5]. For the AC grid, which has already experienced an outage or blackout, it can be started up by using a VSC-HVDC station [6]. It can provide effective voltage and frequency stabilization during the restoring process when the network experiences dramatic changes from zero short-circuit power to normal short-circuit power. This will make the restoration less complicated and more reliable [7].

VSC has two degrees of freedom, namely amplitude modulation index (*ma*) and the phase displacement (φ) [8]. These flexibilities together with its fixed voltage polarity for both rectifier and inverter modes of operation make VSC-HVDC the core component in developing multi-terminal oil and gas platforms as shown in Fig. 7.1.

The main function of the VSC-HVDC is to transmit constant DC power from the rectifiers to the inverters [9]. A VSC-HVDC link is also capable of transferring the active power from the grid and, at the same time, decreasing the disturbances from the utility grid [10]. When a VSC-HVDC supplies the oil and gas platform network, the inverter of the VSC-HVDC can use the AC voltage and frequency controllers to keep the load side AC voltage and frequency constant. In this way power-quality disturbances like voltage dips do not reach the oil and gas platform installations [11][12].

The aim of this chapter is to develop a flexible and robust multi-terminal VSC-HVDC model to implement harmonic power flow computational method. This is necessary for harmonic current injection and to carry out harmonic propagation studies in oil and gas

platform power systems. The harmonic power flow solution is aimed to derive fundamental frequency information for the voltage magnitudes and angles at all nodes of the network.

When using a conventional power flow, the assumption is made that all elements of the power system will not produce harmonics of fundamental frequency voltages and currents. These may include the transmission network, and any devices attached to generator or load buses. Conventional power flows do not allow the inclusion of harmonic devices, which are power system elements which will distort fundamental frequency voltages and currents [13].

A harmonic power flow is a tool which can predict the level and propagation of harmonics created by one or more harmonic device in the power system, the effects thereof, and the exploration of corrective measures using filtering techniques [14].

The harmonic power flows discussed in this chapter, only consider power systems operating in a completely balanced three-phase mode. Each phase of the three-phase power system contains identical fundamental and harmonic voltages and currents. One property of a completely balanced power system is that even harmonic currents and voltages do not exist**.** With completely balanced conditions assumed, a single line admittance (impedance) diagram of the power system may be used for each harmonic considered. In addition, the admittances (impedances) of each single line diagram must be scaled according to the harmonic frequency [15-16].

If unbalanced conditions exist, fundamental and harmonic currents each contain positive-, negative-, and zero-sequence components. The method of symmetrical components must then be used to simplify analysis, but will not be considered in this chapter. For this reason, all buses which contain harmonic producing devices will be referred to as harmonic buses.

All the passive elements are considered to perform linearly with frequency and the linear elements whose harmonic impedance is derived similarly to passive element. All non-linear loads are represented by either a harmonic current injection source or by a harmonic voltage source. Harmonic current injection sources are used to represent the harmonic contributions of rectifiers, inverters, static VAR compensators (SVCs).

Harmonic voltage sources are arc furnaces, and VSC, pulse-width modulation (PWM) converters.

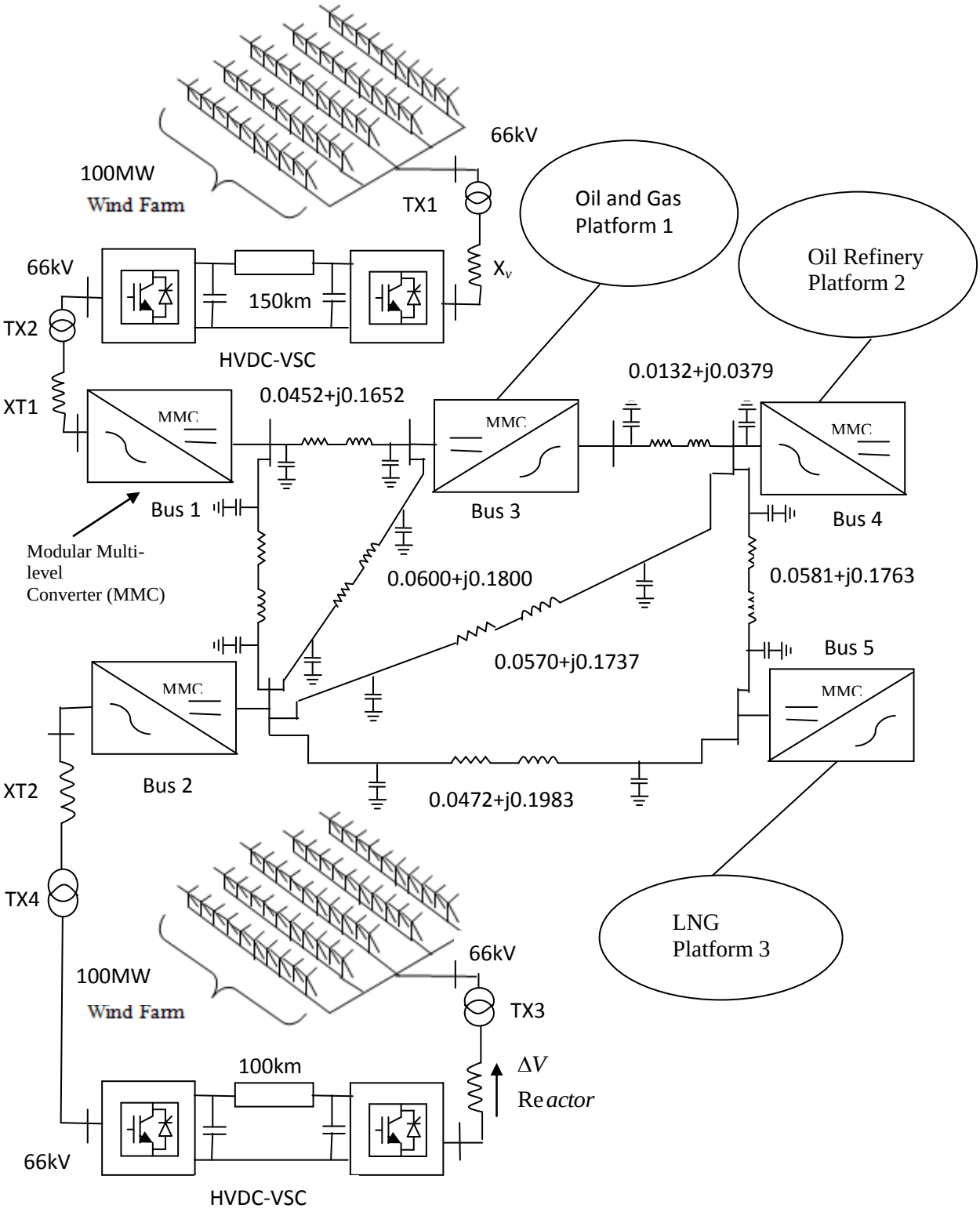

Figure 7.1. Multi-terminal network with modular multi-level converter used to obtain the driving point impedance and harmonic propagation

Transmission elements and linear loads are represented by impedances, at each harmonic *h*, with which the admittance matrix $\mathbf{Y}_h$ of the system is developed. The relevant harmonic current and voltage sources $\mathbf{I}_h$ and $\mathbf{V}_h$ are injected into the partially inverted nodal admittance matrix and the remaining nodal harmonic voltages and currents are derived using the Newton-Raphson method.

7.2. **Harmonic Power Flow**

It was mentioned in chapter one that VSC is referred to as self-commutated converters and is termed harmonic voltage source just as the name implies. With this capability VSC connected at all the nodes as shown in Fig. 7.1 provide voltage required at the nodes. Being a nonlinear component it is a source of harmonics in power networks [17]. This characteristic is of great importance in the harmonic power flow (HPF), to accurately model the nonlinear relationship between the current and voltage waveforms at each bus containing a harmonic device. For this reason, it is convenient to express distorted voltages and currents as Fourier Series (FS). In the case of HPF, the FS of the current entering a bus containing a harmonic device is expressed as a function of the FS of the voltage at this bus, and of any parameters which describe this distorted current waveform.

The harmonic voltage injection into the nodal signal can be expressed as follows

$$v_{an}(t) = M\cos(\omega_0 t + \theta_0) + M_h \cos(\omega_0 t + \theta_h)h \tag{7.1}$$

$$v_{bn}(t) = M\cos\left(\omega_0 t + \theta_0 - \frac{2\pi}{3}\right) + M_h \cos(\omega_0 t + \theta_h)h \tag{7.2}$$

$$v_{cn}(t) = M\cos\left(\omega_0 t + \theta_0 + \frac{2\pi}{3}\right) + M_h \cos(\omega_0 t + \theta_h)h \tag{7.3}$$

7.2.1. Switching Function Mode of the Rectifier Process

In Figure 7.1 input lines are connected to the output lines by bidirectional switching function (SF) and the single frequency (PWM) modulating signal form the matrix

converter. Each switch is operated by a diagonal switching function, *diag*(SF_{rc} (t)), where r denotes the row vectors and c the column vectors as represented in (7.4).

The switching function matrix SF_{rc} connecting the three-phase output voltages in Fig. 7.1 is given as

$$SF_{rc} = \begin{bmatrix} SF_{ab} & 0 & 0 \\ 0 & SF_{bc} & 0 \\ 0 & 0 & SF_{ca} \end{bmatrix} \tag{7.4}$$

The choice of the switching matrix determines the frequency, the amplitude and the phase of the output. The switches must be operated in such a way that the voltage and current Kirchoff's laws are not violated [18]. That is

- At all times, each of the output lines are connected to input lines otherwise fault will be generated by the inductive load which may damage the IGBTs switches
- No two input lines must be connected at the same time to the same outline otherwise a short circuit will emerge.

The output current (I_{dc}), is forced to flow through the load by the output voltage (V_{dc}). The mathematical model for matrix converter representing its basic operation is simple.

From Figure 5.1 (Chapter 5) the harmonics of the six switching functions $SF_{ab,bc,ca}$ voltages are

$$S_{v0} = \frac{1}{3} \tag{7.5}$$

$$SF_{vp} = \frac{1}{2n\pi}\left[\sin n\left(\frac{\pi}{3} - \frac{\mu}{2}\right) + \sin n\left(\frac{\pi}{3} + \frac{\mu}{2}\right)\right] e^{-jn\left(\varphi_r + \phi_p + \pi/2 + \alpha\right)} \tag{7.6}$$

where

φ_r is the shift angle of the AC voltage supply with respect in the reference $v_a(t) = V_a \sin \omega_0 t$

φ_p is the sequence phase angle required to fire the IGBTs per SM. i.e.

Table 7.2 The sequence phase angle

Angle φ_p	0	$\frac{\pi}{3}$	$\frac{2\pi}{3}$	π	$\frac{4\pi}{3}$	$\frac{5\pi}{3}$
IGBT	1	2	3	4	5	6

α is the firing angle

The output voltage of the converter sub-module (SM) leg A, B, C are given by

$$V_{outA} = \frac{ma}{2} SF_{va} h \tag{7.7}$$

$$V_{outB} = \frac{ma}{2} SF_{vb} h \tag{7.8}$$

$$V_{outC} = \frac{ma}{2} SF_{vc} h \tag{7.9}$$

where *ma* is the modulation index and $SF_{v\ldots}$ is switching function voltages

The phase voltage

$$V_a = V_{outA} - V_{nph} \tag{7.10}$$

$$V_b = V_{outB} - V_{nph} \tag{7.11}$$

$$V_c = V_{outC} - V_{nph} \tag{7.12}$$

It is now understood that the operating principle of an ideal converter without commutation process can be linked as the process of modulating the ac side voltage with a switching function to obtain the DC voltage as

$$V_{dc} = SF_{ab} V_a \; ; \; V_{dc} = SF_{bc} V_a \; ; \quad V_{dc} = SF_{ca} V_a \tag{7.13}$$

7.3. Potential Application of the Admittance (Y) Matrix of the Five Buses

The effect of the DC voltages is evaluated by using impedances connected between buses in the harmonic network [19]. The value of these impedances depends on the behaviour of the converter. In the studies performed, the impedance is calculated from the injection power and the applied bus voltage at the fundamental frequency. In the presence of harmonics, the resistance remains constant and the reactance is assumed to vary in direct proportion to the harmonic number. If there is a large compensation or filter capacitor connected to the bus, it is necessary to separate it from the load and consider it as an independent branch [20-21]. The admittance at a harmonic frequency is in direct proportion to the harmonic number.

Transmission lines are distributed parameter devices. In power system analysis, these lines are usually treated as lumped parameters devices, employing either π or T equivalent circuit. It is important to consider the wave solution only for a long line. In

the harmonic domain, the skin effect and wave solution are important and cannot be ignored as investigated in chapter four. The equation for evaluating the admittance matrix of the five buses is given by

$$\begin{bmatrix} I_{dc1} \\ I_{dc2} \\ \cdots \\ I_{dc4} \\ I_{dc5} \end{bmatrix} = \begin{bmatrix} Y_{1,1} & Y_{1,2} & \cdots & Y_{1,4} & Y_{1,5} \\ Y_{2,1} & Y_{2,2} & \cdots & Y_{2,4} & Y_{2,5} \\ \cdots & \cdots & \cdots & \cdots & \cdots \\ Y_{4,1} & Y_{4,2} & \cdots & Y_{4,4} & Y_{4,5} \\ Y_{5,1} & Y_{5,2} & \cdots & Y_{5,4} & Y_{5,5} \end{bmatrix} \begin{bmatrix} V_{dc1} \\ V_{dc2} \\ \cdots \\ V_{dc4} \\ V_{dc5} \end{bmatrix} \tag{7.14}$$

The DC current I_{dc} is given by

$$I_{dc} = Y^{-1}V_{dc} \tag{7.15}$$

where, Y is the admittance matrix of the five bus multi-terminal system

Similarly, the ac current (I_{in}) can be determined by modulating the DC current with the current switching function (SF) given as

$$I_a = SF_{ab}I_{dc};\ I_b = SF_{bc}I_{dc};\ I_c = SF_{ca}I_{dc} \tag{7.16}$$

The six switching functions for the current are

$$S_{i0} = \frac{1}{3} \tag{7.17}$$

$$SF_{ip} = \frac{1}{n^2\pi\mu}\left[\cos n\left(\frac{\pi}{3} - \frac{\mu}{2}\right) - \cos n\left(\frac{\pi}{3} + \frac{\mu}{2}\right)\right] e^{-jn\left(\varphi_r + \phi_p + \pi/2 + \alpha\right)} \tag{7.18}$$

It should be reiterated here that when the converter is operating under unbalanced source conditions the commutation overlap for each phase will differ. Because the switching function for each phase will have a different waveform, and as such will require expression by different equation. Under this condition, the calculation of the harmonics becomes more complex. In order to avert this complexity, the average commutation overlap due to the positive sequence voltage may be utilized.

7.4. **Deriving Unknown Nodal Harmonic Voltages and Currents**

The formulation of Newton-Raphson power flow (NR-PF) begins from the basic network theorems [22]. The voltage source may be transformed to the current source provided that:

$$I_s = \frac{V_g}{Z_{eq}} \tag{7.19}$$

where I_s is the fundamental frequency current flow at bus *i* of n-bus system that corresponds to the one-line diagram of Fig. 7.1.
The apparent complex power *S*, in volt-amperes is given by

$$S = P + jQ = VI^* \quad \text{VA} \tag{7.20}$$

where I^* is the complex conjugate of *I*.

The bus currents flowing through each bus are given by

$$I_x = \frac{1}{jX_{xy}}\left(V_X - V_y\right) \tag{7.21}$$

$$I_x^* = \frac{1}{-jX_{xy}}\left(V_x^* - V_y^*\right) \tag{7.22}$$

Substituting (7.22) into (7.17) yields

$$S_x = \frac{V_x}{-jX_{xy}}\left(V_x^* - V_y^*\right) \tag{7.23}$$

From the complex conjugate Equ. (7.23) voltage magnitude relate to voltage angle by

$$V_1 = |V_1|\angle\delta \tag{7.24}$$

$$V_2 = |V_2|\angle 0^o \quad \text{then } V_2 = V_2^* \tag{7.25}$$

Substituting the value of $I_i = \sum_{k=1}^{n} Y_{ik}^{*} V_k^{*}$ into (7.16).

where n is the number of bus and i = 1,2,3,...n).

Therefore,

$$P_i + jQ_i = V_i\left(\sum_{k=1}^{n} Y_{ik}^{*} V_k^{*}\right) \qquad \text{where k = 1,2,3,...n} \qquad (7.26)$$

where

V_i is the voltage of the ith bus

Y_{ik} is the admittance matrix of the network

Separating (7.26) to real and imaginary parts, yields

$$P_i = \mathrm{Re}\left(V_i\left(\sum_{k=1}^{n} Y_{ik}^{*} V_k^{*}\right)\right) \qquad \text{where k = 1,2,3,...n} \qquad (7.27)$$

$$Q_i = \mathrm{Im}\left(V_i\left(\sum_{k=1}^{n} Y_{ik}^{*} V_k^{*}\right)\right) \qquad \text{where k = 1,2,3,...n} \qquad (7.28)$$

where

P_i is the real power

Q_i is the reactive power

Substituting $V_i = |V_i| e^{j\delta_i}$, $V_k = |V_k| e^{j\delta_k}$, $Y_{ik} = |Y_{ik}| e^{j\theta_{ik}}$ in (7.25), we have

where

$|V_i|$ is the voltage magnitude

δ_i is the voltage angle

θ_{ik} is the load angle

$$P_i + jQ_i = |V_i| e^{j\delta_i} \sum_{k=1}^{n} |V_k| e^{-j\delta_k} |Y_{ik}| e^{-j\theta_{ik}} \qquad \text{where } i = 1,2,3,...n \qquad (7.29)$$

$$P_i + jQ_i = |V_i| \sum_{k=1}^{n} |V_k| |Y_{ik}| e^{j(\delta_i - \delta_k - \theta_{ik})} \qquad \text{where } i = 1,2,3,...n \qquad (7.30)$$

$$P_i + jQ_i = |V_i| \sum_{k=1}^{n} |V_k| |Y_{ik}| \angle(\delta_i - \delta_k - \theta_{ik}) \qquad \text{where } i = 1,2,3,...n \qquad (7.31)$$

$$P_i + jQ_i = |V_i| \sum_{k=1}^{n} |V_k| |Y_{ik}| (\cos(\delta_i - \delta_k - \theta_{ik}) + j \sin(\delta_i - \delta_k - \theta_{ik})) \qquad (7.32)$$

The real and reactive power of (7.32) are given by

$$P_i = |V_i| \sum_{k=1}^{n} |V_k| |Y_{ik}| (\cos(\delta_i - \delta_k - \theta_{ik})) \qquad (7.33)$$

$$Q_i = |V_i| \sum_{k=1}^{n} |V_k| |Y_{ik}| \left(\sin\left(\delta_i - \delta_k - \theta_{ik}\right)\right) \tag{7.34}$$

Equations (7.33) and (7.34) are strong tools for Newton-Raphson iterative method.
They constitute a set of nonlinear algebraic equations in terms of the independent variables, voltage magnitude in p.u., and phase angle in radians. Equation (7.33) gives the solution for each voltage controlled bus. Equation (7.33) and (7.34) can be expanded using Taylor's series neglecting all higher order terms and about the initial estimate will result in linear equation (7.35) called Jacobian matrix. The components of the Jacobian matrix are partial derivatives of (7.33) and (7.34) using $\left(\Delta|V_i|\right)$ and $\left(\Delta\delta_i\right)$.

$$\begin{bmatrix} \Delta P_2 \\ \vdots \\ \Delta P_n \\ \cdots \\ \Delta Q_2 \\ \vdots \\ \Delta Q_n \end{bmatrix} = \begin{bmatrix} \frac{\partial P_2}{\partial \delta_2} & \cdots & \frac{\partial P_2}{\partial \delta_n} & \vdots & \frac{\partial P_2}{\partial |V_2|} & \cdots & \frac{\partial P_2}{\partial |V_n|} \\ \vdots & J_{11} & \vdots & \vdots & \vdots & J_{12} & \vdots \\ \frac{\partial P_n}{\partial \delta_2} & \cdots & \frac{\partial P_n}{\partial \delta_n} & \vdots & \frac{\partial P_n}{\partial |V_2|} & \cdots & \frac{\partial P_n}{\partial |V_n|} \\ \cdots & \cdots & \cdots & & \cdots & \cdots & \cdots \\ \frac{\partial Q_2}{\partial \delta_2} & \cdots & \frac{\partial Q_2}{\partial \delta_n} & \vdots & \frac{\partial Q_2}{\partial |V_2|} & \cdots & \frac{\partial Q_2}{\partial |V_n|} \\ \vdots & J_{21} & \vdots & \vdots & \vdots & J_{22} & \vdots \\ \frac{\partial Q_n}{\partial \delta_2} & \cdots & \frac{\partial Q_n}{\partial \delta_n} & \vdots & \frac{\partial Q_n}{\partial |V_2|} & \cdots & \frac{\partial Q_n}{\partial |V_n|} \end{bmatrix} \begin{bmatrix} \Delta\delta_2 \\ \vdots \\ \Delta\delta_n \\ \cdots \\ \Delta|V_2| \\ \vdots \\ \Delta|V_n| \end{bmatrix} \tag{7.35}$$

In more compact form, (7.35) can be written as

$$\begin{bmatrix} \Delta P \\ \Delta Q \end{bmatrix} = \begin{bmatrix} J_{11} & J_{12} \\ J_{21} & J_{22} \end{bmatrix} \begin{bmatrix} \Delta\delta \\ \Delta|V| \end{bmatrix} \tag{7.36}$$

The Jacobian matrix (7.36) gives the linearized relationship between voltage magnitude $\left(\Delta|V_i|\right)$ and voltage angle $\left(\Delta\delta_i\right)$with respect to changes in real and reactive power.

Also, the admittance matrix (Y_{ik}) in (7.25) its real and reactive parts are separated to obtain the Conductance (G) and Susceptance (B) matrices.

$$P_i + jQ_i = |V_i| e^{j\delta_i} \sum_{k=1}^{n} (G_{ik} - jB_{ik}) |V_k| e^{-j\delta_k} \qquad \text{where } i = 1,2,3,...n \qquad (7.37)$$

where $Y_{ik} = G_{ik} + jB_{ik}$

$$Y_{ik} = G_{ik} - jB_{ik}$$

$$P_i + jQ_i = |V_i| \sum_{k=1}^{n} (G_{ik} - jB_{ik}) |V_k| e^{j(\delta_i - \delta_k)} \qquad \text{where } i = 1,2,3,...n \qquad (7.38)$$

$$P_i + jQ_i = |V_i| \sum_{k=1}^{n} (G_{ik} - jB_{ik}) |V_k| \angle(\delta_i - \delta_k) \qquad \text{where } i = 1,2,3,...n \qquad (7.39)$$

$$P_i + jQ_i = |V_i| \sum_{k=1}^{n} |V_k| (G_{ik} - jB_{ik}) (\cos(\delta_i - \delta_k) + j \sin(\delta_i - \delta_k)) \qquad (7.40)$$

$$P_i + jQ_i = |V_i| \sum_{k=1}^{n} |V_k| \left\{ \begin{vmatrix} G_{ik} \cos(\delta_i - \delta_k) + B_{ik} \sin(\delta_i - \delta_k) \\ + j[G_{ik} \sin(\delta_i - \delta_k) - B_{ik} \cos(\delta_i - \delta_k)] \end{vmatrix} \right\} \qquad (7.41)$$

From (7.42) the real and reactive power of the network can be computed as

$$P_i = |V_i| \sum_{k=1}^{n} |V_k| \{ G_{ik} \cos(\delta_i - \delta_k) + B_{ik} \sin(\delta_i - \delta_k) \} \qquad (7.42)$$

$$Q_i = |V_i| \sum_{k=1}^{n} |V_k| \{ [G_{ik} \sin(\delta_i - \delta_k) - B_{ik} \cos(\delta_i - \delta_k)] \} \qquad (7.43)$$

Equations (7.42) and (7.43) are strong tools for the development of Fast Decoupled Load Flow (FDLF). This is based on the assumption that, for a transmission line, its reactance is more than its resistance. That is $\frac{X}{R}$ >> 1, therefore, G_{ik} can be ignored because $G_{ik} << B_{ik}$.

The Newton-Raphson method has a quadratic convergence and computing time only increases linearly with system size.

7.4.1. **Newton-Raphson Conventional Power Flow: Test Case 1**

The five bus test network of Figure 7.1 has been modelled to perform power flow studies using the Newton-Raphson iterative method. The base reactive power value is 100 kV and base apparent power is 101 MVA. The transmission lines are nominal π-circuit and its corresponding parameters are given in table 7.1. The modular multi-level

dc is based on the multi-level dc system. Therefore, Table 7.2 shows the nodal dc voltages, voltage angles, PV bus active and reactive powers and PQ bus active and reactive powers. Bus 5 is chosen to be the slack bus, the line parameter and bus data are given as in Table A7.1 and Table A7.2.

The appearance of harmonic content in the nodal signal is not rare. It is expected that different control scenarios in grid-connected converters can include unwanted distortions or sometimes distortions introduced by a certain control purpose. One good example is common-mode 3^{rd}-harmonic injection in order to extend linear operation of the modulator.

The harmonic injection into the nodal signal can be expressed as depicted in Figure 7.2. The Fig. 7.6 shows dynamic impedance characteristics in aggregated 200 kV and 201 MVA. The choice of the line impedance parameters plays a significant role in determining the system performance. This is clear because as indicated by Equ. (7.44), a successful implementation of the Newton iterations depends on the input signal, the choice of the desired signal, and the convergence parameter. Figure 7.2(a) corresponds to the node one input signal, (b) to the node two input signal, (c) to the node three input signal, (d) to the node four input signal, and to the node five input signal. The steady-state periodic solution is given in the form of waveform as shown in Figure 7.2. The nodal input signals in the five nodes are all non-sinusoidal due to harmonic current injection.

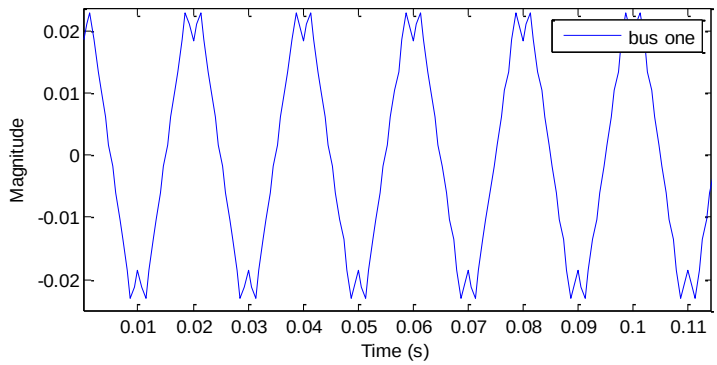

(a)

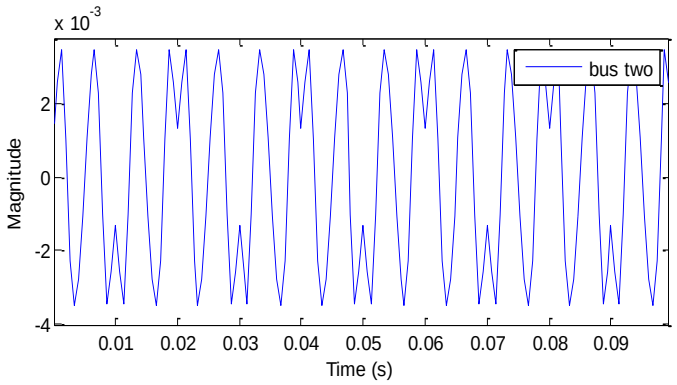

(b)

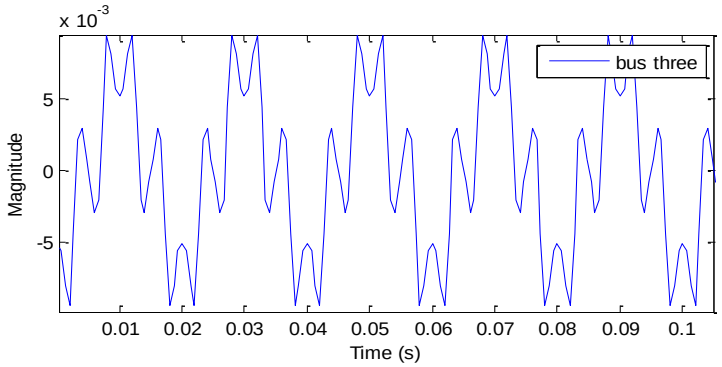

(c)

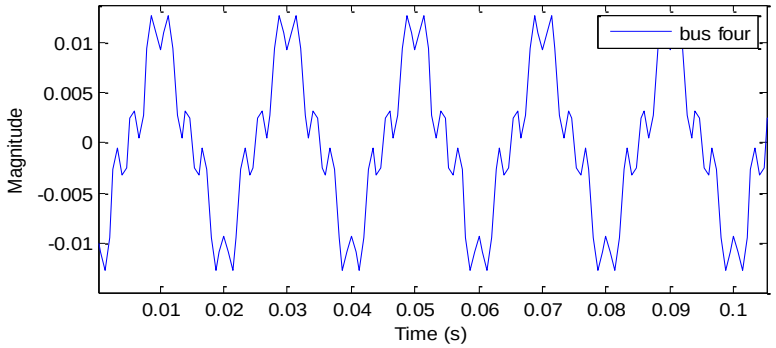

(d)

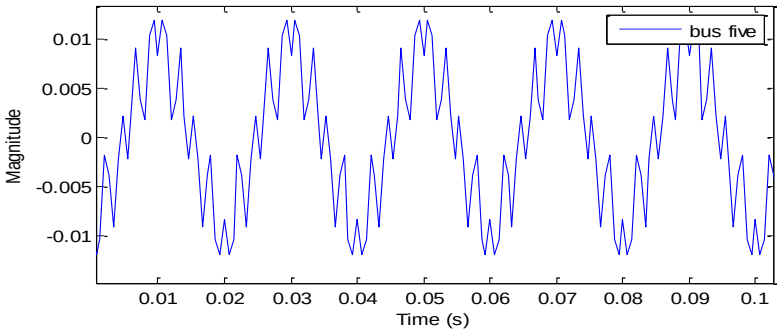

(e)

Figure 7.2. Instantaneous input signal waveforms at (a) bus 1 (b) bus 2 (c) bus 3 (d) bus 4 (e) bus 5

The above results shows that the natural sampled pulse-width modulation with harmonic injection in the nodal signal produces only fundamental harmonic defined by modulation index and dc-link voltage within the baseband harmonics range and injected harmonics with magnitude dependent on M_h and DC-link.

The signal in Fig. 7.2 contains the fundamental component, 3^{rd}, 5^{th} and 7^{th} harmonics. According to the waveforms in Fig. 7.2, the signal swell disturbance of fundamental component starts at the bus three (PQ bus), the 3^{rd} and the 5^{th} harmonic disturbance become more significant at bus four (PQ bus), whilst the 3^{rd}, 5^{th} and 7^{th} harmonic appear more disturbance at bus five (PQ bus). Hence, the information of fundamental frequency and harmonic components can easily be obtained from the waveforms in Fig. 7.2.

Figure 7.3 shows the phase current characteristic corresponding to the ac current obtained by harmonic voltage injection technique. Figure 7.4 depicted the load bus current obtained from the real power, reactive and bus voltage Newton's power flow. The ac voltages are available from ac power flow as shown in Figure 7.5. All currents and voltages in this circuit are non-sinusoidal also for the load currents. Of particular interest are the currents through the capacitive and the inductive elements of the multi-terminal network. In this case the line current at the buses are non-sinusoidal but it is likely that these are due to the harmonic currents injected.

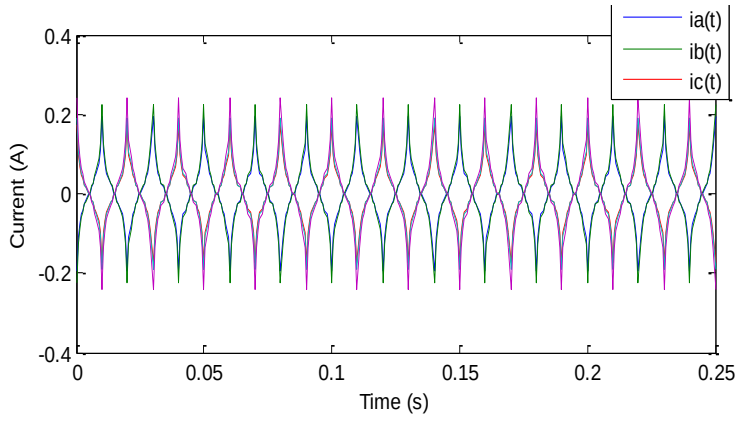

Figure 7.3. Three Phase Current Waveform

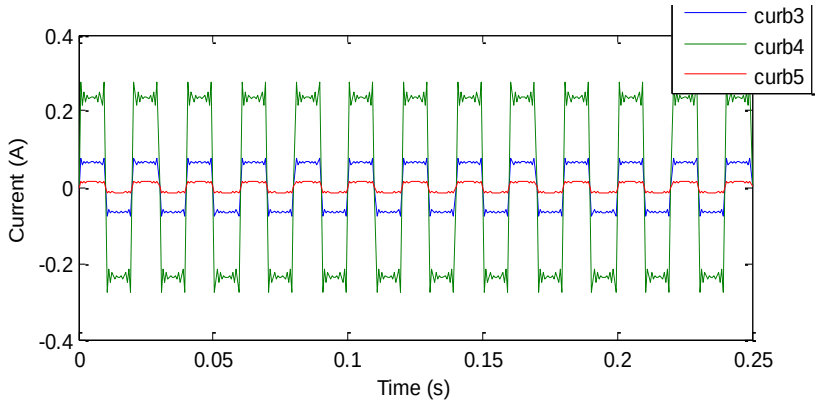

Figure 7.4. Load bus current waveform

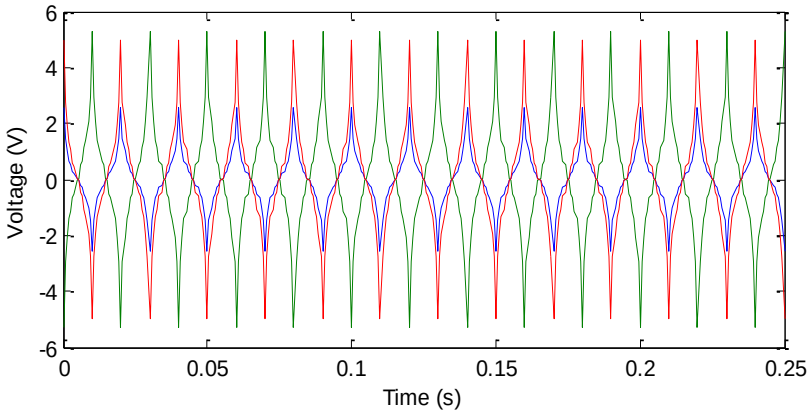

Figure 7.5. Voltage control bus waveform

7.5. **Harmonic Power Flow: Test Case 2**

Simulation studies of the proposed modular multi-level MTDC system for integrating two self-excited induction generators (SEIG) based wind farms (WFs) with the remote grids (oil and gas platforms). The system configuration and parameters are shown in Fig. 7.1. Two SEIG-based wind farms (WFs) are both rated at 200MW. The wind power is collected by aggregated WFs, and then finally transmitted to three remote platforms grids located 200km, 150km and 100km respectively away by VSC-HVDC links.

The proposed model for the five bus multi-terminal VSC-HVDC is implemented using MATLAB and the simulation parameters are as follows:

Table 7.3: Simulation Parameters

Dc-link input voltage Vd	300V
Carrier signal frequency	5 kHz
Control signal frequency (fc)	50 Hz
Modulation index (ma)	0.8
Number of harmonics (h)	200

The simulation DC voltage and current signal are presented in Fig. 7.6. Fig. 7.6a is the DC voltage obtained by modulating the ac side phase voltage with phase-to-phase switching function. The switching frequency on the rectifier side is assumed to be far greater than the fundamental frequency of the input voltage. DC side voltage is essentially decided by the switching function of the rectifier and the input voltage. While, Fig. 7.6b is the DC current obtained via product evaluation of the admittance matrix and the DC voltage. As observed from Fig. 7.6, the DC term at 100Hz separate the rectifier side and inverter side. The ac voltage and current at the left hand side was converted to dc signal by the rectifier (AC to DC) and the dc voltage and current at the right hand side was converted to ac signal by the inverter (DC to AC).

When harmonic components are known, the signal can be presented in a different way that highlights its frequency content rather than its time domain content. Fig. 7.7 show the frequencies content of DC voltage with its complex conjugate. The signal is contaminated, and it is not clear what the cause of this resonance is. However the magnitude spectrum of reveals a peak at 250 Hz which, after some analysis, coincides with the RPM of rated speed induction generator at 15,000rpm at these driving conditions. This prediction opens up a way for determining the capacity of wind farm generator to feed the oil and gas platforms.

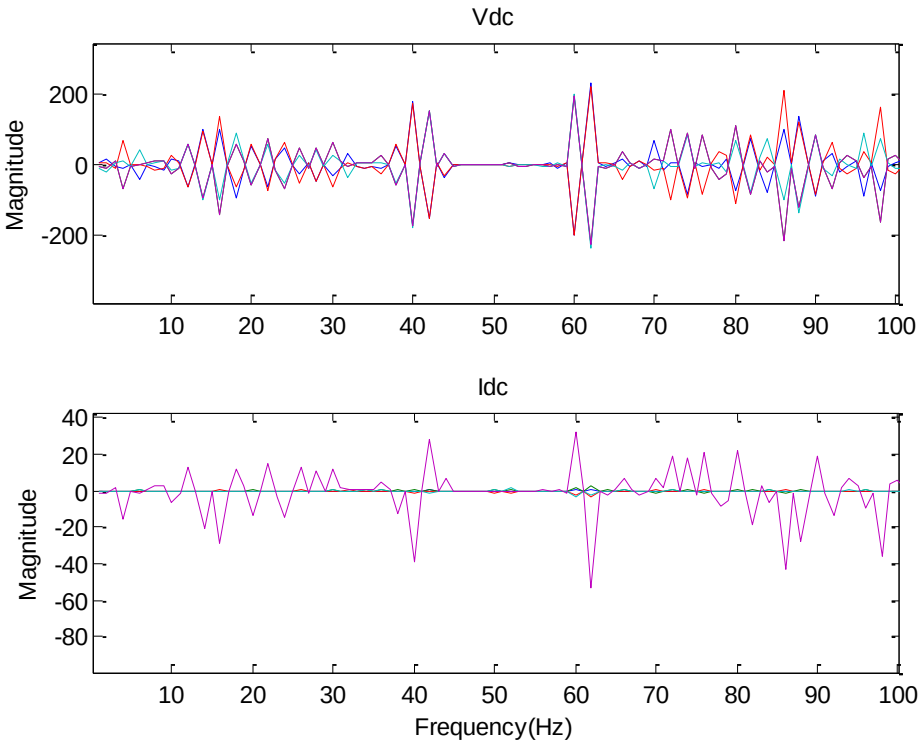

Figure 7.6. DC voltage and current at switching frequency

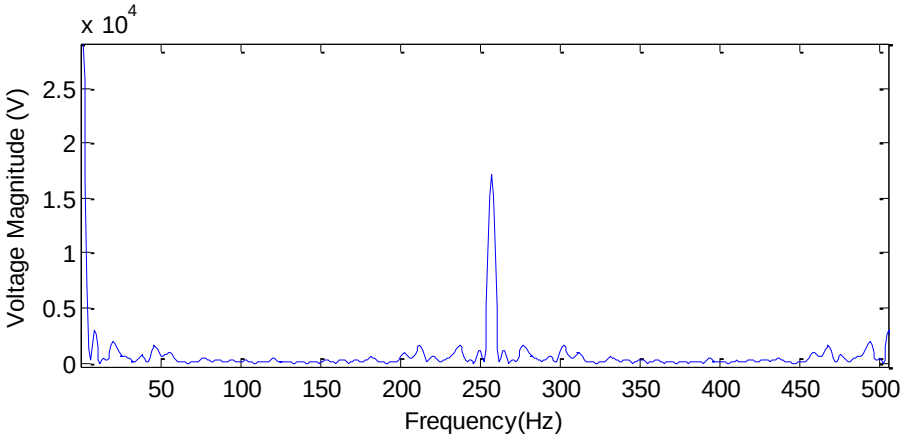

Figure 7.7. Frequency Content of Vdc with its complex conjugate

Figure 7.8 is input ac current (I_{in}) obtained via modulating the DC current with the phase-to- phase current switching function. To ensure a sinusoidal input current, it is mandatory to include a second active switching state of the input stage in the modulation scheme.

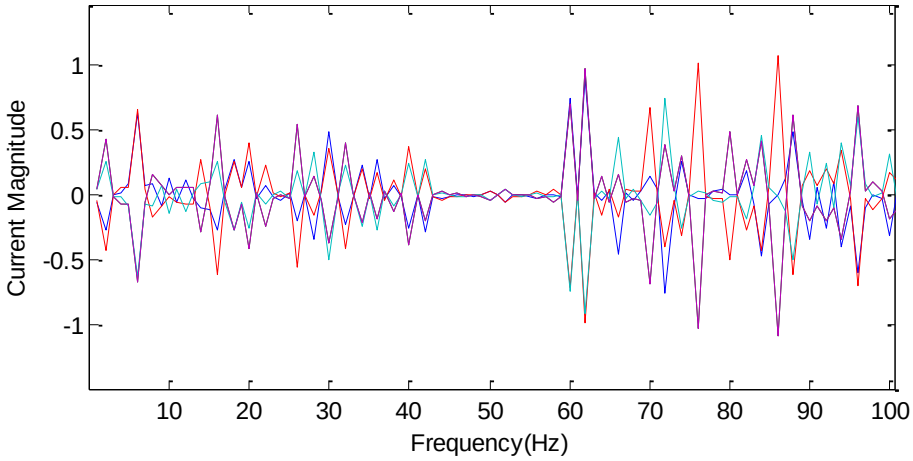

Figure 7.8. Input Current

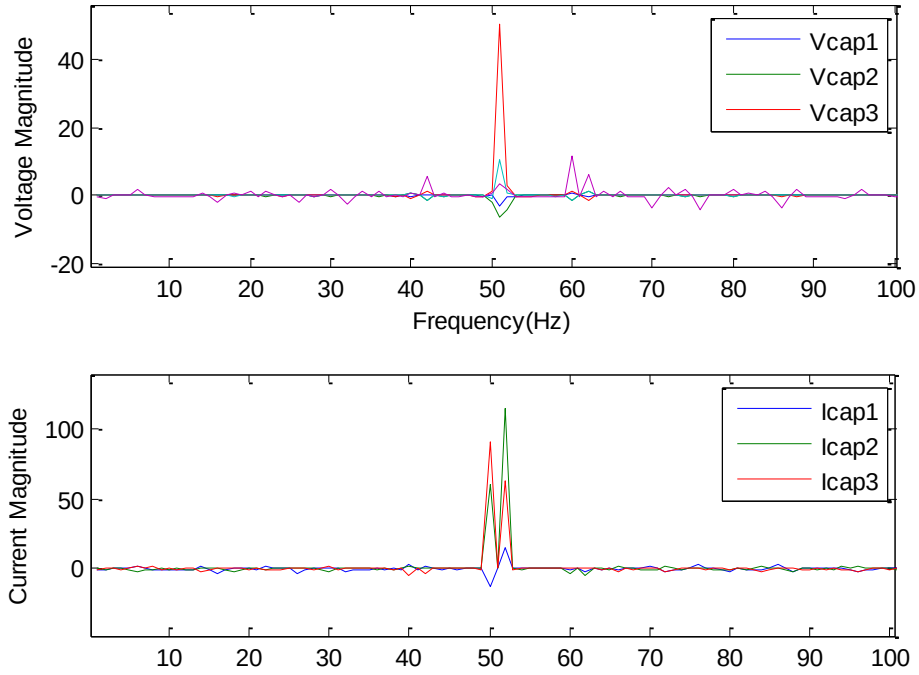

Figure 7.9. (a)Capacitor voltage (b) Capacitor current

Figure 7.9 depicts the capacitor voltage and current which are across the individual converter. The capacitor voltage is directly proportional to the equivalent capacitor impedance and DC current with the DC term. The capacitor current is the sum of the individual node current and the DC current.

The quadrature axis change in voltage due to reactive power has an effect on the resultant voltage magnitude *Vx*, therefore the resultant voltage depends only on the reactive power. Real Power (P) is determined by the desired amount of active power flow. Hence, voltage *Vx* can be maintained constantly by reactive power (Q) compensation.

Figure 7.10 depicts the voltage condition that fixed output voltage magnitude that remains constant regardless of changes to its input voltage or load conditions. As observed when the reactive power is lagging or such leading that QX > PR then the voltage condition is positive (i.e. receiving end voltage V_R is less than the sending end voltage V_S). For a given V_R the voltage condition of the line increases with the increase in reactive power. When the reactive power is leading to this extends that PR>QX, the voltage condition is negative, i.e. the receiving end voltage V_R is more than the sending end voltage V_S.

Switching conditions require a means to vary their output voltage in response to input and output voltage changes. The PWM controls the input to the associated power switch, which controls it's on and off time (duty cycle).

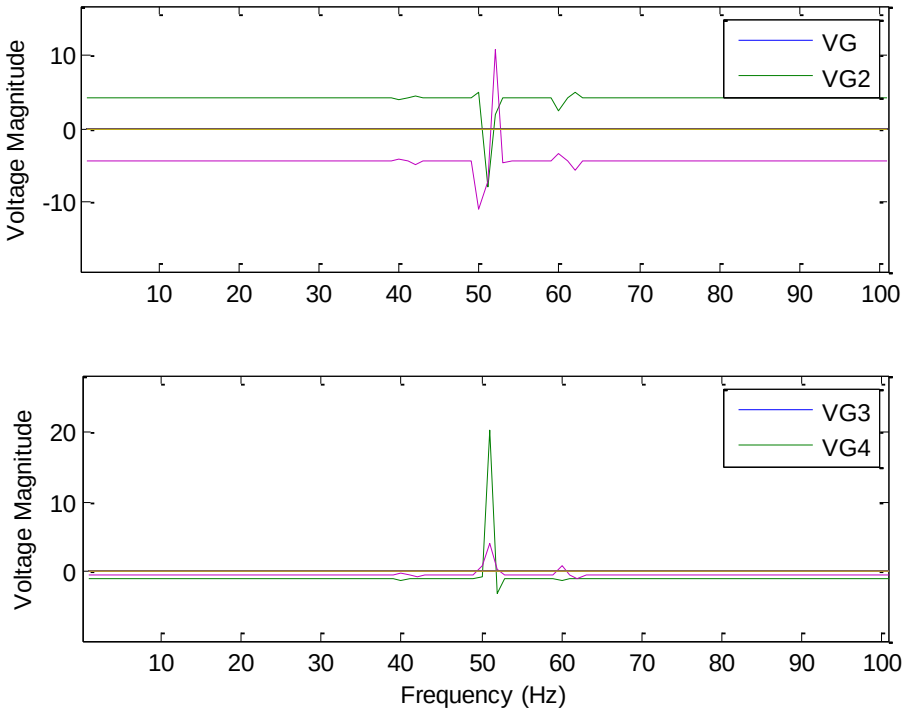

Figure 7.10. Voltage conditions at each node of the five VSCs bus

The instantaneous real and reactive powers of the respective bus network are depicts in Fig. 7.11. From the simulation results, the system reaches stable state at rectifier stage, i.e., from AC to DC before starting HVDC. In Fig.7.11a, wind farm system supplies 100 MW through the HVDC-VSC initially; before reaching node one, the decreased power output of VSC-HVDC are balanced by HVDC, operating at 50 kV eventually. DC voltage and current of HVDC rectifier side reaches the reference values of 1.0 p.u. and 0.2 p.u. respectively, as represented in Fig. 7.13.

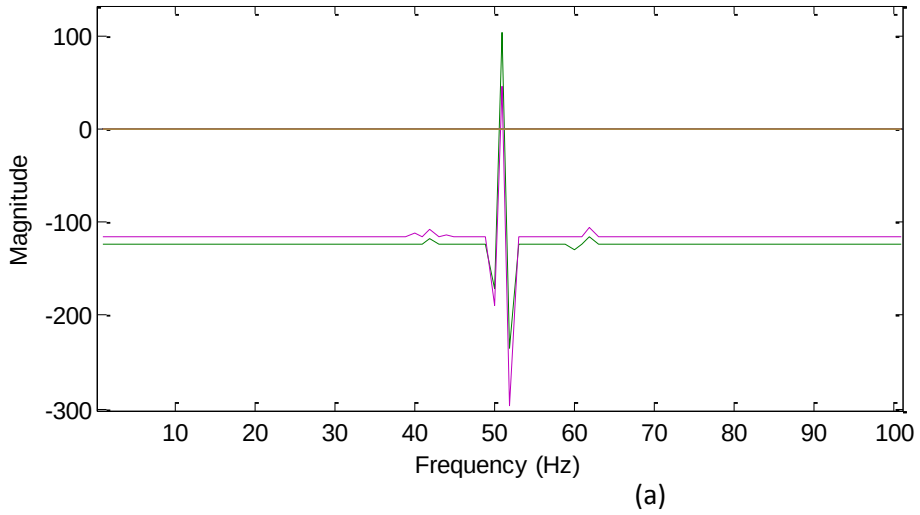

(a)

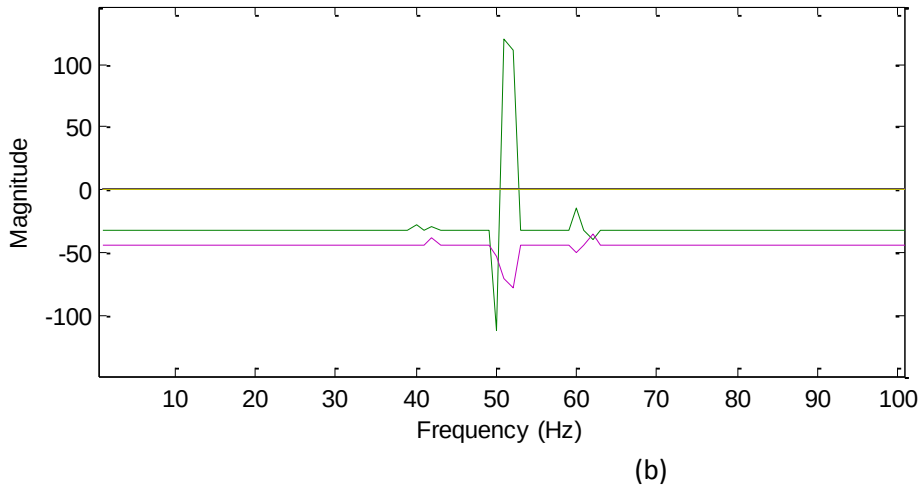

(b)

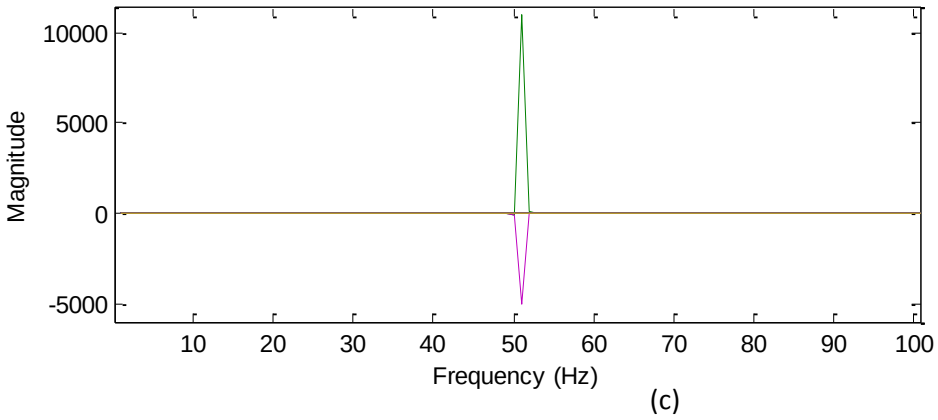

(c)

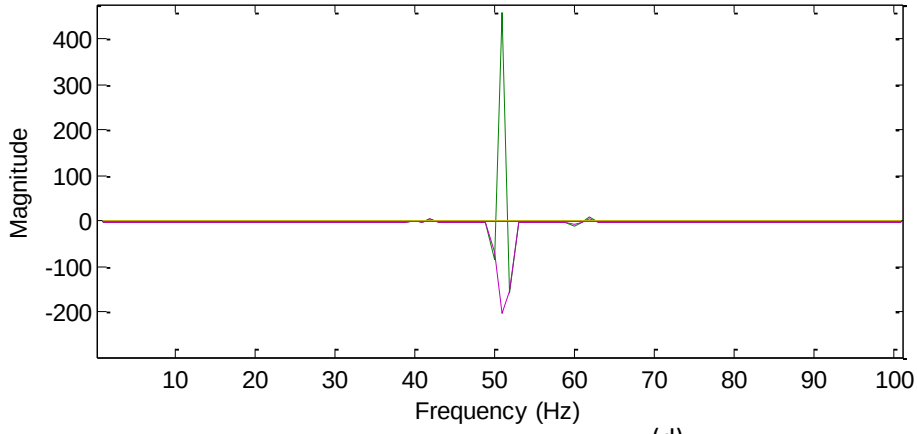

(d)

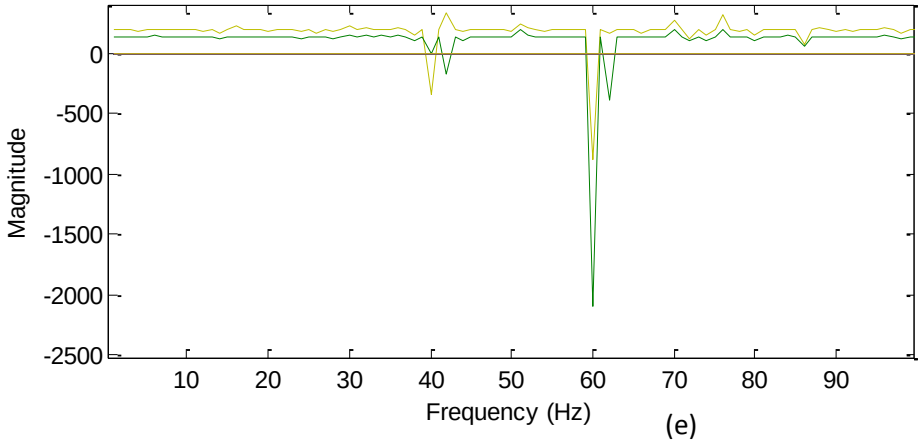

(e)

Figure 7.11. The instantaneous real and reactive powers of the five-bus network of a three SM-VSC Unipolar PWM Converters Switching Function

In Fig. 7.11 b, the wind farm system supplies 100 MW through the HVDC-VSC initially; before reaching node two, its node voltage is 99.96 kV eventually.

Figures 7.11c, 7.11d and 7.11e shows the instantaneous real and reactive powers of the platforms bus (load bus). The platforms node voltages are 74 kV, 72 kV, and 40 kV respectively.

In this simulation, the AC/DC rectifiers of the network have been subjected to three-phase modular multi-level behaviour of the multi-terminal HVDC-VSC network. It can be seen in Figure 7.11 that the three SM-converters have a high magnitude of instantaneous real and reactive power comparable to five SM-converters as depicted in Figure 7.12. This improves the real and reactive power profiles. Also noticeable is that the ten SM-converter as shown in Figure 7.13 has significant improvement on the power quality of the whole system.

Active and reactive power shown in Figure 7.11-7.13, are handled by all nodes. The nodes network has enough reserve to take additional power to account for any mismatches in the DC network as shown in the figures below. Figure 7.11-7.13 shows active power being transferred to the DC via the AC side.

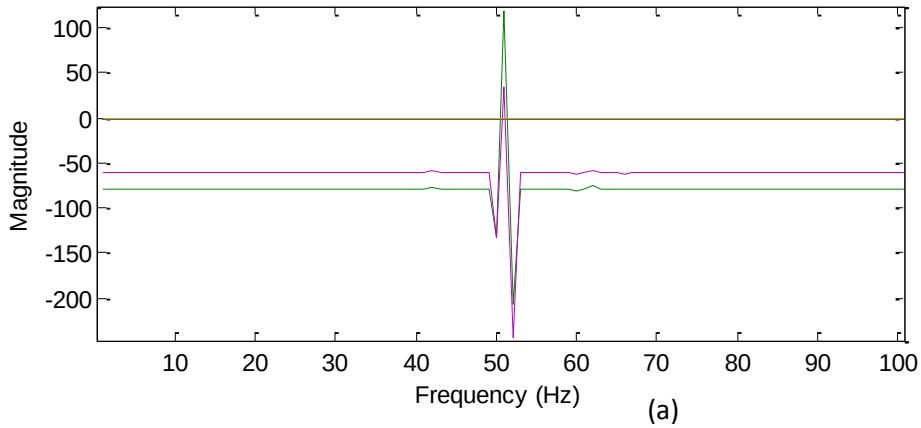

(a)

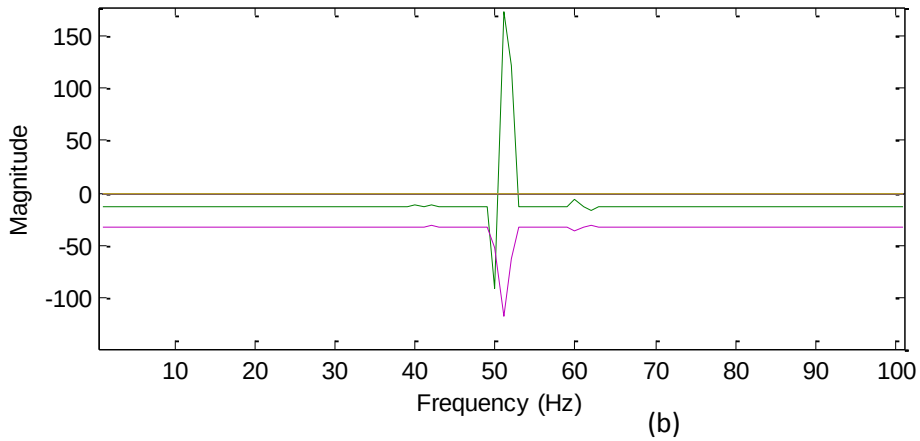

(b)

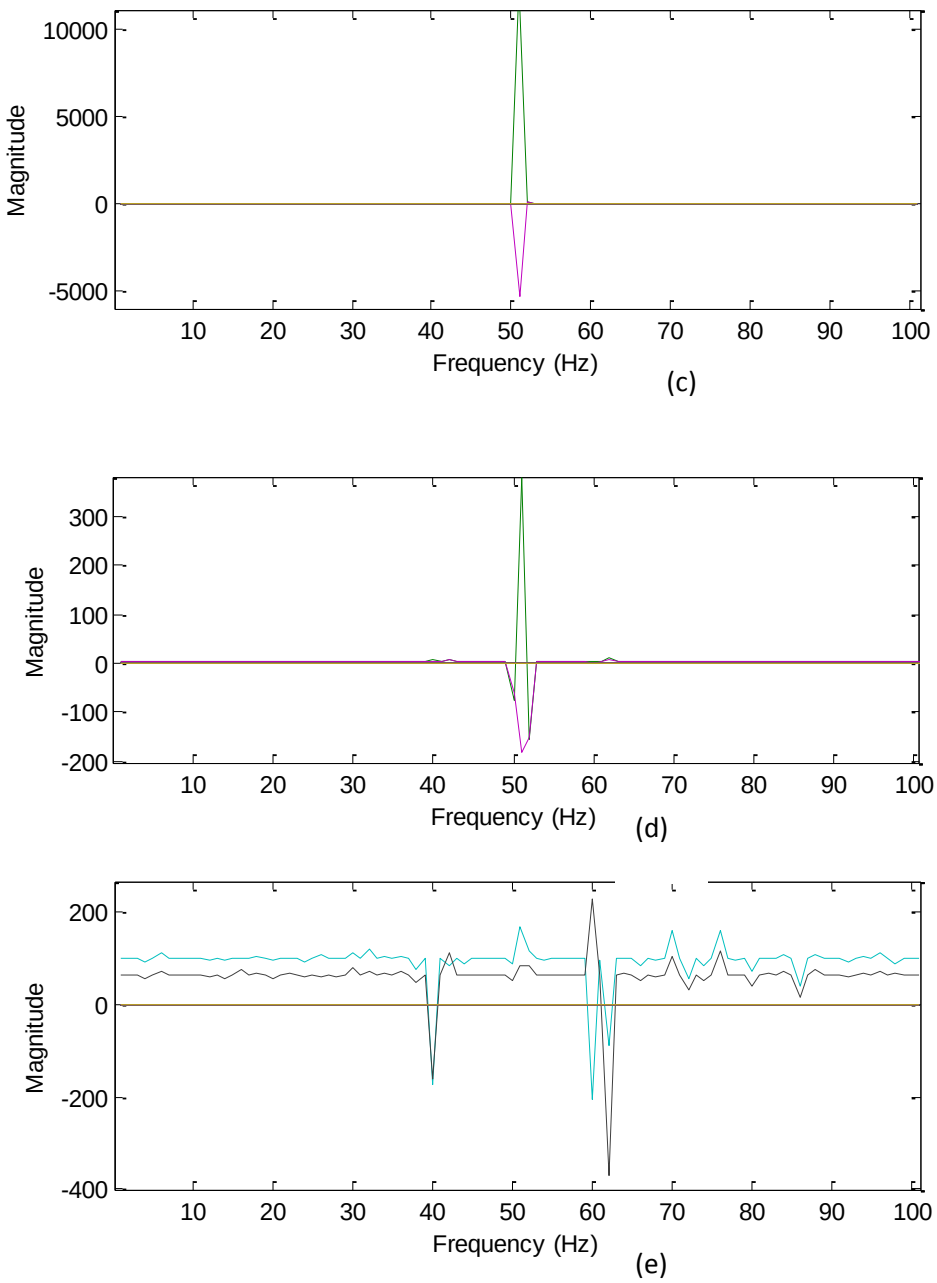

Figure 7.12. The instantaneous real and reactive powers of the five-bus network of a five SM-VSC Unipolar PWM Converters Switching Function

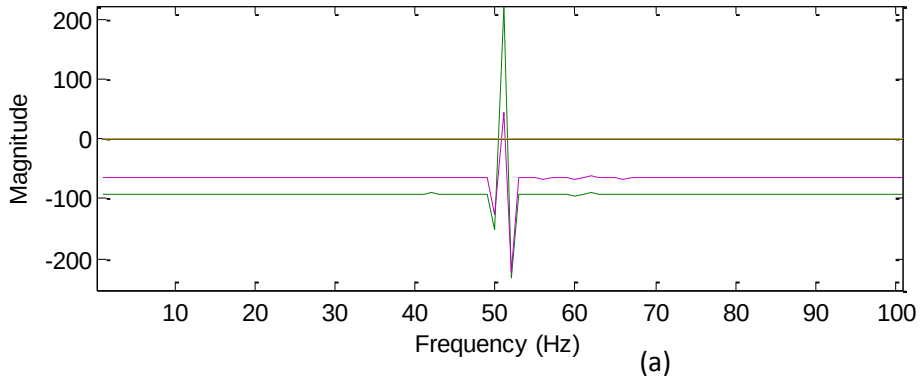
Magnitude
200
100
0
-100
-200
10
20
30
40
50
60
70
80
90
100
Frequency (Hz)

(a)

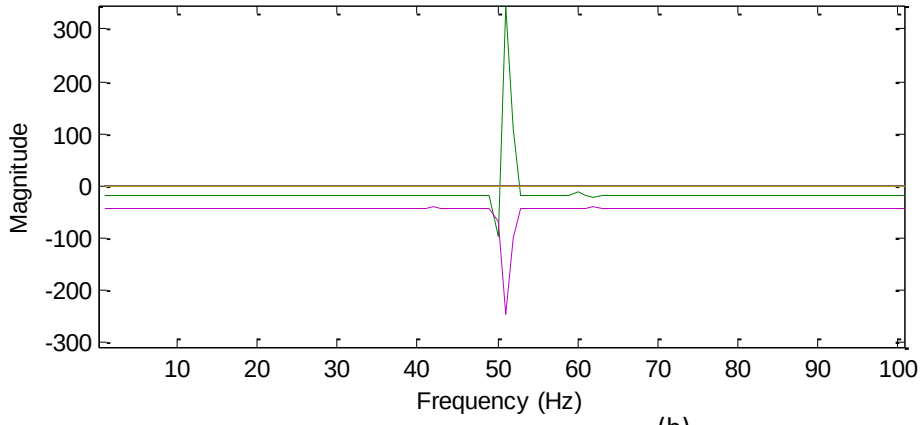
Magnitude
300
200
100
0
-100
-200
-300
10
20
30
40
50
60
70
80
90
100
Frequency (Hz)

(b)

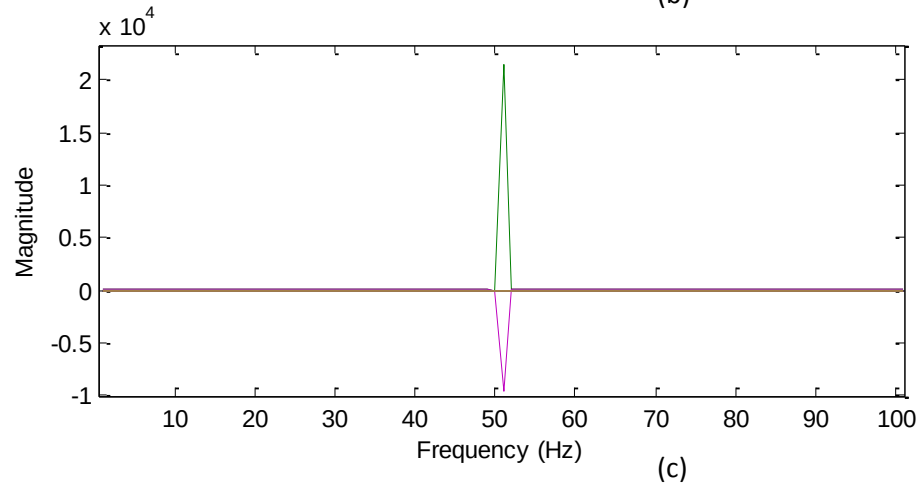
x 10^4
Magnitude
2
1.5
1
0.5
0
-0.5
-1
10
20
30
40
50
60
70
80
90
100
Frequency (Hz)

(c)

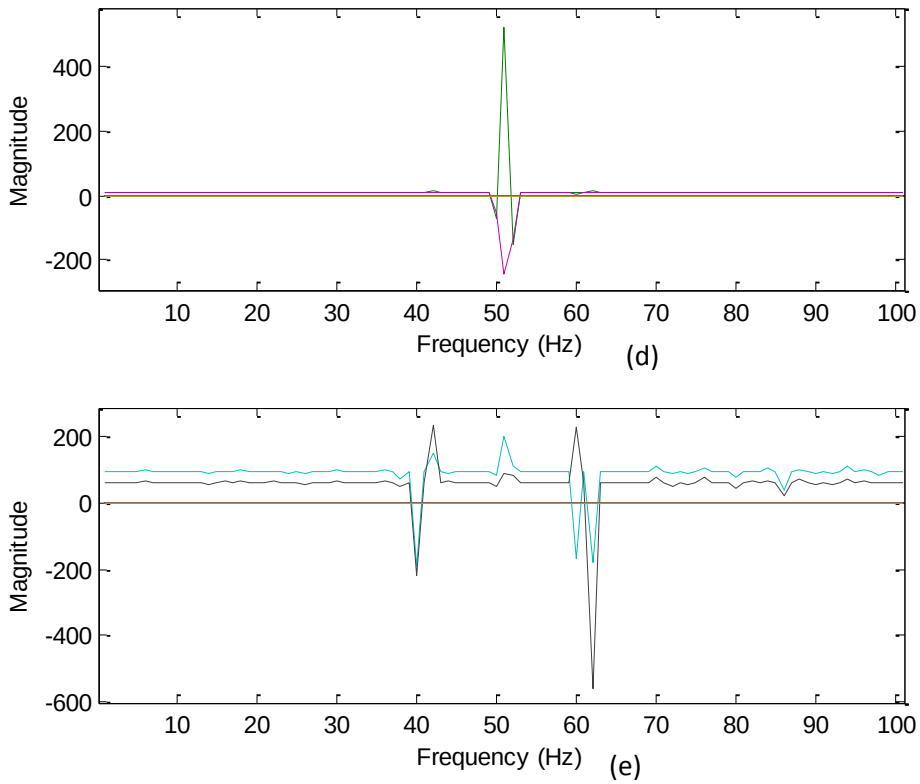

Figure 7.13. The instantaneous real and reactive powers of the five-bus network of a ten SM-VSC Unipolar PWM Converters Switching Function

The full-scale power converter presented in Figure 7.1 typically can include a generator bridge, which in normal operation operates as an active rectifier to supply power to a DC-link circuit. The wind farm-side converter (rectifier) can have suitable topology based on full-bridge converters fully controlled and regulated using pulse-width modulation. The DC output of the generator bridge to the DC terminals of a network bridge through the DC-link circuit. The smoothing reactor is selected to avoid resonance in the DC side at low order harmonic frequencies like 100 or 150 Hz. This is important to avoid the amplification effect for harmonics originally from the AC system, like negative sequence and transformer saturation.

The grid-side converter normally operates as a PQ bus and is also considered within the analysis as an inverter. The network bridge can have a topology as presented in Figure 6.1 fully controlled using the pulse-width modulation strategy. The AC output voltage of the grid-side converter is filtered and supplied to the fixed frequency supply network via a step-up transformer.

A good criterion of harmonic resonance issue is the capacity of the MMC which are shown for all considered cases. The solutions of the frequency response equations regarding the stability of the system are shown in Figs. 7.11 to 7.13. These distorted signals contains just one resonant argument and not damagerous, just a little aggravating will lead to realistic power quality.

Figure 7.11 shows the effect of the three-SM on the multi-terminal MMC-HVDC-VSC for harmonic elimination and stability case. It can be seen from the figure that maximum steady state magnitude occurs when harmonic resonance equal 2 kHz except for Fig. 7.11c, 7.11d, and 7.11e that appears at 1 kHz. It is clear that power quality is achieved after harmonic resonance at 2 kHz.
Figure 7.12, shows the power quality results for the five-SM case. Also, it can be seen that from Fig. 7.12, that the last resonance that was observed in three-SM case has been eliminated or shifted backward. Clean evidence that more power quality is achieved as the SM converter increase.

Figure 7.13, illustrates the simulation for ten-SM, as shown the resonance is greatly reduced and is no longer providing the strong harmonic content. More also, all samples resonance are completely eliminated, which maybe excited by the out of balance harmonics.

7.6. **Conclusions**

A power flow model of the modular multi-level VSC is presented, it is seen that the modified load flow equations improve system performance.

In interconnected power systems different power quality problems exist. The harmonic voltage problem has a significant effect on voltage levels at each bus. In this thesis, the voltage levels at each bus for different types of loads are observed. The low voltage magnitude at all bus can be improved by introducing modular multi-level VSC device at the node locations. In this five bus system the desired location of VSC device is, at which all bus low voltage level is maintained. The performance of modular VSC to improve voltage bus with different type of loads is observed and also the effect of different locations of shunts compensators on voltage magnitude is observed.

Instantaneous power theory gives a piecemeal approach in analysis and control of the active and reactive components of the harmonic load and introduces the active power filter for appropriate corrective measure for the total harmonic distortion for improvement of the power quality as per the scheduled standards. Energy efficient power supplies incorporating active power supplies shall govern the future in the electrical power quality standardizations.

7.7. **References**

[1] R.Balamurugan and G.Gurusamy "Harmonic Optimization by Single Phase Improved Power Quality AC-DC Power Factor Corrected Converters", International Journal of Computer Applications, Volume 1, No. 5, 2010.

[2] J.Conde-Enriques, J.S.Benites-Read, J.L. Duran-Gomez and J.O.Pachecho-Sotelo J "Three-phase six-pulse buck rectifier with high quality input waveforms" 1999 *IEE Proceedings-Electric Power Applications* Vol. 146**.**

[3] W.A.A. De Doncker Rik, Deepakraj M.Divan, and M.H. Kheraluwala. "A Three-Phase Soft-Switched High-Power-Density DC/DC Converter for High-Power Applications". *IEEE Transactions on Industry Applications, 1991.*

[4] D.Czarkowski and M.K.Kazimierczuk. "Spice Compatible Averaged Models of PWM Full-Bridge Dc-Dc Converter". In Industrial electronics, control, instrumentation, and automation, 'Power electronics and motion control' Proceedings of the 1992 inter- national conference, 1992.

[5] T.Ming-Tsung and W. I. Tsai, "Analysis and Design of Three-Phase AC-to-DC Converters with High Power Factor and Near-Optimum Feed forward" *IEEE Transactions On Industrial Electronics, Vol. 46, No. 3, June 1999.*

[6] Y.Jiang-Hafner, H.Duchen, M.Karlsson, L.Ronstrom and B.Abrahamsson, "HVDC with Voltage Source Converters .A Powerful Standby Black Start Facility".*IEEE PES T&D Conference, April 2008.*

[7] M.P. Bahrman and B.K. Johnson, "The ABCs of HVDC Transmisson Technologies". *IEEE* Power & Energy magazine, March/April 2007, p32~44.

[8] W. Lu, "Simultaneous Inter-Area Decoupling and Local Area Damping by Voltage-Source HVdc". 2001 *IEEE*.

[9] R.Critchley, "The role of HVDC & FACTS technologies to enhance the utilisation of existing transmission networks". *AREVA T&D Technology Centre,* March 2009.

[10] M.Khederzadeh, “Power Quality Aspects of Different Control Schemes of Back-to-Back Converters Interfacing Utility-Grid to Microgrid”. C I R E D on Electricity Distribution, June 2011.

[11] B.Singh, B.N. Singh, A. Chandra, K. Al-Haddad, A.Pandey, and P.D.P.Kothari, "A Review of Single- Phase Improved Power Quality AC-DC Converters", *IEEE Transaction on Industrial Electronics*, Vol. 50, No. 5, pp. 962-981, USA, October, 2003.

[12] A.Pandey, and P.D.P. Kothari, "A Review of Three- Phase Improved Power Quality AC-DC Converters", *IEEE Transaction on Industrial Electronics*, Vol. 51, No. 3, pp. 641-660, USA, 2004.

[13] E. López-Luis, M. A. García-Domínguez, and D. Ruiz-Vega, “The Effect of Improved System Modelling in the Continuation Power Flow Method”. 2007 IREP Symposium- Bulk Power System Dynamics and Control - VII, Revitalizing Operational Reliability.

[14] B.Poudel, V.Cecchi, “Harmonic Power Flow Using Multi-Segment Frequency-Dependent Transmission Line Models”. *IEEE* 2013.

[15] M.Robert and D.Vecchio, “Multiterminal Three Phase Transformer Model with Balanced or Unbalanced Loading”. *IEEE Transactions on Power Delivery*, Vol. 23, No. 3, July 2008

[16] R.Stoicescu, K.Miu, C. O. Nwankpa, D.Niebur, and Xiaoguang Yang, “Three-Phase Converter Models for Unbalanced Radial Power-Flow Studies” IEEE Transactions on Power Systems, Vol. 17, No. 4, November 2002.

[17] P.W.Lehn,”Direct Harmonic Analysis of the Voltage Source Converter” *IEEE Transactions on Power Delivery*, Vol. 18, No. 3, July 2003.

[18] M.Rashid “Power Electronics: Circuits, Devices, and Applications”, 3rd Edition, Prentice Hall New Jersey, USA, 2004.

[19] P.Marketos, A.J.Moses and J.P.Hall,“Effect of DC Voltage on AC Magnetisation of Transformer Core Steel”. *Journal of* ELECTRICAL ENGINEERING, Vol 61. No 7/s, 2010, 123-125

[20] T. M. Blooming, and D.J. Carnovale, ”Capacitor Application Issues”

[21] H.P.Tiwari ,”Capacitor Rating Selection for Voltage Sag Compensation in DVR System” International Journal of Innovation, Management and Technology, Vol. 1, No. 3, August 2010

[22] G. Andersson, “Modelling and Analysis of Electric Power Systems”. Power Flow Analysis, Fault Analysis, Power Systems Dynamics and Stability. ITET ETH Z¨urich

CHAPTER 8

8. Conclusions and Further Works

8.1. Conclusions

Harmonic power system analysis, particularly at the planning stage, has become increasingly important as it constitutes a powerful tool for the adequate assessment and enhancement of power quality, and the impact of harmonic distortion upon system components. Accurate representation of power network component nonlinearities and the interaction with other electric network components is of fundamental importance in rigorous harmonic studies.

In this thesis, computer simulations to ascertain harmonic resonance performance of high voltage models under steady-state conditions have been investigated using improved cable models. The study shows that an accurate underground/subsea cable model and its mathematical equations could be a strong tool for predicting the harmonic resonance conditions of power cable in a transmission system. The simulation results shows that the frequency response depends on design lumped parameters such as: the cable length, capacitive and inductive components. The analysis estimates that the potential risks on the voltage and current harmonic amplifications could be avoided or controlled using accurate modelling.

For this purpose, the proposed Bessel function model stands out in investigating the frequency response and harmonic resonances of the system. The results obtained are validated with the simulation results of an approximation model using MATLAB. The two models results show very good agreement as anticipated. This study further contributes towards an insight that underground/subsea cable is influenced by harmonic resonance in transmission systems. It implies that the cable model needs to be carefully assessed in order to represent the harmonic behaviour of the transmission systems. Also, to understand the harmonic behaviour and harmonic distortion, the aspect of power losses must be considered as this is critical to the design of offshore power transmission systems.

A comprehensive model for the periodic, steady-state operation of VSCs was presented in this thesis. Switching functions based on complex Fourier series are used very effectively to represent the operation of the VSC. The modelling approach applies to a wide range of VSC configurations.

The MMC based VSC converter technology is expandable to high level waveforms. Its large number of sub-modules, capacitors in each phase-leg and combined with a proper accurate algorithm regulates the voltage of the sub-module capacitors. With these flexibilities the converter structure operates well under unipolar-PWM voltage switching principle that results in high quality waveforms while maintaining the low switching frequency of the SM switches.

Based on the configuration of the MMC, a phase-shifted modulation scheme is proposed for the unipolar-PWM carrier. It provides high quality waveforms while generating different number of levels in the output voltage waveforms.
Cancellation theory and the notion of resultants can be used to cancel the lower and higher order harmonics in a modular multilevel converter. This method is expected to have widespread application as most modular multilevel converters do not have dc sources that are exactly equal.

The VSC model was used as a building block to assemble harmonic domain models for the VSC-HVDC back-to-back and for the VSC-HVDC transmission station. The model of the VSC-HVDC transmission station works well with an accurate model of the cable since both models are in the frequency domain. Possible applications of the frequency domain models presented in the thesis are: harmonic propagation studies, resonance prediction and harmonic stability analysis.

A new radial oil and gas platform model fed by an offshore wind farm, connected through VSC-HVDC transmission system was studied. The main advantage of this model is that, it is built with Static Var Compensator (SVC), whose compact components are the capacitor and inductor. This compensator brought a new solution technique to a power quality problem on the platform. Low harmonic voltages and reactive power support was achieved through this technique. In this application, the SVC is not a device intended to permit the full, steady state loading of the transmission line to its capacity; it is a device intended to improve power quality. In this model SVC

draw high interest with power quality because of its harmonic impact on the system resonance and voltage regulation.

A new harmonic power flow strategy of the VSC-HVDC system for providing a high-quality supply to oil and gas platforms are proposed. In the proposed strategy, a switching function technique and harmonic injection are implemented in the stations of the VSC-HVDC. The motivation for choosing this strategy is to exploit the harmonic propagation decreasing the frequency of the VSC-HVDC output voltage when needed. Thus, a momentary surplus of harmonic magnitude reduction is achieved.
The increasing interest in integrating renewable electricity from remotely located energy sources, such as offshore wind power, is promoting the development of high-voltage multi-terminal DC networks, which offer several advantages when compared with standard high-voltage AC networks. In view of this, the VSC-HVDC technology stands out as the most promising solution. However, several regulatory as well as technical challenges must be addressed before such multi-terminal DC (MTDC) systems can be established.

In addition, the thesis has described the steady-state models of the main components in an MTDC network. A novel harmonic power flow strategy has been presented to study the DC power flow. The HPF strategy was analysed in combination with a switching function algorithm that minimizes the MTDC system losses. A total of five bus case studies have been conducted, via simulations in MATLAB. The simulation results demonstrate that the proposed power flow strategy is capable of generating power quality and safely controlling the DC power flow. Furthermore, the HPF strategy has fast communications capability and can handle the power flow in complex DC networks.

Oil and gas networks with VSC-HVDC and internal modular multilevel DC network has been proven to enhance drive systems mounted on the DC-bus, the incoming energy from the wind farm delivered energy to the individual DC-bus via aggregated induction generator and slightly decreasing the frequency of the VSC output voltage.

There is a higher flexibility in this approach, in that the frequency reduction can be applied selectively only to those machines that are not sensitive, while the stored energy through the DC-bus can be used to keep the critical ones on line. Further improvement can be obtained by connecting some additional storage to the common DC-bus. This can

result in a more cost-effective solution than increasing the storage (capacitor size) at each DC-bus of the individual drive system, as it is done in the traditional AC solution to increase the ride-through capability of the drive.
Further simulation results show that the developed harmonic control system was able to keep the voltage and frequency variations within the grid code even during large disturbances. We can conclude that the system handles variations in the load very well and that the system configuration studied in this thesis is regarded as a feasible way of integrating oil and gas platforms and offshore wind power to the onshore grid. However more detailed studies are recommended including short circuit analysis.

The HPF program developed in MATLAB environment has been tested on several nonlinear loads such as: VSC, rectifier, and gives satisfactory results for the simulations performed confirming the relevance of this code. The results were consistent and show the influence of higher harmonics on power losses in electrical networks. And we have confirmed the possibility to analyse other nonlinear loads with this computer code HPF generating harmonics in power systems.

8.2. **Recommendations**

Considering the benefit-to-cost ratio, based on our multi-terminal model network, an HVDC-VSC connection to the oil and gas platform network will indeed be most profitable to oil and gas companies. As can be seen from the analysis connection will be cost-effective up to thousands of MW renewable generation. For higher generation, a multi-terminal connection to different platforms is preferred. Also, as the emission price goes higher, the net benefit of multi-terminal connection to the grid becomes more attractive.

The harmonic problems are very high; the cases in which they do occur can result in decreasing power system reliability. An understanding of the causes, potential effects and mitigation means for harmonics can help to prevent harmonic related problems at the design stage and reduce the probability of undesired effects occurring on operation.

It should be kept in mind that if the harmonic producing loads are small in relation to the total plant load, then harmonics are not an issue. When the non-linear loads become a substantial portion of the total load, it becomes worthwhile to give some consideration to harmonics. In these cases, harmonic modelling analysis is recommended to predict

harmonic levels and identify potential resonance problems regardless of the rectifier pulse number.

8.3. **Further Work**

The VSC-HVDC concept includes another development in future the extruded polymer VSC-based HVDC Cable. The technology will shift High Voltage AC cables from paper insulated to extruded polymer cables which will be replicated in HVDC cables.

The cable could be designed with a 300mm copper conductor surrounded by a strong polymeric insulating material. The water sealing of the cable could be design with a seamless layer of extruded lead and finally two layers of armouring steel wire in counter helix for the mechanical properties of the cable. Their strength and the flexibility will make these cables suited for severe installation conditions and deep waters oil and gas platforms. The model is compatible with active filtering that will fight harmonic distortion and resonance conditions.

Space and weight are also scarce resources on offshore installations. However, the use of small filters makes the VSC based HVDC concept relatively compact and lightweight. The offshore environment is also very tough with salt and humid air imposing severe requirements on the choice of materials and surface treatment. To this end, the investigation of harmonic behaviour of this cable is required, the assessment is imperative to enable design engineers consider actual harmonic mitigation approaches.

The power quality and the accuracy of the harmonic resonance mode analysis need to be verified with real life measurements in power systems. The harmonic resonance mode analysis detects the parallel resonances in a power system (i.e. the major resonance problem), but it could be completed to detect the series resonances as well. The role and the physical meaning of the participating factors need further investigation.
A systematic and power quality automatic calculation algorithm based on the harmonic modal analysis would facilitate the resonance analysis of the distribution and transmission networks and help to identify the optimal locations for active filters.

Further work also, may involve the modular multi-level inverter containing series of components each with its own role. The main components are the IGBT units which form the three phases of the inverter. Each phase should contain tens of IGBT units

allowing up to 13 levels per phase and 17 levels. A unit can handle voltages up to 600 V but 800 V can also be achieved if the units are pushed at higher voltages. The system components are: IGBT s ; Current sensors; Voltage sensors; Contactors and DC Power Supply.

Furthermore, future work involves building a small-scale version of the represented MTDC network in a laboratory, testing the harmonic power flow in a real-time environment, and assessing the effect of direct voltage measurement errors on the DC load flow obtained with the proposed strategy.

Integration of photovoltaic (PV) and wind based renewable energy systems, main grid feeding both onshore and offshore oil and gas installations forms part of the future work. To undertake the study an aggregated current source model shall be proposed for the photovoltaic inverter systems and wind farm based on measurement data from available literature and the relevant international standards. A typical medium voltage (MV) and low voltage (LV) distribution feeder including oil and gas production field load arrangements is ideal for the study. The flexible harmonic model for the grid, the cables, linear loads, nonlinear loads and the rectifiers and inverters (harmonic current capacitance and conductance) are to be used to simulate the behaviour of the proposed micro grid topology composed of both linear and nonlinear loads and grid photovoltaic (PV) and wind farm (WF) systems. The harmonic currents injection at the point of connection could be obtained at the output of a grid connected PV and WF systems. Conventional harmonic modelling methods should be applied to determine harmonic emissions and resulting harmonic voltage levels for various penetration levels of photovoltaic inverter systems and wind farm based VSC-HVDC. Based on this study, a recommendation should be made for acceptable penetration levels to limit the harmonic impact of grid connected PV inverter systems and WF VSC-HVDC systems. The distribution network considering distributed generation (DG), the model has to be modelled to analyze the effects of wind farms and PV solar installations ground current contribution to the network. The DG is based on capacitive coupling models of a 100 MW PV solar installation and a 200 MW wind farm respectively. This distribution network feeds six loads through a multi-terminal ring topology. These loads are connected to bus 1, 2, 3, 6, 7 and 8 with a rated power of 500+ j *55* kVA each.

Appendix

Appendix A1

International Harmonic Standards

The purpose of imposing strict limits on the harmonics emissions is to ensure that the current and voltage distortions at the PCC are kept sufficiently low. Thus, the other customers connected at the same point are not disturbed. The international standards related to harmonic distortion limits can be classified as follows:

A. Standards specifying limits for individual nonlinear equipment

- IEC 61000-3-2, which specifies the current harmonic limits for low voltage equipment that has an input current less than 16 A.
- IEC 61000-3-12 , which specifies the current harmonic limits for equipment that has an input current between 16A and 75A
- IEC 61800-3, which specifies the electro-magnetic compatibility (EMC) requirements of the adjustable speed drive systems

As noticed, the above standards are for small rating and low voltage harmonic loads only. In addition, the above standards do not set limits on the overall distribution network.

B. Standards specifying limits for electrical networks

- IEEE 519-1992, this document introduces many useful recommended practices for harmonics control in electrical networks. This document is widely used in the industrial sector and many consultants/clients use the limits indicated in it as contractual limits within their specifications.
- IEC 61000-3-6, this specification performs an assessment of the harmonic emission limits for distorting loads in medium voltage and high voltage power systems.

Up till now, this specification is not widely used in the industrial sector because it is rather new (published in 2008).

- British engineering recommendation G5/4-1, this document provides some helpful engineering recommendations for establishing the allowable harmonic limits of the voltage distortions in the United Kingdom.

Appendix A2

The transmission line consists of three components in its lumped series impedance matrix $[Z]$, while the shunt admittance matrix $[Y]$ contains one element.

$$[Z] = [Z_e] + [Z_g] + [Z_c] \tag{A2.1}$$

$$[Y] = [Y_g] \tag{A2.2}$$

Where

$[Z_e]$ is the earth return path impedance ($\Omega\,\text{km}^{-1}$)
$[Z_g]$ is the impedance due to the physical geometry of the conductor ($\Omega\,\text{km}^{-1}$)
$[Z_c]$ is the internal impedance of the conductors ($\Omega\,\text{km}^{-1}$)
$[Y_g]$ is the admittance due to the physical geometry of the conductor ($\Omega^{-1}\text{km}^{-1}$)

In transmission line theory two transformation matrices are needed. One defines the modal voltages and the other the modal currents

$$V_p = [T_v]V_m \tag{A2.3}$$

$$I_p = [T_i]I_m \tag{A2.4}$$

where V_p and I_p are vectors of phase quantities, V_m and I_m are vectors of modal quantities, $[T_v]$ and $[T_i]$ are linear transformation matrices that require the eigen-solution of the product [Z][Y] and [Y][Z], respectively. The matrices [Z] and [Y] are the lumped parameter matrices derived in the previous section.

Also, as an extension,

$$[Z_m] = [T_v]^{-1}[Z][T_i] \tag{A2.5}$$

$$[Y_m] = [T_i]^{-1}[Y][T_v] \tag{A2.6}$$

At this stage, both $[Z_m]$ and $[Y_m]$ are fully diagonal and scalar operations are permitted. For instance,

$$\gamma_m = \sqrt{z_m y_m} \tag{A2.7}$$

$$z_m = \sqrt{\frac{z_m}{y_m}} \tag{A2.8}$$

where $z_m \in [Z_m]$ and $y_m \in [Y_m]$

The same is true for all of the hyperbolic and transfer functions sections. Furthermore, a transformation from modal to phase domain is also defined,

$$[Z] = [T_v][Z_m][T_i]^{-1} \tag{A2.9}$$

$$[Y] = [T_i][Y_m][T_v]^{-1} \tag{A2.10}$$

A2.1. **Homogeneous Line**

The relationship between sending and receiving end harmonic voltages and currents in a homogeneous line is a transfer impedance matrix, i.e.

$$\begin{bmatrix} V_S \\ V_R \end{bmatrix} = \begin{bmatrix} [Z^1] & [Z^{11}] \\ [Z^{11}] & [Z^1] \end{bmatrix} \begin{bmatrix} I_S \\ I_R \end{bmatrix} \tag{A2.11}$$

where, $[Z^1] = [T_v] \times diag[z_{om} \times \coth(\gamma_m l)] \times [T_i]^{-1}$;

$$[Z^{11}] = [T_v] \times diag\left[z_{om} \times \frac{1}{\sinh}(\gamma_m l) \right] \times [T_i]^{-1}$$

Alternatively, the use of the equivalent π concept, leads to the following equation,

$$\begin{bmatrix} V_S \\ V_R \end{bmatrix} = \begin{bmatrix} [Z_{eq}]^{-1} + \frac{1}{2}[Y_{eq}] & -[Z_{eq}] \\ -[Z_{eq}] & [Z_{eq}]^{-1} + \frac{1}{2}[Y_{eq}] \end{bmatrix}^{-1} \begin{bmatrix} I_S \\ I_R \end{bmatrix} \tag{A2.12}$$

where, $[Z_{eq}] = l[Z][T_i] \times diag\left[\frac{\sinh(\gamma_m l)}{\gamma_m l} \right] \times [T_i]^{-1}$

$$[Y_{eq}] = l[T_i] \times diag\left[\frac{\tanh\left(\frac{\gamma_m l}{2} \right)}{\frac{\gamma_m l}{2}} \right] \times [T_i]^{-1}[Y]$$

This is solved in proportion to the number of harmonics to be considered.

When harmonic voltages rather than currents are to be injected (at the sending end) the following equation is applies:

$$\begin{bmatrix} V_R \\ -I_S \end{bmatrix} = \begin{bmatrix} [Q] & [R] \\ [S] & [Q] \end{bmatrix} \begin{bmatrix} V_S \\ I_R \end{bmatrix} \tag{A2.13}$$

where, $[Q] = [T_V] \times diag\left(\frac{1}{\coth(\gamma_m l)} \right) \times [T_i]^{-1}$

$$[R] = [T_V] \times diag\left(z_{0m} \times \tanh(\gamma_m l) \right) \times [T_i]^{-1}$$

$$[S] = -[T_i] \times diag\left(\frac{1}{z_{0m}} \times \tanh(\gamma_m l) \right) \times [T_v]^{-1}$$

When the aim of the analysis is to study the standing waves along the line or the distribution of harmonic levels in a mesh of lines, it is necessary to obtain the line's parameters in the form of admittance.

$$\begin{bmatrix} I_S \\ I_R \end{bmatrix} = \begin{bmatrix} [Y^1] & [Y^{11}] \\ [Y^{11}] & [Y^1] \end{bmatrix} \begin{bmatrix} V_S \\ V_R \end{bmatrix} \tag{A2.14}$$

where, $[Y^1] = [T_i] \times diag\left(\frac{1}{z_{0m}} \times \coth(\gamma_m l) \right) \times [T_v]^{-1}$

$$= [Z_{eq}]^{-1} + \frac{1}{2}[Y_{eq}]$$

$$[Y^{11}] = [T_i] \times diag\left(\frac{1}{z_{0m}} \times \frac{1}{\sinh}(\gamma_m l) \right) \times [T_v]^{-1}$$

$$= [Z_{eq}]^{-1}$$

A2.2. **Nominal π versus Equivalent Pi Circuit Line Representation**

There are two basic ways of representing transmission lines, namely by creating their nominal Pi circuit or equivalent π circuit. The first model is a simplified lumped equivalent circuit where the whole length line resistance and reactance are concentrated in the middle and shunt capacitance and conductance are concentrated at both ends see Figure A2.1.

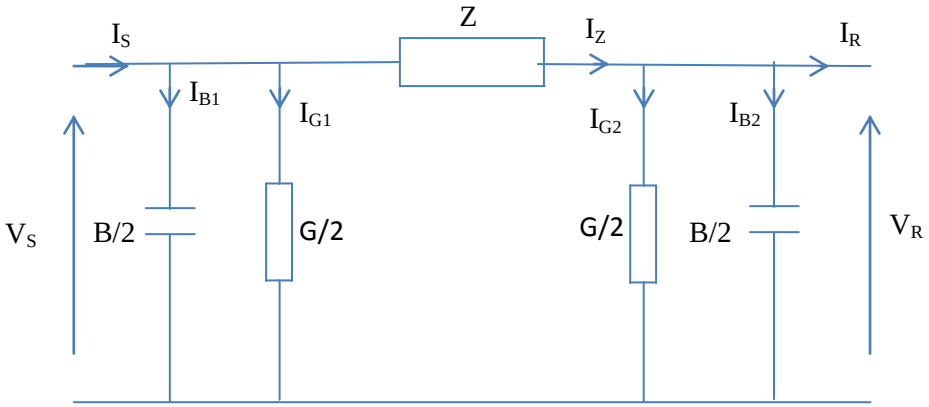

.Figure A2.1 Nominal π circuit of a transmission line

$$V_S = \left(\frac{ZY}{2}+1\right)V_R + ZI_R \tag{A2.15}$$

$$I_S = V_R Y\left(1+\frac{ZY}{4}\right)+\left(\frac{ZY}{2}+1\right)I_R \tag{A2.16}$$

where

$$\frac{Y}{2}=\frac{G}{2}+j\frac{B}{2};\quad Z=R+jX$$

The current I_{B1} through the shunt capacitance $B/2$ is expressed as

$$I_{B1} = V_S \times j\frac{B}{2} \tag{A2.17}$$

The current I_Z flows through the distributed series impedance Z is expresses as

$$I_Z = I_S - I_{B1} - I_{G1} \tag{A2.18}$$

The errors produced via lumped parameters experiences increment with the line length and the frequency. In reality, the shunt capacitance is distributed along the line and therefore the voltage on the capacitance is V_S. This voltage V_S will change to ΔV_S due to increasing voltage drop on the distributed series impedance. More also, I_Z that flows through the distributed series impedance and the resulted voltage drop are not constant, but decreases as the distributed shunt capacitances and conductance increases. It should be reiterated here that these relations are not included when using only single nominal PI circuit as a line topology.

A2.3. **Transmission line with distributed parameters**

An actual transmission line representation with distributed impedance zdx and admittance ydx is shown in Figure A2.2

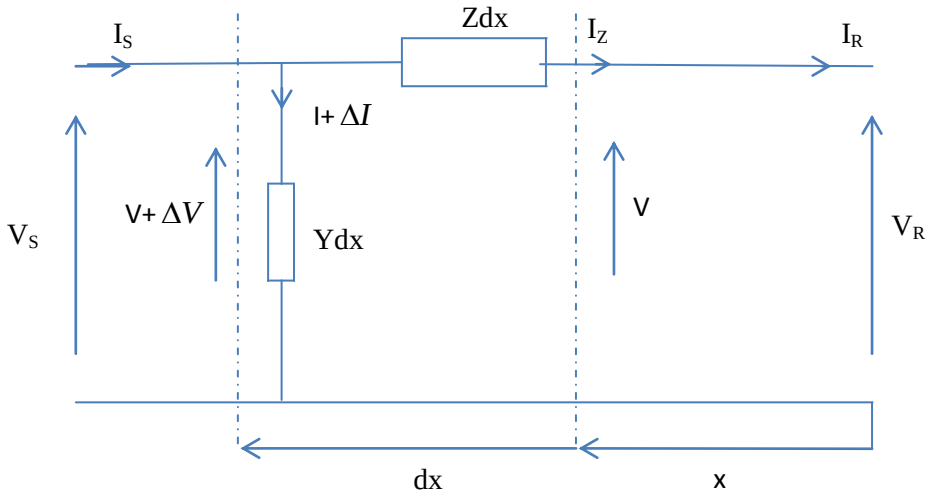

Figure A2.2 Distributed parameters transmission line

The voltage and current change along the line can be express as

$$\frac{dV}{dx} = IZ \qquad \text{(A2.20)}$$

$$\frac{dI_Z}{dx} = VY \qquad \text{(A2.21)}$$

Differentiating for current and voltage we have

$$\frac{d^2V}{dx^2} = ZYV \qquad \text{(A2.22)}$$

$$\frac{d^2I}{dx^2} = YZI \qquad \text{(A2.23)}$$

These equations express the wave propagation along a transmission line. Its transformations express the rms values and phase angles of V and I at any point of the line as

$$V = \frac{V_R + I_R Z_C}{2} e^{\gamma x} + \frac{V_R - I_R Z_C}{2} e^{-\gamma x} \qquad \text{(A2.24)}$$

$$I = \frac{\frac{V_R}{Z_C} + I_R}{2} e^{\gamma x} - \frac{\frac{V_R}{Z_C} - I_R}{2} e^{-\gamma x} \qquad \text{(A2.25)}$$

These expressions may be rewritten using the hyperbolic functions

$\sinh \gamma x = \left(e^{\gamma x} - e^{-\gamma x}\right)/2$ and $\cosh \gamma x = \left(e^{\gamma x} + e^{-\gamma x}\right)/2$

$$V = V_R \cosh \gamma x + I_R Z_C \sinh \gamma x \qquad \text{(A2.26)}$$

$$I = I_R \cosh \gamma x + \frac{V_R}{Z_C} \sinh \gamma x \qquad \text{(A2.27)}$$

At the sending end

$$V_S = V_R \cosh \gamma l + I_R Z_C \sinh \gamma l \qquad \text{(A2.28)}$$

$$I_s = I_R \cosh \gamma l + \frac{V_R}{Z_C} \sinh \gamma l \qquad \text{(A2.29)}$$

where

$Z_C = \sqrt{Z/Y}$ - is the characteristic impedance

$\gamma = \sqrt{ZY} = \alpha + j\beta$ - is the propagation constant

Table A2.1.: Technical data for power line model

Distance	0.46	m
external radius	1.049	cm
internal radius	0.543	cm
Conductivity of the conductor	25785150	m/Ω
Conductivity of the earth	0.01	S/m
Permeability of free space	4π 10^-7	$H.m^{-1}$
Vacuum permittivity	8.8542*10^-12	$F \cdot m^{-1}$
Nominal frequency	50	Hz
Base voltage	500	kV
Base power	100	MVA

A2.4. **Single Core Cables Parameters**

The calculation of the per unit length parameters of a single-core cable, are based on Fig. A2.3. The parameters equations, namely the series impedances *Z* and shunt admittances Y are represented by matrices, which have a dimension [*NxN*], where *N* is the number of conductors excluding the reference. [*2x2*] in the case of a single-core cable. The phase voltages, vectors of dimension [*Nx1*], are reference to the ground conductor.

In the case of [*2x2*], we consider two loops, in one loop the current is injected in the core and returns by the sheath, whereas in the other the current is in injected on the sheath and returns by the ground. We define loop currents and voltages, that I_{Sint} and I_{Sout}, currents on the internal and external surfaces of the sheath, as well as loop voltage V_{12} and V_{23}, which are the core core-sheath and sheath-ground voltages. The sheaths currents currents have physical substance only at high frequency, when the current effectively flow on the conductors surfaces, but the loop quantities must always be defined as means to evaluate phase quantities.

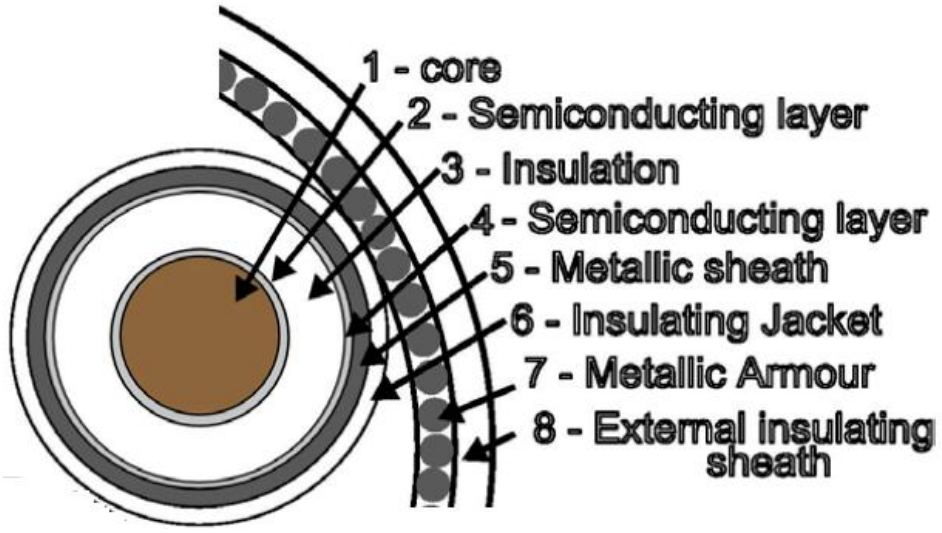

Figure A2.3 Transversal section of a single-core cable

A2.5. **The Impedance and Admittance Matrices of a Cable System**

Analysis of the impedance and admittance of a power cable is necessary for the understanding of its characteristics [57]. Each cable has a cross section similar to the type shown in Figure 4.15, representative of a typical high voltage (HV) underground cable

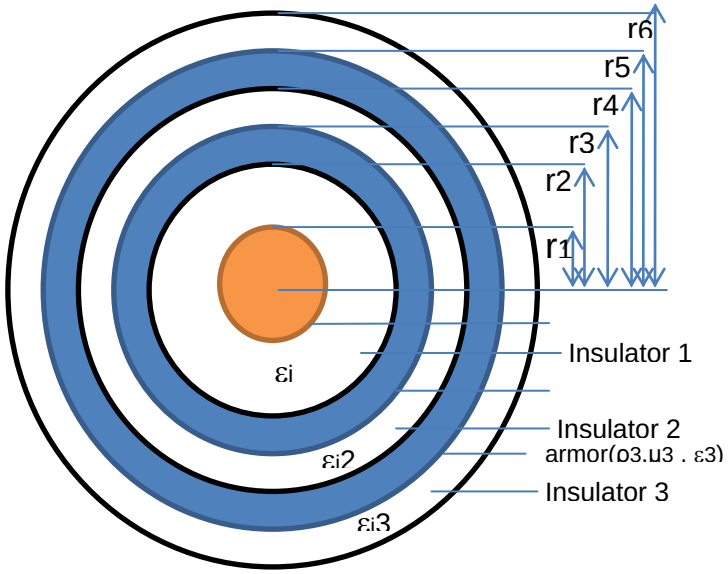

Figure A2.4. Details of the construction of the 23-kV single-core cable with three dielectric, operating frequency is 50Hz.

The impedance and admittance of a cable system are defined by the two matrix equations,

$$\frac{d(v)}{dx} = -[Z] \bullet (I) \tag{A2.30}$$

$$\frac{d(I)}{dx} = -[Y] \bullet (v) \tag{A2.31}$$

where

$[Z]$ is the impedance square matrix

$[Y]$ is the admittance square matrix

I is the vector current along the cable

v is the vector voltage along the cable

In general, the impedance and admittance matrices of a cable can be expressed in the following forms

$$[Z] = [Z_i] + [Z_p] + [Z_C] + [Z_o] \tag{A2.32}$$

$$[Y] = s.[P]^{-1} \tag{A2.33}$$

$$[P] = [P_i] + [P_p] + [P_c] + [P_o] \tag{A2.34}$$

where

[*P*] is the potential coefficient matrix
$s = j\omega$

- the matrices with subscript "*i*" are concerned with single core (SC) cable
- the matrices with subscript "*p*" and "*c*" are concerned with pipe enclosure cable
- the matrices with subscript "*o*" is concerned with cable outer media, that is air space and earth
- when a cable has no pipe enclosure, there exists no matrix with "*p*" and "*c*"

In the formulation of impedance and admittance of the cable system, the following assumptions are necessary:

- The displacement currents and dielectric losses are negligible.
- Each conducting medium of a cable has constant permeability.

A2.6. **Impedance**

When an SC cable consists of a core, sheath and armour the impedance is given in the following

$$[Z]=[Z_i]+[Z_o]+[Z_{skin}]+[Z_{proximity}] \tag{A2.35}$$

where

$[Z_i]$ is the cable internal impedance diagonal matrix. A diagonal sub-matrix expresses the self impedance matrix of an SC cable.

$$[Z_i] = \begin{bmatrix} [Z_{i1}] & [0] & \cdots & [0] \\ [0] & [Z_{i2}] & \cdots & [0] \\ \vdots & \vdots & \ddots & \vdots \\ [0] & [0] & \cdots & [Z_{in}] \end{bmatrix} \tag{A2.36}$$

Each submatrix, e.g. $[Z_{i1}]$ assembled along the leading diagonal is a square matrix of two dimension representing the self impedances of cable *i*, by itself

$$[Z_{11}] = \begin{bmatrix} Z_{c_i c_i} & Z_{c_i s_i} \\ Z_{s_i c_i} & Z_{s_i s_i} \end{bmatrix} \tag{A2.37}$$

where

$Z_{c_i c_i}$ = self impedance of the core of cables *i*

$Z_{c_i s_i} = Z_{s_i c_i}$ = mutual impedance between core and sheath of cable *i*

$Z_{s_i s_i}$ = self impedance of the sheath of cables *i*

$[Z_o]$ is the impedance matrix of the cable outer medium (ground return impedance) and is given by

$$[Z_0] = \begin{bmatrix} [Z_{011}] & [Z_{012}] & \cdots & [Z_{01n}] \\ [Z_{012}] & [Z_{022}] & \cdots & [Z_{02n}] \\ \vdots & \vdots & \ddots & \vdots \\ [Z_{01n}] & [Z_{02n}] & \cdots & [Z_{0nn}] \end{bmatrix} \tag{A2.38}$$

When the SC cable consists of a core, sheath and armour, the self-impedance matrix is given by

$$[Z_{ij}] = \begin{bmatrix} Z_{ccj} & Z_{csj} & Z_{caj} \\ Z_{csj} & Z_{ssj} & Z_{saj} \\ Z_{caj} & Z_{saj} & Z_{aaj} \end{bmatrix} \tag{A2.39}$$

where

Z_{ccj} = core self-impedance

Z_{ssj} = sheath self-impedance

Z_{aaj} = armor self-impedance

Z_{csj} = mutual impedance between the core and sheath

Z_{caj} = mutual impedance between the core and armour

Z_{saj} = mutual impedance between the sheath and armour

When the SC cable consists of a core and sheath the self impedance is the matrix reduced to a 2 x 2 matrix as given below and its equivalent circuit is as shown in Fig. A2.4:

$$\left[Z_{ij}\right]=\begin{bmatrix} Z_{ccj} & Z_{csj} \\ Z_{csj} & Z_{ssj} \end{bmatrix} \tag{A2.40}$$

And when an SC cable consists only of a core the matrix of equation (4.59) is reduced to one element as given below:

$$\left[Z_{ij}\right]= Z_{ccj} \tag{A2.41}$$

A2.7. **The Admittance**

We have the admittance matrix as,

$$\left[Y_i\right]=\begin{bmatrix} \left[Y_{i1}\right] & [0] & \cdots & [0] \\ [0] & \left[Y_{i2}\right] & \cdots & [0] \\ \vdots & \vdots & \ddots & \vdots \\ [0] & [0] & \cdots & \left[Y_{in}\right] \end{bmatrix} \tag{A2.42}$$

Where the $[Y_{s1}]$ and $[Y_{s2}]$ can be defined in a similar way as

$$Y=\begin{bmatrix} \left[Y_{11}\right] & \left[Y_{12}\right] & \cdot & \cdot & \cdot & \left[Y_{1N}\right] \\ \left[Y_{21}\right] & \left[Y_{22}\right] & \cdot & \cdot & \cdot & \left[Y_{2N}\right] \\ \cdot & \cdot & \cdot & & \cdot & \cdot \\ \cdot & \cdot & \cdot & \cdot & \cdot & \cdot \\ \cdot & \cdot & \cdot & \cdot & \cdot & \cdot \\ \left[Y_{N1}\right] & \left[Y_{N2}\right] & \cdot & \cdot & \cdot & \left[Y_{NN}\right] \end{bmatrix} \tag{A2.43}$$

A2.8. **The Potential Coefficient (P)**

The admittance matrix of a cable system is evaluated from the potential coefficient matrix. If the cable is underground all submatrix is zero except $[P_i]$, therefore the cable internal potential coefficient matrix is given as

$$[P_i] = \begin{bmatrix} [P_{i1}] & [0] & \cdots & [0] \\ [0] & [P_{i2}] & \cdots & [0] \\ \vdots & \vdots & \ddots & \vdots \\ [0] & [0] & \cdots & [P_{in}] \end{bmatrix} \quad \text{(A2.44)}$$

A2.9. **The Elements of the Submatrix [Z_{11}]**

The elements of the submatrix [Z_{11}] can be evaluated by using a single cable whose longitudinal cross section is as shown in Fig. A2.16. The longitudinal voltage drops in such a cable are best described by three loop equations, with loop 1 formed by the core and sheath (as return path), loop 2 formed by the sheath and armour and loop 3 formed by the armour and earth (as return path)

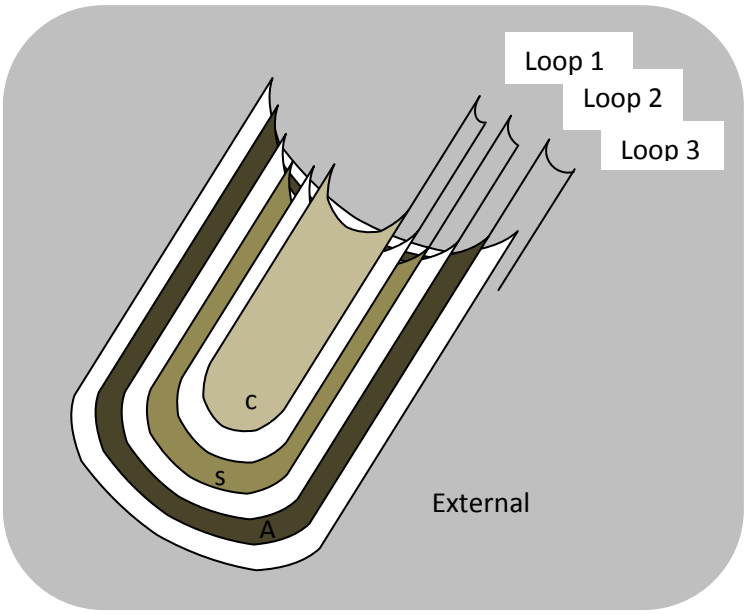

Figure A2.5. Cable bisection

It has been shown by Carson that the change in the potential difference between j and (j + 1) of a concentric cylindrical system is given by

$$\frac{dV_1}{dx} + E_1 - E_{J+1} = -j\omega\mu\phi_j \qquad \text{(A2.45)}$$

where

E_j = longitudinal electric field strength of the outer surface of the conductor j

E_{j+1} = longitudinal electric field strength of the inner surface of conductor $(j + 1)$

The single-core trefoil type is expected to be more influenced by proximity effect compared to the flat formations as shown in Fig. A2.5.

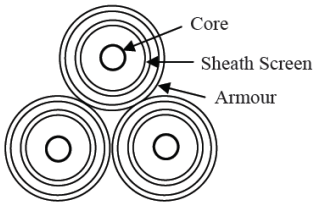

(a) Single-Core Trefoil Formation Cable Structure.

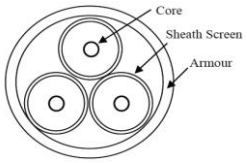

(b) Three-Core Trefoil Formation Cable Structure

(c) Single-Core Flat Formation Cable Structure.

Figure A2.5 Subsea Cable Configurations

A2.10. **Core Conductor**

The core conductor aims to transmit the required electrical energy with low losses. The high voltage conductor is made of copper (Cu) which has lower specific resistance compared to aluminium (Al). Also, the conductor is often stranded in order to lower the effective resistance caused by skin and proximity effect. When modelling such a non-solid conductor, the resistivity is increased as presented in.

A2.11. **Inner Insulation**

The inner insulation aims at ensuring no electrical connection between the two current carrying components of the cable, the conductor and the sheath. The SC screens are placed between the insulation and the conductor and again between insulation and the sheath. The purpose of the SC screens is to reduce the electrical stress in the inner insulation and prevent formation of voids between either core conductor or sheath and insulation due to bending of the cable or other mechanical stress. For flexible and accurate modelling of the insulation and SC screens, the permittivity and thickness of the insulation should be corrected according to the theory.

A2.12. **Cable Sheath**

The cable sheath aims at providing a metallic covering used as an electrostatic screening as well as a earth return path for the cable's charging current and a conduction path for earth fault current in the event of a fault on the cable. As shown in Fig. A2.4, for XLPE cables the sheath consists of several layers. The two conducting sheath layers, the wired sheath layer and the laminated layer, are separated by a SC layer and are directly connected together both at each junction and cable ends. The laminated layer is included for water resistance. The two conducting layers are not touching each other in order to protect the laminate from mechanical stress because of bending and for thermal protection as the laminate cannot tolerate more than 180^{o}C while the wired sheath layer can be up to 250^{o}C.

A2.13. **Cable Armour**

Armoured cable is the name given to any electrical cable constructed with a layer of aluminium wire armour or steel wire armour. The armour sits below the sheath of the cable to provide protection for the conductor and insulating layers. When an electrical cable is required for use outside, burial or in direct subsea projects, it must have mechanical protection. Aluminium wire armour or AWA, and steel wire armour or SWA, provide such protection – as well as enabling the cable to withstand higher pulling loads.

Steel Wire Armoured Cable is a hard-wearing mains electricity cable with class 2 stranded copper conductors, XLPE (Cross-Linked Polyethylene) insulation, PVC (Polyvinyl Chloride) bedding, aluminium or steel wire armour and a black PVC sheath.

A2.14. **Impedance of Two-Layer Conductor**

When the copper conductor and aluminium sheath are short-circuited at the both ends with the receiving end grounded, and voltage V is applied to the sending end, then the following relation is deduced:

$$\begin{bmatrix} V \\ V \end{bmatrix} = \begin{bmatrix} Z_{cc} & Z_{cs} \\ Z_{cs} & Z_{ss} \end{bmatrix} \begin{bmatrix} I_1 \\ I_2 \end{bmatrix} \quad \text{(A2.46)}$$

where

I_1, I_2 are the current of copper conductor and aluminium sheath, respectively.

The total current I of the conductors are obtained as:

$$I = I_1 + I_2 \quad \text{(A2.47)}$$

The total outer surface impedance of two-layer system seen from sending end is obtained:

$$Z_{out} = \frac{V}{I} = \frac{Z_{cc}Z_{ca} - Z_{cs}^2}{Z_{cc} + Z_{ca} - 2Z_{cs}} = z_{20} - \frac{z_{2m}^2}{z_{12} + z_{2i}} \quad \text{(A2.48)}$$

Similarly, the inner surface impedance is obtained:

$$Z_{in} = \frac{V}{I} = \frac{Z_{cc}Z_{ca} - Z_{cs}^2}{Z_{cc} + Z_{ca} - 2Z_{cs}} = z_{2i} - \frac{z_{2m}^2}{z_{12} + z_{3i}} \quad \text{(A2.49)}$$

The mutual impedance between the inner and the outer surface of the two-layer system is given by:

$$Z_m = \frac{z_{2m} \cdot z_{3m}}{z_{12} + z_{3i}} \quad \text{(A2.50)}$$

The above equation is a general formula of the impedance of a two-layered conductor, and is applicable to a semiconducting layer on the outer surface of a core, on the inner surface of a sheath and on the outer surface of the sheath of a cable.

A2.15. **Nodal Equations**

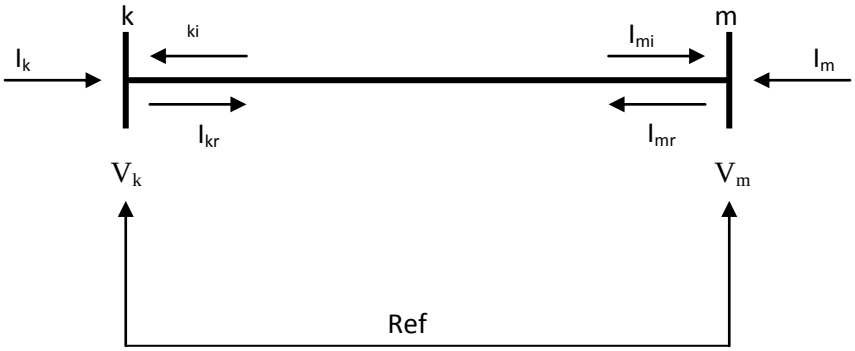

Figure A2.5 Single phase line of cable length L between two nodes k and m

Table A2.2.: Technical data approximation cable model

NC	3	pu
NH	400	pu
Conductor Diameter	0.575*(2.54/100)	mm
Insulation Thickness	(245/1000)*(2.54/100)	mm
Lead Sheath Thickness	(95/1000)*(2.54/100)	mm
X1	24*(2.54/100	pu
X2	0	pu
X3	24*(2.54/100)	pu
Y1	0.6096	pu
Y2	0.6096	pu
Y3	0.6096	pu
Conductor Conductivity	3.6518*10^7	m/Ω
Sheath Conductivity	4.1882*10^6	m/Ω
Earth Conductivity	0.01	m/Ω
frequency	50	Hz

Table A2.3.: Technical data for cable Bessel function model

Conductor diameter	0.575x(2.54/100)	mm
Insulation thickness	245/1000x(2.54/100)	mm
Lead sheath thickness	(95/1000)x(2.54/100)	mm
X1	24x(2.54/100)	
X2	0	
X3	24x(2.54/100)	
Y1 = Y2 = Y3	0.6096	
Conductor conductivity	3.6518x10^7	m/Ω
Sheath conductivity	4.1882x10^6	m/Ω
Earth conductivity	0.01	m/Ω
Rated voltage	23	kV
Core resistivity	1.72x10^-8	$\Omega - m$
Sheath resistivity	2.82x10^-8	$\Omega - m$
Armour resistivity	5.90x10^-8	$\Omega - m$
Seawater resistivity	0.208855472	$\Omega - m$
Earth resistivity	20	$\Omega - m$
Permittivity	3.5	
Vacuum permittivity	8.8542x10^-12	
Permeability	1	$H \cdot m^{-1}$
Permeability of free space	4π 10^-7	$H \cdot m^{-1}$
Euler's Constant	1.7811	

Appendix A3

A3.1. Two-level Voltage Source Converter with PWM

A two-level single-phase full-bridge VSC is depicted in Fig. A3.1. It consists of four switches (T_{A1+}, T_{A1-}, T_{A2+}, and T_{A2-}) with four antiparallel diode (D_{A1+}, D_{A1-}, D_{A2+}, and D_{A2-}) being utilize during transfer of current from the AC side to the DC bus. This takes place when the load power factor is other than unity. The other leg connects the return path of the load, unlike in the half-bridge where the mid-point of the two equal value capacitors (C_1 and C_2) connects the return path of the load which are in series across the DC input. This topology generates a two-level voltage waveform across point A and B. The parallel switches, that is T_{A1+} , T_{A2-} and T_{A2+} , T_{A1-} are turned on and off at the same time and for the same duration. The switches T_{A1+} and T_{A2-} are controlled based on the comparison of reference signals ($V_{control}$) and carrier (triangular) signal (V_{tri}), and the output voltage waveforms result is independent of the direction of i_0 as shown in Fig. A3.2. If the converter is to operate on square-wave then switches T_{A1+} and T_{A2-} are turned on for a half cycle and the voltage at the output is equal to the DC bus voltage $+V_{DC}$. Again, switches T_{A2+} and T_{A1-} are turned on for the other half cycle and the voltage at the output is equal to the DC bus voltage $-V_{DC}$. This topology has quadrants mode of comparison of $V_{control}$ and $-V_{control}$ with the triangular carrier signal (ωt)

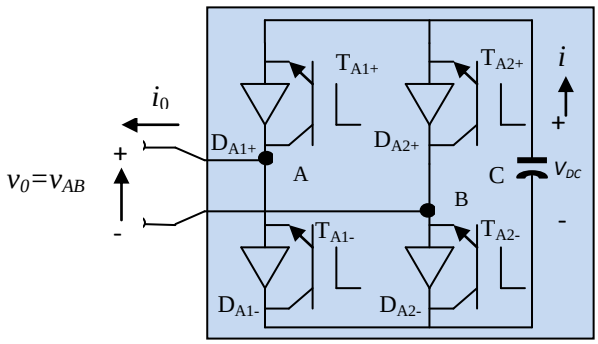

Figure A3.1 Two-level Single-Phase Full Bridge VSC

$$V_{A0} = V_m \sin(\omega t) \quad \text{(A3.1)}$$

$$V_{AN} = V_m \sin(-\omega t) \quad \text{(A3.2)}$$

$$\text{Modulation Index } (m_a) = \frac{V_{control}}{V_{tri}} \quad \text{(A3.3)}$$

$$V_{control} \leq V_{tri} \tag{A3.4}$$

where

$V_{control}$ - is the control voltage V_{A0} or V_{AN}

V_{tri} - is the triangular carrier signal

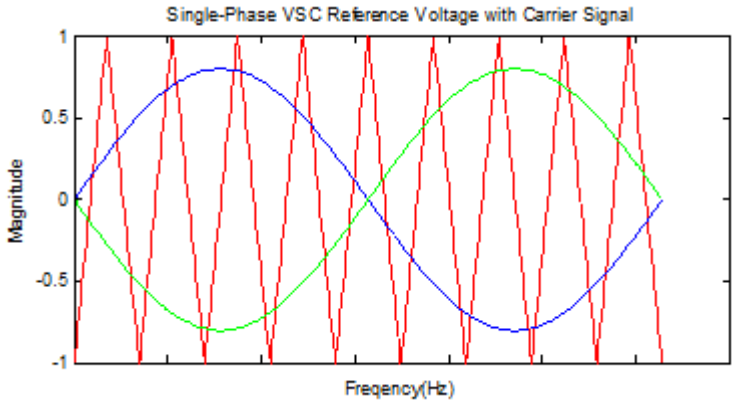

Figure A3.2 Single-phase VSC reference voltages with carrier signal

The switches T_{A+} and T_{A-} are controlled using PWM based on the comparison of $V_{control}$ and V_{tri} , and the following output voltage results independent of the direction of i_0 are obtained as shown in Fig. A3.3:

$$V_{control} > V_{tri};\ \ T_{A+} \text{ is on, } V_{A0} = \frac{1}{2}V_d \tag{A3.5}$$

$$V_{control} < V_{tri};\ \ T_{A-} \text{ is on, } V_{AN} = -\frac{1}{2}V_d \tag{A3.6}$$

The Phase switching function is obtained by:

$$S_{ph} = (V_{control} > V_{tri}) - (V_{control} < V_{tri}) \tag{A3.7}$$

When the polarity of the output current i_o is positive the current flows from switches T_{A1+} and T_{A2-} then the power is moved from the DC side to the AC (inversion). But when the polarity of the current turns negative regardless that switches T_{A2+} and T_{A1-} are turned on, the diode D_{A1+} and D_{A2-} drives the current by so doing power is back to DC from AC side (rectification).

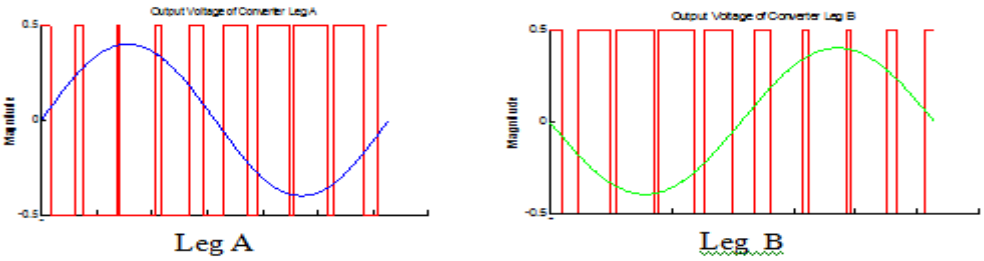

Figure A3.3 PWM output voltage of converter

In the same manner and for the other half cycle, when the polarity of the output current i_o is positive the switches T_{A2+} and T_{A1-} on, diode D_{A3+} and D_{A4-} drives the current, then the power is moved to the DC side from the AC (rectification). But when the polarity of the current is negative, switches T_{A2+} and T_{A1-} drives the current by so doing power is back to AC from DC side (inversion). The comparison of $V_{control}$ with V_{tri} produces the logic signals to control the switches in leg A and B:

vcontrol > vtriangle: TA1+ on and $V_{AN} = V_{DC}$
vcontrol < vtriangle: TA1- on and $V_{AN} = 0$ (A3.8)

vcontrol > vtriangle: TA2+ on and $V_{BN} = V_{DC}$
vcontrol < vtriangle: TA2- on and $V_{BN} = 0$ (A3.9)

In this method of PWM control the output voltage changes between zero and V_{DC} or zero and $-V_{DC}$ voltage levels as represented in Fig. 5.4. The voltage waveforms v_{AN} and v_{BN} are displaced by 180^o of the fundamental frequency with respect to each other. In this regard, the harmonic components at the switching frequency in v_{AN} and v_{BN} are of the same phase, given by :

$$\phi_{AN} - \phi_{BN} = 180^o \quad \text{(A3.10)}$$

The cancellation of the harmonic component at the switching frequency at the output voltage waveform (v_0) as shown in Fig. A3.4.

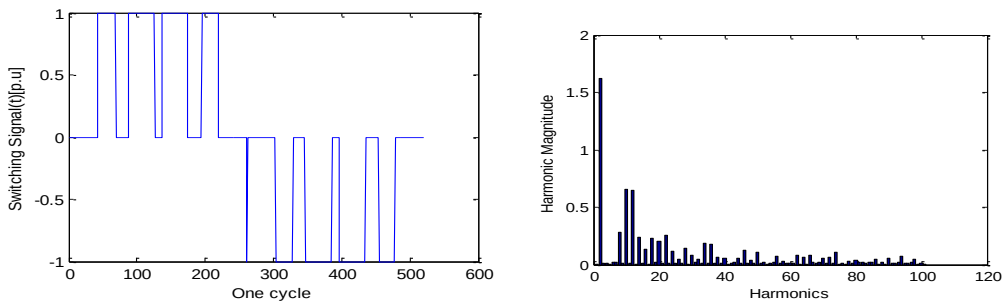

Figure A3.4 Two-level phase output voltage waveform

The magnitude of the fundamental component of the output voltage between point A and B can be determined by

$$V_{AB} = \frac{4.V_{DC}}{\pi} \quad \text{(A3.11)}$$

The Phase switching function is obtained by:

$$S_{ph} = (V_{control} > V_{tri}) - (V_{control} < V_{tri}) \quad \text{(A3.12)}$$

Therefore, the line switching functions are as shown in Fig. A3.7

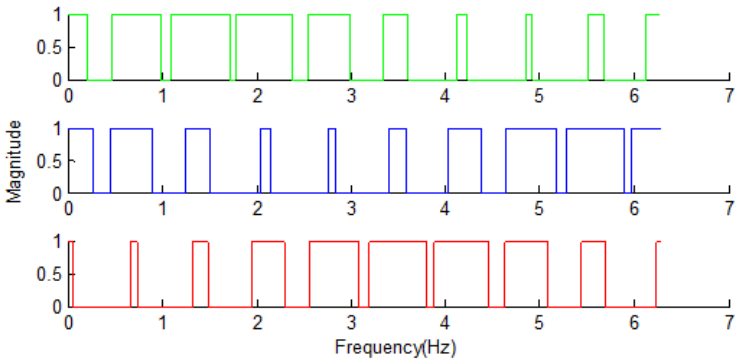

Figure A3.7 Line Switching Function PWM

Phase switching function

$$S_{ab} = SF_{A1+} - SF_{A2+} ; S_{bc} = SF_{A2+} - SF_{A3+} ; S_{ca} = SF_{A3+} - SF_{A1+} \quad \text{(A3.13)}$$

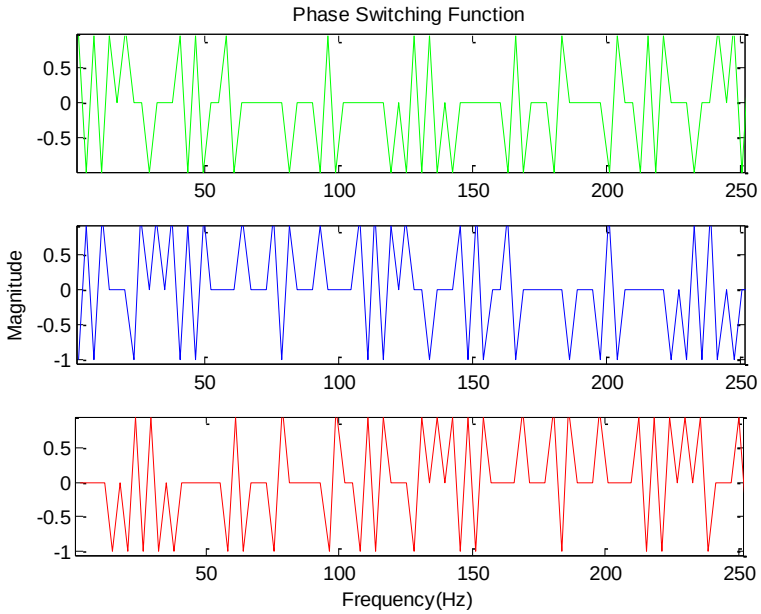

Figure A3.8 Phase Switching Function PWM

The load current block is used to obtain the load current (I_a, I_b, I_c). Assuming the load consists of a balanced R-L load the load currents are derived as the ratio of the phase voltage and respective impedance and is represented as shown in Fig. A3.9:

$$I_a = \frac{V_{AN}}{Z_a} = \frac{V_{AN}}{R + j\omega L} \tag{A3.14}$$

$$I_b = \frac{V_{BN}}{Zb} = \frac{V_{BN}}{R + j\omega L} = I_a(\omega t - 120^o) \tag{A3.15}$$

$$I_c = \frac{V_{CN}}{Zc} = \frac{V_{CN}}{R + j\omega L} = I_a(\omega t + 120^o) \tag{A3.16}$$

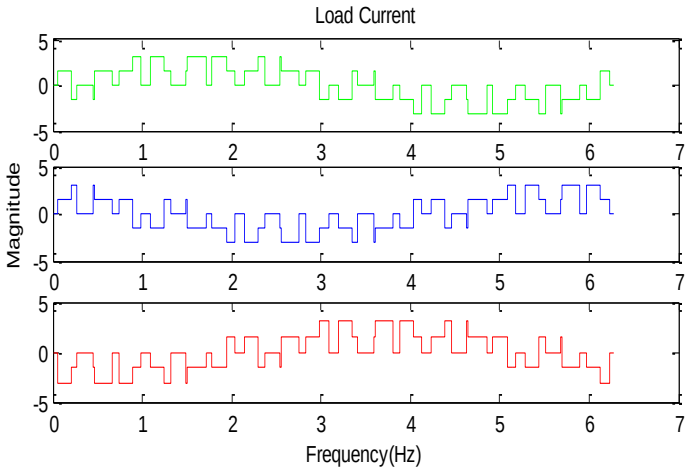

Figure A3.9 Load Current (I_a, I_b, I_c)

The switching current (I_{SFA1-}, I_{SFA2-}, I_{SFA3-}) are determined by the product of the load current with the corresponding switching function as shown in Fig. A3.10:

$$I_{SFA1-} = I_a * <v_{triangle}, T_{A1-} \; ; \; I_{SFA2-} = I_b * <v_{triangle}, T_{A2-} \; ; \; I_{SFA3-} = I_c * <v_{triangle}, T_{A3} \tag{A3.17}$$

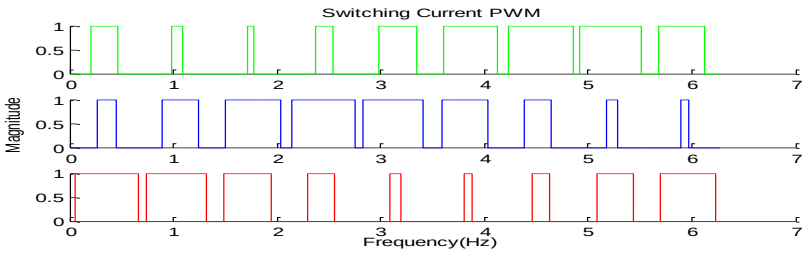

Figure A3.10. Switching Current PWM

The converter input current (I_{in}) can be obtained by

$$I_{in} = I_{SFA1-} + I_{SFA2-} + I_{SFA3-} \tag{A3.18}$$

The converter phase current can be obtained by

$$i_{ab} = I_{SFA1-} - I_{SFA2-} \;;\; i_{bc} = I_{SFA1-} - I_{SFA3-} \;;\; i_{ca} = I_{SFA3-} - I_{SFA1-} \qquad \text{(A3.19)}$$

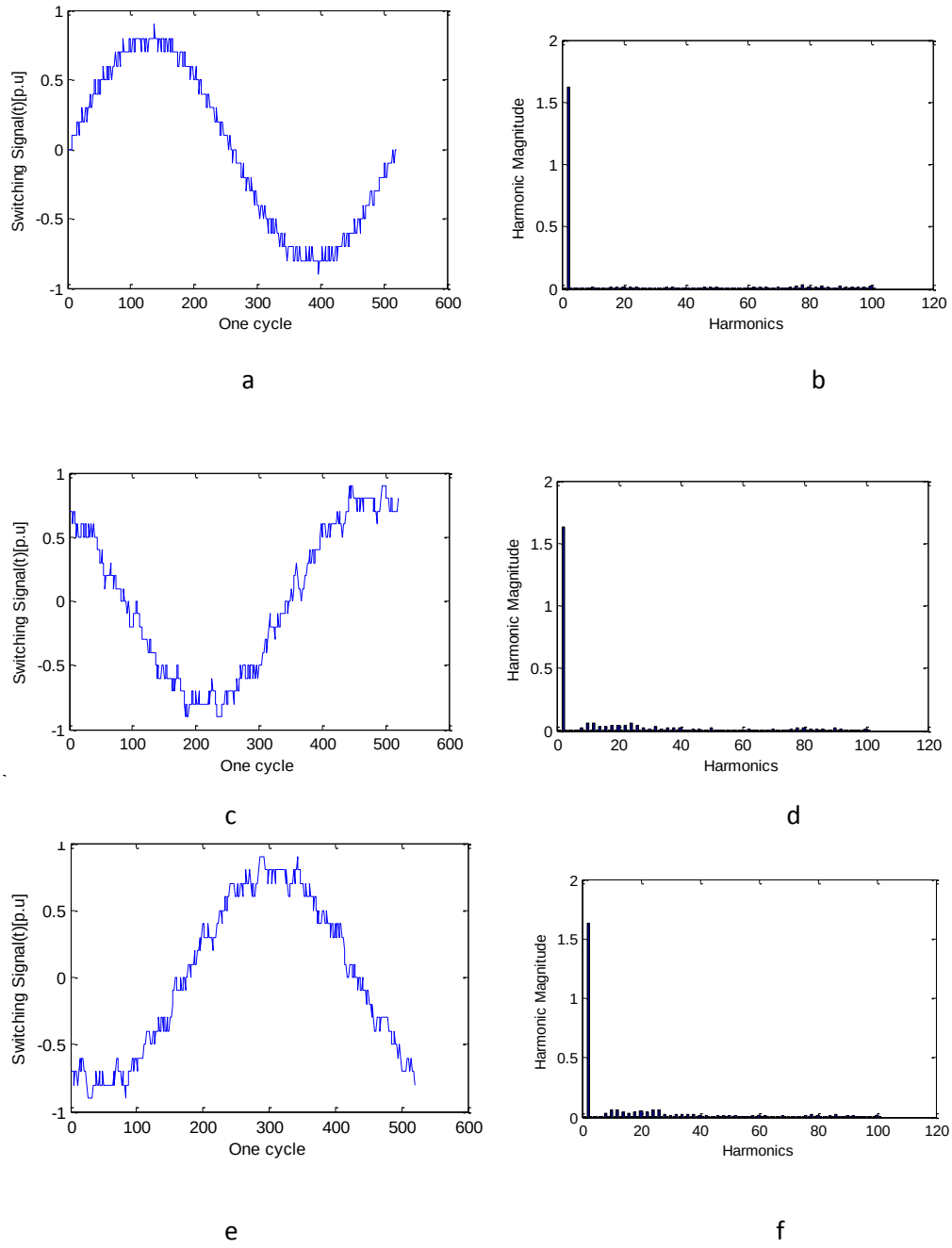

Figure A3.11 Twenty-one-level Phase Switching Function of a ten VSC Unipolar PWM Converters Output voltage of phase a and phase b; (b) The amplitude of all harmonics for the output voltage of phase a and phase b; (c) Output voltage of phase b and phase c; (d) The amplitude of all harmonics for the output voltage of phase b and phase c; (e) Output voltage of phase c and phase a; (f) The amplitude of all harmonics for the output voltage of phase c and phase a

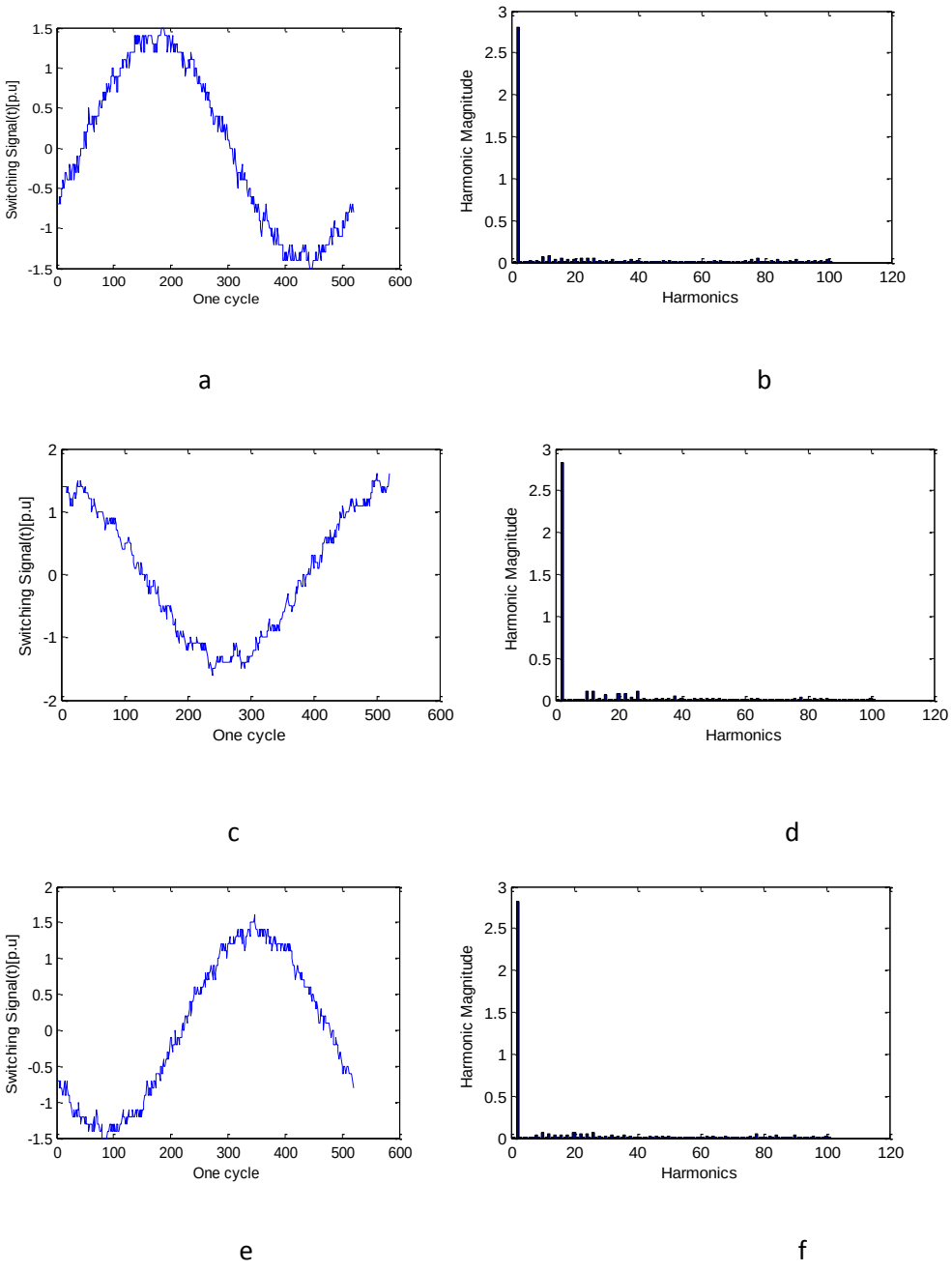

Figure A3.12. Twenty-one-level line-to-line Switching Function of a ten VSC Unipolar PWM Converters Output voltage of phase a and phase b; (b) The amplitude of all harmonics for the output voltage of phase a and phase b; (c) Output voltage of phase b and phase c; (d) The amplitude of all harmonics for the output voltage of phase b and phase c; (e) Output voltage of phase c and phase a; (f) The amplitude of all harmonics for the output voltage of phase c

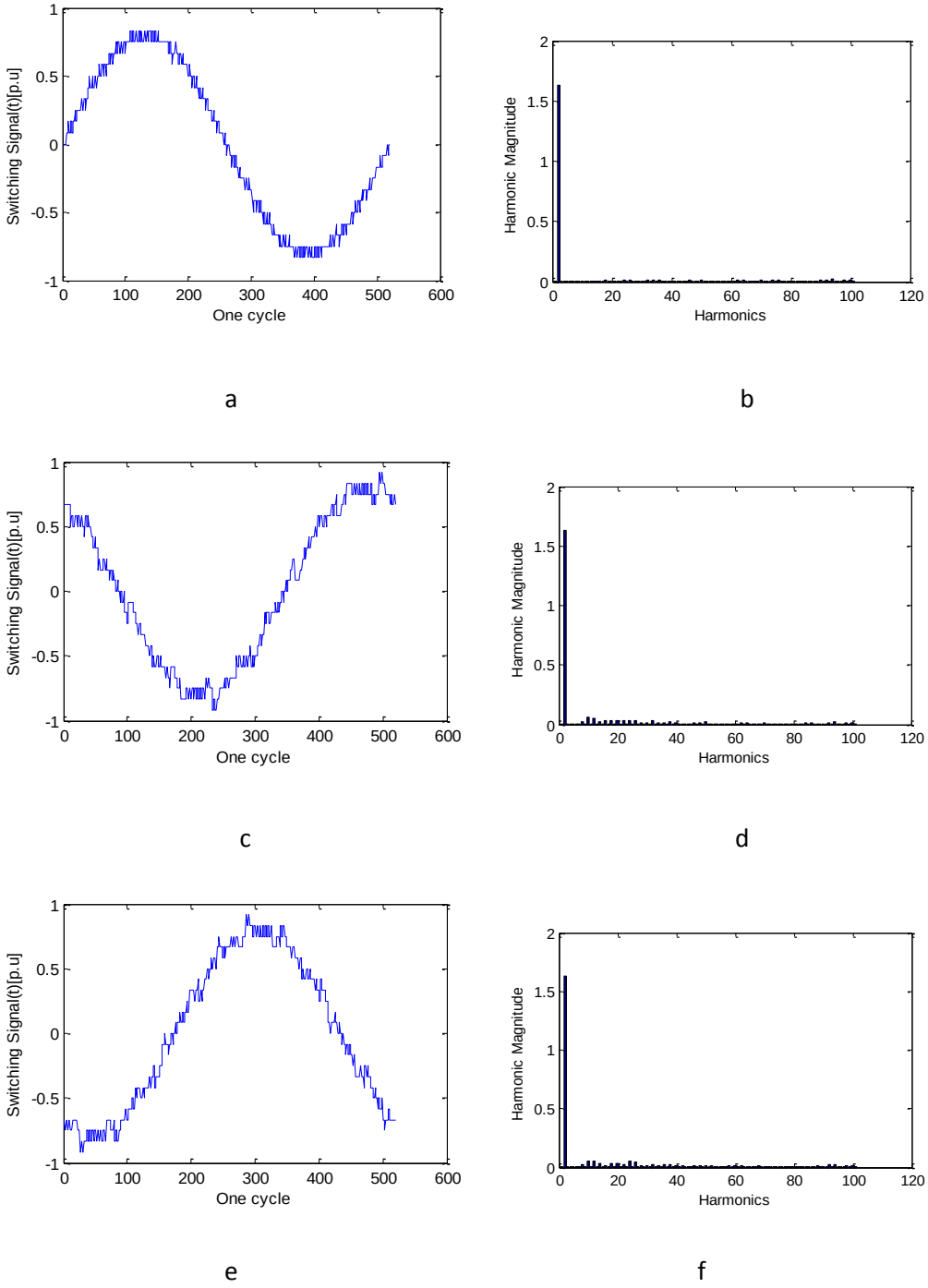

Figure A3.13 . Twenty-five-level Phase Switching Function of a twelve VSC Unipolar PWM Converters. Output voltage of phase a and phase b; (b) The amplitude of all harmonics for the output voltage of phase a and phase b; (c) Output voltage of phase b and phase c; (d) The amplitude of all harmonics for the output voltage of phase b and phase c; (e) Output voltage of phase c and phase a; (f) The amplitude of all harmonics for the output voltage of phase c and phase a

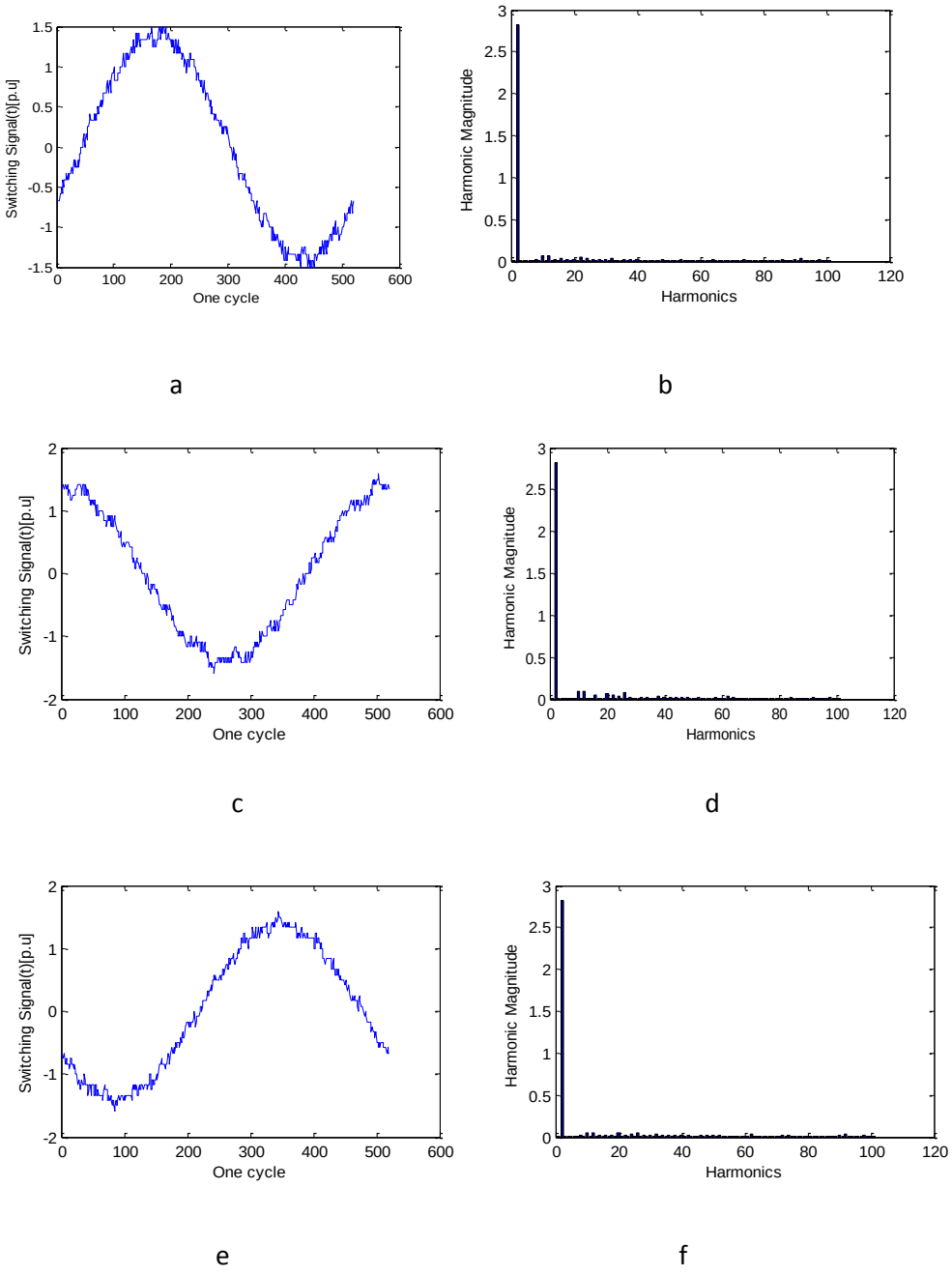

Figure A3.14. Twenty-five-level line-to-line Switching Function of a twelve VSC Unipolar PWM Converters
Output voltage of phase a and phase b; (b) The amplitude of all harmonics for the output voltage of phase a and phase b; (c) Output voltage of phase b and phase c; (d) The amplitude of all harmonics for the output voltage of phase b and phase c; (e) Output voltage of phase c and phase a; (f) The amplitude of all harmonics for the output voltage of phase c

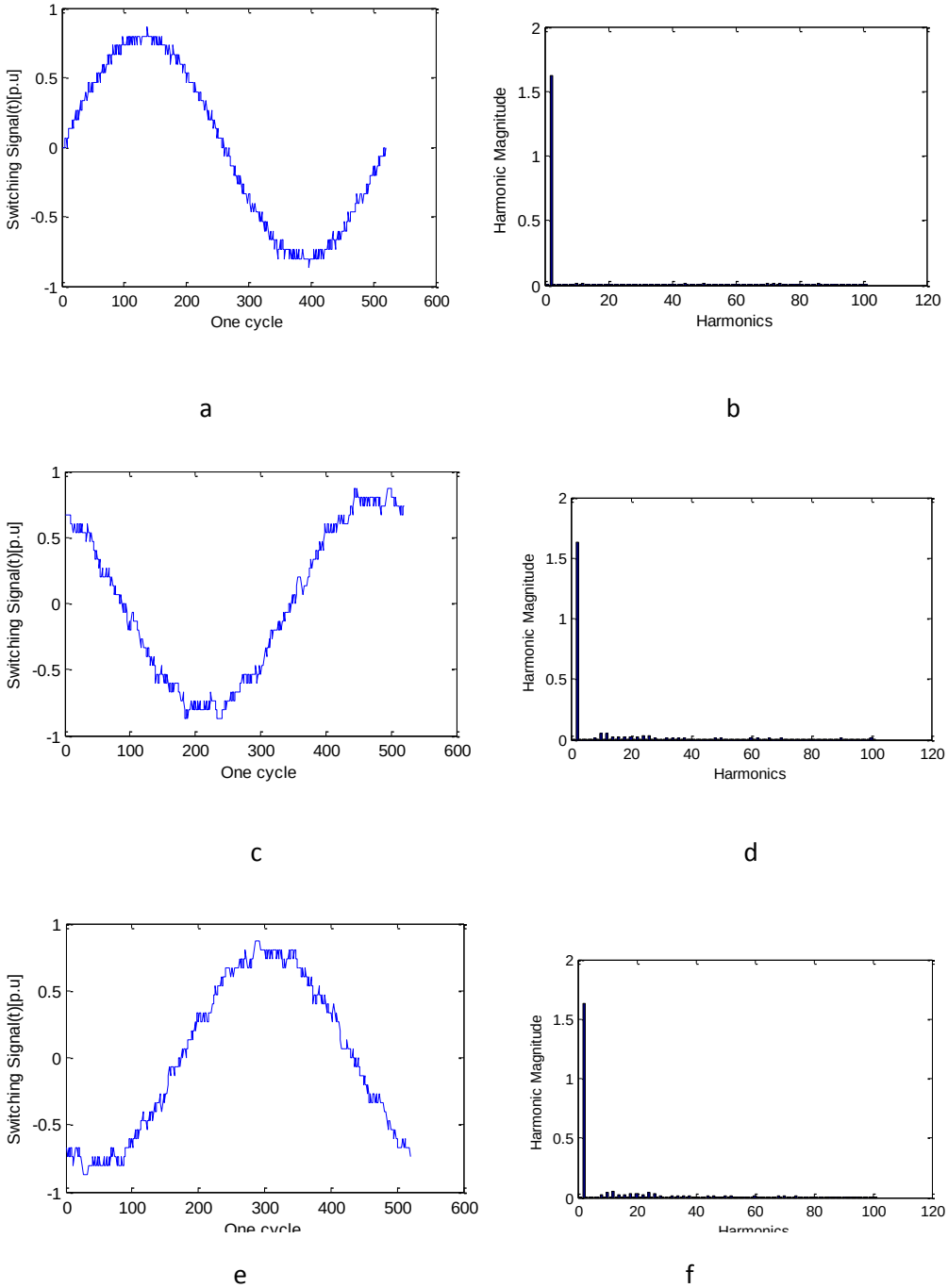

Figure A3.15. Thirty-one-level Phase Switching Function of a fifteen VSC Unipolar PWM Converters
Output voltage of phase a and phase b; (b) The amplitude of all harmonics for the output voltage of phase a and phase b; (c) Output voltage of phase b and phase c; (d) The amplitude of all harmonics for the output voltage of phase b and phase c; (e) Output voltage of phase c and phase a; (f) The amplitude of all harmonics for the output voltage of phase c

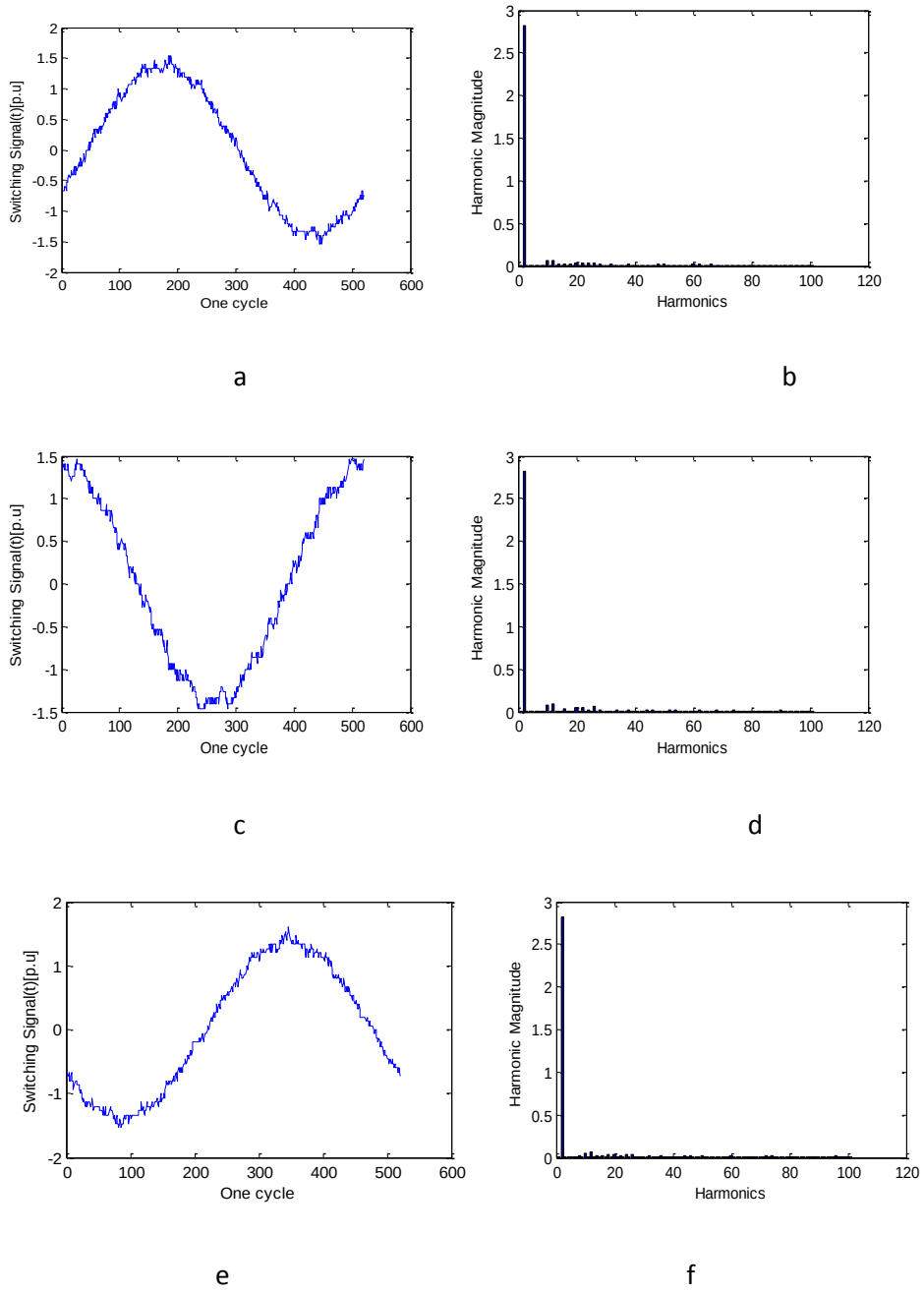

Figure A3.16. Thirty-one-level line-to-line Switching Function of a fifteen VSC Unipolar PWM Converters. Output voltage of phase a and phase b; (b) The amplitude of all harmonics for the output voltage of phase a and phase b; (c) Output voltage of phase b and phase c; (d) The amplitude of all harmonics for the output voltage of phase b and phase c; (e) Output voltage of phase c and phase a; (f) The amplitude of all harmonics for the output voltage of phase c

The waveforms and harmonic spectraof the phase and line-to-line voltages for three-phase 12-level and 15-level respectively. From the figures, it can be seen that the usual stairs structure of the MMC is defined and heading to total sinusoidal waveforms, hence leading to cancellation of all the harmonic contents. Also, the harmonic spectra do not

indicate any highly significant harmonic due to the common mode cancellation between the converter phase legs. Instead, only the occurrence of the first significant harmonic is found which has no significant threat in the network.

Appendix A4

A4.1. **Induction Generator abc model**

The Fig. A4.1 shows induction generator with rotor and stator windings neglecting saturation and losses in the core.

The voltages applied to each stator and rotor phases is given as

$$[V] = [v_A\ v_B\ v_C\ \ v_a\ v_b\ v_c]^T \tag{A4.1}$$

Similarly, the currents in each stator and rotor phases is given as

$$[I] = [I_A\ I_B\ I_C\ \ i_a\ i_b\ i_c]^T \tag{A4.2}$$

Also, the fluxes linked with each stator and rotor phases is obtained as

$$[\psi] = [\varphi_A\ \ \varphi_B\ \ \varphi_C\ \ \varphi_a\ \ \varphi_b\ \ \varphi_c]^T \tag{A4.3}$$

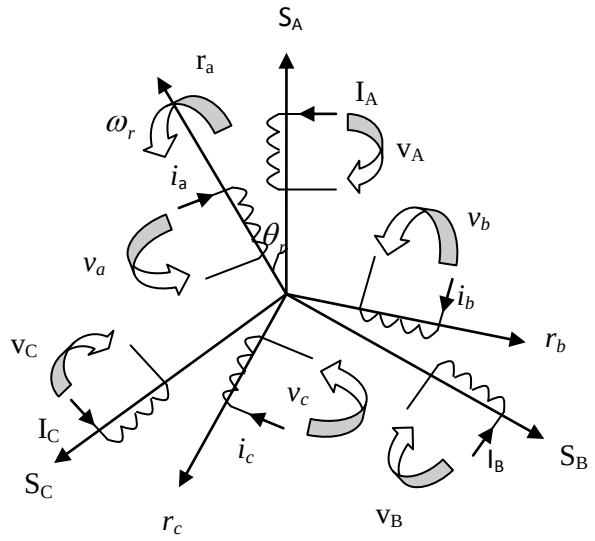

Figure A4.1**.** Six-pole induction generator with rotor and stator windings

The voltage $[V]$ matrix is given as

$$[V] = [R]\cdot[I] + \frac{d[\psi]}{dt} \tag{A4.4}$$

where

[R] is the resistance matrix

$$[\psi] = [L]\cdot[I] \tag{A4.5}$$

where

[L] is the inductance matrix

The state-variable form of Equ. (A4.4) and (A4.5) is given as

$$\frac{d[I]}{dt} = [L]^{-1} \cdot \left\{ -[R] - \frac{d[L]}{dt} \right\} \cdot [I] + [L]^{-1} \cdot [V] \tag{A4.6}$$

The inductance matrix [L] is functions of the rotor position θ_r, therefore

$$\frac{d[L]}{dt} = \frac{d[L]}{d\theta_r} \cdot \frac{d\theta_r}{dt} = \frac{d[L]}{d\theta_r} \cdot \omega_r \tag{A4.7}$$

The state space form of the dynamic equations is the combination of Equ. (A4.6) and (A4.7), which yield

$$\frac{d[I]}{dt} = [L]^{-1} \cdot \left\{ -[R] - \omega_r \cdot \frac{d[L]}{d\theta_r} \right\} \cdot [I] + [L]^{-1} \cdot [V] \tag{A4.8}$$

where

ω_r is the rotor speed

The inductance matrix [L] is represented as

$$[L] = \begin{bmatrix} L_s & -5/10M_s & -5/10M_s & M_{sr}f_1 & M_{sr}f_2 & M_{sr}f_3 \\ -5/10M_s & L_s & -5/10M_s & M_{sr}f_3 & M_{sr}f_1 & M_{sr}f_2 \\ -5/10M_s & -5/10M_s & L_s & M_{sr}f_2 & M_{sr}f_3 & M_{sr}f_1 \\ M_{sr}f_1 & M_{sr}f_3 & M_{sr}f_2 & L_r & -5/10M_r & -5/10M_r \\ M_{sr}f_2 & M_{sr}f_1 & M_{sr}f_3 & -5/10M_r & L_r & -5/10M_r \\ M_{sr}f_3 & M_{sr}f_2 & M_{sr}f_1 & -5/10M_r & -5/10M_r & L_r \end{bmatrix} \tag{A4.9}$$

$$L_s = L_{\sigma s} + M_s \tag{A4.10}$$

$$L_r = L_{\sigma r} + 1.5M_r \tag{A4.11}$$

$$f_1 = \cos\theta_r;\ f_2 = \cos\left(\theta_r + \frac{2\pi}{3}\right);\ f_3 = \cos\left(\theta_r - \frac{2\pi}{3}\right) \tag{A4.12}$$

where

M_s is the stator mutual inductance

M_r is the rotor mutual inductance

L_s is the stator self-inductance

L_r is the rotor self-inductance

$L_{\sigma r}$ is the rotor leakage inductance

$L_{\sigma s}$ is the stator leakage inductance

For a balanced system, that is when

$$I_A + I_B + I_C = 0 \quad \text{and } i_a + i_b + i_c = 0 \tag{A4.13}$$

Equ. (A4.9) is transform to

$$[L] = \begin{bmatrix} L_s & 0 & 0 & M_{sr}f_1 & M_{sr}f_2 & M_{sr}f_3 \\ 0 & L_s & 0 & M_{sr}f_3 & M_{sr}f_1 & M_{sr}f_2 \\ 0 & 0 & L_s & M_{sr}f_2 & M_{sr}f_3 & M_{sr}f_1 \\ M_{sr}f_1 & M_{sr}f_3 & M_{sr}f_2 & L_r & 0 & 0 \\ M_{sr}f_2 & M_{sr}f_1 & M_{sr}f_3 & 0 & L_r & 0 \\ M_{sr}f_3 & M_{sr}f_2 & M_{sr}f_1 & 0 & 0 & L_r \end{bmatrix} \tag{A4.14}$$

$$L_s = L_{\sigma s} + 1.5M_s ; L_r = L_{\sigma r} + 1.5M_r \tag{A4.15}$$

The inductance matrix [L] in functions of the rotor position θ_r, can be derived from Equ. (A4.14) as

$$\frac{d}{d\theta_r}[L] = -M_{sr}\begin{bmatrix} 0 & 0 & 0 & h_1 & h_2 & h_3 \\ 0 & 0 & 0 & h_3 & h_1 & h_2 \\ 0 & 0 & 0 & h_2 & h_3 & h_1 \\ h_1 & h_3 & h_2 & 0 & 0 & 0 \\ h_2 & h_1 & h_3 & 0 & 0 & 0 \\ h_3 & h_2 & h_1 & 0 & 0 & 0 \end{bmatrix} \tag{A4.16}$$

where

$$h_1 = \sin\theta_r ;\ h_2 = \sin\left(\theta_r + \frac{2\pi}{3}\right);\ h_3 = \sin\left(\theta_r - \frac{2\pi}{3}\right)$$

A4.2. Induction Generator dq0 Arbitrary Reference Frame Model

The inductance in functions of the rotor position θ_r speed is time-varying, except when the rotor is at stand-still.

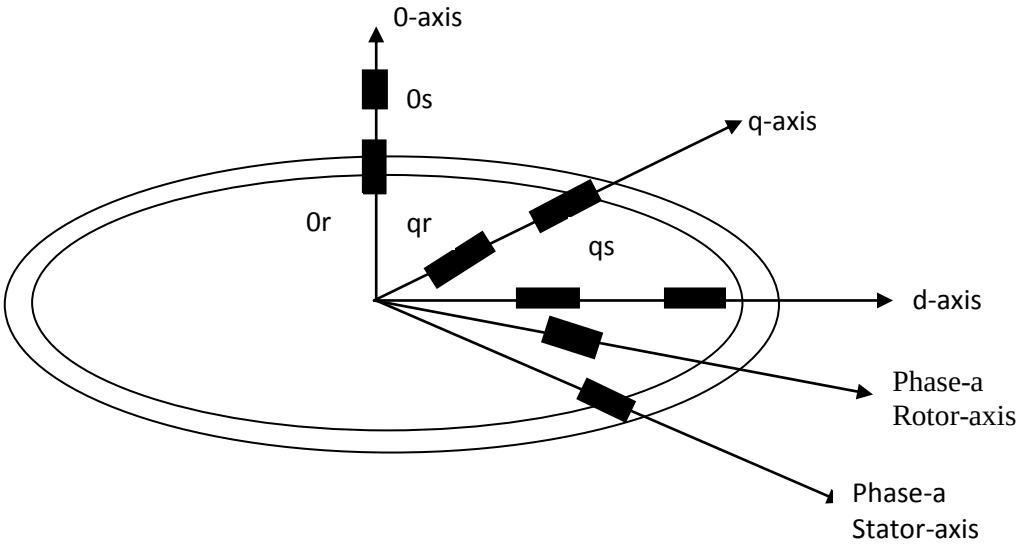

Figure. A4.2. Induction generator dq0 arbitrary reference frame model

The transformation of Equ. (A4.4) yield Equ. (A4.17), which is the voltage in arbitrary reference frame model.

$$\begin{bmatrix} v_{sd} \\ v_{sq} \\ v_{s0} \\ v_{rd} \\ v_{rq} \\ v_{r0} \end{bmatrix} =$$

$$\left\{ \begin{bmatrix} R_{sd} & 0 & 0 & 0 & 0 & 0 \\ 0 & R_{sq} & 0 & 0 & 0 & 0 \\ 0 & 0 & R_{s0} & 0 & 0 & 0 \\ 0 & 0 & 0 & R_{rd} & 0 & 0 \\ 0 & 0 & 0 & 0 & R_{rq} & 0 \\ 0 & 0 & 0 & 0 & 0 & R_{r0} \end{bmatrix} + \frac{d}{dt} \begin{bmatrix} L_s & 0 & 0 & L_m & 0 & 0 \\ 0 & L_s & 0 & 0 & L_m & 0 \\ 0 & 0 & L_{\sigma S} & 0 & 0 & 0 \\ L_m & 0 & 0 & L_r & 0 & 0 \\ 0 & L_m & 0 & 0 & L_r & 0 \\ 0 & 0 & 0 & 0 & 0 & L_{\sigma r} \end{bmatrix} + \right.$$

$$\left. \begin{bmatrix} 0 & -\omega_{gs} & 0 & 0 & 0 & 0 \\ \omega_{gs} & 0 & 0 & 0 & 0 & 0 \\ 0 & 0 & 0 & 0 & 0 & 0 \\ 0 & 0 & 0 & 0 & -(\omega_{gs}-\omega_r) & 0 \\ 0 & 0 & 0 & (\omega_{gs}-\omega_r) & 0 & 0 \\ 0 & 0 & 0 & 0 & 0 & 0 \end{bmatrix} \begin{bmatrix} L_s & 0 & 0 & L_m & 0 & 0 \\ 0 & L_s & 0 & 0 & L_m & 0 \\ 0 & 0 & L_{\sigma s} & 0 & 0 & 0 \\ L_m & 0 & 0 & L_r & 0 & 0 \\ 0 & L_m & 0 & 0 & L_r & 0 \\ 0 & 0 & 0 & 0 & 0 & L_{\sigma r} \end{bmatrix} \right\} \begin{bmatrix} i_{sd} \\ i_{sq} \\ i_{s0} \\ i_{rd} \\ i_{rq} \\ i_{r0} \end{bmatrix}$$

(A4.17)

In more compact form Equ. (A4.17) can be represented as

$$[V]=\left\{[R]+\frac{d}{dt}[L]+[\omega][L]\right\}[I] \tag{A4.18}$$

The linkage fluxes and currents are related as

$$[\psi]=[L][I] \tag{A4.19}$$

where

$L_m=\frac{3}{2}M_{sr}$ is the mutual inductance in the general reference frame

$L_s=L_{\sigma s}+L_m$ is the stator self inductance

$L_r=L_{\sigma r}+L_m$ is the rotor self inductance

A4.3. **Induction Generator model in Steady State**

An equivalent electrical circuit of induction generator is as shown in Fig. A4.3, where r_s = stator resistance, $r_r^{'}$ = rotor resistance, x_s = stator leakage reactance, $x_r^{'}$ = rotor leakage reactance, r_m = iron loss resistance, x_m = magnetizing reactance,

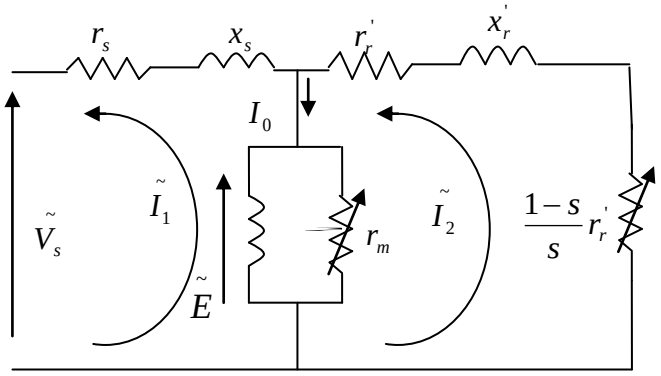

Figure A4.3. Equivalent circuit of induction generator

From Equ. (A4.17) in the rotating reference frame $\omega_{gs}=\omega_r$

The steady-state voltage formulations are obtain as

$$\bar{V}_s=(r_s+jX_s)I_s+r_m\,//\,jX_m(I_r)$$

$$\bar{V}_r=(r_r+jsX_r)I_r+r_m\,//\,jsX_m(I_r) \tag{A4.20}$$

Equ. (A4.20)can be represented in matrix form as follow

$$\begin{bmatrix} \bar{V}_s \\ \bar{V}_r \end{bmatrix} = \begin{bmatrix} r_s + jX_s & r_m \,//\, jX_m \\ r_m \,//\, jsX_r & r_r + jsX_r \end{bmatrix} \begin{bmatrix} I_s \\ I_r \end{bmatrix} \quad \text{(A4.21)}$$

In more compact form Equ. (A4.21)can be represented as

$$[V] = [Z][I] \quad \text{(A4.22)}$$

where

X_s is the self reactance of the stator windings

X_r is the self reactance of the rotor windings

The stator and rotor currents are obtained as

$$[I] = [Z]^{-1} \cdot [V] \quad \text{(A4.23)}$$

The active power P_s of the stator is obtained as

$$P_s = \frac{3}{2}\mathrm{Re}\,al(V_S \cdot I_S) \quad \text{(A4.24)}$$

The reactive power Q_s of the stator is obtained as

$$Q_s = \frac{3}{2}\mathrm{Im}\,ag(V_S \cdot I_S) \quad \text{(A4.25)}$$

Similarly, the active power P_r of the rotor is obtained as

$$P_r = \frac{3}{2}\mathrm{Re}\,al(V_r \cdot I_r) \quad \text{(A4.26)}$$

The reactive power Q_r of the rotor is obtained as

$$Q_r = \frac{3}{2}\mathrm{Im}\,ag(V_r \cdot I_r) \quad \text{(A4.27)}$$

In the equivalent circuit Fig. A4.3, the power loss in r_s and r_m represents the primary copper loss and the core loss. The power loss in the resistance $\frac{1-s}{s} r_r^{'}$ must therefore represent the average input of power to the rotor, for there can be no dissipation of power in the reactance x_m and $x_r^{'}$. Thus the input of power per phase to the rotor is $\left(I_2^{'}\right)^2 \frac{r_r^{'}}{s}$, but the power dissipated in the actual resistance of the rotor circuit is only $\left(I_2^{'}\right)^2 r_r^{'}$.

Therefore, generator input power is $\left(I_2^{'}\right)^2 \frac{1-s}{s} r_r$.

If *P* is the total power absorbed by the rotor, then

Electromagnetic power input to rotor is

$$P = n\left(I_2^{'}\right)^2 \frac{r_r^{'}}{s} \tag{A4.28}$$

The power loss in rotor resistance is

$$sP = n\left(I_2^{'}\right)^2 r_r^{'} \tag{A4.29}$$

Mechanical power output is

$$(1-s)P = n\left(I_2^{'}\right)^2 \frac{1-s}{s} r_r^{'} \tag{A4.30}$$

where n is the number of phases

The torque *T* exerted on the rotor by the rotating magnetic field. If there are *P* pairs of poles, the angular velocity of the field is $\omega_S = \frac{\omega}{P}$, and the rotating field therefore does work at rate $\omega_s T$. This would obviously be true if the rotating field were produced by physical poles on the stator, driven mechanically at a speed ω_s, the electromagnetic field is the same when a poly-phase winding produces the rotating field, so the work done must be the same. Since the rotor runs at a speed $\omega_p = (1-s)\omega_s$,

then mechanical power output given is as

$$\omega_r T = (1-s)\omega_s T \tag{A4.31}$$

The difference between the work done by the field and the mechanical output must be absorbed in rotor losses, that is

$$(\omega_s - \omega_r)T = s\omega_s T \tag{A4.32}$$

Thus,

Electromechanical power input to rotor

$$P = \omega_s T \tag{A4.33}$$

Power loss in rotor resistance

$$P = (\omega_s - \omega_r)T = s\omega_s T \tag{A4.34}$$

Mechanical power output

$$P = \omega_r T = (1-s)\omega_s T \tag{A4.35}$$

The fraction of the input power lost in rotor resistance is equal to the fractional slip s, since there must always be some slip between the rotor and the rotating magnetic field,

this present an unavoidable power loss. The ratio of mechanical power output to electromagnetic power input is known as the rotor efficiency, and is equal to $1-s$.

The torque may be determined for a given value of slip by equating expressions (A4.28) and (A4.33) for electromagnetic power, and obtaining the value of $I_2^{'}$ from the equivalent circuit of Fig. A4.3..

For a machine with n phases and *P* pole pairs, the torque is

$$T = \frac{nP}{\omega} \cdot \frac{r_2^{'}}{s} \cdot \frac{V_1^2}{X^2 + \left(\frac{r_2^{'}}{s}\right)^2} \tag{A4.36}$$

Alternatively,

$$T = \frac{nP}{\omega} \cdot \frac{V_1^2}{X} \cdot \frac{1}{\frac{sX}{r_2^{'}} + \frac{r_2^{'}}{sX}} \tag{A4.37}$$

A4.4. Motoring and Generating Regions of Induction Machine

Since the slip s is related to the rotor speed ω_r by $s = \frac{\omega_s - \omega_r}{\omega_s}$ and equ. (A4.37) gives the torque /speed relationship for the induction machine. Fig. A4.4a and Fig. A4.4b shows a typical torque/slip characteristic.

The slip of induction generator at harmonic frequency is given as

$$S_h = \frac{h\omega_s - h\omega_r}{h\omega_s} \tag{A4.38}$$

The synchronous speed is

$$\omega_s = \frac{\omega}{p} \tag{A4.39}$$

where

S_h = slip for h^{th} harmonics, ω_r = rotor speed, ω_s = synchronous speed, $\omega = 2\pi f$, p = number of poles.

It is noted that $\omega_s < \omega_r$, the slip s is always negative as it should be for generator action.

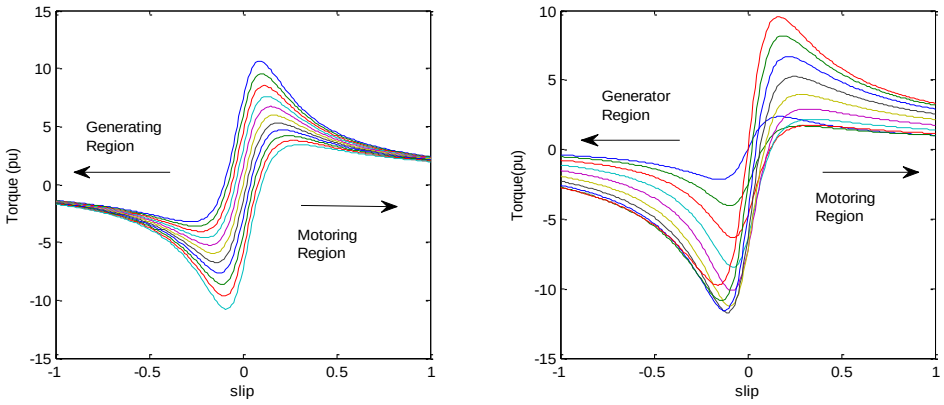

(a) (b)

Figure A4.4. (a) Typical torque-slip characteristic of an induction machine (b) Torque-slip curves with increased rotor resistance

It should be noted here that there can be no induced rotor currents when s = 0 and $\omega_r = \omega_s$, so the torque must be zero at this point. There are two distinct regions to the torque/slip characteristic shown in Fig. A4.4a and Fig. A4.4b which is generating region and motoring region.

A4.4.1. Motoring region

In the motoring region as shown in Fig. A4.4, the rotor speed ω_r is positive but less than the synchronous speed ω_s, the torque is also positive; in addition the machine converts electrical power into mechanical power. The slip varies from 1 when the rotor is on standstill to 0 when the rotor runs at the synchronous speed. The resistance $\frac{1-s}{s} r_2^{'}$ is positive and greater than $r_2^{'}$, thus the total electrical power absorbed by the rotor exceeds the power dissipated in the rotor resistance, and the balance is extracted as mechanical power at the shaft. The overall efficiency of the machine cannot exceed the rotor efficiency of 1 – s, induction motors operate with a small value of slip. The full-load slip can be as low as 1 per cent in large machines and can exceed 5 per cent in small machine; therefore the normal rotor speed is always close to the synchronous speed [37].

A4.4.2. Generating region

In the event that the rotor is driven mechanically so that its speed exceeds the synchronous speed, the torque reverses and the machine absorbs mechanical power.

Both the slip and $\frac{1-s}{s} r_2^{'}$ are negative in this region, the rotor therefore transmits electrical power to the stator, and the induction machine exhibit generator characteristic as shown Fig. A4.4.

An induction machine requires an external source of reactive power for it to act as a generator, since the magnetising current flowing in X_m cannot be provided by the rotor. While the synchronous machine provides its own magnetising current because of the field winding on the rotor, there is no need for external source. An AC grid fed induction generator will require reactive power for its operation, but can also operate without an external AC grid by connecting a capacitor bank to the stator terminals which will supply the required reactive power and the machine will self-excite.

As a result, induction generators have gained an advantage in industrial plants and as well as wind turbine feeding oil and gas platforms, because they are more robust and light in weight than synchronous generators.

The presence of negative resistance (i.e., when slip is negative), implies that during the generating mode, power flows from the rotor to the stator in the induction generator.

An induction generator needs AC excitation current for its running. The machine is either self excited or externally excited. The steady-state per-phase equivalent circuit of a self-excited induction generator is as shown in the Fig. A4.4.

A4.4.3. Asynchronous motor

It is evident that single cage induction motor model as shown in Fig. A4.5 is not able to capture both the starting characteristics and the breakdown torque characteristics of a cage induction motor. Therefore, for motor start-up simulations the double cage model is recommended and is as represented in Fig. 6. A4.6. The induction motor has remained the most popular type of motor for industry applications. The primary advantage of the induction motor is its straightforward rotor construction leading to low-cost, ruggedness, and low-maintenance requirement.

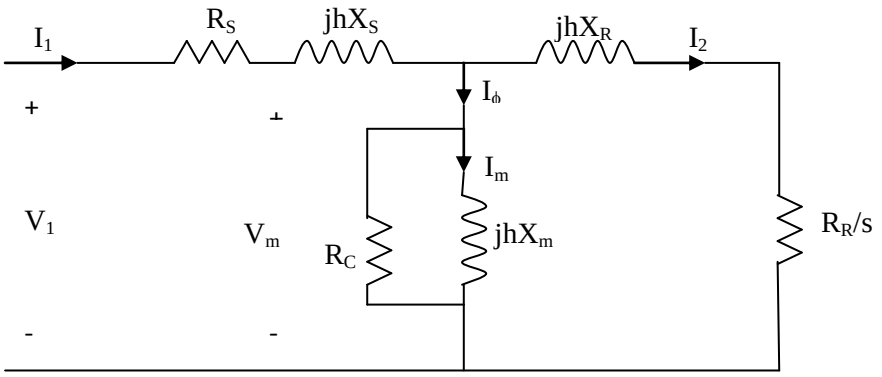

Figure A4.5. Per-phase single-cage equivalent circuit of an induction motor

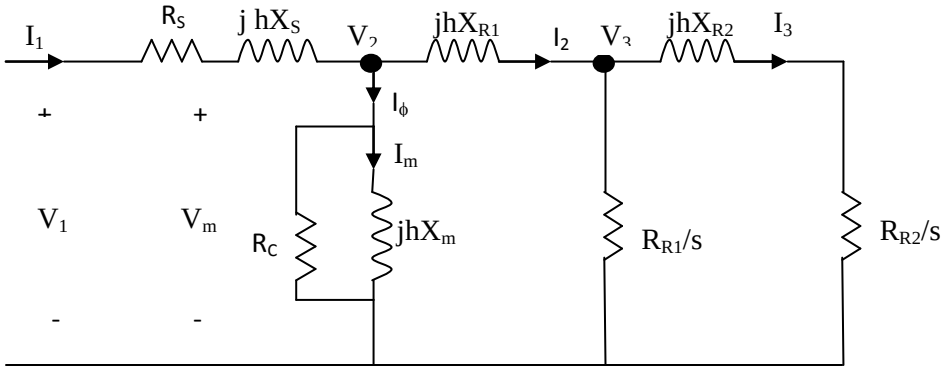

Figure A4.6. Per-phase double-cage equivalent circuit of an induction motor

The equivalent circuit for the double cage model is shown in Fig. A4.6, the impedances as admittances are obtained in harmonic domain as follows:

$$Y_S = \left(R_S + jhX_S\right)^{-1} \tag{A4.40}$$

$$Y_m = \left(\frac{1}{R_C} + \frac{1}{jhX_m}\right)^{-1} \tag{A4.41}$$

$$Y_{R1} = \left(\frac{R_{R1}}{s} + jhX_1\right)^{-1} \tag{A4.42}$$

$$Y_{R2} = \left(\frac{R_{R2}}{s} + jhX_2\right)^{-1} \tag{A4.43}$$

Total admittance is

$$Y = \frac{1}{\left(R_S + jhX_S\right)} + \frac{\left(jhX_m\right)R_c}{R_C + jhX_m} + \frac{s}{\left(R_{R1} + jhX_1 s\right)} + \frac{s}{\left(R_{R2} + jhX_2 s\right)} \tag{A4.44}$$

Applying Kirchoff's law at node V_2:

$$\left(V_1 - V_2\right)Y_S = V_2\left(Y_m + Y_{R1} + Y_{R2}\right) \tag{A4.45}$$

$$V_1 Y_S = V_2\left(Y_S + Y_m + Y_{R1} + Y_{R2}\right) \tag{A4.46}$$

$$V_2 = \frac{V_1 Y_S}{Y_S + Y_m + Y_{R1} + Y_{R2}} \tag{A4.47}$$

The stator current I_s is given as

$$I_s = (V_1 - V_2) Y_S \tag{A4.48}$$

While the rotor current I_{R1} and I_{R2} are obtain as:

$$I_{R1} = V_2 Y_{R1} \tag{A4.49}$$
$$I_{R2} = V_2 Y_{R2}$$

The torque developed in the motor (N-m) is:

$$T = \frac{R_{R1}}{s} I_{R1}^2 + \frac{R_{R2}}{s} I_{R2}^2 \tag{A4.50}$$

Induction motor Data
r1 = 0.220; % Stator resistance
x1 = 0.430; % Stator reactance
r2 = 0.127; % Rotor resistance
x2 = 0.430; % Rotor reactance
xm = 15.0; % Magnetization branch reactance
v_phase = 208 / sqrt(3); % Phase voltage
n_sync = 1800; % Synchronous speed (r/min)
w_sync = 188.5; % Synchronous speed (rad/s)

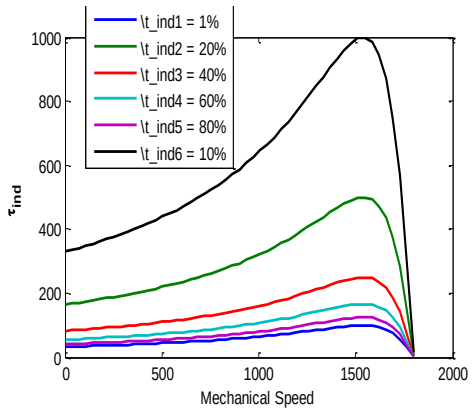

(a)

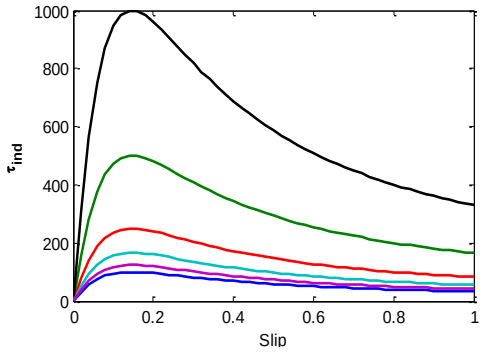

(b)

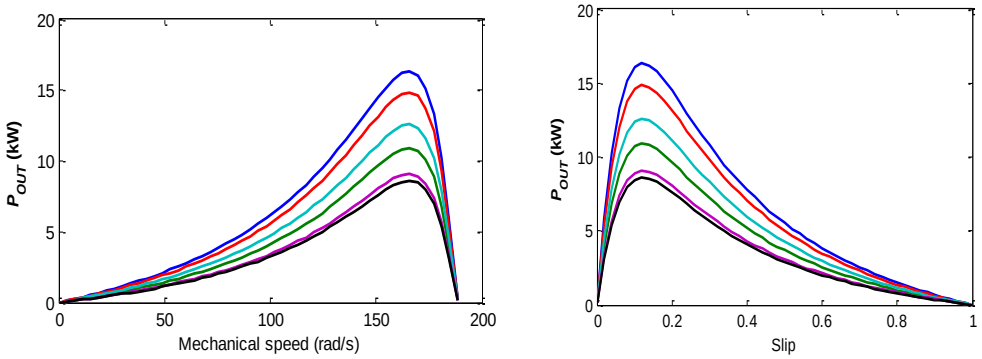

(c) (d)

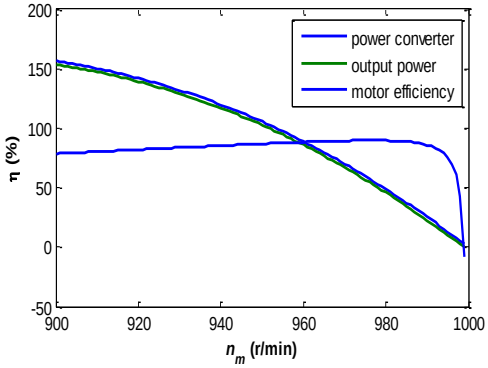

(e)

Figure A4.7. Induction motor: (a) Motor Torque versus Speed Characteristic (b) Motor torque versus slip (c) output power versus Speed (d) output power versus slip (e) output power and efficiency

Harmonic model of transformers

The physical model of a single-phase transformer is as shown in Fig. A4.8.

The corresponding electrical and magnetic equations are

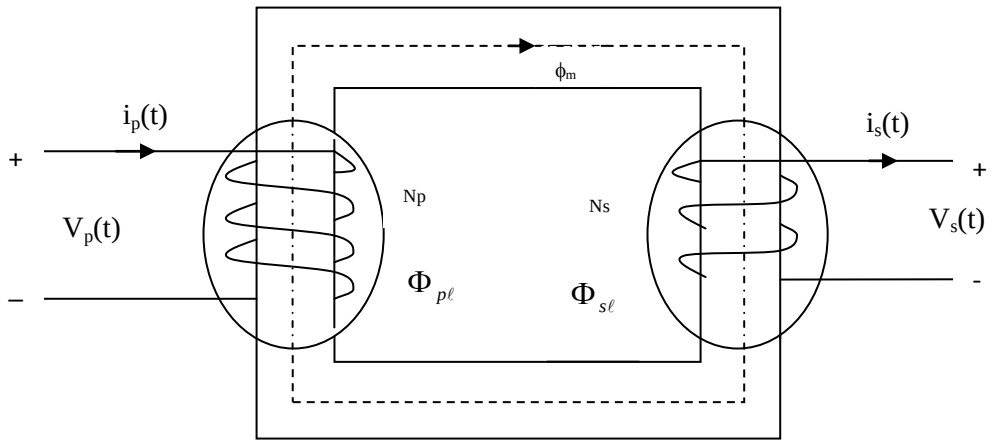

Figure A4.8. Physical model of a single-phase transformer

$$V_P(t) = R_P i_P(t) + X_P \frac{di_p(t)}{dt} + E_P(t) \quad \text{(A4.51)}$$

$$V_S(t) = R_S i_S(t) + X_S \frac{di_S(t)}{dt} + E_S(t) \quad \text{(A4.52)}$$

$$\Phi_m = BA \quad \text{(A4.53)}$$

$$B = f_{\text{nonlinear}}(H) \quad \text{(A4.54)}$$

$$N_P i_p(t) + N_S i_s(t) = H\ell \quad \text{(A4.55)}$$

where

R_p and R_S are the resistances of the primary and the secondary windings, respectively,

X_P and X_S are the leakage inductances of primary and secondary windings, respectively,

$E_P(t) = N_P \frac{d\phi_m}{dt}$ and $E_S(t) = N_S \frac{d\phi_m}{dt}$ are the induced voltages of the primary and the secondary windings, respectively,

N_p and N_s are the number of turns of the primary and the secondary windings, respectively,

B, H and Φ_m are the magnetic flux density, the magnetic field intensity, and the magnetic flux in the iron core of the transformer, respectively,

A and ℓ are the effective cross section and length of the integration path of transformer core, respectively.

From Equ. I_{exc} could be obtained as

$$i_p(t) + \frac{N_S i_s(t)}{N_P} = \ell_{exc}(t) \quad \text{(A4.56)}$$

where $i_{exc}(t) = H\ell / N_P$ is the transformer excitation (no-load) current, which is the sum of the magnetizing ($i_{\text{mag}}(t)$) and core-loss ($i_{\text{core}}(t)$) currents. Combining Eqs. (A4.53) and (A4.54), it is clear that the no-load current is related to the physical parameters, that is, the magnetizing curve (including saturation and hysteresis) and the induced voltage.

Based on Eqs. (A4.51), (A4.52), and 2-33, the general harmonic model of transformer is obtained as shown in Fig. A4.10.

There are four dominant characteristic parameters:

- Winding resistance,
- Leakage inductance,

- Magnetizing current, and
- Core-Loss current

Some models assume constant values for the primary and the secondary resistances. However, most references take into account the influence of skin effects and proximity effects in the harmonic model. Since primary $(\Phi_{p\ell})$ and secondary $(\Phi_{s\ell})$ leakage fluxes mainly flow across air, the primary and the secondary leakage inductances can be assumed to be constants. The main difficulty arises in the computation of the magnetizing and core-loss currents, which are the main sources of harmonics in power transformers.

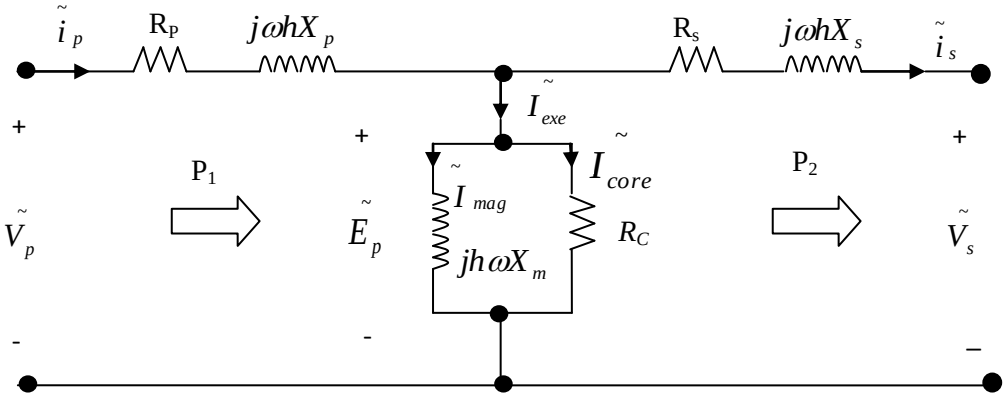

Figure A4.9. Equivalent circuit linear single-phase, steady state transformer model

The total admittance of the transformer is:

$$Y_{TRANS} = \frac{1}{R_P + j\omega hX_P} + \frac{(j\omega hX_m)R_C}{R_C + j\omega hX_m} + \frac{1}{R_S + j\omega hX_S} \qquad \text{(A4.57)}$$

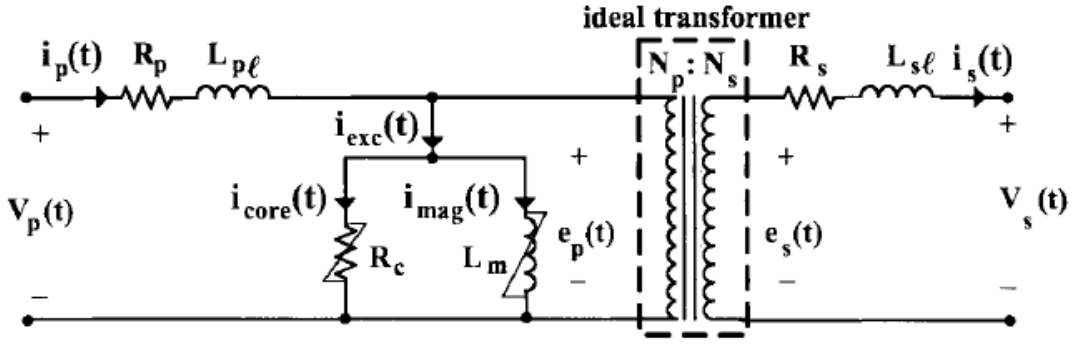

Figure A4.10. General harmonic model of a transformer

When considering the addition of a large non-linear load to an oil and gas power system, it may be warranted to perform harmonic modelling analysis of the system if it comprises 25% or more of the plant load. Harmonic modelling is a mathematical way of predicting harmonic distortion levels and potential resonances based on available power network data. All but the simplest of systems will require computer software such as MATLAB/SIMULINK to perform this analysis. Components such as transformers, capacitors, motors, and the utility system impedance are taken into account, and non-linear loads are represented by multiple frequency harmonic current sources. Such a modelling study will indicate if harmonic levels will fall within limits.

Appendix A5

A5.1. AC-DC Converter

AC-DC converters (rectifiers) are classified into two main categories i.e. controlled and uncontrolled rectifiers. In an uncontrolled rectifier, the dc output is constant if the ac input voltage is constant. These converters are classified according to their input supply and the way the diodes are connected. They are half wave, full wave bridge type and full wave centre tapped transformer type [1-5]. DC obtained from this rectifier is further converted into desired amplitude and frequency.

PWM rectifiers have replaced the conventional three phase controlled rectifier (PCR) due to their high efficiency, good voltage regulation, nearly unity power factor and small input/output filter size depending upon switching frequency. PWM rectifiers are normally operated at high switching frequency where low frequency harmonics are easily suppressed. PWM rectifiers are becoming more popular due to the availability of fast switching, high voltage and high current IGBT's [6-8].

A three-phase PWM regenerative boost rectifier [9] is shown in figure 5.5a. The output voltage is greater than the peak of the line to line RMS voltage in this rectifier. This is a four quadrant rectifier capable of bidirectional power flow. Operation of this rectifier is similar to a High Voltage Switch Mode Power Supply (HV-SMPS) boost converter. When D_{A1+} is turned on, voltage is applied across the inductor and it gets energized. When D_{A2+} is turned off, inductor de-energizes through the diode of D_{A1+} charging the capacitor. Unity power factor is achieved by controlling the current in the inductor.

Multi-level ac-dc converters can also be used to develop modular multi-level converter (MMC) as depicted in Fig.5.11. This device can act as a node device in multi-terminal network, where the first node acts as rectifier and the node directly connected to it acts as an inverter as depicted in Fig. 7.1. The preferred ac-dc converter topology is suitable for high-power applications; operates at constant frequency under a PWM strategy. The sub-module full-bridge of the modular multi-level converter consists of a DC input voltage source v_i and a six controllable switching sequence as shown in Table 7.1.

Table A5.1. Switching Sequence

Phase	Line	Switching States		
Voltage	Voltage	Leg 1	Leg 2	Leg 3
V_{a0} V_{b0} V_{c0}	V_{ab} V_{bc} V_{ca}	T_{A1+} T_{A1-}	T_{A2+} T_{A2-}	T_{A3+} T_{A3-}
0 $-V_{d2}$ V_{d2}	V_{d2} V_d $-V_{d2}$	1 0	0 1	1 0
V_{d2} $-V_{d2}$ 0	V_d $-V_{d2}$ V_{d2}	0 1	1 0	0 1
V_{d2} 0 $-V_{d2}$	$-V_{d2}$ V_{d2} V_d	1 0	0 1	1 0
0 V_{d2} $-V_{d2}$	$-V_{d2}$ V_d V_{d2}	0 1	1 0	0 1
$-V_{d2}$ V_{d2} 0	$-V_d$ V_{d2} $-V_{d2}$	1 0	0 1	1 0
$-V_{d2}$ 0 V_{d2}	$-V_{d2}$ $-V_{d2}$ $-V_d$	0 1	1 0	0 1

A5.1.1. Converter Capability Chart

The converter bridge can be represented as a variable voltage source, where the amplitude, the phase and the frequency can be controlled independently. In steady state, the fundamental frequency components of the phase voltages and the phase currents are represented in phasor diagram as shown in Fig. A5.1.

The current through the converter needs to be limited in order to protect the switching elements. Active and reactive power can be independently chosen, but must remain within certain limits. Neglecting the operating limits can lead to unrealistic consequences on the model. The three factors that limit the operation range of a HVDC-VSC model includes; current through the converter, DC voltage, and rating of the cable.

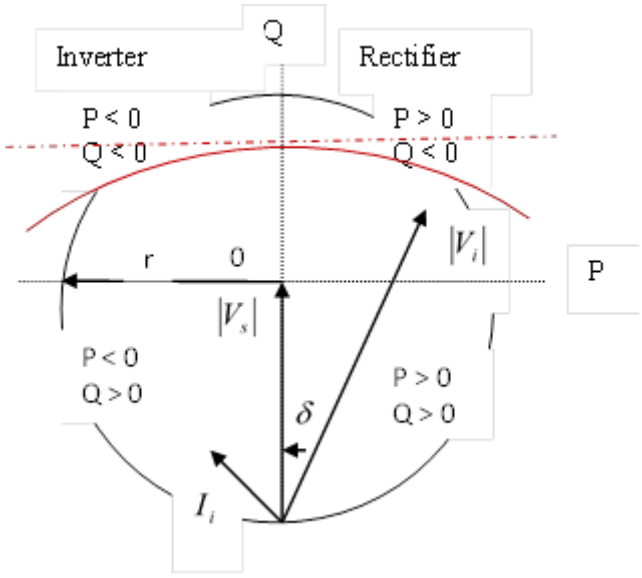

Figure A5.1. Phasor diagram of VSC equivalent model and direction of power flows (PQ)

During faults, the converter is blocked: the diodes take over the current and the switching elements are protected. The locus of maximal current in the PQ diagram (Fig. A5.1) is a circle with centre 0 at the origin, and radius r.

The apparent power in the connection point of the converter is defined by:

$$S = P + jQ = |V_s| I_i \tag{A5.1}$$

In high power applications the transformer or inductors losses are negligible when determining the active and reactive power from the converter following Fig. A5.2.

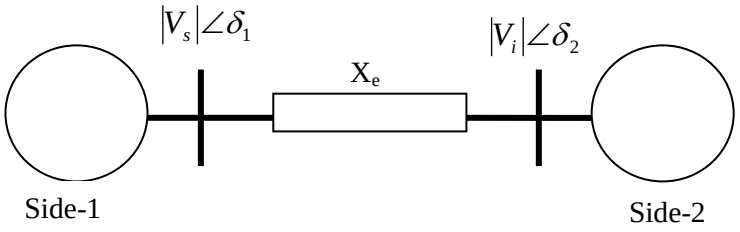

Figure A5.2. HVSC-VSC Line Model

$$P = \frac{|V_s||V_i|}{X_e}\sin(\delta_1 - \delta_2) \tag{A5.2}$$

$$Q = \frac{|V_i|^2}{X_e} - \frac{|V_i||V_s|}{X_e}\cos(\delta_1 - \delta_2) \quad \text{(A5.3)}$$

where X_e is the equivalent reactance of the coupling transformer

Real power flow:
• δ1> δ2 =>P12 is +ve: Real power flows from Side-1 to Side-2
• δ1< δ2 =>P12 is -ve: Real power flows from Side -2 to Side -1
Reactive power flow:
• |V1| > |V2|: Reactive power flows from Side -1 to Side -2
• |V1| < |V2|: Reactive power flows from Side -2 to Side -1

It can be deduced from (A5.2) and (A5.3) that the VSC neither injects nor absorbs active and reactive power from the system when $|V_i|$ - $|V_s|$ = 0, this follows that δ_{is} = 0.

Also, the VSC inject reactive power when $|V_i| > |V_s|$ and absorb reactive power when $|V_i| < |V_s|$.

As shown in Fig. A5.2 the voltage drop ΔV over the reactor X_v can be described as:

$$\Delta V = \Delta V_p + j\Delta V_q \quad \text{(A5.4)}$$

$$= \frac{R_v P + X_v Q}{V_i} + j\frac{X_v P - R_v Q}{V_i} \quad \text{(A5.5)}$$

If $\Delta V_q << V_i + \Delta V_p$

then $\Delta V \approx \frac{R_v P + X_v Q}{V_i}$

For AC networks most power circuit satisfy $X_v >> R_v$, therefore the voltage drop ΔV Knowing that depends only on the reactive power flow Q.

$$\sin^2 \delta_{is} + \cos^2 \delta_{is} = 1 \quad \text{(A5.6)}$$

Therefore, sin δ_{is} and cos δ_{is} could be eliminated, hence

$$\left(\frac{PX_e}{|V_s||V_c|}\right)^2 + \left[\left(Q + \left(\frac{|V_s^2|}{X_e}\right)\right)\frac{X_e}{|V_s||V_c|}\right]^2 = 1 \quad \text{(A5.7)}$$

and

$$\left(\frac{|V_s||V_c|}{X_e}\right)^2 = P^2 + \left(Q + \frac{|V_s^2|}{X_e}\right)^2 \quad \text{(A5.8)}$$

Equation (A5.8) is useful tools for the determination of the centre and radius of the circle of PQ diagram of Fig. A5.1. Where the centre equation is $\left(0,-\frac{|V_s^2|}{X_e}\right)$ and

radius = $\frac{|V_s||V_c|}{X_e}$.

The converter current can be obtained from the equation:

$$I_c = \frac{\sqrt{P^2+Q^2}}{|V_s|} \tag{A5.9}$$

The maximum current of the converter is determined when the reactive and active power from the energy sources at their rated values, and the grid voltage is at minimum, which yields:

$$I_{c,\max} = \frac{\sqrt{P_R^2+Q_R^2}}{|V_{s,\min}|} = \frac{\sqrt{P_R^2+(P_R tah\theta_R)^2}}{|V_{s,\min}|} \tag{A5.10}$$

Taking P_R as a mega volt ampere base of the system the previous expression can be reduced to a pu. equation

$$I_{c,\max} = \frac{\sqrt{1+\tan^2\theta_s}}{|V_{s,\min}|} \tag{A5.11}$$

The converter voltage is obtained as:

$$\left(\frac{|V_c||V_s|}{X_e}\right) = P^2 + \left(P\tan\theta + \frac{|V_s^2|}{X_e}\right)^2 \tag{A5.12}$$

$$\Rightarrow |V_c| = \frac{X_e}{|V_s|}\sqrt{P^2+\left(P\tan\theta+\frac{|V_s^2|}{X_e}\right)^2} \tag{A5.13}$$

The maximum current of the converter is determined when the reactive and active power from the wind power plant (WPP) at their rated values, and the grid voltage is at minimum, which yields:

$$|V_{c,\max}| = \frac{X_e f_{\max}}{|V_{s,\max}|}\sqrt{1+\left(\tan\theta_s+\frac{|V_{s,\max}^2|}{X_e f}\right)^2} \tag{A5.14}$$

The maximum reactive power injection capability is given as

$$Q = \min(Q_c, Q_v) \tag{A5.15}$$

where

$$Q_c = \sqrt{\left(|V_s||I_{c,\max}|\right)^2 - P^2}$$ - the converter-current-rating

$$Q_v = \sqrt{\left(\frac{|V_{c,\max}||V_s|}{X_e}\right)^2 - P^2} - \frac{|V_s^2|}{X_e}$$ - the converter-voltage-rating limits

A5.2. Operation Modes

The operating modes which can be adopted in AC and DC sides of each station are examined.

A5.2.1. AC side Operating Modes

VSC on its AC side can either control the reactive power or AC voltage at the point of the common connection (PCC) as depicts in Fig. 7.4.

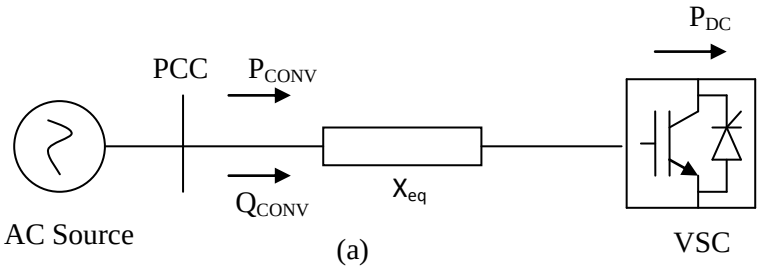

(a)

Active and reactive power control mode

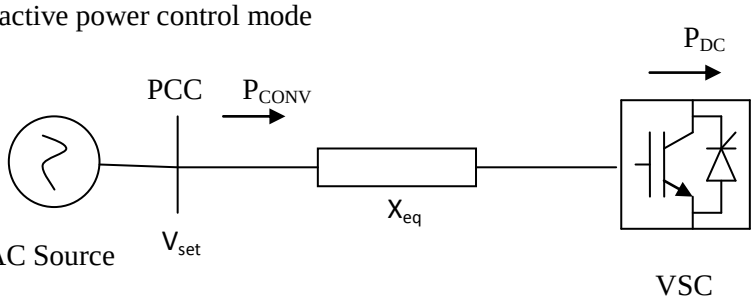

(b)

Active and AC voltage control mode

Figure A5.3: (a) PQ bus connected to VSC converter.(b) PV bus connected to VSC converter.

If in an *N* multi-terminal HVDC-VSC, the reference power of all converters at the PCC is known, every PCC from AC system's point of view can be seen as either a PV or PQ bus depending on the control mode of converter connected to that bus as shown in

Figure A5.3. Therefore all *N* converters excluding the slack converter can be separately modelled at each AC bus.

A5.2.2. DC side Operating Modes

In a two terminal VSC-HVDC, at least one of the two converters must have dc voltage regulation mechanism for normal operation of a point-to-point VSC-HVDC connection. Similarly, in a multi-terminal VSC-HVDC configuration there must be dc voltage regulation for normal operation of the system. As described in the previous chapter there are two options for dc voltage control of a single VSC station; namely: constant dc voltage control and dc voltage droop control. It was also mentioned in section 2.5 that stable operation cannot be achieved if both converters of the two-terminal VSC-HVDC are assigned to constant dc voltage control mode.

The same condition applies to multi-terminal VSC-HVDC, i.e. there must not be more than one converter station in the dc grid assigned to constant dc voltage control mode. (If there are two converters with constant dc voltage control, there will be a hunting phenomena, analogous to frequency hunting in ac grids in the presence of multiple synchronous generators with fixed frequency control). Taking the constraints mentioned above, we get three possible control modes of MTDC; namely: master-slave control, dc voltage droop control and master-slave with dc droop. Each of these is explained below.

A5.2.3. PQ Bus/Load Bus

A pure load bus is a ***PQ*** bus. A load bus has no generating facility, that is,

$\boldsymbol{P_{G1}} = \boldsymbol{Q_{G1}} = 0$.

At this type of bus, the net real power $\boldsymbol{P_i}$ and the reactive power $\boldsymbol{Q_i}$ are known as

$$P_i = P_{G1} - P_{D1} \text{ and } Q_i = Q_{G1} - Q_{D1} \qquad \text{(A5.16)}$$

$\boldsymbol{P_i}$ known ($\boldsymbol{P_{Di}}$ known, $\boldsymbol{P_{Gi}}$ zero)
$\boldsymbol{Q_i}$ known ($\boldsymbol{Q_{Di}}$ known, $\boldsymbol{Q_{Gi}}$ zero)
$\left|\tilde{V}_i\right|$ unknown – this is voltage magnitude
δ_i unknown – this is voltage angle

where

P_{G1}, Q_{G1} are the real and reactive power generations at the bus respectively
P_{D1}, Q_{D1} are the real and reactive power demands at the bus respectively
P_{G1} and Q_{G1} are specified and P_{D1} and Q_{D1} are known from forecasting

A5.2.4**. PV Bus/Generator Bus**

A generator whether wind or gas turbine are always connected to a ***PV*** bus. Therefore the net power $\boldsymbol{P_i}$, known as $\boldsymbol{P_{Di}}$ is known from forecasting
$\mathbf{P_i}$ known
$\mathbf{Q_i}$ unknown
$\mathbf{P_i}$ known ($\mathbf{P_{Gi}}$ specified, $\mathbf{P_{Di}}$ known)
$\left|\tilde{V}_i\right|$ known (specified)
$\mathbf{Q_i}$ unknown ($\mathbf{Q_{Di}}$ unknown, $\mathbf{Q_{Gi}}$ known)
δ_i unknown

A5.2.5. **Slack Bus/Swing Bus/Reference Bus, Generator with Larg Capacity**

In this bus, normally voltage magnitude is set to 1 pu and voltage angle is set to zero. The real and reactive powers are not specified.

$\left|\tilde{V}_1\right|$ known (specified)
δ_1 known (specified, typically $\delta_1 = 0 \Rightarrow$ reference)
$\mathbf{P_1}$ unknown ($\mathbf{P_{D1}}$ known, $\mathbf{P_{G1}}$ unknown)
$\mathbf{Q_1}$ unknown ($\mathbf{Q_{D1}}$ known, $\mathbf{Q_{G1}}$ unknown)

Real and reactive powers cannot be fixed prior at all the buses, since the net complex power flow into the network is not known beforehand. Therefore, the power losses are unspecified until the load flow study is ended. This follows that it is imperative to have one bus at which complex powers is unspecified as to supply the difference in the total system load with losses. Also, the sum of the complex powers known at the other buses. This type of bus is named swing bus and irrevocable termed generator bus. On the event that the swing bus is not known, then the bus connected to the largest generating station is usually chosen as the reference bus. It should be reiterated here that wind farm (wind turbine) bus should not be named slack bus, due to its variable voltages as a result of wind speed variation.

Table A7.1. Line parameter

From Bus	To Bus	R pu	X pu	B/2 pu	X'mer TAP (a)
1	2	0.0192	0.0575	0.0264	1
1	3	0.0452	0.1652	0.0204	1
2	3	0.0600	0.1800	0.0200	1
2	4	0.0570	0.1737	0.0184	1
3	4	0.0132	0.0379	0.0042	1
2	5	0.0472	0.1983	0.0209	1
4	5	0.0581	0.1763	0.0187	1

Table A7.2. VSC multi-terminal bus data

Node	Vsp	theta	PGi	QGi	PLi	QLi	Pmin	Pmax	Bus Type
1	50	0	40	0	0	0	0	40	PV
2	100	0	100	0	0	0	0	60	PV
3	40	0	0	0	-5	-10	10	30	PQ
4	40	0	0	0	-20	-30	5	25	PQ
5	40	0	0	0	0	0	0	0	Slack

P =

1.0e+003 *

2.2326
0.0009
0.0000
0.0002
-0.0000

Q =

1.0e+004 *

-0.9822
2.4605
0.0000
0.0000
-0.9111

J =

1.0e+004 *

9.1856	-1.6072	-1.5282	-1.7197	-0.0111	-0.0109
-1.6487	4.0556	-1.4091	0	0.0172	-0.0011
-1.5581	-1.4078	3.8949	-0.9290	-0.0015	0.0209
-1.8581	0	-1.0050	2.8631	0	-0.0069
0.4803	-0.9368	0.0582	0	0.0746	-0.0274
0.4694	0.0839	-1.0759	0.5226	-0.0259	0.0756

Bus No	kV pu	Angle Degree
1	50.0000	0.0000
2	99.9600	-32.2111
3	74.4223	-25.1607
4	71.8498	-28.7345
5	40.0600	-19.9862